ROLE OF CRYSTALLOGRAPHIC TEXTURE AND GRAIN SIZE ON LOW TEMPERATURE DEFORMATION AND FORMABILITY OF A MG ALLOY

A Dissertation

by

EBUBEKIR DOGAN

Submitted to the Office of Graduate Studies and Professional Studies of
Texas A&M University
in partial fulfillment of the requirements for the degree of

DOCTOR OF PHILOSOPHY

Chair of Committee,	Ibrahim Karaman
Committee Members,	Raymundo Arroyave
	Ahmed Amine Benzerga
	Karl Ted Hartwig
Head of Department,	Andreas A. Polycarpou

December 2014

Major Subject: Mechanical Engineering

ABSTRACT

Interest in Mg alloys has significantly increased in recent years for weight-critical applications. However, Mg alloys show low strength and poor low temperature formability, due to the limited available slip systems and the strong final texture in wrought products. This limits extensive usage of Mg as a structural material. Mg alloys have a hexagonal close-packed crystal structure that shows lower symmetry compared to its cubic counterparts, which causes activities of various Burgers vectors and slip planes under different stress fields. In this study, it was shown that detailed knowledge of multiple deformation mechanisms can be utilized to engineer the microstructure and flow anisotropy of magnesium alloys, subjected to severe plastic deformation, for ultrahigh strength, ductility, and formability.

Using a microstructure based visco-plastic self-consistent crystal plasticity model with detailed electron backscatter diffraction analyses and transmission electron microscopy, new equal channel angular processing (ECAP) methodologies were developed in order to achieve the desired microstructure and grain refinement to a few hundred nanometers. Both experimental and simulation results clearly indicated that the formation of compression/double twins causes deformation localization, followed by dynamic recrystallization within the twins. This non-uniform DRX causes local softening and macro shear banding, and eventual failure. However, it was shown that with proper modification of the texture and grain size, the shear localization and macro shear bands can be suppressed by limiting the twinning activity and, instead, promoting

non-basal slip activities at low temperatures (<200°C). These studies led to the ultrahigh strength levels in the Mg-3Al-1Zn (AZ31) alloy.

To date, ECAP of Mg alloys is limited to bar/billet form, and a scale-up of the ECAP technology was not utilized for Mg plate and sheet processing. This work is one of the initial studies where commercially available wrought AZ31 plates are processed via the equal channel angular plate extrusion (ECAPE) tool in order to refine grains and weaken the strong wrought texture. The ECAPE tool provided scaled-up samples for further tests, such as stretch formability, a capability which was not possible with bar samples. It has been shown that ECAPE processing tremendously increased the room temperature stretch formability of AZ31 alloy sheets.

To my wonderful parents, my lovely wife and my precious son for their tremendous support

ACKNOWLEDGEMENTS

First of all, I would like to thank my graduate advisor, Dr. Ibrahim Karaman, who gave his endless encouragement and support during my six years of graduate studies. He has been a good model for me, influencing me in almost every aspect of my academic life with his great enthusiasm for research.

Thanks also to my committee members, Dr. Amine Benzerga, Dr. Raymundo Arroyave, and Dr. Ted Hartwig, for sharing their valuable suggestions during my study.

I would like to express my gratitude to Dr. Georges Ayoub and Dr. Yuriy Chumlyakov for their valuable help with my research and generous sharing of their knowledge and experience with me. Additionally, a very special thanks to Dr. Gwenaelle Proust for her invaluable help on EBSD experiments and for comprehending the results. Also, special thanks to Dr. Ghassan Kridli for assisting with stretch formability tests and explaining the results. I am also thankful to Dr. Shujuan Wang for her tremendous help and endless patience during TEM sessions. Furthermore, a very special thanks to Robert Barber, P.E., for his help primarily with equal channel angular extrusion, but also including many additional engineering problems.

I also wish a very special thanks to the best undergraduate researcher, Matthew Vaughan, for his very valuable help with this study. Without his help, this dissertation would not be finished by this date.

Furthermore, I also wish to thank my colleagues with whom I have worked with over the years: Murat Kaynak, Ji Ma, James Monroe, Can Atli, Nevin Ozdemir, Alper

Evirgen, Ruixian Zhu, Sonia Razavi, Pinar Karpuz, Ceylan Hayrettin, Ankush Kothalkar, Nick Barta, Taymaz Jo, Nick Bruno, Li-Wei Tseng, Liangfa Hu, Brian Franco, Hande Ozcan, and Omer Karakoc, who provided a great environment and support during my study. A special thanks to Murat Kaynak, Alper Evirgen, Ceylan Hayrettin, and Hande Ozcan for their great friendship both in work and social life.

Additionally, I would like to thank my mother, Hacer, and father, Ali, who have provided their endless love, support, and trust throughout my life. I would like to thank my sisters and brothers for their continuous support, and have always felt very lucky for having them.

Finally, I would like to express my very special thanks to my wife, Ceyda, for her never-ending patience, support, and love. She is the best young mother and the best wife in the world, who has consistently self-sacrificed for us. Words cannot adequately express how much I appreciate her and what she has brought to my life. Last but not least, I would like to thank to my son for the peace and happiness he brings to my life each day.

TABLE OF CONTENTS

CHAPTER Page

CHAPTER Page

LIST OF FIGURES

Page

Page

Page

Page

Page

Page

Page

LIST OF TABLES

CHAPTER I

INTRODUCTION AND LITERATURE REVIEW

1.1 Motivation

Currently, there exists a pressing need for lightweight structures for energy conservation, better fuel economy, and lower exhaust emissions, creating a tremendous interest in lightweight structural materials. The low density of Mg (1.74g/cm^3) makes it attractive for structural applications since it has high specific stiffness and specific strength among all structural materials. Interest in magnesium alloys has increased in recent years for weight-critical applications, especially in the transportation industry (automotive and aerospace). In addition, due to its high bio-degradability, Mg alloys are a promising material for future biomedical applications such as resorbable stents and bodily implants. The growing interest in the use of these once-forgotten alloys has generated a need for developing a detailed understanding of successful processing techniques to both enhance the material properties and reduce production costs.

A few challenges still exist for extensive use of Mg alloys, primarily due to the limited low-temperature formability, a consequence of their hexagonal closed packed (hcp) crystalline structure and an insufficient number of active slip systems especially at low temperatures (defined here as below 200°C). The low symmetry crystal structure, hcp, causes activities of different Burgers vectors and slip planes under different stress fields at different temperatures. Twinning is an additional deformation mode in Mg

alloys which leads to low temperature anisotropy, tension-compression asymmetry, and additional strain hardening.

To date, the majority of Mg components are produced by die-casting. Although wrought Mg alloys show superior mechanical properties for structural components, their use has not progressed significantly. Pronounced texture in wrought forms of Mg alloys is another limiting factor for low temperature formability, in addition to the limited available slip systems. Wrought Mg alloys exhibit a strong basal texture (i.e. the c-axes are mostly perpendicular to the rolling plane or extrusion direction). This predominantly basal texture negatively affects the formability and causes high anisotropy at low temperatures due to the large differences in the critical resolved shear stresses (CRSS) of basal and non-basal slip systems, as well as twinning modes [1].

An effective method for improving formability and strength of Mg alloys has been shown to be altering the microstructure and refining the grain size through severe plastic deformation. Alloying with rare-earth (RE) metals can also improve the low temperature formability by increasing the non-basal slip activity and weakening the basal texture [2-7]; however, those RE elements are relatively expensive and not readily available.

Formability of a Mg alloy was significantly improved by weakening the basal texture through thermo-mechanical treatment[8]. The grain refinement was shown to promote non-basal slip activities which enhance the ductility[9]. For this purpose, equal channel angular processing (ECAP) has been utilized for grain refinement and crystallographic texture change in Mg alloys [10-19]. The ECAP can refine the

microstructure and induce various deformation textures, in contrast to the conventional rolling process of Mg alloys [12, 14]. In addition, since the cross section of the sample does not change during ECAP, multiple passes are possible to achieve further grain refinement and adjustment of the deformation texture.

It is widely reported that crack or localization-free ECAP (and other thermo-mechanical processing techniques) of Mg alloys are possible at temperatures above 200°C [10-14, 20-21]. At these temperatures, a much higher strain rate sensitivity [22-23], significant dynamic recrystallization (DRX) activity [24], and a non-basal slip activity are evident [23].

However, grain refinement via ECAP is limited to the micron level since 200°C, at ~0.5Tm, is still a relatively high processing temperature for Mg alloys. Therefore, one must process Mg alloys at lower temperatures (i.e. below 200°C) in order to obtain an ultra-fine (<1μm) grained microstructure. However, macro-defect-free thermo-mechanical processing of Mg–3Al–1Zn (AZ31), the most common wrought Mg alloy, is a challenge at temperatures below 200°C due to deformation localization in combination with the formation of shear bands [20]. To the best of our knowledge, only the effects of macroscopic parameters on formability, such as the strain hardening rate and the strain rate sensitivity, have been previously investigated [20, 22]. The microscopic reasons for shear band formation and DRX during ECAP of Mg alloys remain unclear. Specifically, to the extent of the author's knowledge, the roles of deformation modes on shear band formation during ECAP have not been investigated.

Grain size was effectively refined down to <1μm by utilizing the multi-pass, multi-temperature ECAP [15-16, 18]. However, these complex multi-temperature hybrid route processing schemes requires additional processing steps at higher temperatures (~200°C) prior to processing at lower temperatures to obtain ultra-fine grained microstructure. In addition, the strength and the ductility is highly depends on the loading direction.

As twinning causes non-uniform deformation and yield asymmetry, the suppression of twinning seems to be a logical solution to improve formability of AZ31 at low temperatures. In addition, promotion of non-basal slips could be possible at low temperatures under certain stress states. It is possible for a simulation based approach to guide the experimental study and reduce the processing temperature of AZ31 by suppressing the twining and promoting the non-basal slip during processing. In the past, a viscoplastic self-consistent (VPSC) crystal plasticity model[25] and the predominant twin reorientation (PTR) scheme [26] was successfully employed to simulate plastic deformation and the corresponding texture evolution of Mg alloys [2, 12, 14, 27].

To date, ECAP of Mg alloys are limited to bar/billet form, and a scale-up of the ECAP technology was not utilized for Mg plate and sheet processing. This work is one of the initial studies where commercially available wrought AZ31 plates are processed via the equal channel angular plate extrusion (ECAPE) tool. The ECAPE tool provides a new, unconventional processing route and scaled-up samples for further tests, such as stretch formability, a capability which was not possible with bar samples.

1.2 Objectives

Despite the different studies focused on various aspects of magnesium alloy research, some of the fundamental issues about these alloys still remain unclear. Fundamental understanding of low temperature (<200°C) plasticity of Mg alloys is scarce in the literature. Some examples include low temperature formability, failure mechanisms and low temperature DRX; shear band formation, grain size effect on slip and twinning modes; effect of texture and grain size on stretch formability.

The AZ31 Mg alloy is selected for this study since it is the most common commercially available Mg alloy that can be found in various forms, such as rods, sheets, plates and coils. Since it has good room-temperature strength and ductility combined with corrosion resistance and weldability, it is used in a large variety of applications. In addition, since it has single phase microstructure, it is easy to model the deformation and deformation texture.

A large number of studies focused on high temperature (>200°C) processing and DRX behavior of AZ31 [12, 14, 24, 28-35]. However, a detailed investigation of low temperature plasticity, DRX, failure mechanisms of AZ31, and the role of deformation modes on these properties is scarce in the literature.

Upon the above short background and some brief objectives, more explicitly, the objectives of this study can be briefly summarized in the following list:

1. A fundamental understanding of low temperature plasticity, dynamic recrystallization (DRX), and failure mechanisms of Mg alloys will be achieved via the use scanning electron microscopy (SEM), electron back-scattered

diffraction pattern (EBSD), and transmission electron microscopy (TEM) analyses. The results will be combined with the VPSC model to understand the role of deformation modes on DRX mechanisms, shear band formation, and ductility in the AZ31 Mg alloy.

2. An investigation into deformation modes' effect on ductility, the failure mechanisms, and the DRX at temperatures between 25 and 200°C will be conducted via uniaxial mechanical tests of samples cut from a strongly basal textured, wrought AZ31 plate. Since the highly textured samples will be orientated differently with respect to the loading axis, mainly one deformation mechanism will be favorable in each case. VPSC modeling will be used to quantify relative activity of each deformation mode and to investigate coupled deformation and damage mechanisms. Detailed microstructural investigation including SEM and EBSD of tested samples will address possible failure mechanisms. Additionally, crystallographic orientation maps, along with the predicted deformation mode activities, will reveal more clearly the role temperature and deformation modes play on the ductility and the DRX mechanism for these alloys.
3. This study identifies the role that various starting crystallographic textures and deformation modes have on the shear formability of AZ31 Mg alloy at temperatures below 200°C. At these temperatures, the material shows large flow strength anisotropy, deformation twinning, and tension-compression asymmetry. VPSC modeling will be employed to design new low temperature (<200°C)

ECAP routes by alternating the starting texture and thus the active deformation modes. This will be the first study, to the best of our knowledge, where twinning will be considered in an ECAP simulation. Specifically, the role of deformation modes on shear formability, shear band formation, and DRX after large straining by ECAP will be studied. Incorporation of EBSD and TEM analyses of deformed samples with the predicted deformation modes will be one of the unique features provided in this study.

4. An analysis of the secondary particle formation during uniaxial testing and ECAP of AZ31 Mg alloy at lower temperatures (<200°C) will be conducted. Detailed SEM and TEM investigations will be performed to characterize the secondary particles.
5. Under a carefully selected starting texture, processing of AZ31 Mg alloys will be performed via equal channel angular processing (ECAP) at 150°C and lower temperatures under multiple passes to obtain an ultra-fine grained bulk material. As a result of the low processing temperatures, the grain size of the AZ31 alloy will be systematically refined from micron range to submicron range via ECAP. The ultimate goal is to obtain a grain size around 100-500 nm to monitor the Hall-Patch relation of different deformation modes in different grain size ranges (micron and nano).
6. An investigation into the mechanical behavior of ECAP processed AZ31 alloy samples by determining flow stress anisotropy and tension-compression asymmetry as functions of grain size and texture will be conducted. Here, the

effect of grain size on tension-compression asymmetry due to twinning will be studied, and the twinning nucleation mechanism in ultra-fine grains will also be investigated. TEM investigations will be performed to have a detailed study of the aforementioned phenomenon.

7. Processing large wrought AZ31 samples in plate and sheet form via the ECAPE tool, to weaken the strong basal texture and refine the grains, will be conducted. Room temperature mechanical behavior of ECAPE processed samples will be examined as the function of processing temperature and routes. Stretch formability tests on ECAPE processed sheets will be conducted to disclose the effect of texture and grain size on formability. The optimum grain size and crystallographic texture that promotes uniform plastic deformation will be identified.

1.3 Background and Literature Review

1.3.1 Deformation Mechanisms of Magnesium Alloys

Mg alloys have the hcp crystal structure, which exhibits lower symmetry compared to its cubic counterparts. This causes activation of different Burgers vectors and slip planes under different stress fields and temperatures. At low temperatures (<200°C), the predominant deformation modes of Mg and its alloys are basal slip and $\{10\bar{1}2\}$ tension twinning owing to their very low critical resolved shear stresses (CRSS) [36]. Basal slip, as the softest slip mechanism in Mg and its alloys, is thus frequently

responsible for accommodating a significant amount of plastic strain at ambient and low temperature deformation [37]. However, basal slip provides only two independent slip systems, which is not enough for Von Misses criterion (requires five).

Prismatic and pyramidal <a> slips are non-basal slips providing <a> type dislocations. It was argued that pyramidal <a> slip does not provide an additional independent slip mode since the strain accommodation by pyramidal <a> slip can be accumulated via a combination of basal and prismatic slips [37]. Prismatic slip provides two independent slip systems [37]. Earlier, pure Mg single crystal studies showed CRSS of prismatic slip as to be 50-100 times higher than the basal slip at room temperature as given in Fig.1.1 [38]. Pyramidal $\{11\bar{2}2\}$ (referred to as 2nd order or <c+a>) slip is the most difficult slip system to activate due to its larger Burger vector ($|<c+a>| \sim 1.9 |<a>|$) compared to <a> type dislocations. The activation of this slip system is crucial for the plasticity of Mg alloys since it is the only slip system providing c-axis deformation. In addition, it provides five independent slip systems. Prismatic and pyramidal <c+a> slip systems are usually active at elevated temperatures due to very high CRSS at low temperatures [23, 38]. It's worth mentioning here that activation of these slip systems was shown even during room temperature deformation of some Mg alloys [9, 39-40] depending on the initial texture and strain level. In addition, alloying with RE elements promotes activities from these non-basal slip systems at room temperatures [40].

Deformation twinning plays an important role in the plastic deformation of hcp metals such as Mg and its alloys. It is reported that twinning shear is related to the axial

ratio (c/a) of hcp crystals [41]. Fig.1.2 presents twinning shear versus axial ratio for the seven hcp metals [41-42]. The active twinning modes are given in filled symbols for the given metal. Mg c/a ratio is 1.624, an indication that $\{10\bar{1}2\}$, $\{10\bar{1}1\}$, and $\{10\bar{1}3\}$ twinning modes are the most commonly activated ones (Fig.1.2). Specifically, $\{10\bar{1}2\}$ twinning is readily active at low temperatures, and, as it provides extension along the c-axis, is dubbed tension (extension or tensile) twinning. The $\{10\bar{1}1\}$ and $\{10\bar{1}3\}$ twinning, alternative twinning modes observed in Mg alloys, provide c-axes contraction and are termed compression (contraction) twinning.

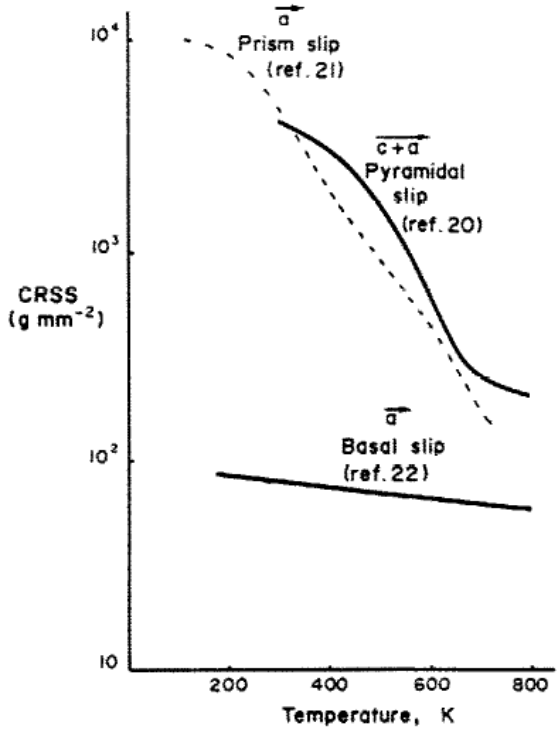

Figure 1.1 The CRSS of basal, prismatic and pyramidal<c+a> slip systems in pure Mg [38]

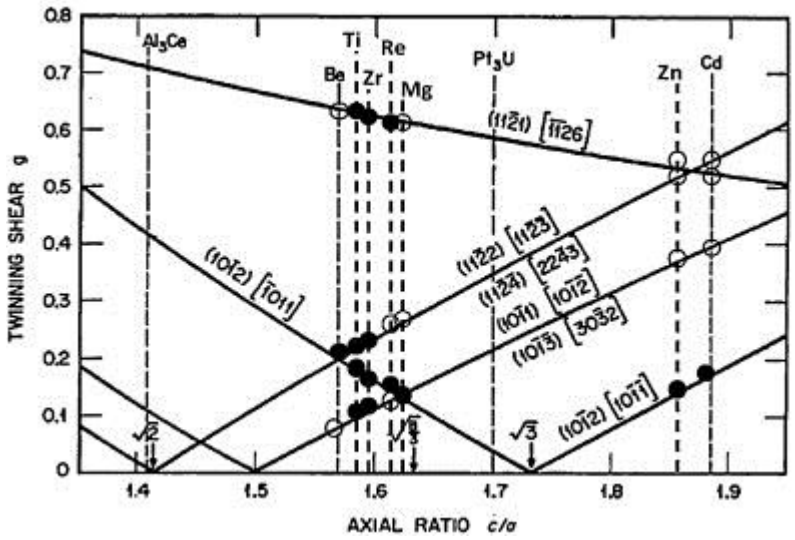

Figure 1.2 Twinning shear versus axial ratio. For the seven HCP metals, the filled symbols indicate that the twin mode is active [41-42].

The most commonly activated deformation systems in Mg alloys are shown in Figure 1.3. Here, note that c-axes deformation of the hcp unit cell can only be accommodated by pyramidal slip <c+a> and deformation twins (either tension or compression), as these have Burgers vectors along the c-axis [36, 43].

The CRSS of different deformation modes in magnesium single crystals were experimentally determined by several studies [1, 43-46]. Single crystal studies of Mg alloys (i.e. the AZ series) are scarce in the literature due to the difficulty of growing single crystals of these alloys. Most of the CRSS values reported for Mg alloys are acquired from crystal plasticity simulations [2, 27, 47-48]. Alloying elements considerably alter the CRSS of deformation systems and consequently the active deformation modes [2, 40, 42, 46]. Although the level of CRSS differences of deformation modes show very wide variations [1, 49], room temperature CRSS of

different deformation modes for magnesium based alloys can be compared as the following:

Basal < Tension Twinning ≤ Prismatic < Pyramidal < Compression Twinning

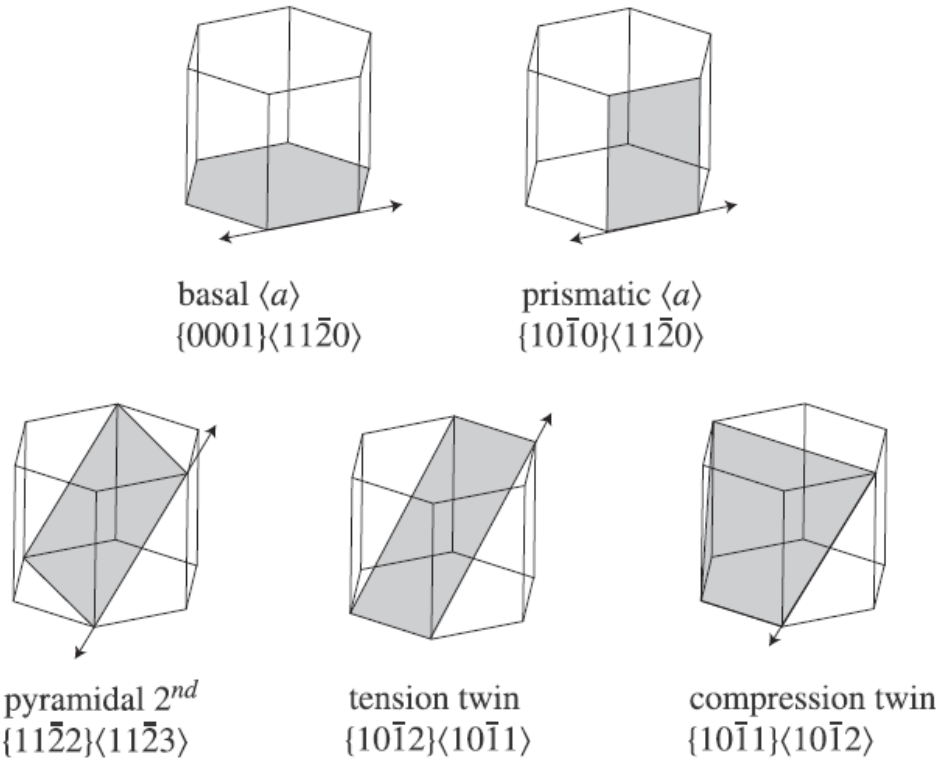

Figure 1.3 Most common deformation modes of Mg alloys [47].

It was demonstrated that the CRSS of basal slip and tension twinning shows less temperature dependency, whereas prismatic and pyramidal<c+a> slip CRSS values are highly temperature-dependent and decrease significantly with temperature increase (Fig 1.1&Fig.1.4) [1, 27, 38]. Recently, a single crystal Mg study along with previously published literature data revealed that $\{10\bar{1}1\}$ and $\{10\bar{1}3\}$ compression twins have

higher CRSS values than other modes, yet such CRSS values decreased considerably with increasing temperature, similar to the phenomenon observed for prismatic and pyramidal <c+a> slips (Figure 1.4) [1].

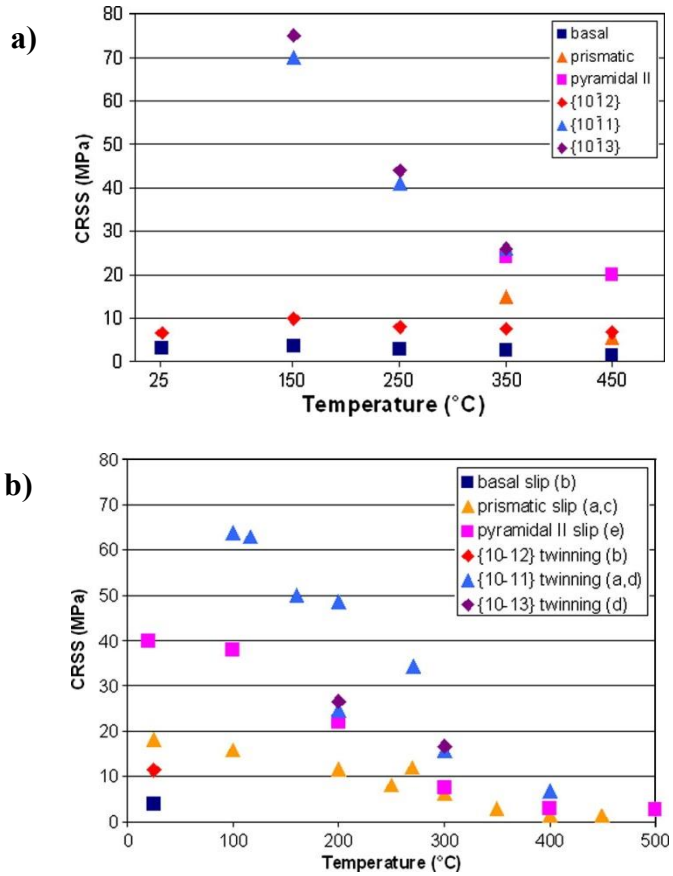

Figure 1.4 (a) Estimated CRSS of slip and twinning systems in Mg at 1% strain. (b) Previously published Mg CRSS data from different sources [1].

Prismatic slip was found to be considerably active at even room temperature in the most common wrought AZ31 alloy under certain loading conditions [39, 50]. Solute strengthening of Mg (i.e. with Al and Zn) was shown to harden basal slip and soften the

prismatic slip[46]. Therefore, prismatic slip activity is expected to be more active than Pyramidal<c+a> slip, which is difficult to activate at low temperatures due to its relatively high CRSS compared to other systems[38, 43].

1.3.1.a Role of twinning modes on fracture

Although in many studies tension twinning was shown to be an extra source of ductility [27, 51], twinning is also known to deteriorate the ductility/formability [37] via early failure due to crack formation inside twins and along twin boundaries. Especially at high strains, localized compression twinning was widely observed when the c-axis of the Mg alloys experienced compression [39, 52]. However, compressive twins (either the $\{10\bar{1}1\}$ or $\{10\bar{1}3\}$ planes) and double twins ($\{10\bar{1}1\}$-$\{10\bar{1}2\}$) act as sources of fracture at low temperatures due to localization and micro-cracking in these regions [52-54]. Figure 1.5 [54] shows a micro-crack formed parallel to the compression and double twin boundaries. Tension twin boundaries are also evident near the crack, but usually the tension twin boundaries are perpendicular to the crack.

1.3.2 Processing & Forming of Magnesium and Its Alloys

It is well known that poor low temperature ductility of Mg alloys is a consequence of a limited number of deformation systems [55]. Deformation modes of Mg with their number of independent systems are given in Table 1.1. Readily activated basal slip provides two independent slip systems, but the Taylor criterion requires 5 independent slip systems. Thus, limited ductility is obvious when non-basal slip systems

are not active at low temperatures (<200°C). In addition, formability is hindered by both the very low strain rate sensitivity [23] and the limited DRX potential at temperatures below 200°C. Mechanical twinning is a source of extra ductility by providing more independent deformation modes, but it is not as effective as a slip system due to its unidirectional nature. In addition, in Mg only one twinning mode ($\{10\bar{1}2\}$ tension) is readily active at low temperatures, while additional twining systems are profusely active in hcp materials (i.e Zr, Ti) which exhibit extensive ductility [41].

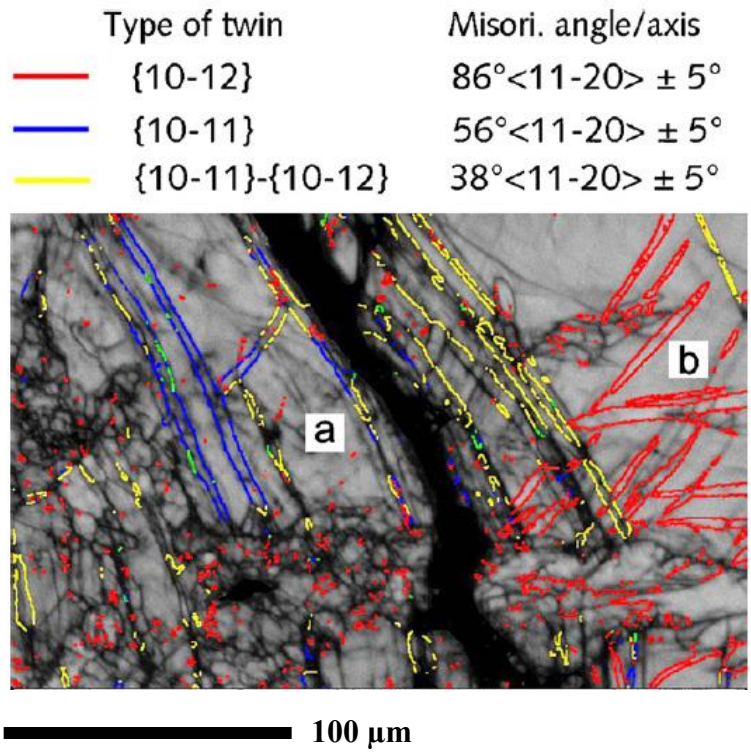

Figure 1.5 EBSD-Kikuchi band contrast map showing a twin sized void parallel to existing $\{10\bar{1}1\}$-primary twin boundaries and $\{10\bar{1}1\}$-$\{10\bar{1}2\}$ double twin boundaries (area a), and $\{10\bar{1}2\}$ twin boundaries (area b) that are formed perpendicular to the void [54].

The pronounced fiber texture in wrought Mg alloys further deteriorates the mechanical isotropy of Mg alloys, causing poor formability at low temperatures (<200°C). Low temperature formability can be improved by weakening the basal fiber texture in Mg alloy sheets [56-64] through different process techniques, including multiple step rolling at different temperatures and differential speed rolling. Differential speed rolling is a new processing technique that introduces intense shear deformation and modifies the texture and microstructure of the Mg sheets [34, 59]. However, the texture gradient and the non-uniformly deformed through thickness are some disadvantages of this technique, in addition to thickness limitation [65-66].

Table 1.1 Deformation modes in Mg alloys

Deformation mode	**Slip Plane and direction**	**# of independent slip systems**	**# of variants**
Basal<a>	$\{0001\}<11\bar{2}0>$	2	-
Prismatic<a>	$\{10\bar{1}0\}<11\bar{2}0>$	2	-
Pyramidal<c+a>	$\{11\bar{2}2\}<11\bar{2}3>$	5	-
Tensile Twinning	$\{10\bar{1}2\}<10\bar{1}1>$	-	6
Compression twinning	$\{10\bar{1}1\}<10\bar{1}2>$	-	6

Figure 1.6 shows the values of limiting dome height (LDH) that were measured by the Erichsen cupping tests at room temperature as a function of room temperature

yield strength, which was well summarized in [67] using different literature data. LDH is a good indication for stretch formability of the tested sheet. As seen in Fig.1.6, RE-containing and texture-modified AZ series alloys have good stretch formability comparable to Al alloys [67]. Please note that these LDH values are from the Erichsen cupping tests with different sample thickness and sizes. A better comparison can be done by normalizing the punch radius with the sheet thickness and then comparing it with the LDH values [68].

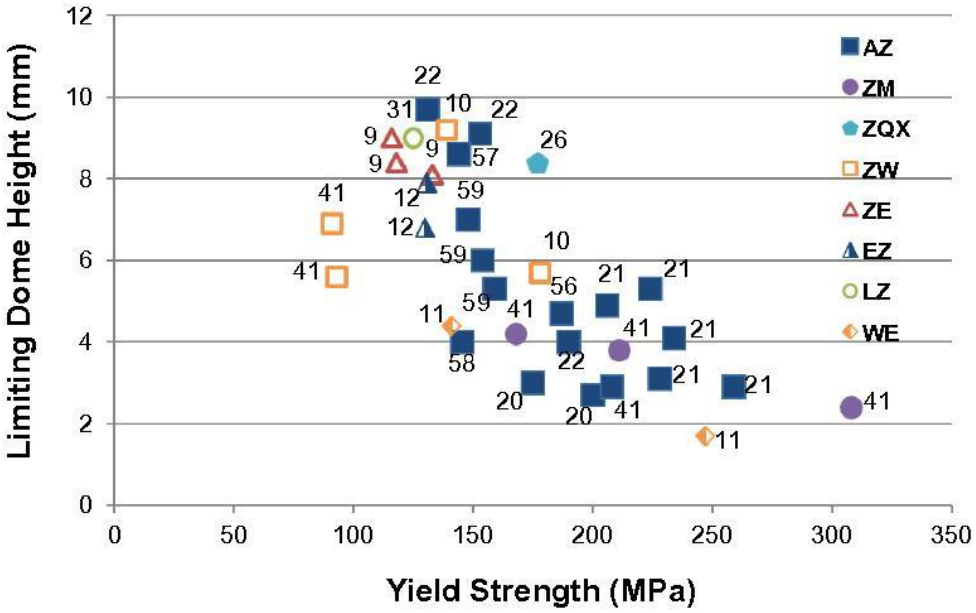

Figure 1.6 Room temperature limiting dome height values vs. yield strengths of different Mg sheet alloys [67]. The numbers adjacent to the data points belong to the reference number given in [67].

1.3.2.a Equal channel angular processing (ECAP) of Mg alloys

As briefly mentioned above, one effective method for improving formability and strength of Mg alloys is to alter the microstructure through severe plastic deformation.

One of the most common and efficient severe plastic deformation methods is ECAP that was invented in 1981 by Segal [69]. The general ECAP tool is shown in Fig. 1.7. The tool is a block with two intersecting channels with the same cross-sectional area. Usually, back pressure is applied to increase hypostatic pressure and create a more uniform deformation [22, 70]. When the sample is moved inside the die, a deformation is applied to the sample by simple shear at the crossing plane of the channels. The magnitude of simple shear (γ) along the crossing plane is dependent on the die angle ϕ and the corner angle ψ and estimated[69, 71] with the following equation

$$\gamma = 2\cot\left(\frac{\phi}{2}+\frac{\psi}{2}\right)+\psi\,\mathrm{cosec}\left(\frac{\phi}{2}+\frac{\psi}{2}\right) \quad (1)$$

When the corner angle is sharp and $\psi = 0$

$$\gamma = 2\cot\left(\frac{\phi}{2}\right) \quad (2)$$

In order to apply intensive shear, ϕ should be sufficiently small. When $\phi < 90°$ a dead metal zone is formed at the die corner [72]. Thus, the optimum angle for maximum shear is ϕ=90°. ECAP has been utilized for grain refinement and crystallographic texture change in Mg alloys [10-18]. It is widely reported that crack/localization-free ECAP (with ϕ=90°) of Mg alloys is possible at temperatures above 200°C [10-14, 20-21]. Figure 1.8 shows the images of AZ31 billets that were ECAP processed at different temperatures with different stain rates [20]. As seen in the figure, it wasn't possible to process an AZ31 specimen at 150°C with a die having ϕ =90° and $\psi = 20$ [20]. However, at 200°C and 250°C, it was successfully ECAP

processed with a reasonable extrusion speed. Different processing routes (Fig. 1.8) can be applied to the ECAP sample, which creates different final textures for a given temperature [73].

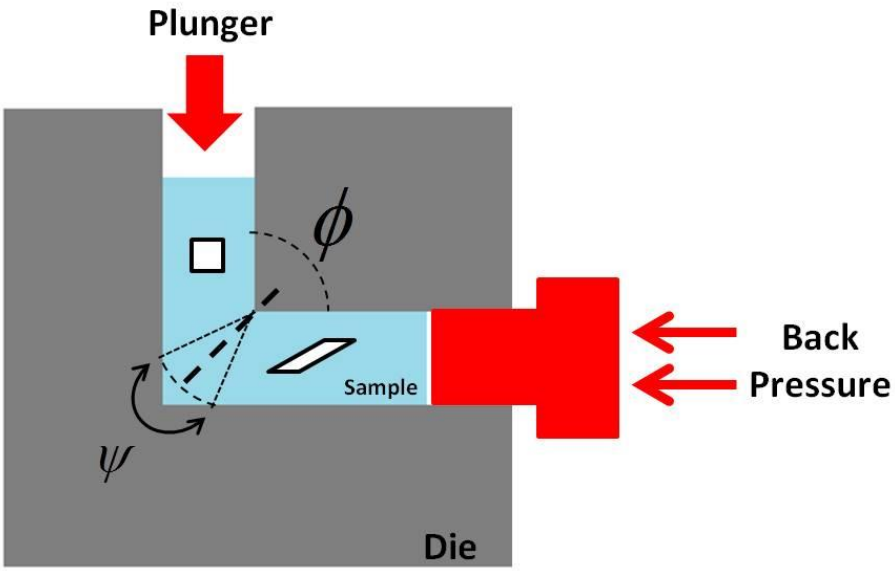

Figure 1.7 Schematic illustration of typical ECAP. ϕ is the angle between the channels and ψ is the curvature angle in bottom corner of the die.

1.3.3 Polycrystal Plasticity Modeling of Mg Alloys

In the past, a viscoplastic self-consistent (VPSC) crystal plasticity model[25] and the predominant twin reorientation (PTR) scheme [26] was successfully employed to simulate plastic deformation and the corresponding texture evolution of Mg alloys[2, 12, 14, 27]. The VPSC model treats each model as a viscoplastic inclusion embedded in an isotropic and viscoplastic homogenous effective medium represented by a polycrystal aggregate. The PTR scheme replaces the original grain orientation by the orientation of

the most active twin system. Usually, a simple Voce hardening law was employed to capture strain hardening as

$$\tilde{\tau}^s = \tau_0^s + (\tau_1^s + \theta_1 \Gamma)\left\{1 - exp\left(\frac{\theta_0 \Gamma}{\tau_1^s}\right)\right\}, \quad (3)$$

where $\Gamma = \sum_s \left|\Delta\gamma^s\right|$ is the accumulated shear in the grain; that is, the sum of shear deformation (γ) contributed by each active deformation mode "s" in a grain. $\tilde{\tau}, \tau_0, \theta_0, \theta_1, (\tau_0 + \tau_1)$ are the threshold stress, initial CRSS, the initial hardening rate, the asymptotic hardening rate, and the back-extrapolated CRSS, respectively [74]. Latent hardening due to slip-slip and slip-twin interaction was usually modeled by empirical parameters.

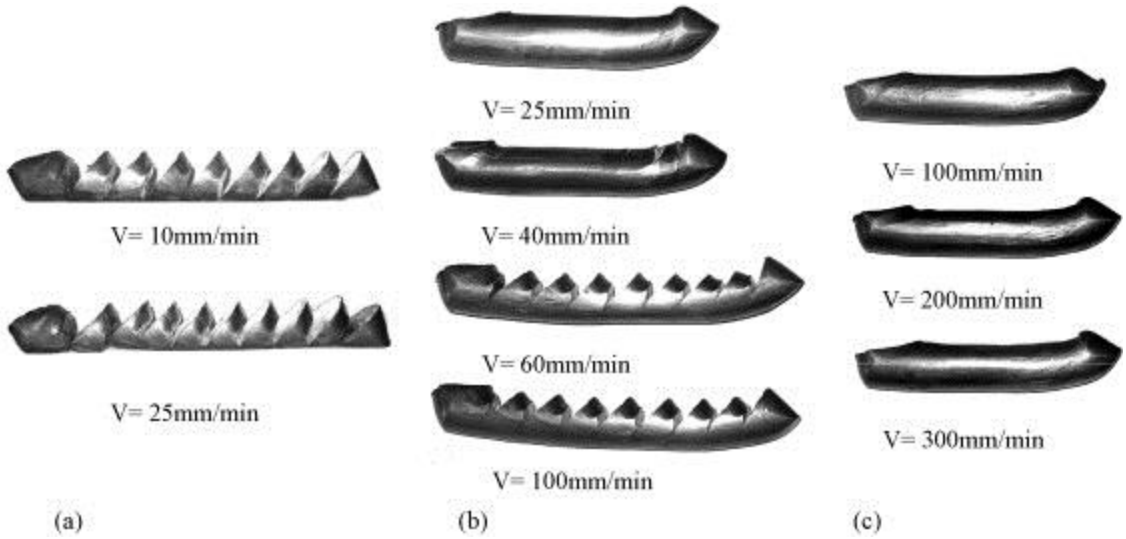

Figure 1.8 AZ31 specimens after single-pass ECAP at (a) 150 °C, (b) 200 °C and (c) 250 °C, extrusion speeds V = 10–300 mm/min, corresponding to average effective strain rates in the deformation zone of 0.01–0.25 s^{-1}, respectively[20].

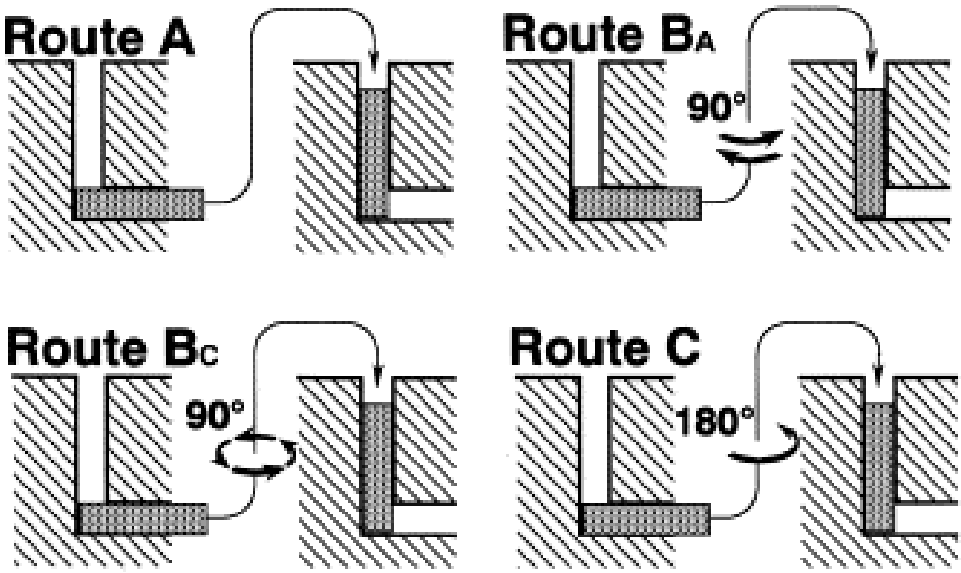

Figure 1.9 The four fundamental processing routes in ECAP[75]

Recently, more sophisticated constitutive models for twin-detwinning and slip were developed for hcp polycrystals [48, 76-78]. A composite grain (CG) twin model was developed by Proust *et al*. [77-78], where each twinned grain consists of layers of both the original (parent) grain and twin reoriented (child), and a twin barrier effect is directional as opposed to PTR model. Beyerlein and Tome [76] presented a dislocation-based temperature-dependent constitutive model for Zr applicable to other hcp metals, which accounts dislocation substructures and separate hardening laws for each deformation mode with their own temperature sensitivities. More recently, Wang *et al.*[48] developed a new model for both twinning and detwinning, which worked well for AZ31 under cyclic loading and strain path changes.

1.3.3.a Modeling of ECAP in VPSC

According to the shear model of ECAP [79-80] the velocity gradient is given as

$$L = \frac{\dot{\gamma}}{2}\begin{pmatrix} 1 & -1 & 0 \\ 1 & -1 & 0 \\ 0 & 0 & 0 \end{pmatrix} \tag{3}$$

in terms of the global coordinate system X:ED, Y:LD and Z:FD in Fig 1.9. $\dot{\gamma}$ is the constant applied strain rate during ECAP with an applied time increment, and $\gamma = 2$ (i.e. total shear strain is $\varepsilon_{xy} = 1$) after one pass [80]. The velocity gradient indicates tension in the ED direction, compression along the LD, and rigid body rotation about the FD [79].

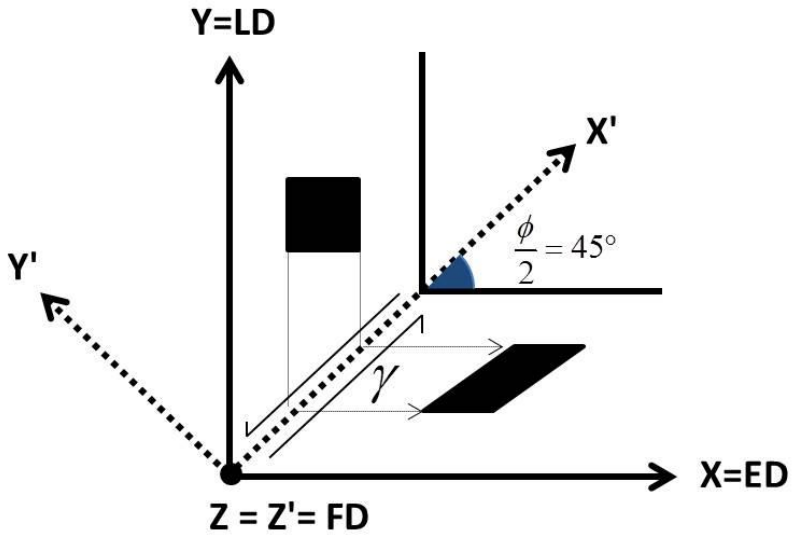

Figure 1.10 Schematic of the ECAP process with $\phi = 90°$ showing shear plane(X', Y', Z') and global(X:ED, Y:LD, Z:FD) coordinate systems. It illustrates the deformation of a square element by simple shear as it passes through the corner. ED: Extrusion direction, LD: Longitudinal direction, FD: Flow direction

1.3.4 Precipitation in Mg-Al-Zn-(Mn) Alloy Systems

The ternary phase diagrams of Mg-Al-Zn alloys were studied in detail and different ternary and binary intermetallic phases were reported as shown in a isothermal section at 320°C in Fig.1.10[81-82]. The binary γ-$Mg_{17}Al_{12}$ (also called β) phase is a common equilibrium phase in ternary Al-rich AZ series Mg alloys, forming fine and coarse precipitates in the wide temperature range[83]. MgZn is another equilibrium binary phase in the MgAlZn alloy systems as seen in Fig.1.10.

There are two mainly reported ternary phases in Mg-Al-Zn alloy systems – the ϕ and τ phases. The literature has inconsistent and incomplete results concerning the composition and the crystal structure of these complex ternary phases [83-90]. The τ phase has been determined to be $Mg_{31}(Al,Zn)_{49}$ (at.%) with a body-centered cubic structure (space group $Im\bar{3}$, a ~ 1.4 nm)[84]. The crystal structure of the ϕ phase is not well understood but was shown to be a primitive orthorhombic crystal structure [89]. Generally, the approximate composition of ϕ phase is reported as $Mg_{21}(Al,Zn)_{17}$ (at%) [83, 89]. A recent study showed the broad homogeneity range at high temperature corresponds to two different variants of ordered ϕ phase at 0 K, with the compositions $Mg_{50}Al_{16}Zn_{34}$ and $Mg_{50}Al_{10}Zn_{40}$ [90].

Addition of Mn to commercial AZ series Mg alloys improves the corrosion resistance by forming intermetallics with aluminum and the iron impurity [91]. Commercial AZ31 Mg alloys typically contain 0.2-1 wt% Mn. Recently, Stanford et. al. [92] reported the thermodynamic prediction of phase stability in AZ31-0.5Mn wt% as

shown here in Fig.1.11. As seen in the figure, several additional Al-Mn intermetallic components are predicted when Mn is added to the Mg-3Al-1Zn alloy.

1.3.5 Dynamic Recrystallization in Mg Alloys

DRX in Mg alloys has unique features and different types of DRX take place under different deformation conditions [93]. In Mg and its alloys, DRX occurs across a broad temperature range. Although many studies on DRX of Mg alloys were reported [24, 28-29, 32, 38, 94-96], the literature has a complex picture of the DRX mechanisms that operates in magnesium. However, the main DRX mechanisms that were observed in Mg alloys are Continuous DRX (CDRX), Discontinuous DRX (DDRX), and Twinning DRX (TDRX) [93].

CDRX involves deformation transformation of low angle boundaries to high angle boundaries via strain [93]. New grains are formed in the process, within the original deformed grains. CDRX is strongly dependent on the active deformation modes, and activities of non-basal slip systems are required[32]. CDRX is a strong recovery process, as accumulated dislocations do not contribute to the strain hardening [93]. A special type of CDRX is named as low temperature DRX (LTDRX) [32] that operates at temperatures between room temperature to 200°C during cold deformation via the strain. LTDRX is not a classical DRX process since it does not provide restoration [93]. The new grains formed through LTDRX provide an extensive strain hardening [94].

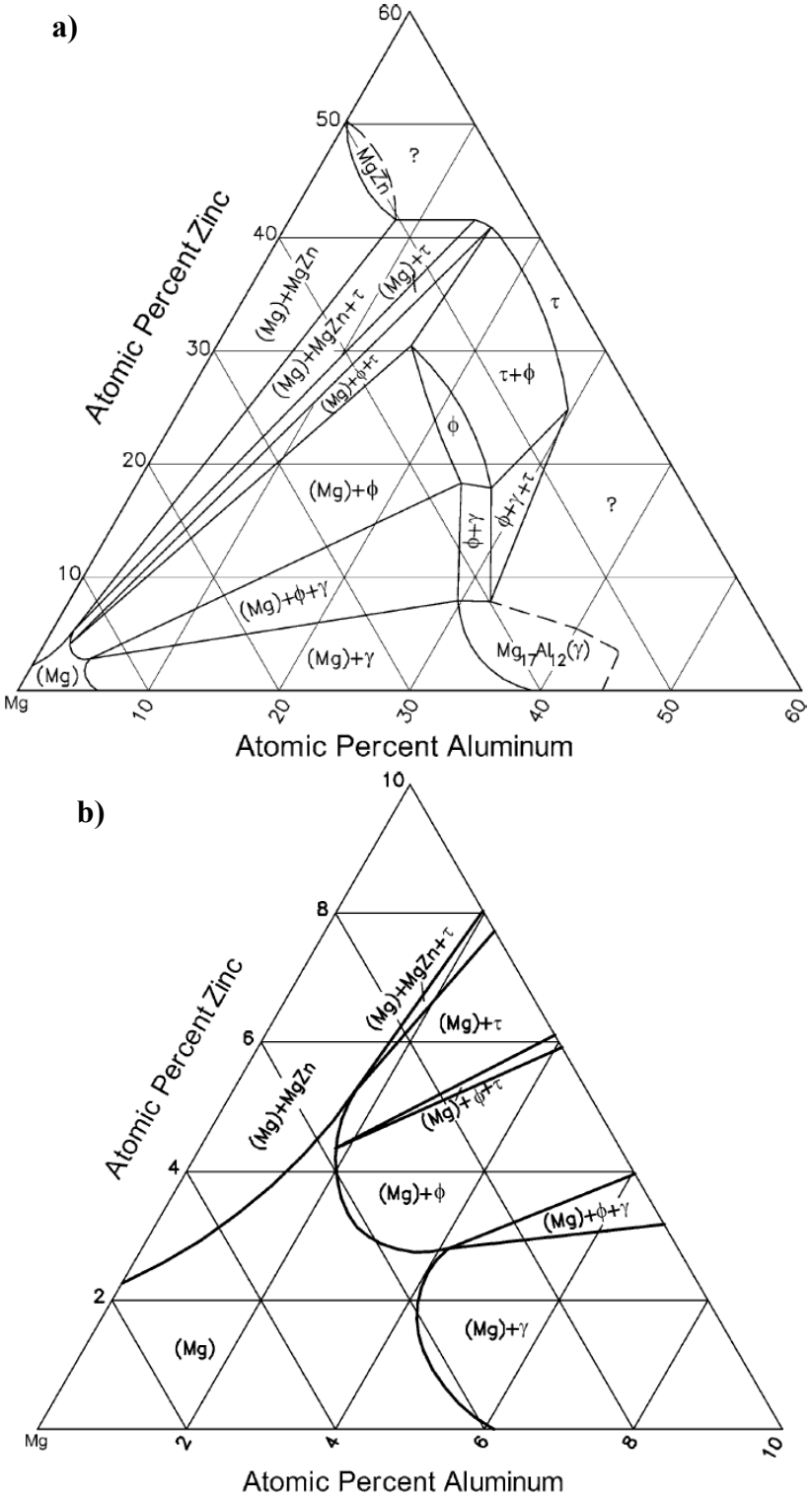

Figure 1.11 (a) Al-Mg-Zn isothermal section at 320 °C (b) near the Mg corner.[81-82]

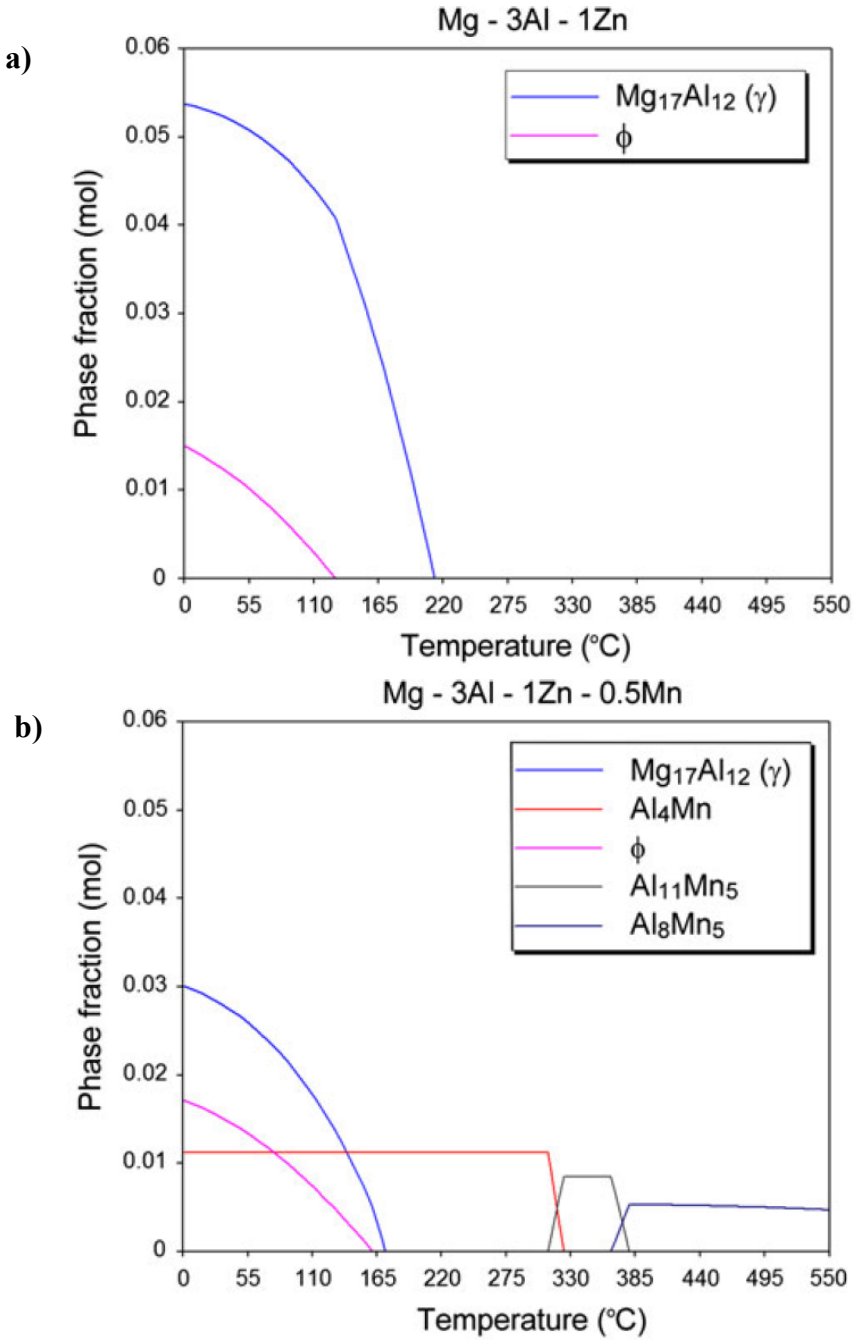

Figure 1.12 Thermodynamic prediction of phase stability in (a) AZ31 and (b)AZ31 with 0.5wt% Mn using the Pandat software[92].

DDRX occurs through nucleation and growth of high angle boundaries through a bulging mechanism. Bulging grain boundaries are an indicator for DDRX. As DDRX grains grow and consume lattice dislocations, they provide significant strain softening, especially at intermediate and low temperatures [29, 32, 94]. DDRX usually occurs in low stacking materials.

TDRX is a specific DRX mechanism that is a unique mechanism of Mg and its alloys. TDRX mechanism can occur through the following three different nucleation mechanisms: (1) mutual intersection of primary twins, (2) secondary twinning within the primary twin lamella, and (3) deformation induced low angle boundaries inside the twin lamellas that transform to high angle boundaries upon further straining[93].

1.3.6 Effect of Grain Size on Ductility and Strength

Ductility and strength of Mg alloys can be enhanced by microstructural refinement. Koike *et al*. [9] have attributed ductility improvement at room temperature to the activation of non-basal slip systems after grain refinement through severe plastic deformation. In fine-grain Mg alloys, more non-basal slip should be involved in deformation due to the plastic compatibility stress that requires a non-basal glide around large numbers of grain boundaries [9]. In addition, the activation of twinning, which is the source of tension-compression asymmetry at low temperatures, is more difficult in fine-grained microstructures [97].

The effect of grain size on twinning was found to be more pronounced than slip mechanisms, which is valid for body-centered cubic, face-centered cubic, and hcp

materials [97]. The Hall-Petch parameters of the AZ31 alloy further confirmed that twinning yield strength increased faster than that of slip, with grain refinement to a few microns [98-99]. Recently, the influence of grain size on each slip system was shown to be different, where basal slip showed less grain size dependence compared to prismatic slip in Mg alloys [16, 100-101].

1.4 Outline

With above introduction and a brief literature review, the outline of this dissertation is as follows;

Chapter II gives the details of experimental methods and materials that are used in this study.

Chapter III investigates the tensile ductility and microstructures at failure of AZ31 alloy samples with different texture with respect to the loading axis at the temperature range of 25°C-200°C.

Chapter IV investigates the role of various starting crystallographic textures and deformation modes on the shear formability via ECAP and shear localization of AZ31 alloy at temperatures lower than 200°C, where the material shows large flow strength anisotropy, deformation twinning, and tension-compression asymmetry.

Chapter V investigates the DRX and precipitation formed regions during ECAP at 150°C with detailed TEM and STEM analyses.

Chapter VI investigates the multi -pass and -temperature ECAP of AZ31 alloy billets for an ultra-fine grained microstructure.

Chapter VII investigates the effect of equal channel angular plate extrusion (ECAPE) on microstructure and mechanical flow responses of twin-rolled cast AZ31 sheets.

Chapter VIII investigates the final texture, grain size and mechanical flow responses of ECAPE AZ31 plates and the stretch forming of ECAPE samples through Olson formability tests.

Chapter VIII gives main conclusions and future directions.

CHAPTER II

EXPERIMENTAL METHODS

The aim of this chapter is to give details of experimental techniques used in this study. Details of processing and characterization tools used in this study will be listed in this chapter.

2.1 Materials

The Mg alloy studied in this work is the commercially available AZ31 Mg alloy (~3wt.% Al, ~1 wt.% Zn, ~0.5wt% Mn and balance-Mg). The AZ31 Mg alloy is selected for this study since it is the most common commercially available Mg alloy that can be found in different forms such as rod, sheet, plate and coil. Since it has good room-temperature strength and ductility combined with corrosion resistance and weldability, it is used in different engineering applications. In addition, since it has single phase microstructure it is easy to conduct some fundamental studies including modeling without worrying too much about the effect of massive secondary particle formation and complex microstructure.

Different sample forms were obtained from different vendors. A commercial 25mm-thick AZ31 hot-rolled plate was acquired from Kelbin Metals and 13mm-thick AZ31 hot-rolled plates were acquired from Mark Metals. Both plates are annealed under an argon atmosphere at 350°C for 12 hours in order to have a fully recrystallized initial

microstructure. 3mm-thick AZ31 twin-roll casting (TRC) sheet was acquired from POSCO.

2.2 Severe Plastic Deformation of AZ31 Mg Samples via Equal Channel Angular Processing (ECAP)

Different 25mm x 25mm x 150mm bulk billet specimens have been cut from the 25mm-thick hot-rolled plate. Two different orientations with respect to the die frame, as shown in Fig.2.1 (Texture1 and 2), were investigated at different temperatures. The samples were ECAP at 150°C or 200°C with a backpressure of 20 MPa and an extrusion rate of 4.57mm/min through the 90° die with sharp corners (Fig. 2.1). Two Texture2 specimens were tried directly to be ECAP at 125°C and 100°C using a backpressure of 50MPa and an extrusion rate of 1.52mm/min, however samples failed at these temperatures. Therefore, multi-temperature step-down approach was used to process the specimens at these temperatures. Different Texture2 specimens were sequentially processed for two or four passes at 150°C and then processed at 125°C and 100°C. The billets were placed in the heated ECAP die for 20 minutes before the each extrusion pass in order to ensure temperature homogeneity. The ECAP processed specimens were subsequently water quenched after the extrusion to avoid possible microstructural changes that could occur during slow cooling.

Please note that only route A (no rotation between passes) was used since route B initiated strong strain localization and failure when it was processed at 150°C, that will be briefly discussed in Chapter VI. The details of processing condition for billet

specimens are given in Table 2.1. The conventional area reduction extrusion texture (Texture3 in Fig. 1) has been simulated to investigate the reasons for the reported ECAP failures at 150°C [20] and was not experimentally ECAP processed in this study.

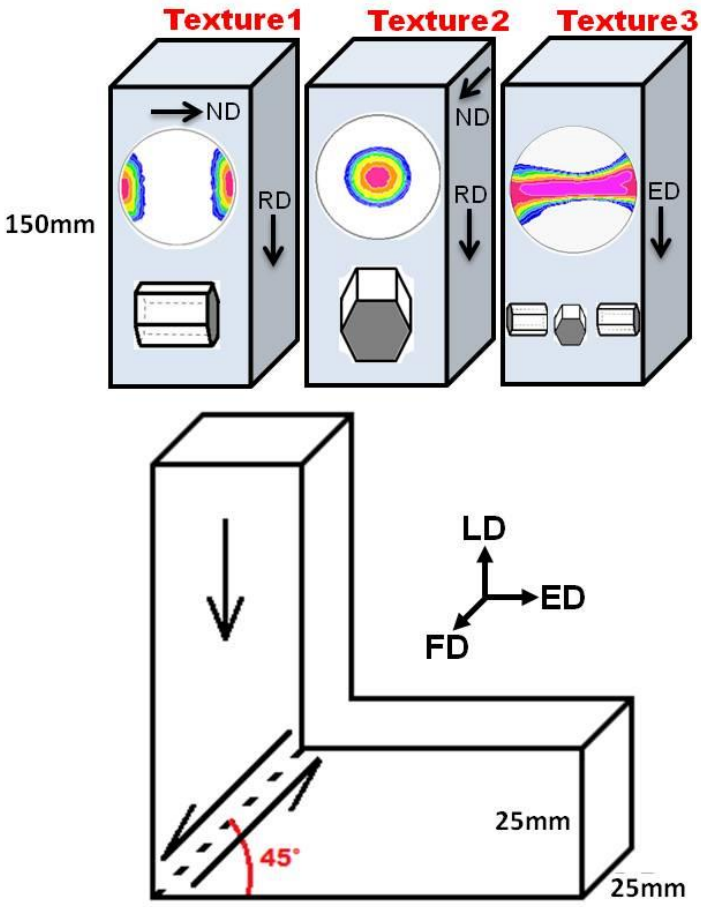

Figure 2.1 Schematics of the three ECAP cases studied in the present work with (0002) pole figures showing different AZ31 Mg alloy texture, Texture1: hot-rolled texture, basal poles are parallel to ED, Texture2: hot-rolled texture but basal poles are parallel to FD, Texture3: typical conventional area reduction extrusion texture; basal poles are aligned around the center rim. ED: Extrusion direction, LD: Longitudinal direction, FD: Flow direction.

2.3 Severe Plastic Deformation of AZ31 Mg Sheets and Plates via Equal Channel Angular Plate Extrusion (ECAPE)

Different 150x150x13 mm^3 AZ31 plates are processed via the equal channel angular plate extrusion (ECAPE) tool such that rolling direction is aligned with the extrusion direction, as illustrated in Figure 2.2. Two extrusion routes were used: route A (no rotation between passes) and route Bcp (90° CW rotation around the plate normal) both at 200°C with an extrusion speed of 0.25 mm s-1. Route C initiated a rapid crack formation. It is worth mentioning that the Bcp route used in this study is completely a new route and different from the traditional Bc route used for bar specimens where the rotation is about the extrusion axis. The present Bcp route in the plate tool is not accessible in the billet ECAP tool.

It is worth pointing out that the plate was not possible to ECAPE process at 150°C directly, so multi-temperature step-down approach used to process at 150°C. Firstly, several plates are ECAPE processed at 200°C and then they were additionally processed at 150°C. A plate was ECAPE processed for 4 passes at 200°C (route A) followed by additional two passes (using route A) at 150°C after 180° rotation about the extrusion axis. The aforementioned rotation and the following two passes (route A) at 150°C is named as route F here. All ECAPE details are listed in Table 2.1. The plates were placed in the heated ECAPE die for 20 minutes before the each extrusion pass and were subsequently water quenched after the extrusion like the procedure applied to billet specimens.

Table 2.1 Processing conditions for the AZ31 Mg billets examined in this study. Multi passes ECAP studies were conducted with Texture2.

Designation	# of passes	ECAP Temperatures	Extrusion rate (mm/min)
Texture1@200°C	1	200°C	4.57
Texture1@150°C	1	150°C	4.57
Texture2@150°C	1	150°C	4.57
Texture2@125°C	1	125°C	1.52
Texture2@100°C	1	100°C	1.52
2A@150°C	2	150°C	4.57
4A@150°C	4	150°C	4.57
4A +4A	4+4	150°C+125°C	4.57+1.52
2A+2A+1A	2+2+1	150°C+125°C+100°C	4.57+1.52+1.52

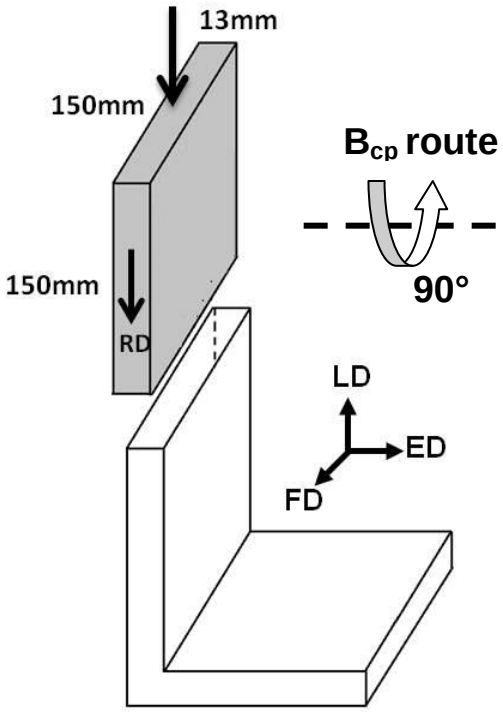

Figure 2.2 Schematic of ECAP die for processing of 150mmx150mmx13mm plates. There is only one possible starting texture where basal poles are parallel to the extrusion direction like Texture1 in Figure 2.1. ED: Extrusion direction, LD: Longitudinal direction, FD; Flow direction.

Table 2.2 List of AZ31 Mg alloy plates processed via ECAPE

Designation	# of passes	ECAP Temperatures	Extrusion rate (mm/min)
4A	4	200°C	7.62
4Bcp	4	200°C	7.62
4A+1A	4+1	200°C+150°C	7.62+3.81
4A+2F	4+2	200°C+150°C	7.62+3.81
4Bcp+2A	4+2	200°C+150°C	7.62+3.81
4Bcp+2Bcp	4+2	200°C+150°C	7.62+3.81
4Bcp+3Bcp	4+3	200°C+150°C	7.62+3.81

2.4 Mechanical Testing

Flat, dog-bone tensile specimens with gage dimensions of 8 x 3 x 1.5 mm^3 and rectangular prism compression samples (4 x 4 x 8 mm^3) were cut from the starting hot-rolled plates and the uniformly deformed regions of processed (ECAP or ECAPE) materials using wire electrical discharge machining (EDM) as illustrated in Fig. 2.3. Tension experiments were performed at different temperatures in a servo-hydraulic MTS test frame with a strain rate of 5×10^{-4} s^{-1}. An MTS high temperature extensometer was used to measure the axial strain. The extensometer had a pair of ceramic rods, 3.5 mm in diameter with V-chisel ends, exerting a 300 g force per rod on the sample. The room temperature compression experiments were conducted using an electromechanical MTS testing system. A miniature extensometer (3 mm gage) was used to measure the axial strain. Strain was measured via MTS high temperature extensometer during high temperature compression tests.

The nanoindentation measurements were conducted using a The Hysitron Triboindenter Nanoindenter. An array of indents was made to have hardnesses of

dynamically recrystallized and the deformed grains. 5000μN is applied to have a maximum penetration depth of ~200 nm for all the indents.

2.5 Formability Tests

Biaxial stretch formability tests were performed using an Olsen tool set (a Interlaken ServoPress 075 die set). It is an instrumented double action servo hydraulic press with a maximum punch load of 60,000 lb and maximum clamping load of 75,000 lbs. Schematic of the Olsen formability test frame with dimension are given in Figure 2.4. The specimen size of 90x45x1.7 mm^3 was used for stretch formability tests. After surface grinding the final thickness of sheets was around 1.5mm. The punch speed was 0.05mm/s and the 133 kN clamp load was applied to ensure pure stretching. After the test, specimens were checked and it was clearly noticed that the material was not drawn into the die, and actually biaxially stretched.

2.6 Microstructural Characterization

Samples for microstructural characterization were cut from the mid-section of the hot-rolled plate and ECAP/ECAPE processed specimens from the uniformly deformed region. The microstructure of the samples was examined using a digital Keyence VH-Z100 Optical microscopy (OM), FEI Quanta-600 scanning electron microscopy (SEM) with Oxford Energy Dispersive X-Ray Spectroscopy (EDS) and HKL/Oxford Electron Backscatter Diffraction (EBSD) systems, a FEI Tecnai G2 F20 ST Transmission electron microscopy (TEM) operated at an accelerating voltage of 200 kV. In addition, EBSD analyses were performed using a Zeiss Ultra Plus FEGSEM, equipped with an

Oxford Instrument AZtec EBSD system and a Nordlys-S EBSD detector. The accelerating voltage was set at 12 keV and the aperture at 120µm for EBSD data acquisition. The step size used to scan the areas of interest on the different samples was 100nm. EBSD data acquisition and the analyses were performed using HKL software.

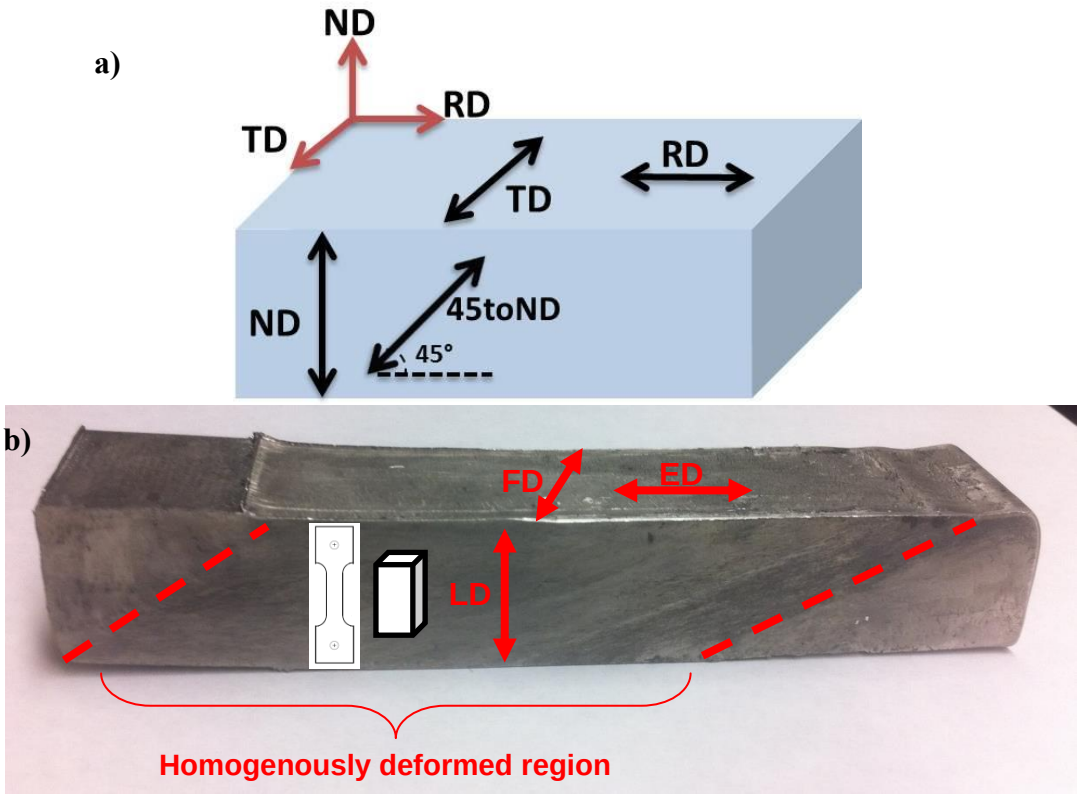

Figure 2.3 Schematic of orientation of the different tension and compression samples cut from the hot-rolled AZ31 alloy and the ECAP/ECAPE processed specimens.

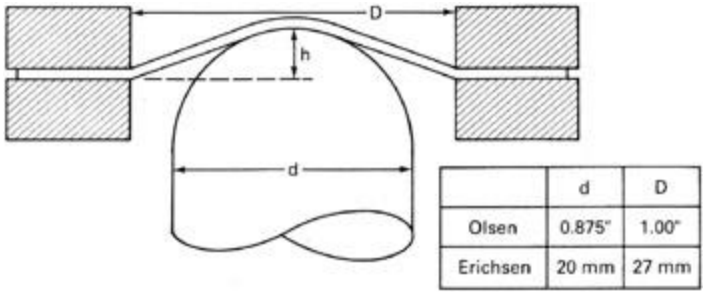

	d	D
Olsen	0.875"	1.00"
Erichsen	20 mm	27 mm

Figure 2.4 Schematic of Olsen/Erichsen stretch formability tool [102].

Samples for microstructural characterization were mechanically ground and subsequently polished with diamond paste to 0.1 μm. For the EBSD samples, an additional step after diamond paste was conducted via a colloidal silica solution with a 0.04 μm particle size. The OM and SEM samples were etched via an acetic-picral acidic mixture (20 mL acetic acid, 3 g picric acid, 20 mL H2O, 50 mL ethanol (95%)). TEM foils were prepared by mechanically grinding down to the thickness of 30 μm, and subsequently prepared by using a twin-jet electrolytic polishing in an electrolyte consisting of 3% perchloric acid and 97% alcohol using 70V at -20° for 3 min.

The texture characterization of bulk samples were performed using a Bruker-AXS D8 X-ray diffractometer (XRD) with Cu Kα (wavelength = 0.15406 nm) radiation. The popLA (preferred orientation package - Los Alamos) texture analysis software was used to correct and plot experimental pole figures. The MTEX Matlab open source software[103] was used to convert experimental pole figures to the orientation distribution function (ODF) for simulation inputs. In addition, the predicted textures were also plotted using MTEX.

CHAPTER III

DUCTILITY AND FAILURE MECHANISM OF MG-3AL-1ZN ALLOY AT LOW TEMPERATURES *

In this chapter, the ductility, the microstructures at failure, and the dynamic recrystallization behavior of as-received (hot-rolled) AZ31 alloy samples were investigated at the temperature range of 25°C-200°C under uniaxial tension tests. $\{10\bar{1}1\}$ compression twins and $\{10\bar{1}1\}-\{10\bar{1}2\}$ double twins (tension twins inside compression twins) were shown to act as a source of fracture at room temperature due to localization and cracking in these regions [52]. In this chapter, failure mechanism will be investigated at moderately elevated (<200°C) temperatures.

Samples were cut from a strongly textured, hot rolled AZ31 plate from three different orientations (Fig 3.1) in order to activate alternate deformation mechanisms during uniaxial tensile loading. Dynamic recrystallization (DRX) behavior was found to be highly dependent on the active deformation modes at temperatures between 100°C and 200°C, where non-basal slip mechanisms (prismatic and pyramidal <c+a>) retards DRX whereas basal slip promotes DRX. The final microstructure and elongation to failure vary with active deformation modes at moderately elevated temperatures (>50°C), while at room temperature elongation to failure seems to be insensitive to the deformation modes.

* Part of the data reported in this chapter is reprinted with permission from "The Role of Deformation Modes on Ductility and Dynamic Recrystallization Behavior of AZ31 Mg Alloy at Low Temperatures" by E. Dogan, M. W. Vaughan, C. Hayrettin, I. Karaman, and G. Ayoub, 2014. *Magnesium Technology 2014*, pp. 155-160, Copyright [2014] by The Minerals, Metals & Materials Society.

There is a significant indication that twinning initiated shear localization and induced an earlier fracture at elevated temperatures. More homogenous deformation until necking was observed when prismatic slip was the main active deformation mode with limited twinning activity. At temperatures of 100°C and higher, cracks formed and eventually failure occurred in DRX regions.

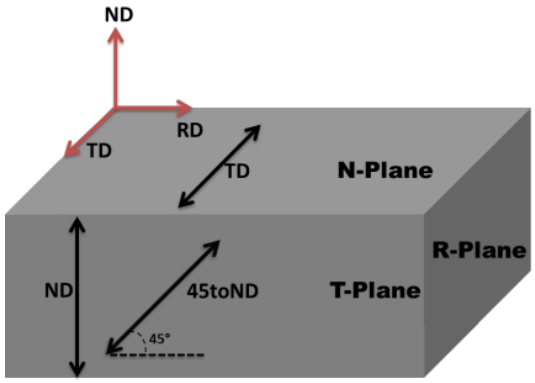

Figure 3.1 Schematic of orientation of the different tensile samples cut from the hot-rolled AZ31 alloy.

3.1 Initial Microstructure and Texture

Fig. 3.2a and b displays $(10\bar{1}0)$ and (0002) pole figures for the hot-rolled AZ31 material from N- and T- Planes, respectively. Here, a typical hot-rolled AZ31 texture is evident; basal poles are parallel to the normal direction, and the spread in the basal pole is towards the rolling direction (RD).

Figure 3.3a and b display OM and SEM images of the initial microstructure from T- and N planes, respectively. The initial microstructure consists of equiaxed grains with average size of around ~25μm. As indicated by circles Fig.3.3, Al-Mn(~Al_8Mn_5)

secondary particles in different sizes(1-30μm) are present and mostly align themselves along the rolling direction (Fig.3.3) both in N- and T- planes.

3.2 Tensile Properties

Figures 3.4a-c presents true stress-strain curves of TD, 45toND, and ND samples at different temperatures, respectively. Room temperature (RT) samples for each direction show a similar elongation to failure (EF) strain of around ~15%. Increased temperature significantly improves the ductility of TD and 45toND samples, as shown in Figs 3.3a and b. The EF levels for each case, TD and 45toND, are close but the former has higher EF strain at elevated temperatures. On the other hand, EF strain of ND specimens only slightly increased with temperature, and much lower ductility was obvious compared to other directions.

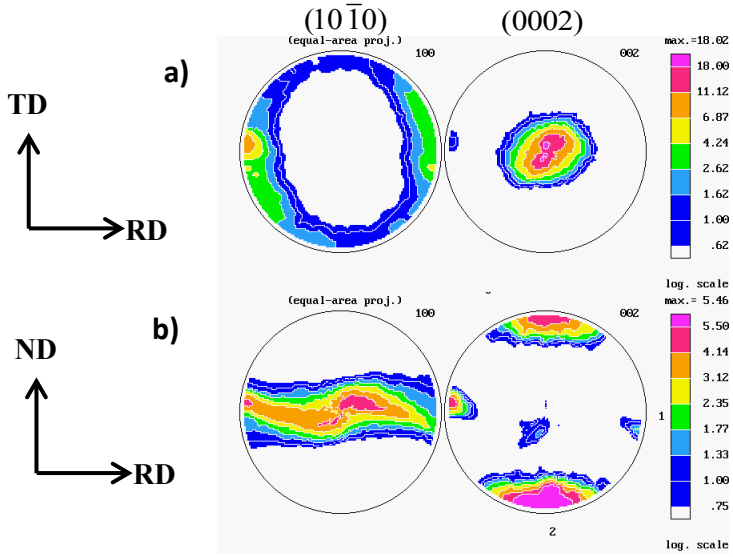

Figure 3.2 (10$\bar{1}$0) and (0002) pole figures of hot-rolled AZ31 Mg alloy from (a) N- and (b) T- Planes.

Significant hardening, a prominent feature of the 45toND and ND samples tested up to 200°C, is an indication of tensile twinning activity. Both the yield and ultimate stresses of TD samples dramatically decreased with increasing temperature. The decrease in yield stress of 45toND samples is less pronounced than in the TD case. However, the yield stress does not change with temperature in ND specimens, suggesting an athermal twin-dominated yielding [27]. In all cases the ultimate/peak stress levels are decreasing significantly with increasing temperature.

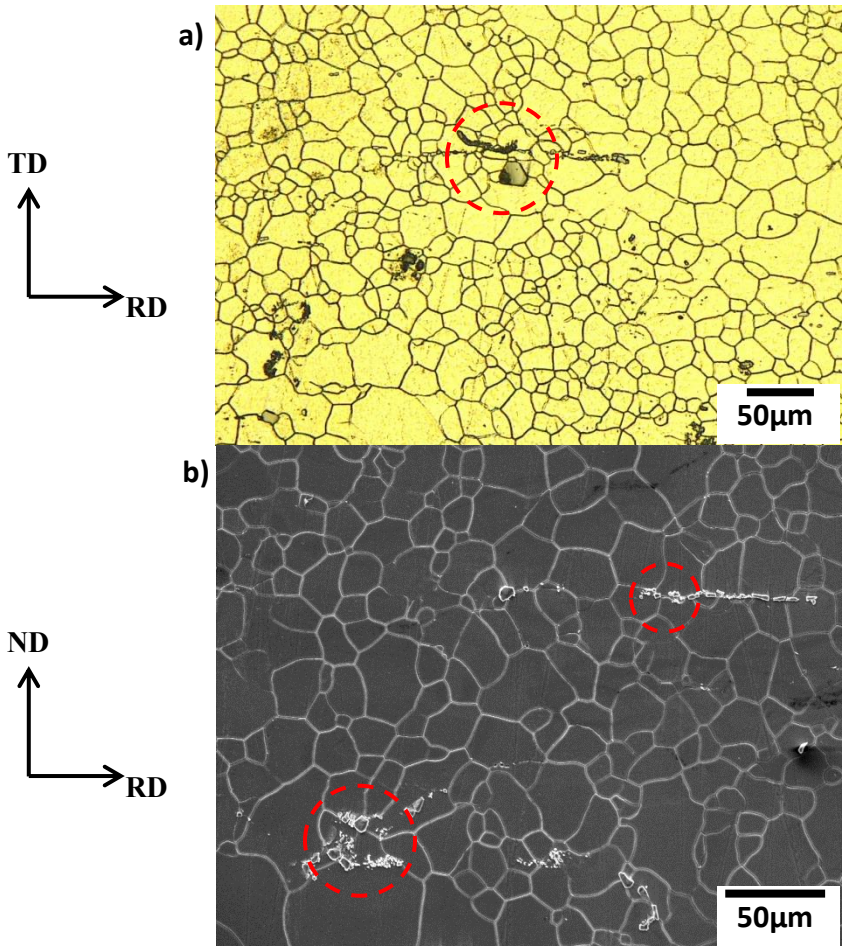

Figure 3.3 OM and SEM images of hot-rolled AZ31 Mg alloy material before uniaxial tensile tests. (a) from T-Plane and (b) from N-Plane.

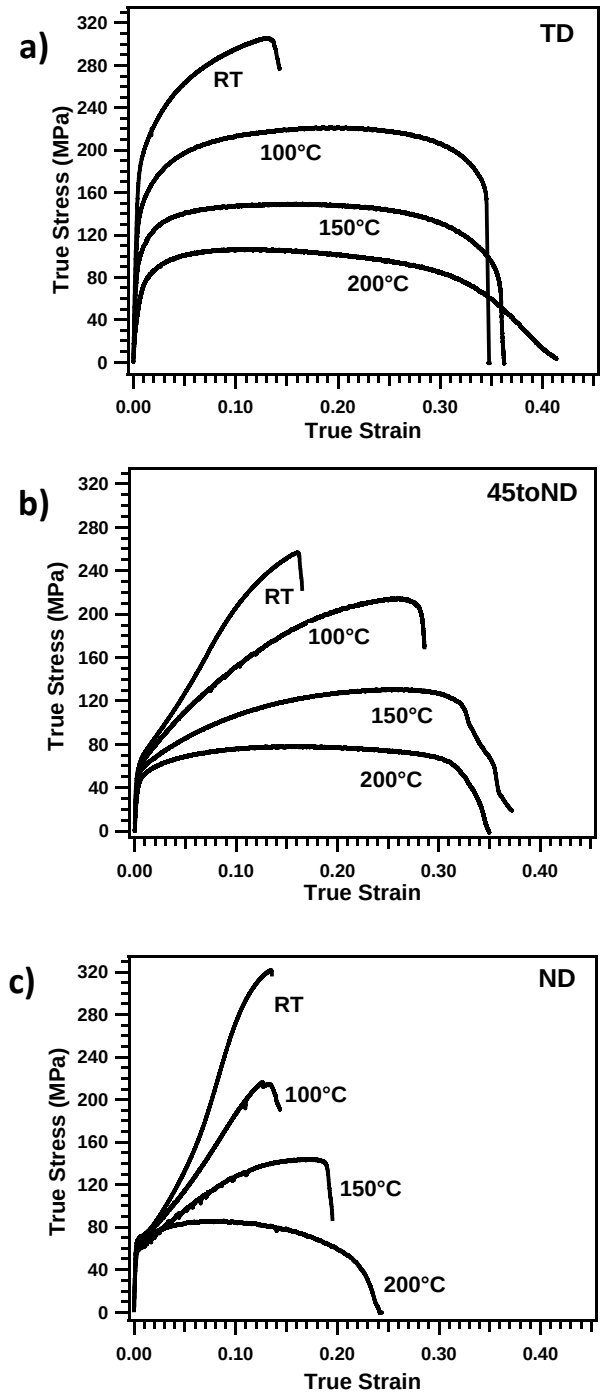

Figure 3.4 True stress vs. strain response of AZ31 specimens from tensile tests at a temperature range of 25°C to 200°C. (a) TD, (b) 45toND and (c) ND. TD: Transverse direction, ND: normal direction.

3.3 Microstructure at Failure

The final microstructures of all samples tested at room temperature consisted of significant twin concentrations. Figure 3.5a-c shows OM images of tested samples at room temperature for TD, 45toND, and ND, respectively. In the TD and 45toND specimens, the twins are more prevalent in areas close to the fracture surface, as seen in Figs. 3.5b and 3.6b, respectively. The TD sample has thin twin bands with straight edges, whereas the 45toND and ND samples have more complex microstructures in terms of twin boundaries (Fig.3.5).

The texture evolutions for all samples after tensile deformation of around 16% at room temperature were given in Figure 3.7. It is well known that when tension twins form, the matrix reorients by 86.3°. It is clear that very limited tension twin forms in the TD sample (Fig. 3.7a and b), whereas significant tension twinning activity is evident after same amount of deformation in the 45toND and ND samples as seen in Figs. 3.7c-d. From the given microstructures and the final texture, it can be concluded that the twin volume fractions can be compared as ND>45toND and ND>TD. It is not possible to evaluate the volume fraction of compression twins from the bulk textures of all specimens since it was well reported they are usually activated in small regions near fracture surface right before the failure and they act as a source of fracture especially at room temperature[52, 54]. In addition, the reorientation associated with compression and double twinning is 56° and 38°, respectively, so it is more difficult to evaluate the amount of reorientation due to these twinning modes from the bulk texture given in Figure 3.7.

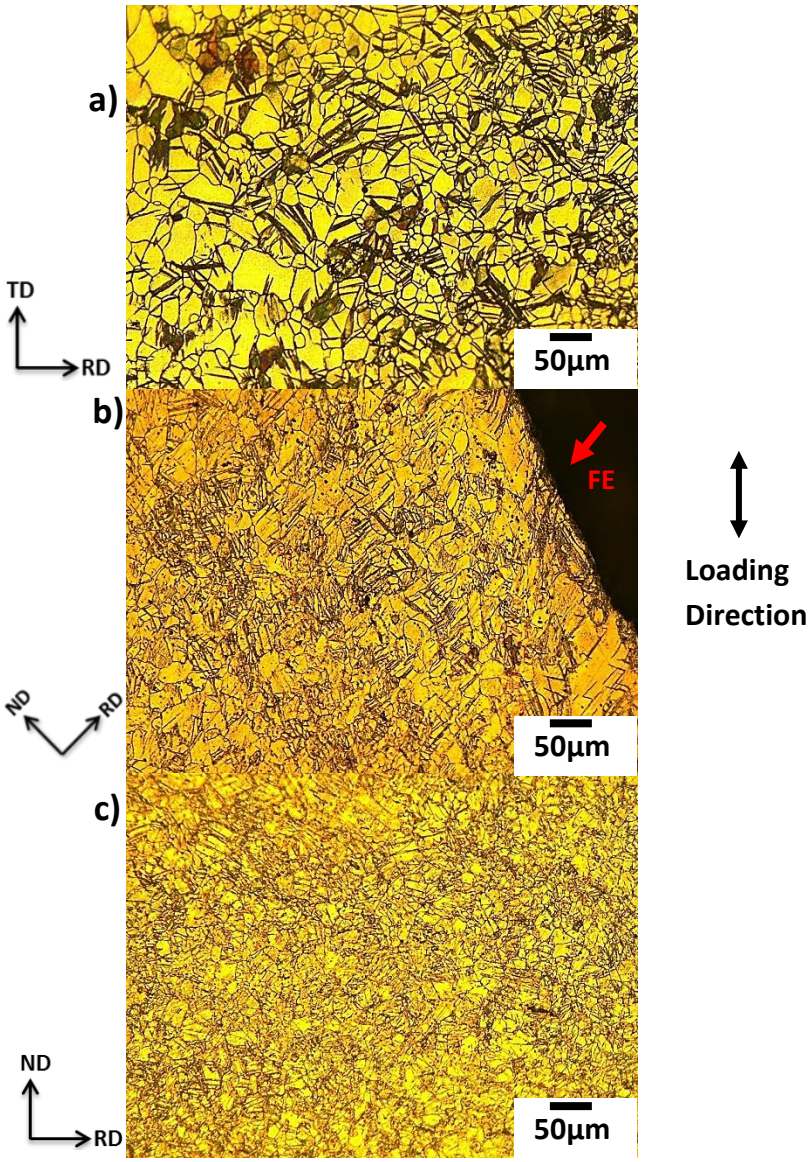

Figure 3.5 OM micrographs of uniaxial tension tested samples at room temperature (a) TD, (b) 45toND and (c) ND. Loading direction is vertical. FE: Fractured edge

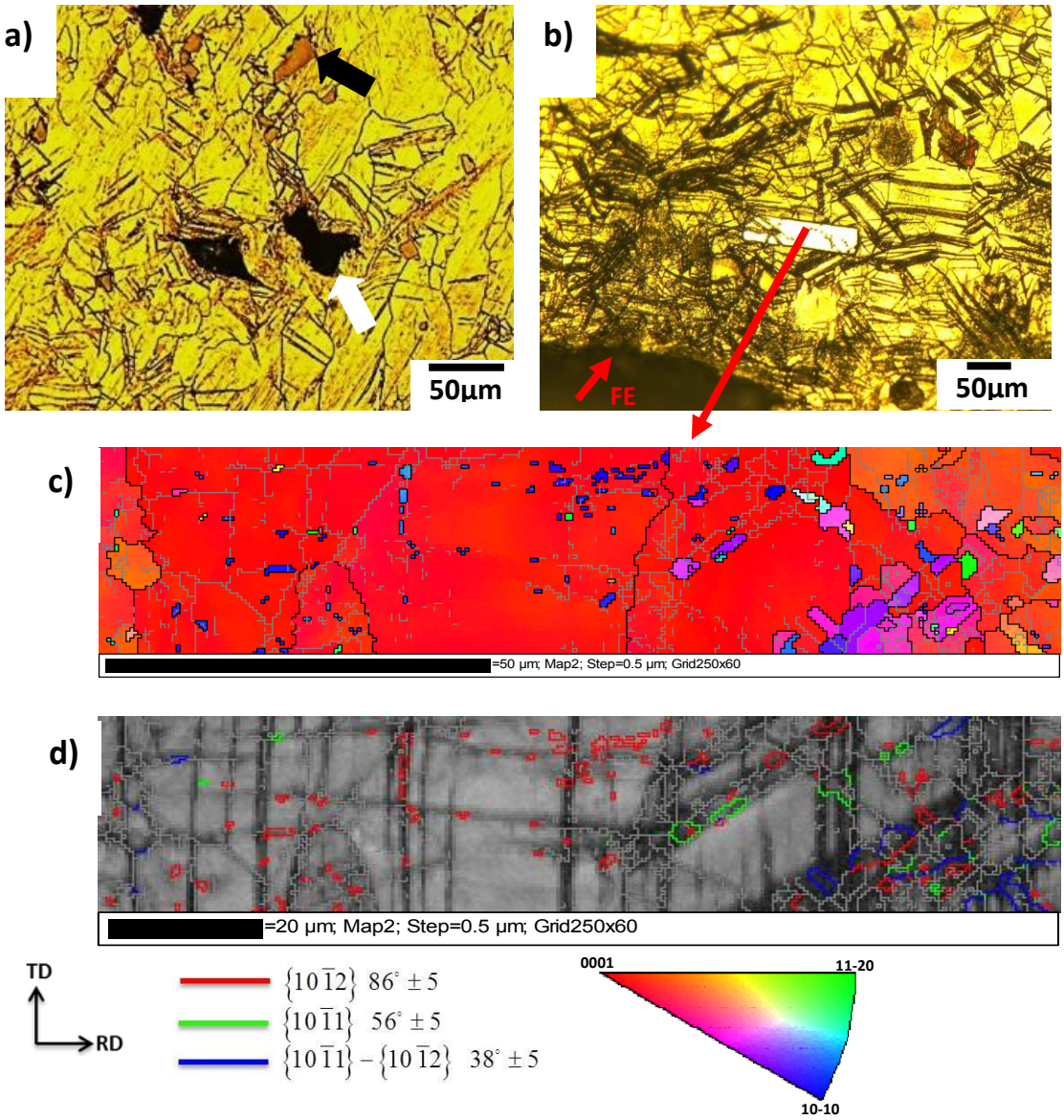

Figure 3.6 OM image of TD specimen tested at room temperature (a) showing a crack formed in the twinned area with a white arrow. (b) OM image near FE: Fracture edge, (c) the EBSD images and (d) EBSD-Kikuchi band contrast map showing different boundaries of white rectangular region in (b).

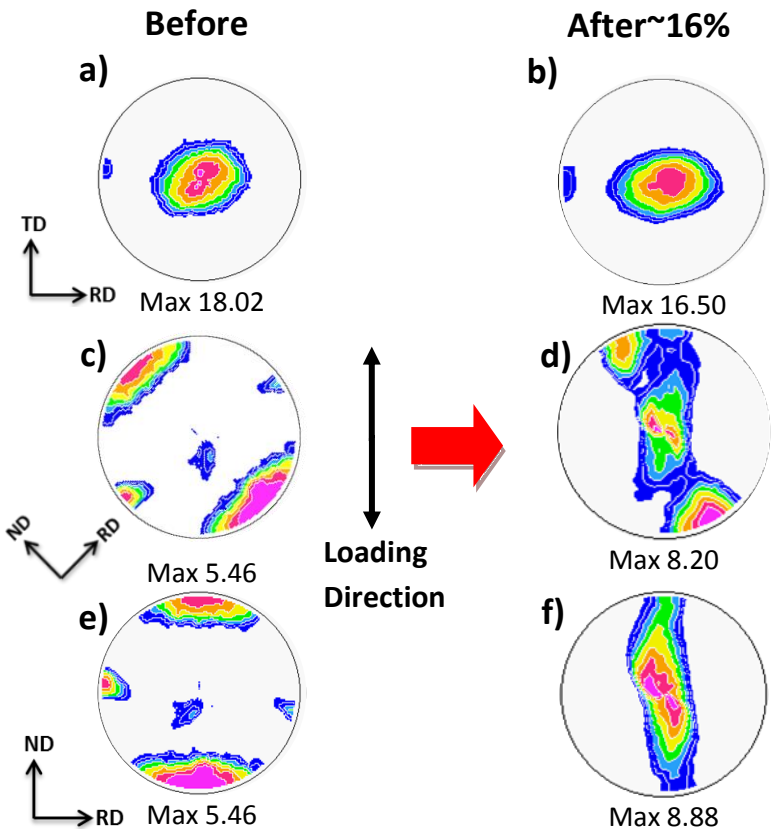

Figure 3.7 (0002) pole figures (a&b) TD, (c&d) 45toND and (e&f) ND specimens before and after ~16% tensile deformation, respectively.

The twins near the fracture surface of the TD sample (Fig.3.6b) are identified by EBSD analysis given in the Fig.3.6c. The inverse pole figure map of the small bright rectangular region in Fig. 3.6b showed that straight dark twin bands are compression and double twins as shown in the Fig. 3.6c.

Cracks that formed in twinned regions are prominent features of all samples, and one example image is given in Fig. 3.6a from the TD sample with the white arrow. Al-

Mn particles are also visible in Fig.3.6a (indicated by black arrow), showing no crack associated with them.

The microstructures of specimens become remarkably different at 100°C, as shown in Fig. 3.8. Grains are mostly elongated, and twins are only present very near to the fracture surface in the TD specimen tested at 100°C (TD@100°C) (Fig.3.8a). Significant necking was observed in TD@100°C in contrast to alternative cases at 100°C as seen in Fig. 3.9. It is believed that this is an another indication of limited tensile twinning activity in TD@100°C specimen since it was reported that tensile twinning activity was shown to promote uniform elongation in tensile tests[51]. This suggests that twins formed after necking (they are only observed in the necked region) caused deformation localization. The twins are passing across the grain boundaries of elongated grains, further confirming that they formed after elongation/deformation of the grains by slip. It is worth noting that, for the TD@100°C case, the volume fraction of twins and the number of cracks significantly decreased compared to the RT specimens for the TD case. In the TD@100°C case, no DRX-formed grains were observed in the microstructure, which was also free of shear bands/zones except in the necking region.

Figures 3.8b and c show the microstructure of the 45toND sample after tensile testing at 100°C (45toND@100°C). The sample failed due to a shear band formation which consisted of twins, as shown in Fig.3.8b. Small shear bands (with twinning inside) were prevalent throughout the specimen. Some grains are free of twins and elongated. Cracks are still present near the fracture surface, as shown via the arrow in Fig. 3.8b. As shown in Fig.3.9b, more uniform elongation up to fracture was observed compared to

the TD@100°C case due to a more pronounced tensile twinning activity[51]. DRX within the twin were observed in the 45toND@100°C specimen, and a micro-crack initiation can be seen inside the twin (Fig. 3.8c).

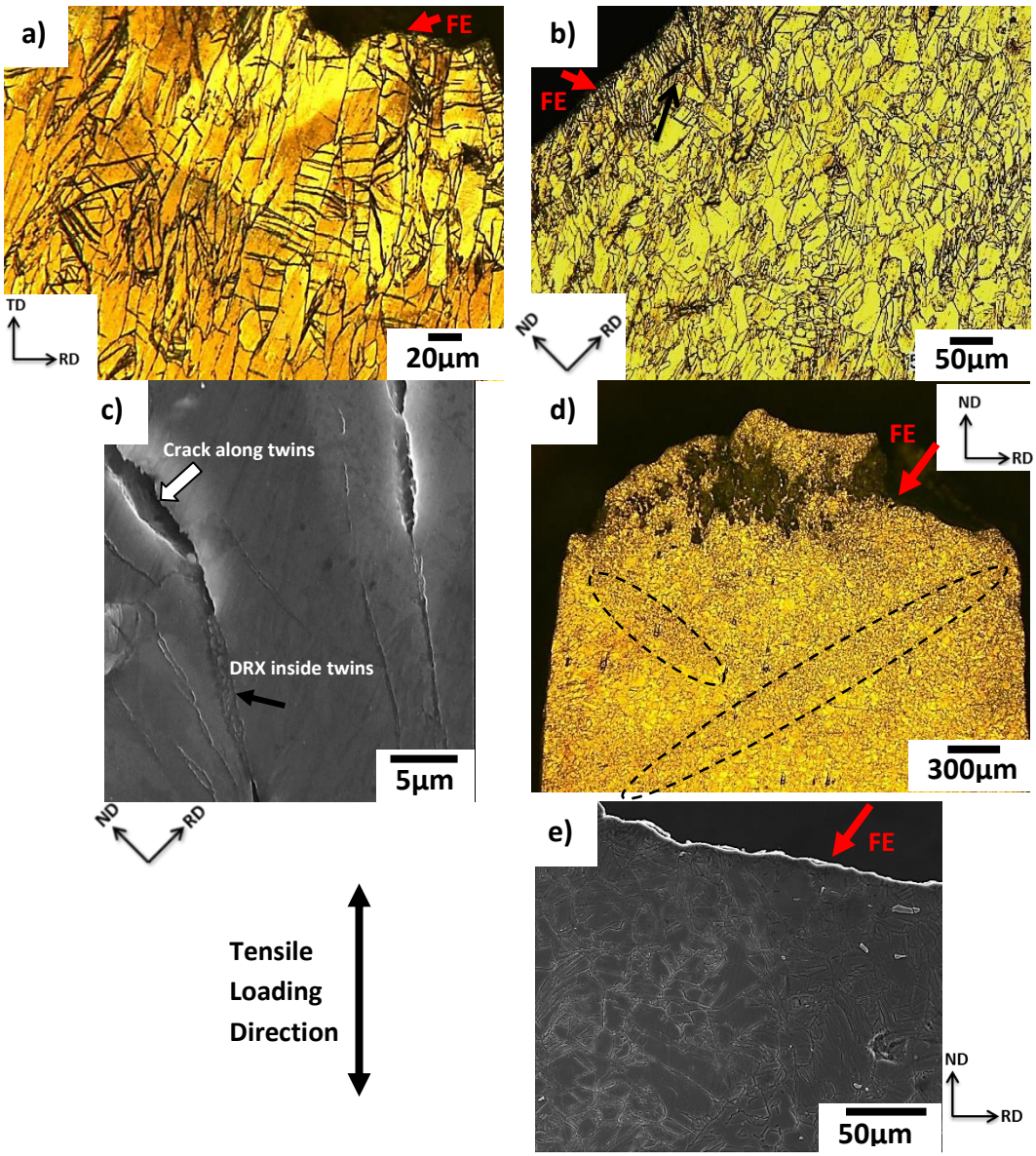

Figure 3.8 OM and SEM micrographs of uniaxial tension tested samples at 100°C (a) TD, (b and c) 45toND and (d and e) ND. Loading direction is vertical. FE: Fractured edge.

OM and SEM images of the ND specimen tested at 100°C (ND@100°C) are given in Figures 3.8d and e. Numerous twins are observed throughout the specimen, and most of the twin boundaries are not straight and mostly serrated (Fig.3.8e). It was proposed [104] that these type of twin boundaries occur when tension twins form on different $\{10\bar{1}2\}$ planes, once they impinge on one another. Grain boundaries are unclear, and most of the grains are segmented. More uniform elongation up to fracture (Fig.3.9c) was observed similar to the 45toND specimen but with much lower EF strain. Voids are abundantly prevalent just near the fracture surface, as seen in Figs. 3.8d. Large sample–scale shear bands (indicated by the oval in Fig.3.8d) are obvious in the ND@100°C, as compared to 45toND@100°C. In addition, no trace of DRX was apparent here, even inside the shear bands and twins (Fig.3.8e).

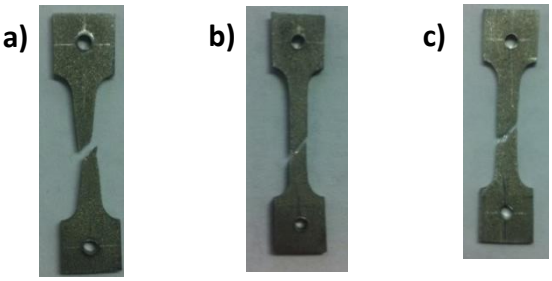

Figure 3.9 Images of tensile specimens after uniaxial tension tests at 100°C. (a) TD, (b)NDto45 and (c) ND.

Figure 3.10 displays the SEM images from the fracture surfaces of the TD@100°C, 45toND@100°C, and ND@100°C specimens. Higher quantities of dimples with elongated structures are evident in the TD@100°C specimen (Figs. 3.10a-b)

compared to the 45toND specimen (Figs. 3.10c-d). Several areas of microvoid coalescence-like features are seen in Fig.3.10b from the TD@100°C specimen. The large dimple shown in Figure 3.10d seems to be a boundary related fracture that might be a twin interface or boundary in the 45toND specimen. The equiaxed and elongated dimples are present in the ND@100°C specimen; however, a transgranular, cleavage-like feature is also evident in certain regions (Figs. 3.10e-f).

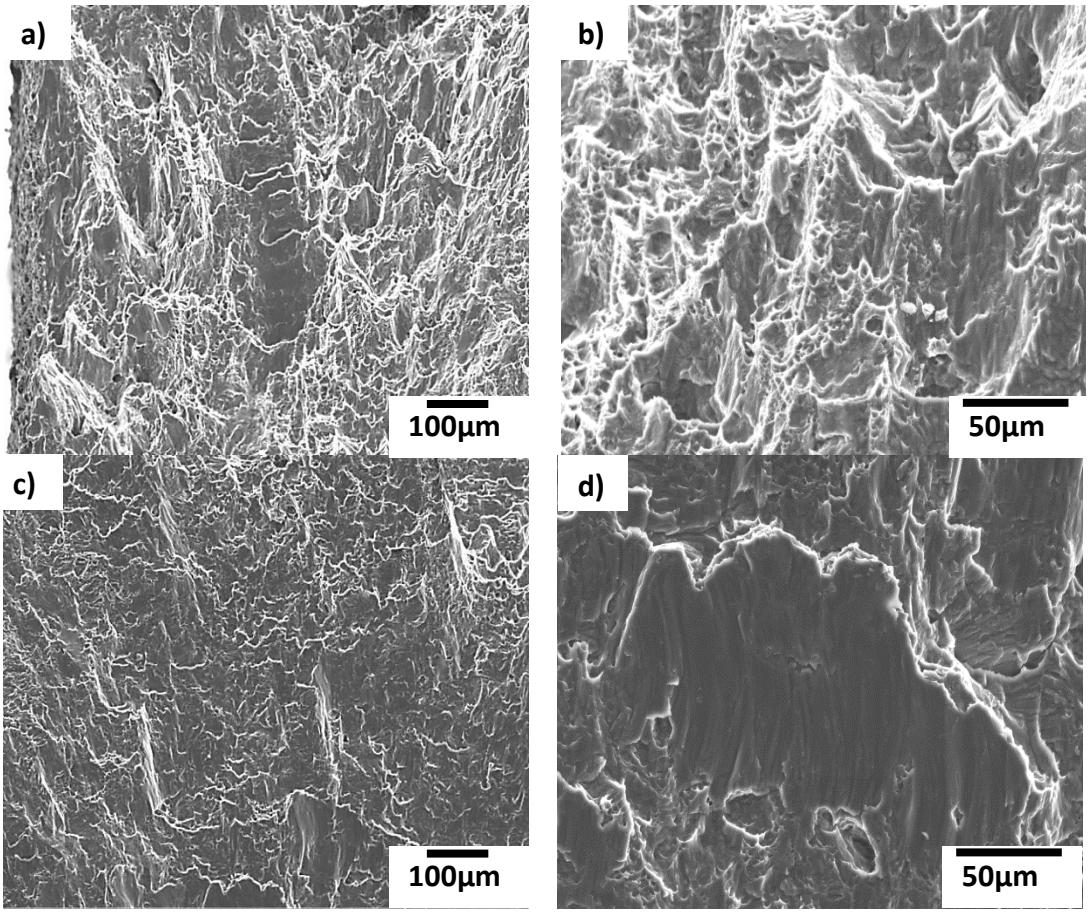

Figure 3.10 SEM images of fracture surfaces from (a-b) TD, (c-d) 45toND and (e-f) ND specimens

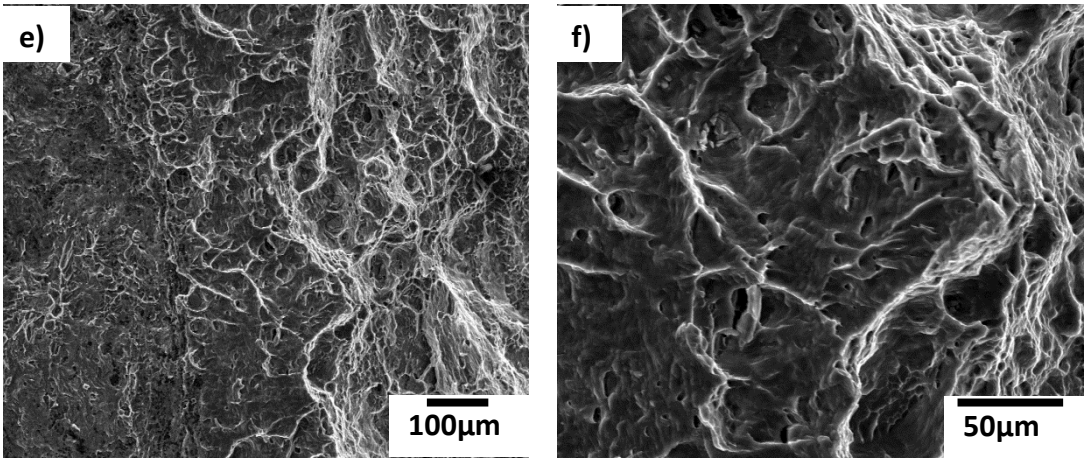

Figure 3.10 Continued.

Figures 3.11a and b display the microstructure of the TD sample which failed at 150°C (TD@150°C). Contrary to the TD@100°C sample, twinning was not observed near the fracture surface of TD@150°C (Fig. 3.11a). Here, grains were elongated, and necklace-type DRX were evident around them (Fig.3.11b). Similar to TD@100°C, a remarkable necking was detected in TD@150°C (Fig. 3.12a). Interestingly, the sample is free of shear bands/zones, except in the necking region.

Micrographs of the 45toND specimen after failure at 150°C (45toND@150°C) are given in Figs. 3.11c and d. 45toND@150°C failed due to the prevalent shear band which consisted of twins similar to 45toND@100°C, but with a larger shear band width in the former one (Figs. 3.8b and 3.11c). The 45toND@150°C specimen displayed successive, extensive shear bands throughout the specimen that macroscopically showed uniform elongation (Fig. 3.12a) similar to the 45toND@100°C specimen. A micrograph taken from a shear band is given in Fig. 3.11d. Grains are segmented, and very fine DRX grains are also present. In addition, twinning is evident in Fig.3.11d.

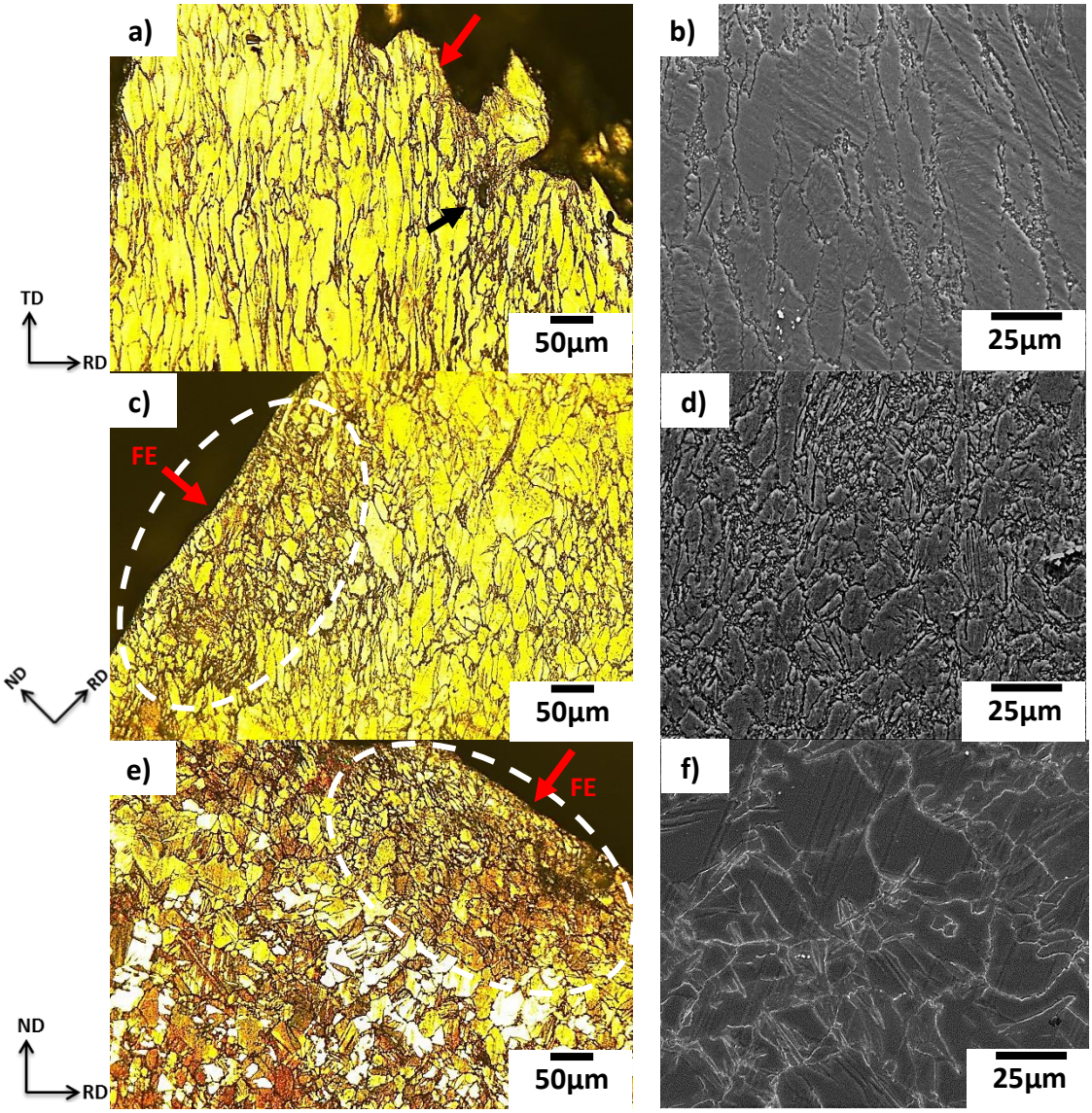

Figure 3.11 OM and SEM micrographs of uniaxial tension tested samples at 150°C (a and b) TD, (c and d) 45toND, and (e and f) ND. Loading direction is vertical. FE: Fractured edge

Fig. 3.11e shows an OM image near the fracture surface of the ND sample tested at 150°C (ND@150°C). Shear localization near the fracture surface is obvious in Fig. 3.11e. Grains are serrated by twins similar to ND@100°C; however, the twin volume

fraction is less than in ND@100°C (Figs. 3.8e and 3.11f). DRX were not observed in ND@150°C, as shown in a micrograph taken from a shear band (Fig 3.11f).

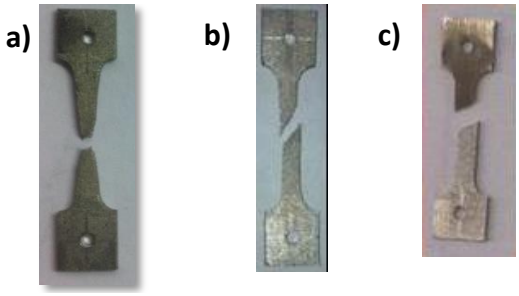

Figure 3.12 Images of tensile specimens after uniaxial tension tests at 150°C. (a) TD, (b) NDto45 and (c) ND.

Micrographs of the TD sample which failed at 200°C (TD@200°C) are given in Figs. 3.13a and b. The TD@200°C microstructure approximately resembles that of TD@150°C; however, a higher volume fraction of DRX is observed in the former (Figs 3.11a and 3.13a). Crack initiation started from the DRX-formed region, as shown by arrow in Fig.3.13a. The pictures of specimens tested at 200°C are given in Fig. 3.14. The picture of TD@200°C specimen is given in Fig. 3.14a, here a significant necking is obvious similar to the other TD specimens

The 45toND sample tested at 200°C (45toND@200°C) displayed pronounced DRX, and these DRX grains formed large shear bands (Fig. 3.13c). Here, the microstructure is mostly free of twins, and more pronounced DRX is a distinctive characteristic of 45toND@200°C in contrast to the alternate 45toND specimens. In addition, a significant necking was observed at different places throughout the gauge section of the 45toND@200°C specimen (3.14b), unlike the 45toND specimens tested at

lower temperatures. This might be because of limited tensile twinning activity that promotes uniform elongation. Crack formation inside the DRX shear bands (dashed circles) can be seen in Figs. 3.13c and d.

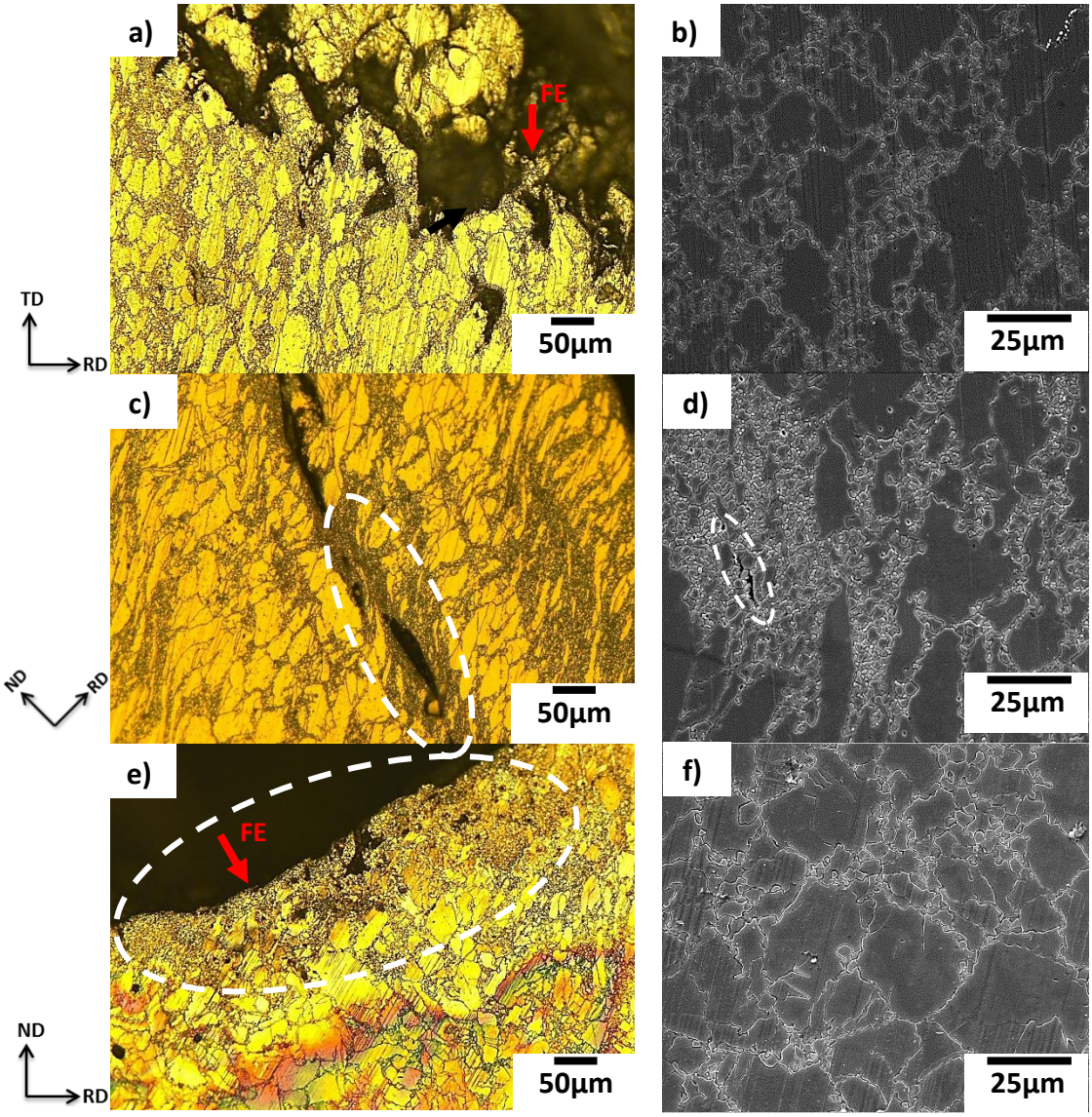

Figure 3.13 OM and SEM micrographs of uniaxial tension tested samples at 200°C (a and b) TD, (c and d) 45toND and (e and f) ND. Loading direction is vertical. FE: Fractured edge

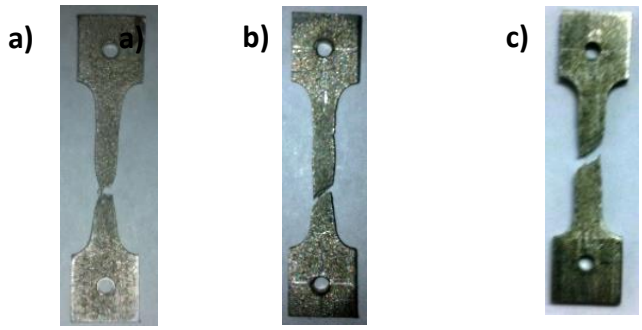

Figure 3.14 Images of tensile specimens after uniaxial tension tests at 200°C. (a) TD, (b) NDto45 and (c) ND.

Figs. 3.13e and f display the micrographs of the ND sample tested at 200°C (ND@200°C). Similar to other samples tested at 200°C, failure occurred from the DRX-formed region (Fig. 3.13e). However, large DRX-free grains are evident just near the fracture surface. Twin volume fraction seems to be significantly decreased at this temperature, although scattered twin boundaries (Fig. 3.13f) and twins away from the shear bands are visible. Deformation is highly localized in contrast to other samples tested at 200°C. Smaller EF strain with limited and localized DRX is the unique feature of ND@200°C (Figs. 3.13e, f and Fig. 3.14c).

3.4 Active Deformation Modes

When the basal planes are perpendicular to the tensile loading axis, the schmid factor of basal slip is close to zero. Therefore, prismatic slip is the most favorable deformation mode in TD samples [16, 39]. A large decrease in yield stress of TD specimens with temperature further confirms that thermally activated prismatic slip is the main deformation mode [38].

On the other hand, when basal planes are oriented 45° to the tensile loading axis (45toND), basal slip should be the most favorable deformation mode since it has the lowest CRSS and highest schmid factor with the aforementioned configuration. Since the CRSS of basal slip is less temperature-sensitive than the prismatic slip[38], the yield stress of 45toND samples showed less dependence on temperature (Fig. 3.4b).

Tensile loading of the c-axis (ND case) promotes tensile twinning at low temperatures. Therefore, in the TD, 45toND, and ND samples, prismatic and basal slips along with tensile twinning are the most favorable deformation modes at low temperatures, respectively. It is worth mentioning that thermally activated pyramidal <c+a> slip, which provides c axis deformation, should initiate activation at elevated temperatures in the ND case.

The stress-strain curve of ND@200°C indicates a slip-dominated yielding and, most importantly, the yield stress at this temperature is slightly higher than the others (Fig.3.4c). This indicates that a significant contribution of pyramidal <c+a> systems is evident. In addition, the microstructure of ND@200°C has fewer twins compared to other ND specimens at lower temperatures (Fig.3.13f).

Grains are reoriented by ~86° after tensile twinning. However, the reorientation direction depends on the loading condition. For example, basal planes reorient towards the loading axis under compression loading, whereas they reorient away from the loading axis in tension loading [105]. Therefore, in current loading conditions after tensile twinning activity (45toND and ND cases) grains are reoriented such that basal planes are almost perpendicular to the loading axis as seen in Fig. 3.7f, which afterwards

promotes prismatic slip. This is also evident from the stress-strain curves given in Fig. 3.4; the final stage of the curves has similar hardening behavior and stress levels for a given temperature until 200°C.

Compression and double twins were reported with prismatic slip activity after in-plane tensile loading of AZ31 sheets[39] and also observed here in Fig. 3.6c. Tensile loading of the TD sample (which promotes prismatic slip) cause a c-axis contraction which promotes compressive twinning at low temperatures. Thin twins with straight edges were found to be compression/double twins in RT specimens (Fig. 3.6). Twins with similar morphology are evident in TD@100°C (Fig.3.8a), especially near the fracture surface.

Fig.3.15a displays the EBSD inverse pole figure map of the TD@100°C specimen from the fracture surface after Xenon focus ion-polishing. A Kikuchi band contrast map showed different twin boundaries (Fig. 3.15b-e). The black regions in Fig. 3.15a couldn't be indexed and these regions have shear band and twin-like morphology. In addition, these regions may consist of micro-cracks. Tension twins with serrated boundaries as well as with band structure are evident in Fig. 3.15b, especially in the top-left part of the region. Compression and $\{10\bar{1}1\}-\{10\bar{1}2\}$ double twin boundaries are given in Figs. 3.15c and d, respectively. Very thin, needle-like compression twin bands are evident in Fig.3.15c, and usually those previously compression twinned regions are double twinned (one example is indicated by an arrow). Interestingly, some of the compression and double twinned regions were not indexed, indicating these regions have micro-cracks. The reorientation due to $\{10\bar{1}2\}-\{10\bar{1}2\}$ tension-tension double twins is

7.4°; thus, it is difficult to distinguish tension-tension double twin boundaries from the low angle grain boundaries (LAGBs). However, the lamella structure can be used effectively to distinguish tension-tension double twins from LAGBs. The boundaries having 7.4±3° misorientation are indicated in Fig. 3.15e. As seen in the figure, tension-tension double boundaries are abundant and some of the twins with lamella structure are indicated by arrow.

3.5 Shear Localization and Failure Mechanisms

Microstructures at failure of all samples tested at RT are similar, and EF strain levels are also identical. Cracks are prevalent in all samples; however, they are more pronounced in the TD sample (Fig. 3.6a). The EBSD map (Fig. 3.6a) of a TD specimen tested at room temperature showed compression and double twins near the fracture surface. Therefore, failure at room temperature seems to occur due to compressive/double twinning related crack initiation [52] in all cases.

Different twinning modes were observed especially near and at fracture surfaces of TD@100°C specimen as seen in Fig. 3.8a and 3.15, respectively. This indicates that similar to the TD specimen tested at room temperature, twin-related cracks should have a role on fracture. However, Figs. 3.11a and b indicate that the near fracture surface of TD@150°C is free of twins. Therefore, the failure mechanisms should be different at these temperatures. Fig. 3.11a indicates that cracks/voids initiate in the soft DRXed region around grain boundaries at 150°C (Fig. 11b). A crack is indicated by an arrow in Fig. 3.11a, where DRX-formed grains are accumulated in the junction of grains. The

micrographs demonstrate that twinning is less active at temperatures higher than 100°C in TD cases that promote mostly prismatic slip and twinning afterwards, at the late stage of the deformation in especially the necked/fractured region.

On the other hand, shear localization due to twinning was observed in 45toND and ND specimens and is more pronounced in the latter case (Figs. 3.8 and 3.11). The localization seems to occur much more rapidly and severely in the ND case; thus, EF stain is much lower than the 45toND specimens at all temperatures. The results indicated that twinning promotes shear localization. As discussed earlier, tensile twinning reorients the grains in such a way that prismatic slip is favorable afterwards. It is not yet clear whether compressive/double twinning causes crack/void initiation at 100°C and 150°C for 45toND and ND cases. A detailed orientation map is required. However, a micro-crack inside a twin that has DRX inside is evident in Figure 3.8c. Here, the DRX-formed region seems to act as a soft region, and appears crack initiated. DRX inside the tensile twinning was reported before [24]. However, the type of twinning in Fig. 3.8c must be identified.

A large number of voids are observed in ND@100°C, exclusively near the fracture surface; however, the sample failure is caused via localized regions consisting of twins and free of Al-Mn particles (Fig. 3.8e). Figures 3.16a and b show micro-cracks at the interface of an Al-Mn particle surrounded by twins. It is believed that cracks and twins are formed at the interface of Al-Mn particles due to stress concentration. Cracks seem to be more opened near the fracture surface (Fig. 3.16a).

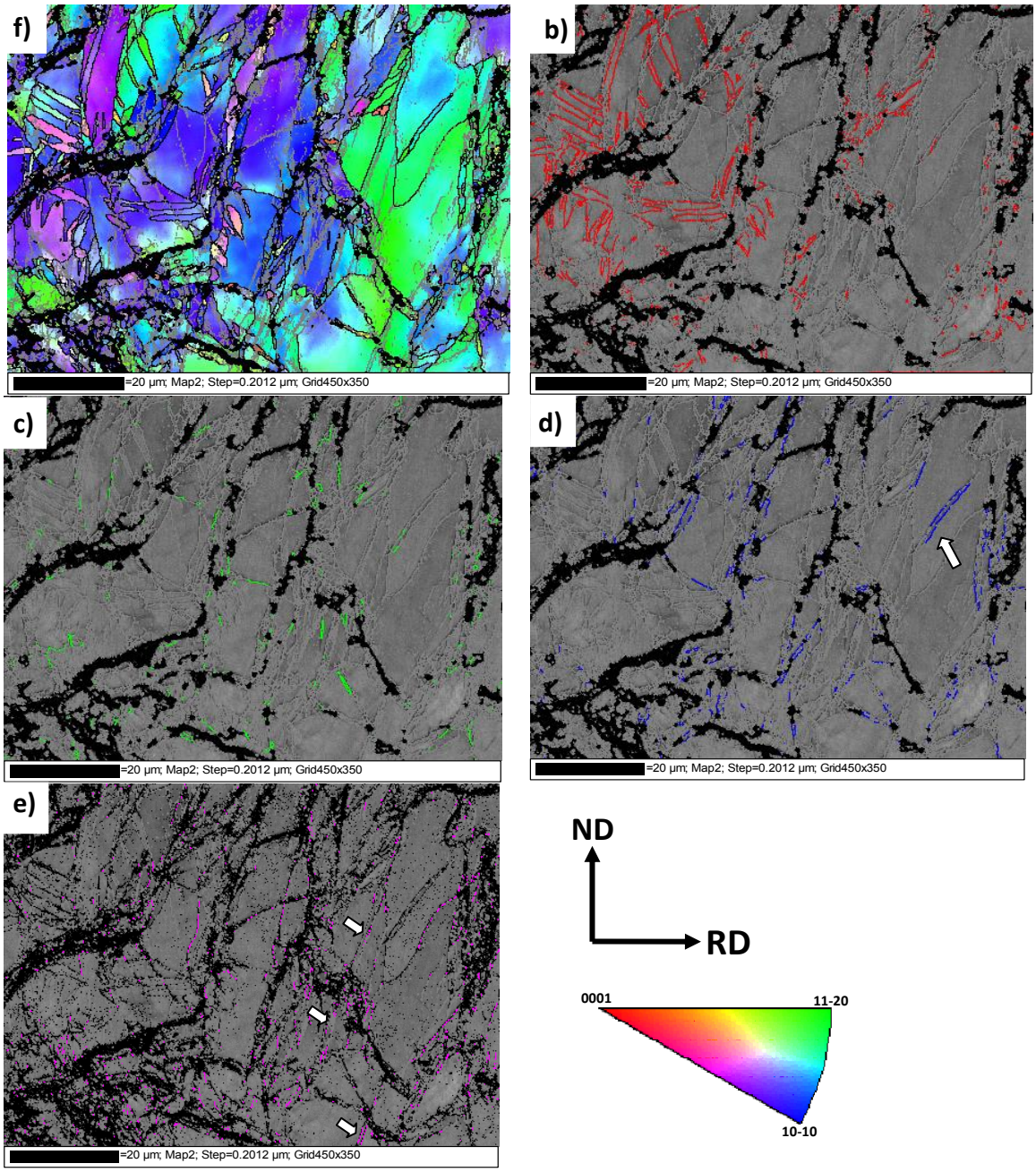

Figure 3.15 (a) EBSD inverse pole figure map of TD@100°C specimen. EBSD-Kikuchi band contrast map showing different twin boundaries. (b) Tension (86°±5), (c) Compression (56°±5), (d) Compression+Tension double (38°±5) and (e) Tension-Tension double (7.4°±3) twin boundaries.

Failure occurred at a shear band consisting of twins in the 45toND@150°C and ND@150°C samples (Figs. 3.11c and e), where the former possesses DRX inside (Figs. 3.11d). DRX seem to provide extra ductility in the 45toND@150°C specimen since higher EF was recorded compared to ND@150°C (Figs 3.4b and c).

Microstructures at failure of the TD@200°C and 45toND@200°C specimens look similar (Figs, 3.13a and c, respectively). Accumulation of small DRX-formed soft grains formed easy shear paths, as by Ion et al.[38], and failure occurred in these regions. However, these shear bands are more pronounced in 45toND@200°C (Figs. 3.13c and d). DRX is only evident near the fracture surface of ND@200°C (Fig. 3.13e), which indicates that failure occurred due to localized DRX regions as a result of deformation localization.

The micrographs of TD specimens indicated that twinning seems to be involve in the crack initiation and eventual failure up to 100°C (Figs. 3.6a, 3.8a and 3.15). However, at higher temperatures (150°C and 200°C) crack initiation initiated from soft DRX-formed regions/bands (Figs. 3.11a and 3.13a).

Failure in 45toND specimens initiated from the shear bands which consist of twins up to 200°C (Figs. 3.8b and 3.11c). DRX-formed grains were observed even at 100°C. Figs. 3.8d and c clearly showed that soft shear zones which consist of DRX-formed grains caused the failure at 200°C.

Microstructure at failure of ND specimens indicated that failure is due to shear bands which consist of twins but are free of DRXed grains up to 200°C (Figs 3.8e and

3.11e). At 200°C, twins are replaced by DRX-formed grains in highly localized shear zones (Fig. 3.13e).

3.6 The Role Al-Mn Particles

The Al-Mn particles are mostly aligned along the rolling direction (Fig. 3.3a-b) and are present in all specimens. They are aligned perpendicular to the tensile loading axis in the TD and ND cases, at which the stress state promotes the crack initiation around the Al-Mn particles. However, the ductility levels of the TD and ND specimens are remarkably different at elevated temperatures, indicating that failure is not mainly associated with the Al-Mn particles. At 100°C, the numerous voids near the fracture surface and the crack initiation around the particles are shown in Fig.3.8d and Figs.3.16a-b, respectively. However, the ND@100°C specimen failed at a shear band that is free of particles (Fig.3.8e), although many voids are present near the fracture surface. Figure 3.16c displays the SEM image of the 45toND@100°C specimen, which shows cracks formed along twins, and Al-Mn particles are free of cracks around them. This indicates that twin related cracks form faster than the ones around Al-Mn particles.

Crack initiation around the Al-Mn precipitates was observed in all specimens at 100°C and higher temperatures. Fig.16d is the micrograph of TD@150°C specimen that shows void initiation around the Al-Mn particles. However, it seems that the voids formed in the DRX formed regions just near the Al-Mn particle, as shown by an arrow. The crack/void initiation from the DRX formed region around the grain boundaries were shown in Figures 3.11a and 3.13a-b. DRX around the Al-Mn particle is evident in

45toND@200°C specimen as seen in Fig.3.16e. It appears that DRX start primarily around these particles. Interestingly, a void growth can be seen in Fig.3.16f, where the void progresses in the DRX formed region. Here, the Al-Mn precipitate prevents two voids from coalescence in the 45toND@200°C specimen.

3.7 Effect of Deformation Modes on DRX and Ductility

It was reported that the stacking fault energy for non-basal slip systems is much higher than that for the basal slip [106]. Less pronounced DRX was observed in the TD specimens, where prismatic slip is readily active compared to the 45toND specimens (mostly basal slip) at all temperatures. In addition, DRX seems to be sparse in the ND case. Basal slip is the least favorable slip system in the ND case since initially the basal planes are parallel to the loading direction and thus are perpendicular to the loading axis after reorientation due to tensile twinning (Fig. 3.7e). However, prismatic slip after tensile twinning and pyramidal<c+a> slip at elevated temperatures are favorable in the ND case. Therefore, ready activation of non-basal slips remarkably retards the DRX in the ND case, even at 200°C (Figs. 3.13b, d and f). Indeed, the EF strain levels in the ND cases at all temperatures are usually lower than the TD and 45toND specimens; thus, it is important to consider EF strain levels when comparing these different microstructures.

It is worth mentioning that the yield stress of the ND sample slightly increased at 200°C, suggesting a pronounced pyramidal<c+a> slip (higher CRSS than that of tensile twinning[27]) compared to lower temperatures. The large EF strain difference between

the ND@200°C specimen and other directions at 200°C (Fig.3.4) appears due to low volume fraction of DRX.

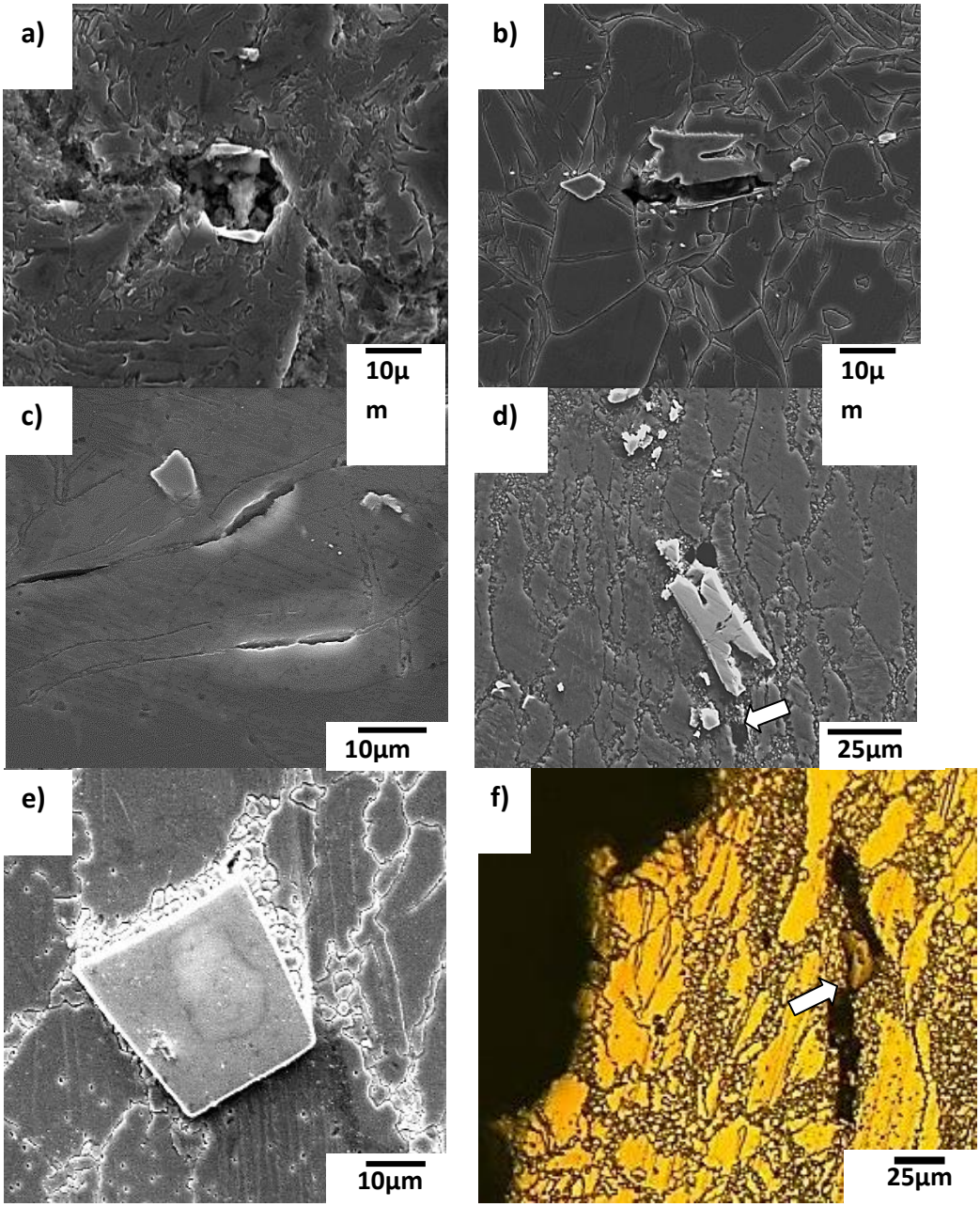

Figure 3.16 SEM images of ND specimen tested at 100°C showing crack/void near Al-Mn particles (a) near fracture surface (b) away from the fracture surface. SEM images of (c) 45toND@100°C, (d) TD@150°C and (e-f) 45toND@200°C specimens.

Readily activated prismatic slip in the TD case promotes uniform deformation until necking in comparison to the tensile twinning cases (45toND and ND). Therefore, a higher EF strain is a distinctive characteristic of TD samples at all temperatures (Fig.3.4). On the other hand, uniform elongation up to failure and no significant post-necking was observed in the 45toND and ND specimens, up to 200°C, as a result of pronounced tensile twinning activity. High twinning activity seems to cause deformation localization and thus non-uniform DRX in the ND and 45toND cases. Results indicated that twining deteriorates ductility at moderately elevated temperatures due to deformation localization, whereas it is an extra source of ductility at room temperature [27] (Fig. 3.4).

3.8 Summary and Conclusions

Final microstructures of AZ31 specimens cut from different directions of a strongly textured, hot-rolled plate were examined after uniaxial tension tests at different temperatures (25-200°C). The active deformation modes showed a great influence on dynamic recrystallization (DRX) behavior and the ductility of the AZ31 Mg alloy at low temperatures (≤200°C). The main findings of this study can be summarized in the following:

1. Elongation to failure (EF) strain increased and flow strength decreased dramatically with increasing temperature when the sample is uniaxially loaded along the transfer direction. However, EF strain and the yield strength didn't change with increasing temperature when the sample is uniaxially loaded along the normal direction.

2. When tensile twinning is activated, uniform elongation is more pronounced due to the hardening associated with tensile twining. Twinning caused shear localization and thus non-uniform DRX, thereby inducing earlier fractures at moderately elevated temperatures (≤200°C).
3. DRX formed regions around the grain boundaries and Al-Mn particles act as a source of fracture at 150°C and higher temperatures for all differently oriented specimens. However, crack formation was observed both inside and along the interface of the twins at temperatures lower than 150°C.
4. Higher ductility, homogeneous deformation, and widespread DRX were observed when prismatic slip is the primary deformation mode at temperatures above room temperature.

CHAPTER IV

ROLE OF STARTING TEXTURE AND DEFORMATION MODES ON LOW TEMPERATURE SHEAR FORMABILITY AND SHEAR LOCALIZATION OF MG-3AL-1ZN ALLOY

This chapter investigates the role of various starting crystallographic textures and deformation modes on the shear formability via ECAP and shear localization of AZ31 alloy at temperatures lower than 200°C, where the material shows large flow strength anisotropy, deformation twinning and tension-compression asymmetry. Detail microstructural characterization and VPSC simulations were used to reveal the relationships between the deformation modes, formability, dynamic recrystallization and shear band formation under shear deformation at a lower temperature (150°C).

It is widely reported that defect-free ECAP of AZ31 and other Mg alloys is possible at temperatures above 200°C [10-14, 20-21] due to high strain rate sensitivity [22-23], pronounced DRX activity [24], and readily active non-basal slips [23]. However, processing at lower temperatures promotes twinning and introduces heterogeneous deformation, thereby causing shear bands and cracks during ECAP. In addition to the lack of alternate slip systems available, twinning seems to be a main deformation-limiting mechanism of AZ31 at low temperatures.

One of earlier study in our group showed [73] that the starting texture has a significant effect on DRX characteristics and slip modes during ECAP at 200°C [14], at which different initial textures were successfully processed without significant twinning

activity. With this in mind, our initial attempt was to design new low temperature (<200°C) ECAP routes by alternating the starting texture and thus the active deformation modes. Indeed, we tried to find the starting texture/configuration from the commercially available wrought AZ31 Mg alloy textures (Fig. 4.1a) that gives minimum amount of twinning activity during ECAP at 150°C. Our preliminary VPSC simulations using the only published VPSC parameters [27] for AZ31 Mg alloy at 150°C indicated that tensile twinning activity is highly depend on the starting texture (Fig.4.2). Please note that, the compression twinning activity was not considered in the preliminary VPSC simulations due to lack of information. Detailed VPSC analyses using the best-fit parameters obtained in this study for each deformation modes including the compression twinning will be presented in the following sections.

Under careful texture modifications, the low temperature limit for ECAP of AZ31 has been reduced from 200°C down to 150°C by suppressing the compression twinning activity and instead, promoting prismatic slip. At 150°C with the basal poles initially parallel to the extrusion direction (ED) (Texture1 in Fig. 4.1a), the sample failed during ECAP; however, it was successfully processed at the same temperature when the basal poles were perpendicular to the ED (Texture2 in Fig. 4.1a). VPSC model was utilized to gain a deeper understanding of operating deformation modes and dynamic recrystallization during ECAP of different starting textures at 150°C, the latter of which was found to play a significant role in shear localization during ECAP. Detailed SEM, EBSD and TEM analyses and the simulation results clearly indicated that the formation of compression twins causes deformation localization, followed by dynamic

recrystallization within the compression twins at 150°C. This non-uniform DRX causes local softening and large shear bands, and eventual failure during ECAP.

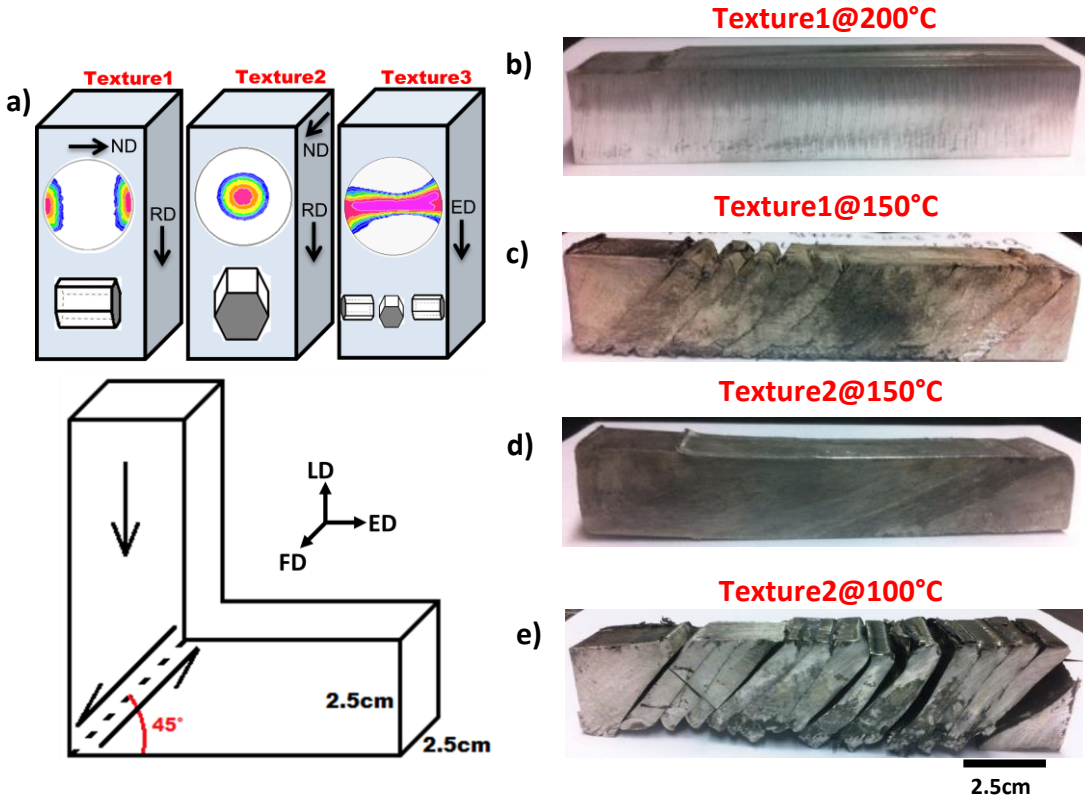

Figure 4.1 (a) Schematics of the three ECAP cases studied in the present work with (0002) pole figures showing different AZ31 Mg alloy texture, Texture1: hot-rolled texture, basal poles are parallel to ED, Texture2: hot-rolled texture but basal poles are parallel to FD, Texture3: typical conventional area reduction extrusion texture; basal poles are aligned around the center rim. ED: Extrusion direction, LD: Longitudinal direction, FD: Flow direction. Images of the billets after ECAP: (b) Texture1@200°C, (c) Texture1@150°C, (d) Texture2@150°C and Texture2@150°C.

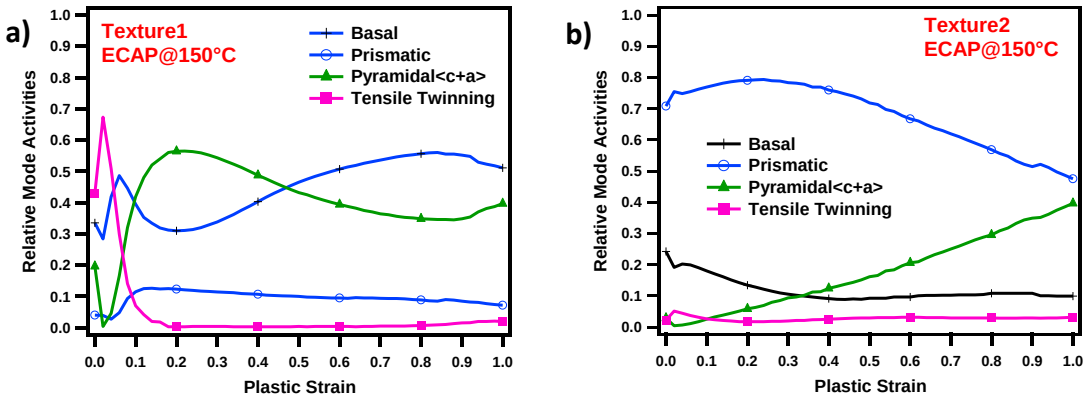

Figure 4.2. Predicted relative deformation mode activities of (a)Texture1, (b)Texture2 during ECAP at 150°C using reported VPSC parameters[27].

4.1 Microstructural Evolution and DRX Characteristics of Texture1 and 2 Specimens after ECAP at 150°C

Figs. 4.3a and b provide OM and SEM images of the hot-rolled plate before ECAP processing. Here, the microstructure shows fully recrystallized grains with an average grain size of around 25µm. Al-Mn (~Al_8Mn_5) particles, shown by dashed circles in Figs. 4.3a and b, are in sizes ranging from 1 to 30 µm are present as also shown in Fig.3.3. The volume fraction of these precipitates is very low (<1%).

The Texture1 specimen failed during ECAP while the Texture2 specimen was successfully processed at 150°C (see Figs.4.1c and d, respectively). In the former, cracks are present throughout the cross-section and the specimen is divided into relatively uniform, discrete segments as shown in Fig. 4.1c. A similar ECAP failure has been reported at 150°C for Texture3 [20] using an identical strain rate. In contrast, the same material with Texture2 (i.e. a differently oriented billet with respect to the ECAP die)

was successfully processed at the same temperature with identical extrusion rate and back pressure values but exhibited a crack-free deformation (Fig. 4.1d).

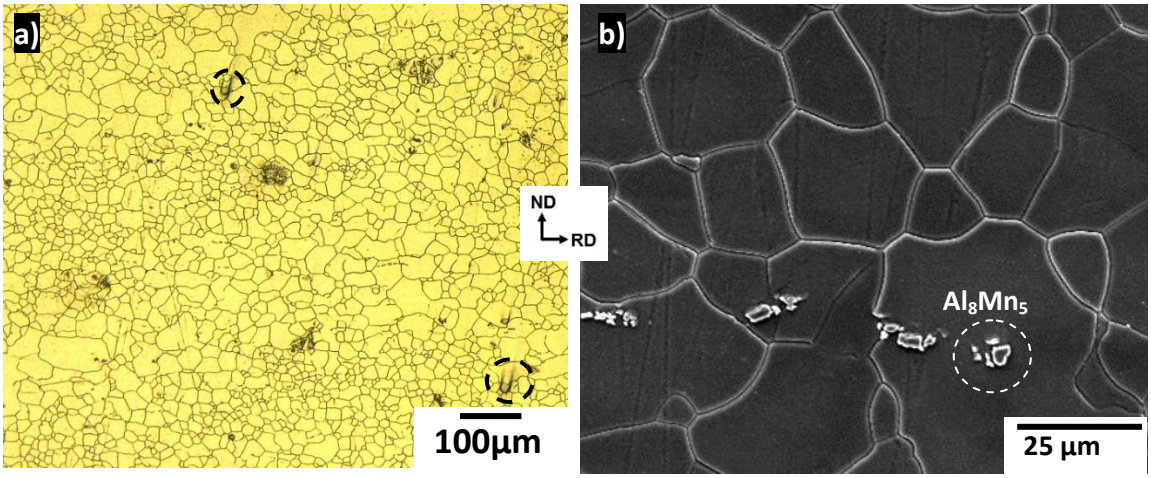

Figure 4.3 (a) OM and (b) SEM images of hot-rolled AZ31 Mg alloy before ECAP.

OM and SEM images of the Texture1 specimen after ECAP clearly reveal the presence of twin lamellas (Figs. 4.4a, c and e). In addition, the accumulation of very fine DRX grains forms large shear bands which are parallel to the macro-cracks (Fig. 4.4a and c), and large grains lie between these successive shear bands (Fig. 4.4a). A micro-crack formed inside a shear band consists of very fine DRX grains (Fig. 4.4c). In addition, recrystallized grains inside twins can be seen in Fig. 4.4e indicated by dashed circle. Non-uniform deformation with a twinned microstructure and failure is the prominent feature of the Texture1 specimen.

More uniform deformation, on the other hand, is evident throughout the ECAP sample in the Texture2 case (Figs. 4.4b, d and f). Here, the sample is free of large shear

bands and micro cracks; instead, very small micro shear bands are present throughout the sample (Fig. 4.4b). All grains seem to be significantly deformed, divided, and elongated (Figs. 4.4b and d). In addition, there are some very fine DRX grains (Figs. 4.4d and f). However, these are accumulated around the grain boundaries (Fig. 4.4f), creating a "necklace" structure [14, 32, 38]. Fewer, smaller DRX grains are obvious in the Texture2 case, in stark contrast to the Texture1 specimen (Figs. 4.4c and d).

4.2 Texture Change after ECAP at 150°C

The $(10\bar{1}0)$ and (0002) pole figures of the Texture1 and Texture2 specimens before and after ECAP are given in Figs. 4.5a&c and 4.5b&d, respectively. Fig. 4e presents the locations of the ideal fibers in ECAP of Mg (hcp crystal) under simple shear loading on $(10\bar{1}0)$ and (0002) pole figures, which was previously reported in [30, 107]. Figs. 4.4a and b display the $(10\bar{1}0)$ and (0002) pole figures of the hot-rolled AZ31 plate. A typical hot-rolled AZ31 texture is evident in Figs. 4.4a and b. These textures are measured from different planes of the same hot rolled plate, where the Texture1 and 2 specimens were cut. Basal poles are mostly parallel to the normal direction, and the spread in the basal pole is towards the rolling direction (RD).

The texture for the Texture1 specimen changed considerably after ECAP, where (0002) basal planes rotated towards the longitudinal direction (LD) by about 120° in the counter-clock-wise direction (Fig. 4.5c). Basal fiber approaches to B fiber position that is at 135° as indicated in Fig.4e. A spread towards to C_2 is also evident in the basal fiber (Fig.4c).

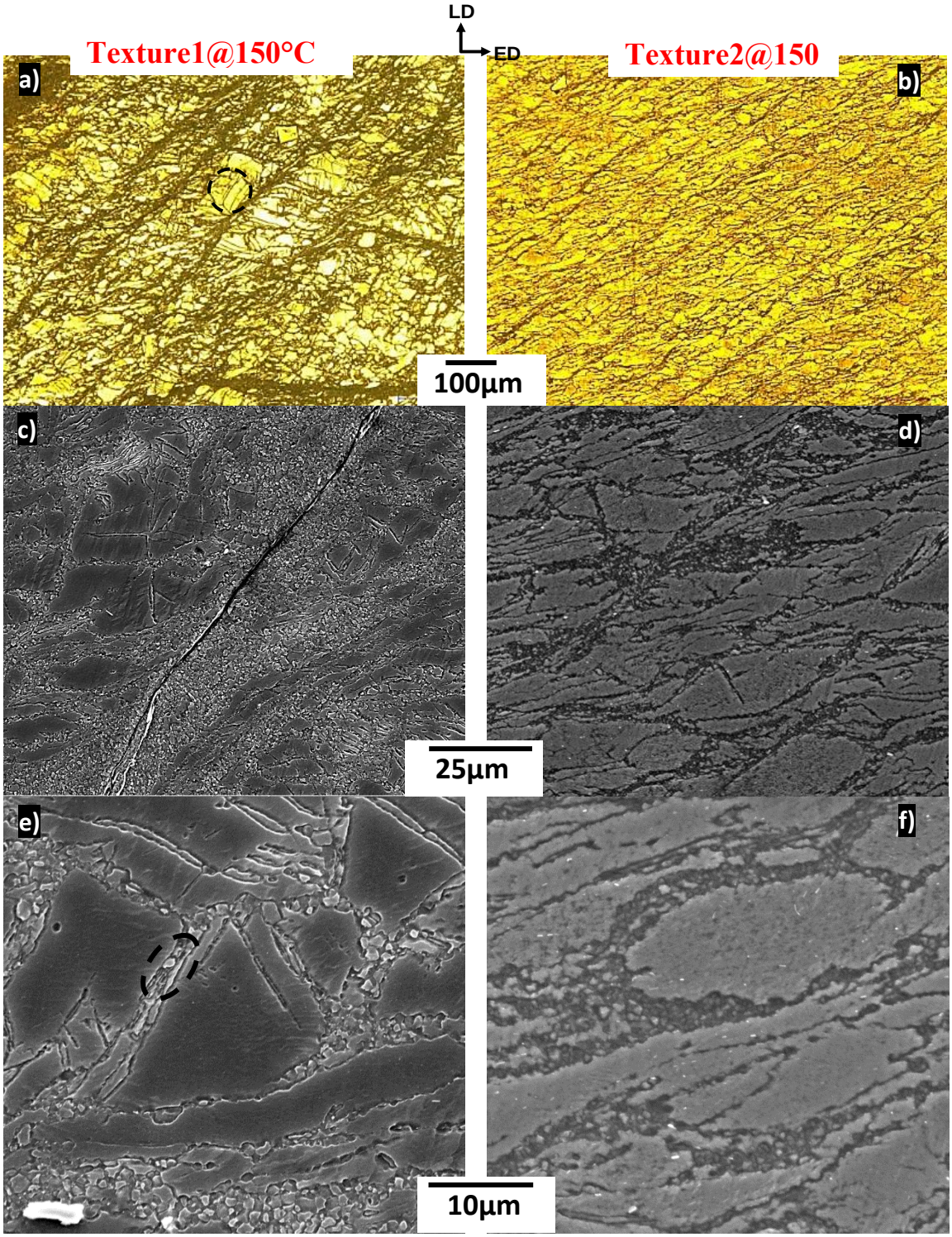

Figure 4.4 OM images of (a)Texture1 and (b)Texture2 specimens after ECAP at 150°C and corresponding SEM images for (c and e)Texture1 and (d and f)Texture2 samples.

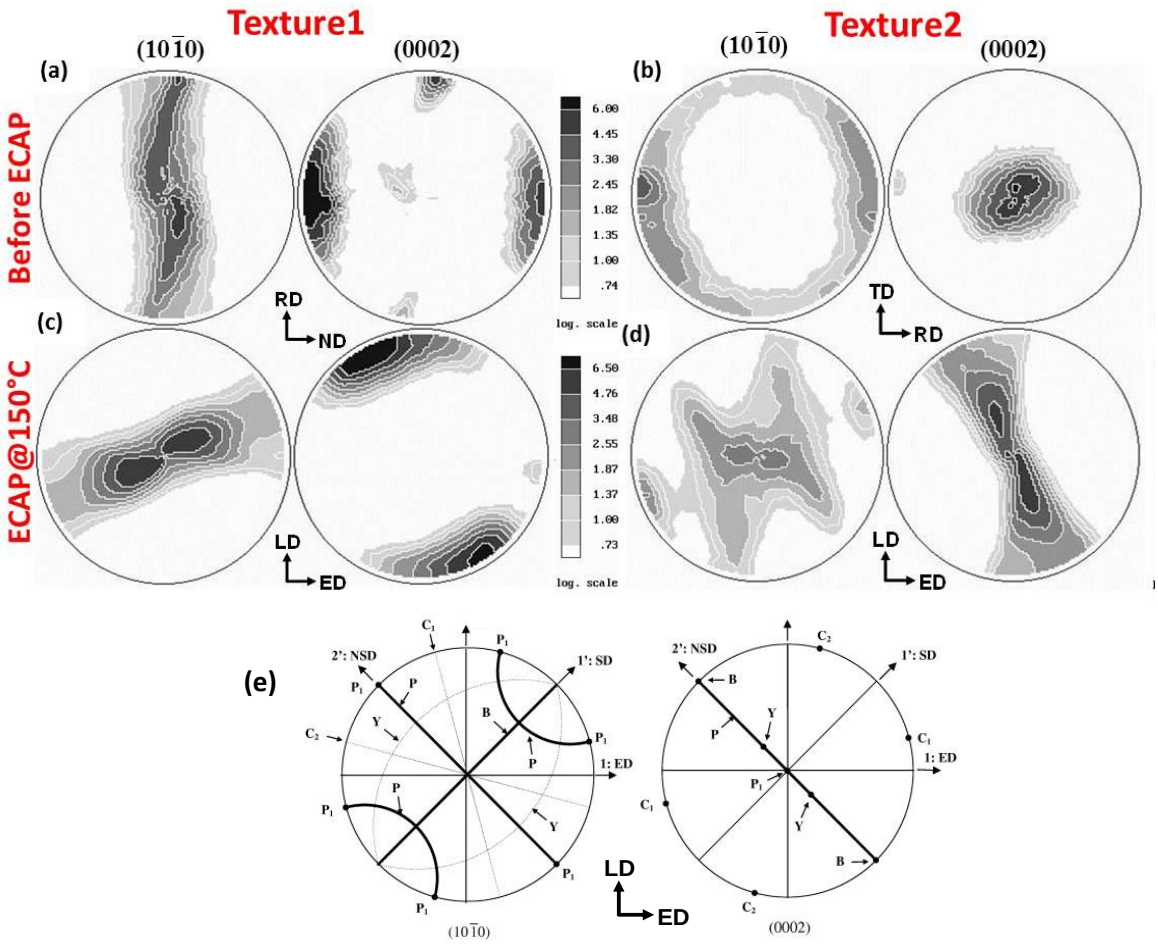

Figure 4.5 Experimentally measured $(10\bar{1}0)$ and (0002) pole figures of Texture 1 specimen (a) before and (b) after; Texture 2 specimens (c) before and (d) after ECAP at 150°C. (e) A key figure showing the locations of the ideal fibers in ECAP of Mg (hcp crystal) under simple shear loading on $(10\bar{1}0)$ and (0002) pole figures, which was previously reported in Refs.[19,29].

Texture modification is not very severe after ECAP for the Texture2 case; the initial (0002) basal texture was split into two and was spread out along P and Y fibers (Figs. 4.5b and d). In addition, an accumulation of prismatic planes at the center of the

$(10\bar{1}0)$ pole figure (Y fiber) is evident, which was not visible before ECAP (Fig.4.5b and d).

4.3 EBSD Analysis of Texture 1 and 2 Specimens after ECAP at 150°C

The EBSD inverse pole figure (IPF) map of the Texture1 specimen after ECAP and is given in Figs. 4.6a. The large grains and DRX bands between them are visible in Fig. 4.6a. Large grains are usually free of sub-boundaries (<2°). Their equiaxed shape like in initial material (Figs. 4.3a and b) appears preserved, indicating that these grains are less deformed and not elongated/divided typically during ECAP.

The recrystallization inside a twin is apparent in Figs.4.6a (as marked with an arrow). The EBSD-Kikuchi band contrast map in Fig. 4.6b where specific grain boudaries are higlighted in different colors shows that different twinning modes have accommodated deformation. The twin lamella with recrystallized grains inside is indexed as a compression twin (in green in Fig.4.6b), and some double twin boundaries ($\{10\bar{1}2\}$ tensile twinning inside $\{10\bar{1}1\}$ compression twin, in blue) are also evident. Twin boundaries which are mostly indexed in the shear band region consist of DRXed grains.

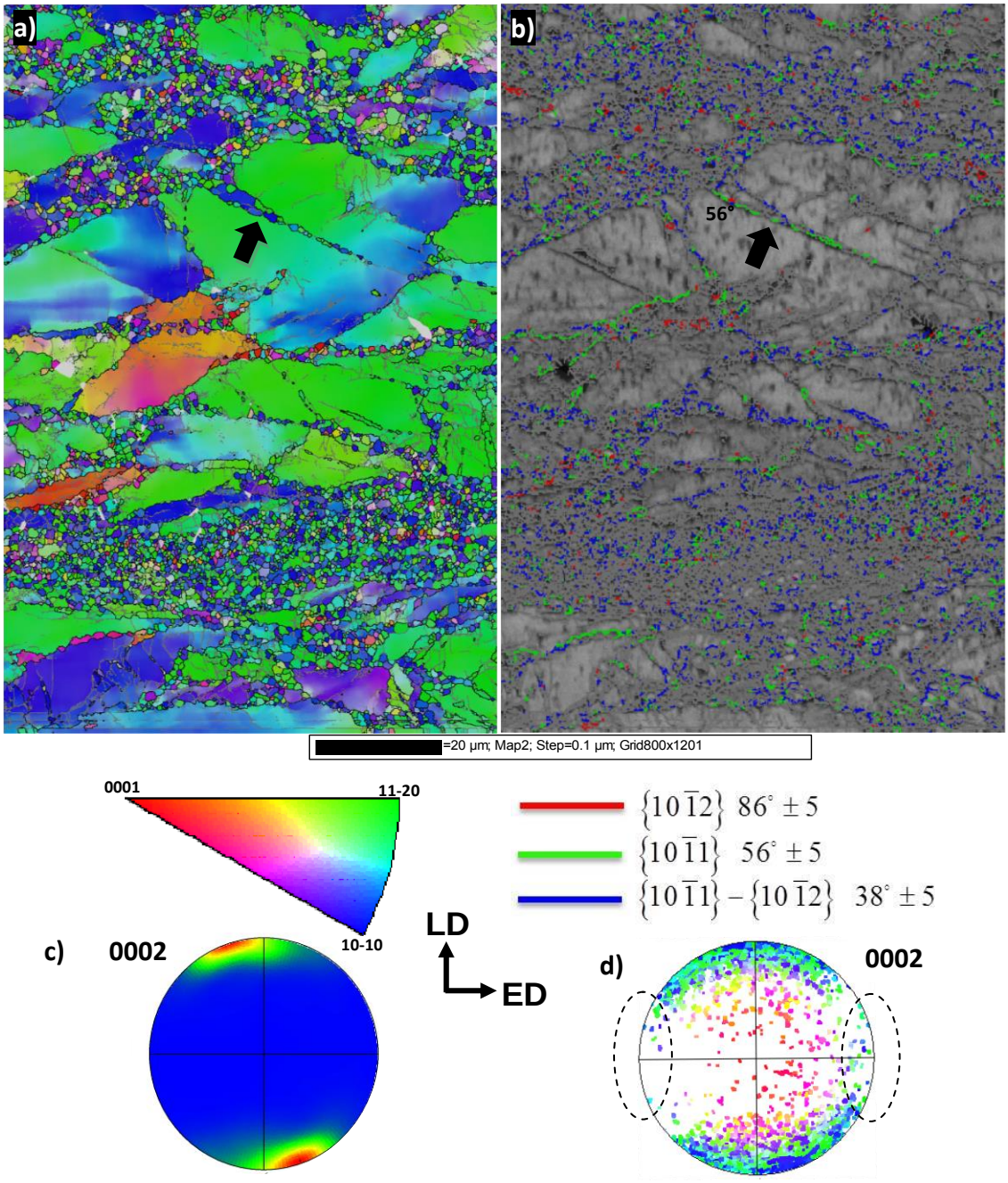

Figure 4.6 (a) EBSD inverse pole figure map of Texture1 specimen after ECAP at 150°C. (b) EBSD-Kikuchi band contrast map showing different twin modes. Corresponding (c) contour and (d) scattered (0002) pole figures.

A minimal amount of $\{10\bar{1}2\}$ tensile twin boundaries (in red) are visible in Fig. 4.6b. These boundaries correspond to $\{10\bar{1}1\}$-$\{10\bar{1}2\}$ double twin and $\{10\bar{1}1\}$ compression twin modes, as listed in Table 4.1 and in Fig. 4.6b. Please note that the misorientation angles of $\{10\bar{1}1\}$ and $\{10\bar{1}3\}$ compression twins are 56° and 64°, respectively. It is difficult to distinguish them with 5° deviation angle, thus only $\{10\bar{1}1\}$ compression twins twin boundaries are reported in Fig. 4.6b.

The (0002) pole figure (Fig. 4.6c) of the EBSD map given shows a strong basal texture which is similar to the bulk specimen texture (Fig. 4.5b). In addition, the (0002) pole figure, with scattered data using the same color code from the EBSD IPF map (Fig.4.6a), is given in Fig.4.6de and shows the position of each grain in Fig.4.6a (identifiable by its color) on the pole figure. The initial texture position on the pole figure is marked with a circled black-dashed line (Fig. 4.6de). Here, we observe that very few grains maintain their initial orientation.

Table 4.1. Twinning modes and their misorientation angles.

Name	**Twin Type**	**Misorientation angle to $\langle 11\bar{2}0\rangle$ axis**
Tension	$\{10\bar{1}2\}$	86°
Compression	$\{10\bar{1}1\}$	56°
Compression	$\{10\bar{1}3\}$	64°
Double	$\{10\bar{1}1\}\{10\bar{1}2\}$	38°

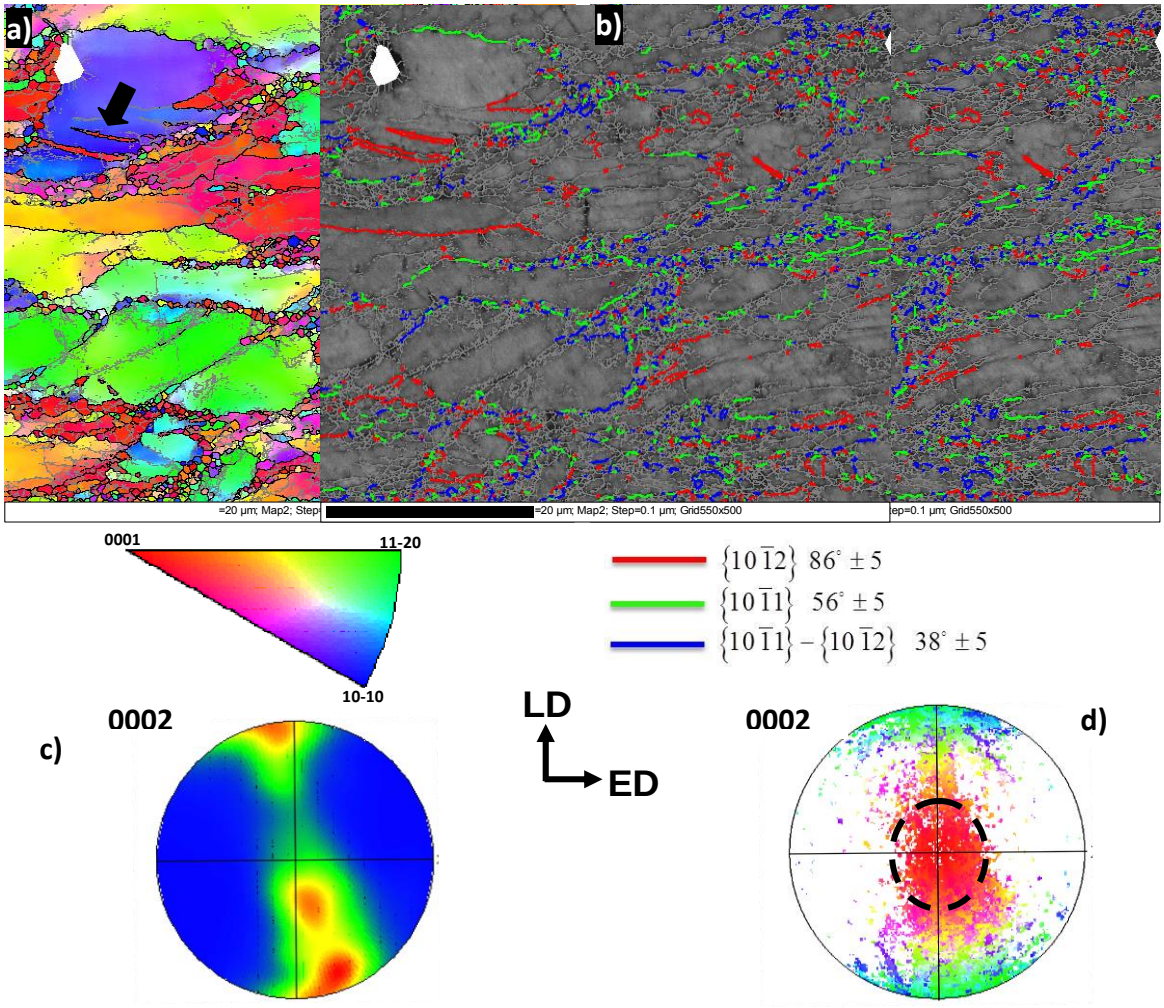

Figure 4.7 (a) EBSD inverse pole figure map of Texture2 specimen after ECAP at 150°C. (b) EBSD-Kikuchi band contrast map showing different twin modes. Corresponding (c) contour and (d) scattered (0002) pole figures.

The EBSD results of the Texture2 specimen are given in Figure 4.7. Unlike the Texture1 specimen, in the Texture2 sample, grains are smaller, divided, and elongated along ED with dense, low angle grain boundaries (Fig. 4.7a). The DRX grains lie mostly around the grain boundaries of the large grains and are smaller in size as compared to the DRX grains in the Texture1 specimen (Fig. 4.6a).

Fig. 4.7b shows different twin boundaries where tensile twin boundaries are prevalent; please note, compression and double twins are present mostly in DRXed regions around the grain boundaries. The (0002) pole figure for the EBSD area is given in Fig. 4.7c. Here, the texture is somewhat similar to the bulk texture given in Fig. 4.5d. Fig. 4.7d shows the position of colored grains on the (0002) pole figure, indicating that most of the grains (in red in Fig. 4.7a) have similar orientations in the initial texture which is circled with the dashed-black line. However, the green and blue grains are reoriented around 86° from the initial orientation (in red), indicating that these grains have deformed by tensile twinning and entirely reoriented by the twins (Figs. 4.7a and d). The remnant parent grain (the region of the grain which has not twinned) are obvious in Fig. 4.7a as for example the one shown by an arrow (and by red color in green blue grains).

4.4 VPSC Polycrystal Modelling

In order to quantify the active deformation modes during ECAP for Texture1, Texture2, and Texture3 specimens, the VPSC crystal plasticity model was utilized. The details of the model is not repeated here for the sake of brevity, but they can be found in[25] and in Chapter I. Prodominant Twin Reorientation scheme [26] was used to consider reorientation by twinning. Fig. 4.8 shows the simulated and experimental flow curves of the starting material during uniaxial loading along the three different directions: transverse direction (TD), normal direction (ND) and 45° to ND direction (45toND) at 150°C. The TD sample was cut from the plane normal to the ND direction,

whereas the ND and 45toND specimens were cut from the plane perpendicular to the TD. More details about the location of the specimens on the hot-rolled plate can be found in [108]. These directions were selected to activate different deformation modes during each uniaxial test, in order to accurately capture hardening parameters for each deformation mode. Since mechanical responses along the TD and RD are nearly the same, only the TD results are reported here.

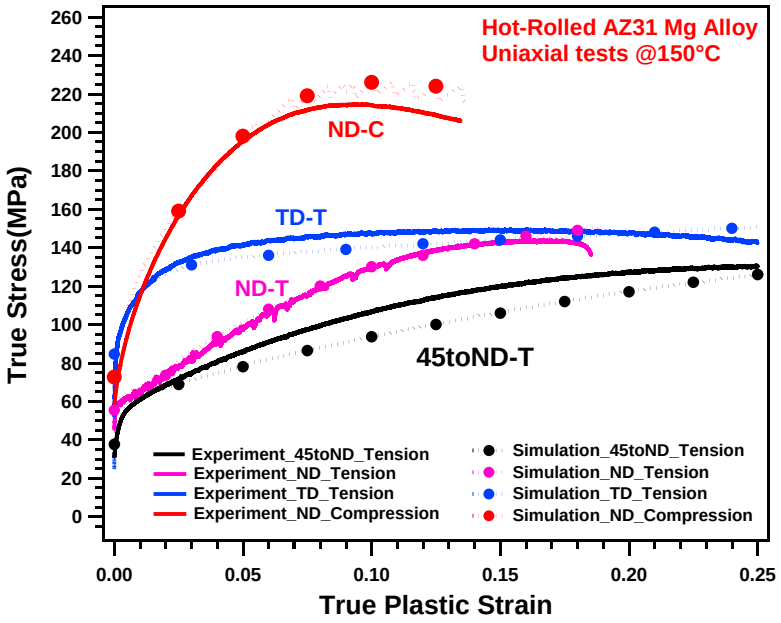

Figure 4.8 A comparison of simulated (symbols) and experimental (solid lines) uniaxial tension and compression responses of AZ31 Mg alloy at 150°C along different directions using the VPSC crystal plasticity model. TD:Transverse direction, ND:Normal direction, 45toND: 45° to ND direction from the TD plane.

Table 4.2 Model paramaters for AZ31 Mg alloy at 150°C after the best-fit calibration of uniaxial tests shown in Figure 4.8 The values are normalized by the CRSS for basal slip, which is fixed at 12MPa for this study and was fixed at ~25MPa by the refence study in the table.

Mode	Initial CRSS $\tau 0$	Back-extrapolated CRSS($\tau 0+\tau 1$) $\tau 1$	Initial hardening rate ($\boldsymbol{\theta_0}$)	Asymptotic hardening rate ($\boldsymbol{\theta_1}$)
Basal	1	1	125	2.5
Prismatic	5	2.08	100	0
Pyramidal <c+a>	5.41	14.58	291.6	0
$\{10\bar{1}2\}$ Tensile Twinning	3.75	0	0	0
$\{10\bar{1}1\}$ Compression Twin	10	6.67	100	0
Reference [27]				
Basal	1	0.5	80	3
Prismatic	2	2.5	20	0
Pyramidal <c+a>	2	5	100	0
$\{10\bar{1}2\}$ Tensile Twinning	1.7	0	0	0
$\{10\bar{1}1\}$ Compression Twin	-	-	-	-

A Voce hardening law was employed that was described in Chapter I. The total of 20 calibrated VPSC parameters used in this study for basal, prismatic, and pyramidal <c+a> slips, and $\{10\bar{1}2\}$ tensile and $\{10\bar{1}1\}$ compression twinning are listed in Table 4.2 together with the only reported data for AZ31 alloy for 150°C [27]. Latent hardening is considered constant for all deformation modes and was set to 1 such that self and latent hardenings are indistinguishable, and the evolution of the threshold stress ($\tilde{\tau}$) is given by

$$\Delta\tau^s = \frac{d\tilde{\tau}^s}{d\Gamma}\Delta\Gamma \ , \tag{4.1}$$

which depends only on the equation (1) given in Chapter I. As seen in Fig. 4.8, the simulations of uniaxial tension and compression along different directions accurately reproduce the experimental responses. The flow anisotropy is still obvious, even at 150°C, due to the different active modes in each direction. For example, tensile twinning is readily active during tension along the ND (Fig. 4.9a) while compression along the ND (Fig. 4.9b) activates hard compression twinning and pyramidal <c+a> slip. This observation is clear from the peak stress levels of each test in Fig. 4.8. In both cases predominant basal slip activity is evident (Figs. 4.9a-b). Tensile loading of the 45toND specimen activates almost fully basal slip (Fig. 4.9c), whereas tension along the TD activates mostly prismatic slip (Fig. 4.9d). Interestingly, prismatic slip is active later part of the deformation during tension along ND, 45toND and TD (Figs. 4.9a,b-c). This is obvious in Fig. 4.8 where peak stress levels are very close especially in ND and TD tension cases.

The experimentally measured initial texture (Fig. 4.5a) of Texture1 specimen was discretized into around 1000 orientations (grains) to use as an input texture (Fig. 4.12a) in the simulation. The same procedure is applied for Texture2 and Texture3 specimen. In three cases, there is a good agreement between experimentally measured (Figs. 4.5a) and discretized (Fig.4.12a) textures (under Texture1 condition, Texture2 and Texture3 cases are not reported here).

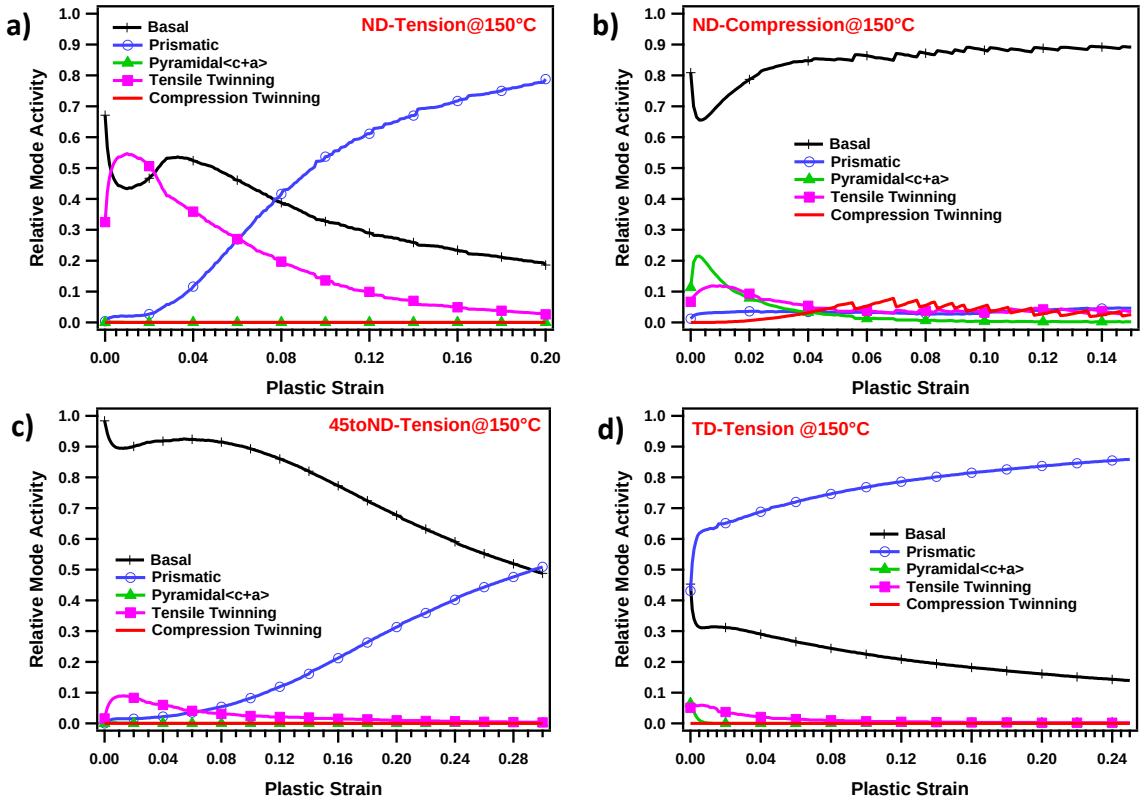

Figure 4.9 Predicted relative deformation mode activities of AZ31 Mg alloy samples uniaxially tested at 150°C. (a) ND-Tension, (b) ND-Compression, (c) 45toND-Tension and (d) TD-Tension.

Using the same parameters listed in Table 4.2, the relative mode activities during ECAP at 150°C of three starting textures (1-3) have been predicted and shown in Figs. 4.10a-c. There is a significant difference in the relative deformation activities for the different starting textures. The Texture1 and 3 specimens show a similar trend in relative activities, but compression and tensile twinning are more prominent in the Texture1 specimen (Figs. 4.10a and c). Most importantly, in both cases there are pronounced basal and twinning activities. In contrast, almost no compression twinning is predicted in the

Texture2 case, where prismatic slip followed by basal slip is the most dominant modes (Fig. 4.10b).

Predicted $(10\bar{1}0)$ and (0001) pole figures for Textures1 and 2 specimens are given in Figs. 4.11a and b, respectively. There is a good agreement between the predicted and measured pole figures after ECAP (Figs.4.5 and 4.11), confirming the validity of the model parameters acquired from the uniaxial tension and compression tests at the same temperature. The small differences between simulated and experimental pole figures are believed to be due to deformation of subgrains and dynamic recovery/recrystallization during ECAP, which were not considered in the model.

4.5 Reorientation due to Tensile Twinning

Pronounced tensile twinning activity was predicted during ECAP of the Texture1 specimen; however, very limited tensile twinning boundaries are visible in the EBSD map given in Fig.4.6 (the typical tensile twinning misorientation angle is 86° and represented by the red boundaries on the figure). Usually, tension twins grow easily and consume the parent grain completely. This is observed for the Texture2 specimen (Fig. 4.7a); tension twins consume most of the parent grains (in red), and only several lamellas remain in the twinned grains (in blue and in green). An example is shown by an arrow in Fig. 4.7a.

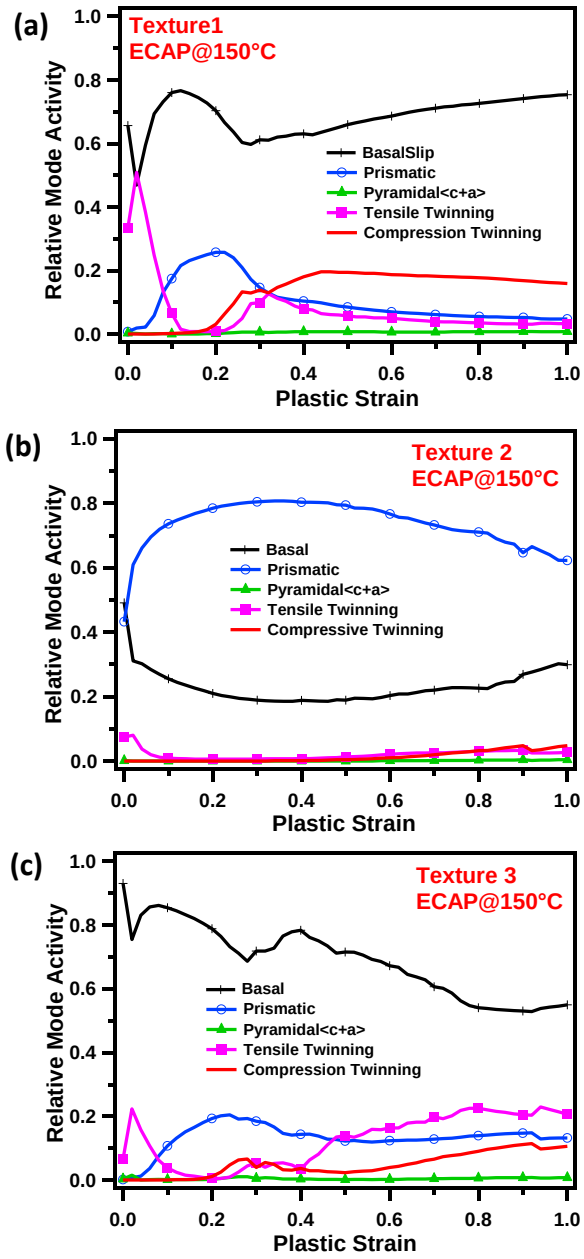

Figure 4.10 Predicted relative deformation mode activities of (a) Texture1,(b) Texture2 and (c) Texture3 during ECAP at 150°C.

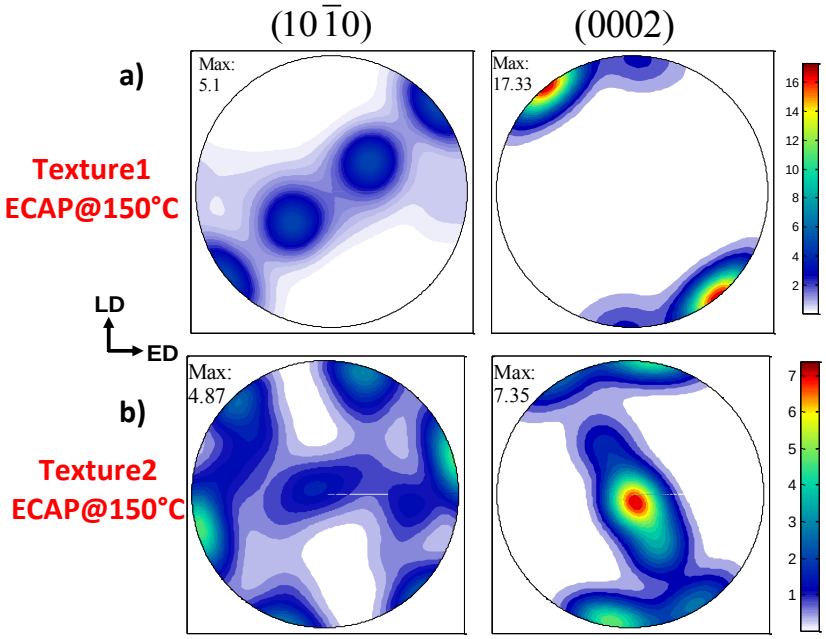

Figure 4.11 Simulated (10$\bar{1}$0) and (0001) pole figures of two different starting textures; (a) Texture1 and (b) Texture2 specimens after ECAP at 150°C.

During one pass of ECAP, shear strain of $\frac{\gamma}{2} = \varepsilon_{xy} = 1$ is applied to the specimen. The majority of the tensile twinning activity transpires at the early stage of deformation for the Texture1 specimen, as seen in Fig. 4.10a. In addition, it is evident from Fig. 4.6d that most of the grains are reoriented around 90° from the initial orientation circled by the dashed line. It is likely that these grains (in green and blue) are reoriented due to tensile twinning activity.

Since an interrupted ECAP experiment is not possible, texture evolution of the Texture1 specimen was simulated using the VPSC model and the results are shown using the (0002) pole figures (Fig. 4.12). Most of the grains are reoriented around 86° towards the LD direction after 4% plastic strain (Figs. 4.12a-b). After 10% plastic strain,

almost all grains are reoriented 86° due to the pronounced tensile twinning activity (Figs. 4.10a and 4.12c). The predicted textures clearly indicate that the initial orientation has been altered rapidly due to tensile twinning activity at the beginning of deformation. In particular, the stress state during ECAP is shown to be tension along the ED and compression along the LD. It is well known that the c-axis tension initiates pronounced tensile twinning activity and causes a rapid texture change. The current stress state applied to the Texture1 specimen that has a strong texture encourages tensile twinning activity since both the ED tension and LD compression provide c-axis extension. Therefore, at the beginning of the deformation high tensile twinning activity is inevitable.

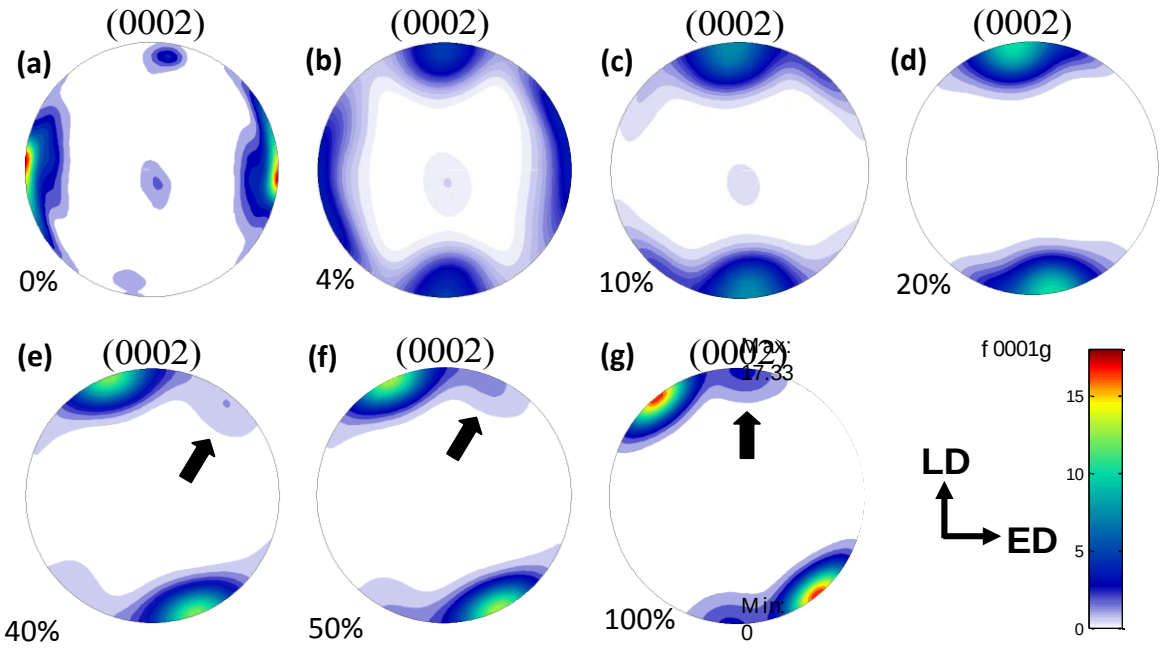

Figure 4.12 Predicted texture evaluation (as shown in (0002) pole figures) during ECAP of Texture1 specimen with increasing plastic strain of (a) 0%, (b) 4%, (c) 10%, (d) 20%, (e) 40%, (f) 50%, (g) 100%.

The large texture rotation due to the intense basal slip activity during ECAP (at 200°C and higher temperatures) of Texture1 starting texture was reported and VPSC model predicted the experimental texture successfully in different studies[12, 14, 30] in which only slip mechanisms are considered in VPSC. The reason(due to the nature of basal slip) for a rotation larger than the imposed rigid-body rotation during ECAP are analyzed in detail in [30]. The relative deformation mode activities and the final texture of Texture1 specimen predicted by using the VPSC parameters for 150°C (Table 4.2) but considering only the slip systems are given in Figs. 4.13a and b, respectively. However, the predicted (only slip systems are active) texture given in Fig. 4.13b does not match with the experimental texture given in Fig. 4.5c. The intense basal fiber rotated by 90° around FD; however in the experimental texture it rotated by 120°. It appears that without considering twinning, the simulation cannot predict the experimental texture (Figs. 4.5c, 4.11a and 4.13b). Interestingly, the predicted texture given in Fig. 4.13b when only slip systems are active is very similar to the ECAP (at 200°C and higher temperatures) texture given in [12, 14, 30]. This clearly shows that the larger rotation towards B fiber in this study is due to massive tensile twinning activity.

Reorientation due to tensile twinning in the Texture2 specimen is also evident in Figure 4.7d. The blue and green grains are reoriented towards the LD direction from the center of the (0002) pole figure. Interestingly, the green grains are more deformed and distorted in the Texture2 specimen compared to the Texture1 sample.

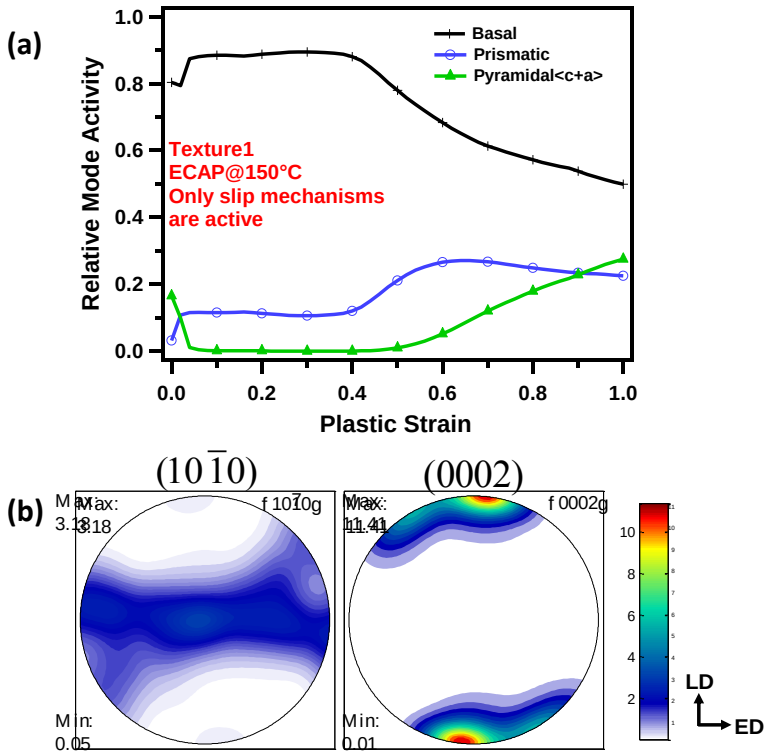

Figure 4.13 (a) Predicted relative deformation mode activities during ECAP of Texture1 specimen at 150°C and corresponding final texture by using the VPSC parameters given in Table2 but only slip mechanisms are allowed to be active.

4.6 Deformation Localization and Recrystallization inside Compression and Double Twins

As evidenced in Texture 1 and 3 cases, similar mode activities lead to ECAP failure (Fig. 4.1c and [20]). Compression twinning, the only deformation mode active for the Texture 1 and 3 cases but not for the Texture2 specimen, appears, therefore to be correlated with failure since Texture2 specimen alone was successfully ECAP at 150°C. In addition, there exists a major difference in the activated deformation modes between these cases, Textures 1&3 and Texture2. In the former, pronounced tensile and compression twinning are the governing deformation mechanisms (accompanied by

excessive basal slip activity), whereas in the latter these are mainly replaced by prismatic slip.

The reoriented grains due to compression (reorientation of 56° ($\{10\bar{1}1\}$) or 64°($\{10\bar{1}3\}$) or double twinning (reorientation of 38°($\{10\bar{1}1\}$-$\{10\bar{1}2\}$)) were shown to be much more favorably oriented for basal slip than in their original orientations [52]. With this in mind, the predicted relative deformation mode activities inside the reoriented grains due to the primarily compression twinning (Reo-by-CTw) in Texture1 specimen during ECAP at 150°C are given in Fig. 4.14a. It clearly shows high basal slip activity accompanied by tensile twinning activity inside the Reo-by-CTw grains. As evident from Figs. 4.10a and 4.14a, Reo-by-CTw grains are much more favorable for the softest slip system, basal slip, since the basal slip activity fraction (Fig.4.14a) inside these Reo-by-CTw grains is higher than the overall basal slip activity fraction (Fig.8a). Double twinning $\{10\bar{1}1\}$-$\{10\bar{1}2\}$ was also captured via VPSC, where tensile twinning is highly active inside the Reo-by-CTw grains (Fig. 4.14a). Also, basal slip activity showed a second peak right after double twinning $\{10\bar{1}1\}$-$\{10\bar{1}2\}$ was activated after 0.3 plastic strain (Fig.4.14a).

The Schmid factor maps for different slip systems of the $\{10\bar{1}1\}$ compression twinned area (with DRX grains inside) for the Texture1@150°C specimen are given in Fig. 4.14 for loading along the ED and LD (longitudinal direction), respectively. As evident from Fig.4.14, the compression twinned area is much more favorable for the softest slip system, basal, than the surrounding area. On the other hand, difficult to

activate prismatic and pyramidal<c+a> slip systems are more favorable outside of the compression twin since the Schmid factor is generally lower (color code in Fig. 4.13) inside the compression twin.

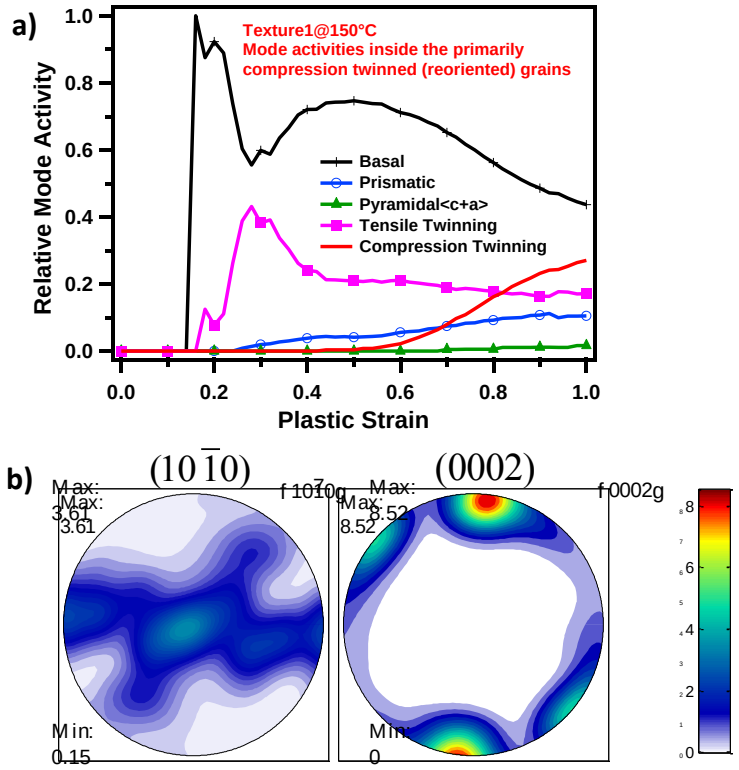

Figure 4.14 (a) Predicted relative deformation mode activities inside the grains roeriented by compression twinning in Texture1 specimen during ECAP at 150°C. The mode activities inside the compression twinned grains are normalized. (b) predicted final texture for the grains that have been reoriented by compression twinning.

Both VPSC results and Schmid factor map indicate that deformation through basal slip is localized inside compression twins; this non-uniform deformation is believed to trigger earlier DRX inside the compression twins than in the surrounding regions. In terms of orientation, the compression twinned region acts as a soft region

since the softest slip mode, basal slip, is much more favorable. These regions primarily deform like a soft region in a composite material. Therefore, deformation is expected to occur more within the compression twinned region than in the surroundings.

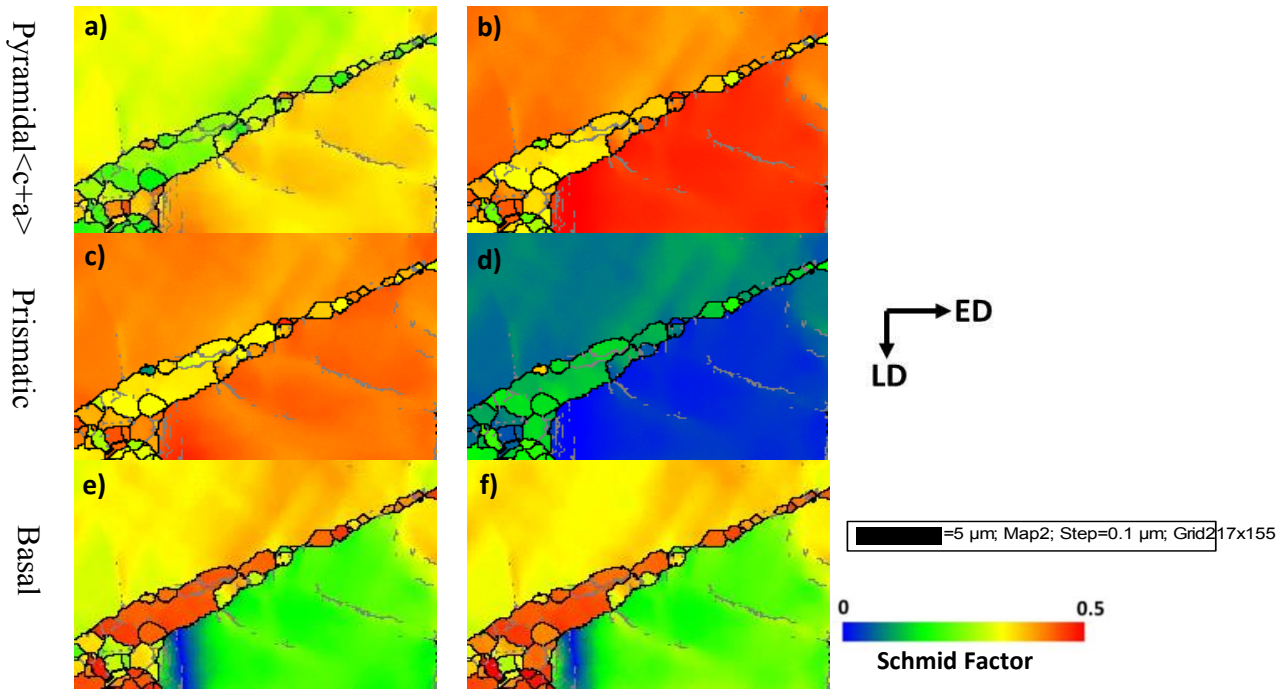

Figure 4.15 Schmid factor maps for different slip systems in the Texture1@150°C specimen, with a compression twin and recrystallized grains inside. Schmid factor maps for (a) pyramidal<c+a>, (c) prismatic, and (e) basal slips during loading along ED; (b) pyramidal<c+a>, (d) prismatic, and (f) basal slips during loading along LD.

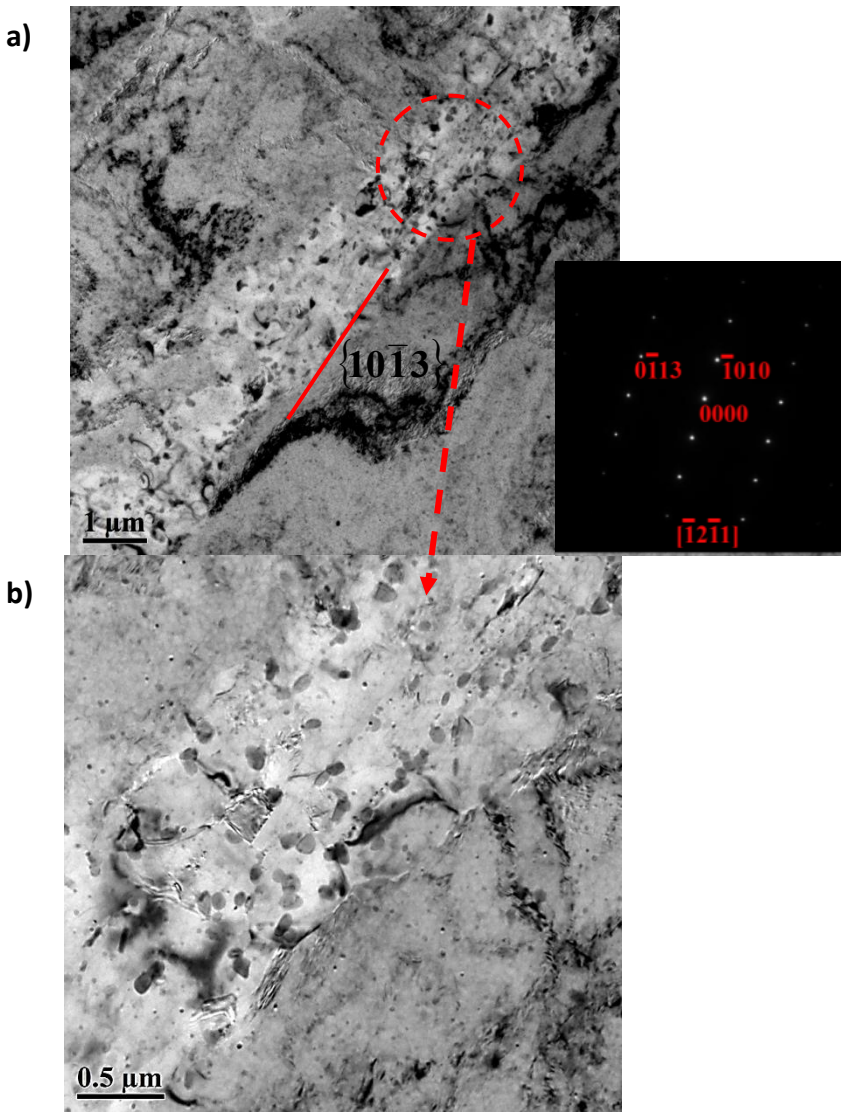

Figure 4.16 TEM bright field images of the Texture1 specimen after ECAP@150°C showing (a) $\{10\bar{1}3\}$ Compression twin and (b) recrystallized grains inside the twin.

Figure 4.16 displays the TEM images of the Texture1 specimen from a twinned area. The twinned region with recrystallized grains is identified as $\{10\bar{1}3\}$ compression twin (Fig.4.16a). It is evident from Fig. 4.16b that recrystallized grains are observed only

inside the $\{10\bar{1}3\}$ twin, however matrix is free of DRX grains. Fig.4.15 and Fig.4.16 clearly indicate that $\{10\bar{1}1\}$ and $\{10\bar{1}3\}$ compression twins are preferential site for DRX. Interestingly, small precipitates especially around grain boundaries of DRX grains inside the twin-DRX region are visible in Fig.4.14b with the size of ~40nm. The detailed analysis of those precipitates along with the scanning TEM results will be given in the following Chapter.

In the Texture1 specimen, compression twinning is activated roughly after 20% plastic strain, with a peak response at 45% strain (Fig. 4.10a). During compression twinning, rapid texture change is evident in Figs. 4.12d and e, where a new peak appears in the (0002) pole figure shown with an arrow. Upon further deformation, the peak intensity increases and rotates towards the B fiber (Figs. 4.12f and g). Basal slip activity inside the Reo-by-CTw grains was shown in Fig.4.14a. Figure 4.14b presents the final texture of these Reo-by-CTw grains that were further deformed through mostly basal slip and tensile twinning during the final stage of ECAP. As seen in Fig. 4.14b, it is different than the overall texture (Figs. 4.5c). The separate peak shown by the arrow in the overall predicted texture (Figs. 4.12e-g) appears to be correlated with Reo-by-CTw grains.

Figures 4.17a and b display the EBSD IPF maps of DRX grains having a grain size less than 3μm for the Texture1 and Texture2 specimens, respectively (which correspond to full maps in Fig.4.6a and Fig.4.7a, respectively). The (0002) pole figures of the DRX grains (<3μm) of Texture1 and Texture2 specimens are given in Figs. 4.17c and d, respectively. Interestingly, the orientation of DRX grains in the Texture1 specimen

shown in Fig. 4.17a is similar to the predicted orientation (Fig. 4.14b) associated with Reo-by-CTw grains that were further deformed through basal slip accompanied by tensile twinning. On the other hand, it is quite different than the texture of the complete specimen (large and small grains shown together in Figs. 4.6a).

The VPSC model does not consider the recrystallization process, thus alteration of the original deformed texture after the recrystallization process is not evaluated. However, it has been shown that at temperatures below 300°C the recrystallization process does not significantly alter the original deformation texture of Mg [38]. Therefore, it is believed here that the predicted texture that represents the deformed texture can be correlated to DRX texture by assuming that DRX itself does not considerably alter the texture at 150°C.

The relationship between deformation twinning and DRX in Mg alloys has been previously studied [28, 38, 94, 109]. Galiyev et al.[32] argued that <c+a> dislocations are activated after twinning at temperatures below 200°C and are required for DRX nuclei to form. On the other hand, Ion *et al*. [38] proposed DRX as the successive operation of twinning, basal slip, and lattice rotations at grain boundaries, forming new grains with high angle grain boundaries in the temperature range of 150 to 300°C. The main difference between these two arguments is the role of <c+a> dislocations on DRX when DRX and twinning appear in the same sample. Recently, Al-Samman *et. al* [109] reported recovery and recrystallization within the compression twins formed during plane strain compression of Mg single crystals at 200°C and 370°C, which was shown to be due to high basal slip activity inside compression twins.

During ECAP of the Texture1 specimen, almost no pyramidal <c+a> slip is predicted (Fig. 4.10a), although the CRSS is much smaller for pyramidal slip than for compression twinning (Table 4.2). This indicates that the Schmid factor for compression twinning should be much higher than for pyramidal<c+a> during ECAP. On the other hand, the VPSC model does not consider deformation near grain boundaries where the stress state is more complex than the majority of the grain. Therefore, pyramidal <c+a> slip may be activated near grain boundary regions also contributes to the DRX formation as discussed in Galiyev et al[32] but the model may not be able to capture it. Actually, the activity of pyramidal<c+a> (Fig.11a) is evident when twinning is suppressed in Texture1 case and the corresponding texture (Fig.11b) is similar to the texture of DRX grains (Figs.14a and c). However, two observations clearly indicate that the DRX mechanism is related to twinning; (1) the experimental overall final texture cannot be predicted without twinning activity and (2) the DRX is mostly localized inside the twins in Texture1 case. The observed DRX localization cannot be related to pyramidal<c+a> slip since it should promote uniform DRX and deformation as it does at 200°C and higher temperatures in [12, 14, 30].

Despite the shortcomings of the model that cannot predict deformation near grain boundaries, it is clear from the references [38, 109] and the current findings (including the following paragraph) that the formation of compression twins followed by tension twins (to form double twins) and very high basal slip activity promotes recrystallization and shear band formation.

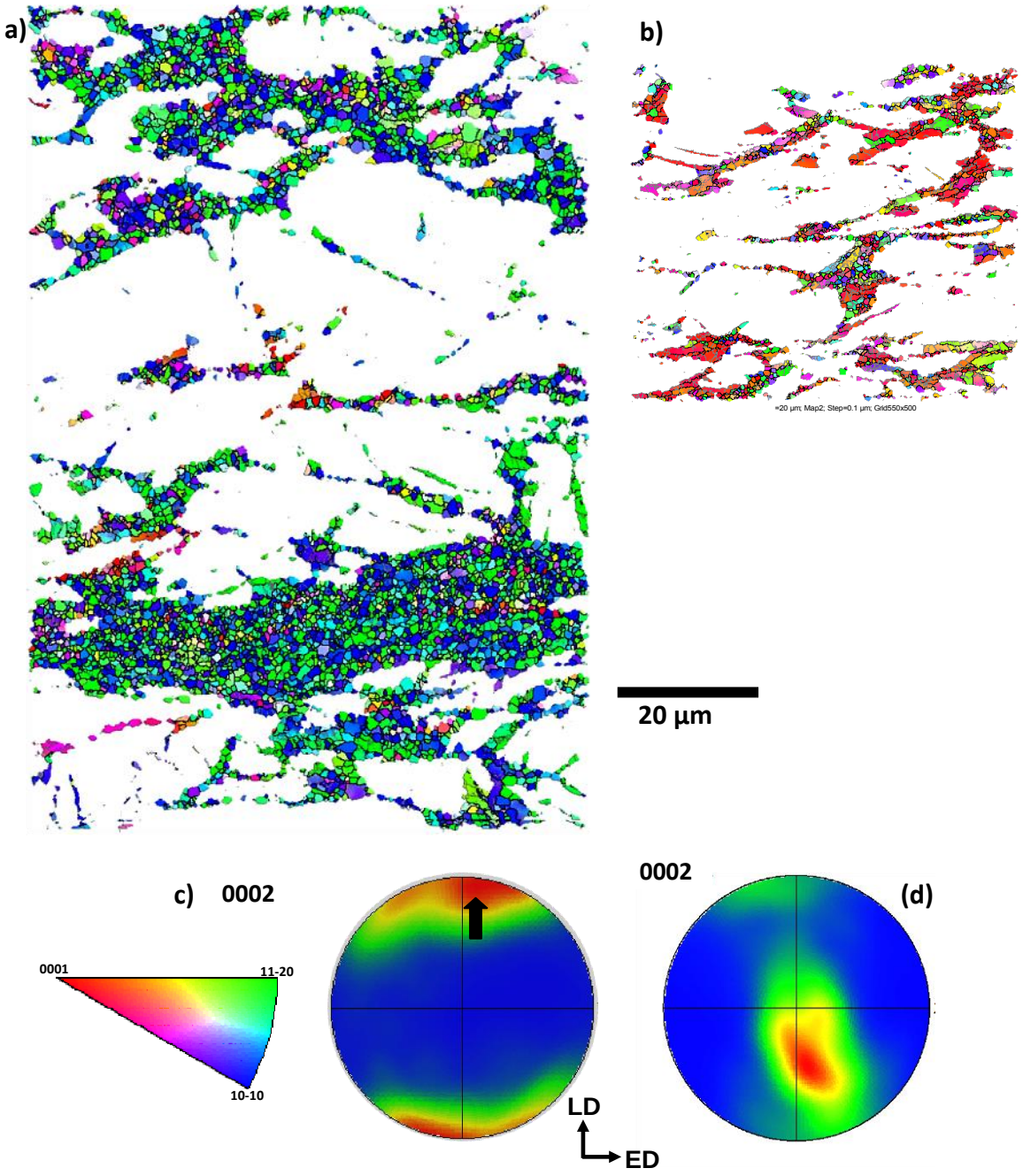

Figure 4.17 EBSD maps of the DRX grains having grain size less than 3µm (a) Texture1 (Fig. 4.6a) and (b) Texture2 (Fig. 4.7a) specimens. Corresponding (0002) pole figures of the DRX grains in (a) Texture1 and (b) Texture2 specimens.

Double twinning boundaries are also evident in the Texture1 specimen especially inside shear bands (Fig. 4.7a). It was reported [94] that secondary twinning form inside the primary twins and creates random high-angle boundaries upon further straining in pure Mg. These random boundaries have a high tendency for migration at low and intermediate temperatures [94]. Fig. 4.18b displays the misorientation profile along the red line given in Fig.4.18a. Here, it is obvious that the recrystallized grains are created by the activity of double twinning. These newly formed DRX grains have random high angle boundaries (Fig.4.18b), indicating they have a high ability of migration [94].

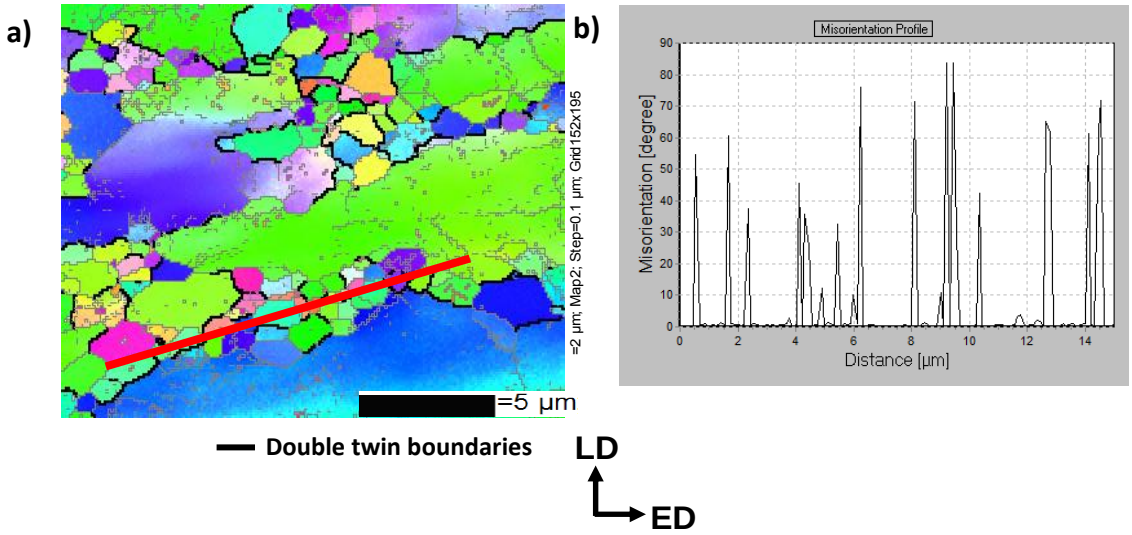

Figure 4.18 (a) EBSD map of the Texture1 specimen after ECAP at 150°C showing formation of random high angle boundaries due to double twinning. (b) misorientation profile along the red line shown in (a).

4.7 Shear Band Formation and Cracking during ECAP

The deformation localization, DRX inside compression twins and random high angle random boundary formation due to double twins were presented in the previous section. However, it is still not clear how exactly the shear bands formed with the Texture1 specimen and caused failure. Mobility of DRX grains that formed inside twins is expected to be high due to their random high angle boundaries (Fig. 4.18). Therefore, local accumulation of soft DRX grains and mobile boundaries can provide easy shear paths as described by Ion et al. [38] In addition, the deformation is mainly concentrated in those regions due to localized high basal slip activity. This leads to repetitive DRX and micro-shear bands, as illustrated in the schematic in Fig. 4.19a and exemplified by the micrographs in Figs. 4.19b and c.

These bands broaden with further straining, and finally cracks initiate within the bands (Fig. 4.4c). Fig. 4.19 illustrates the proposed mechanism for shear band formation and deformation localization in the Texture1 specimen. Figs. 4.4a and 4.6a show large and lightly deformed grains located between the shear bands; these grains have a similar size with the initial grains. They support the presented argument since it is unlikely to have such a large undistorted grains remaining after about 1 strain during one pass of ECAP the latter indicates that those large and mostly tensile twinned grains (the green and blue grains in Fig.4.6a) were not significantly deformed further after twinning, and deformation, instead, was accommodated throughout the shear bands. Macroscopic cracks shown in Fig. 4.1c initiate from these shear bands (Figs. 4.4c and 4.19c), since

void formation is likely to happen in those regions at low temperatures due to high strain and stress concentrations.

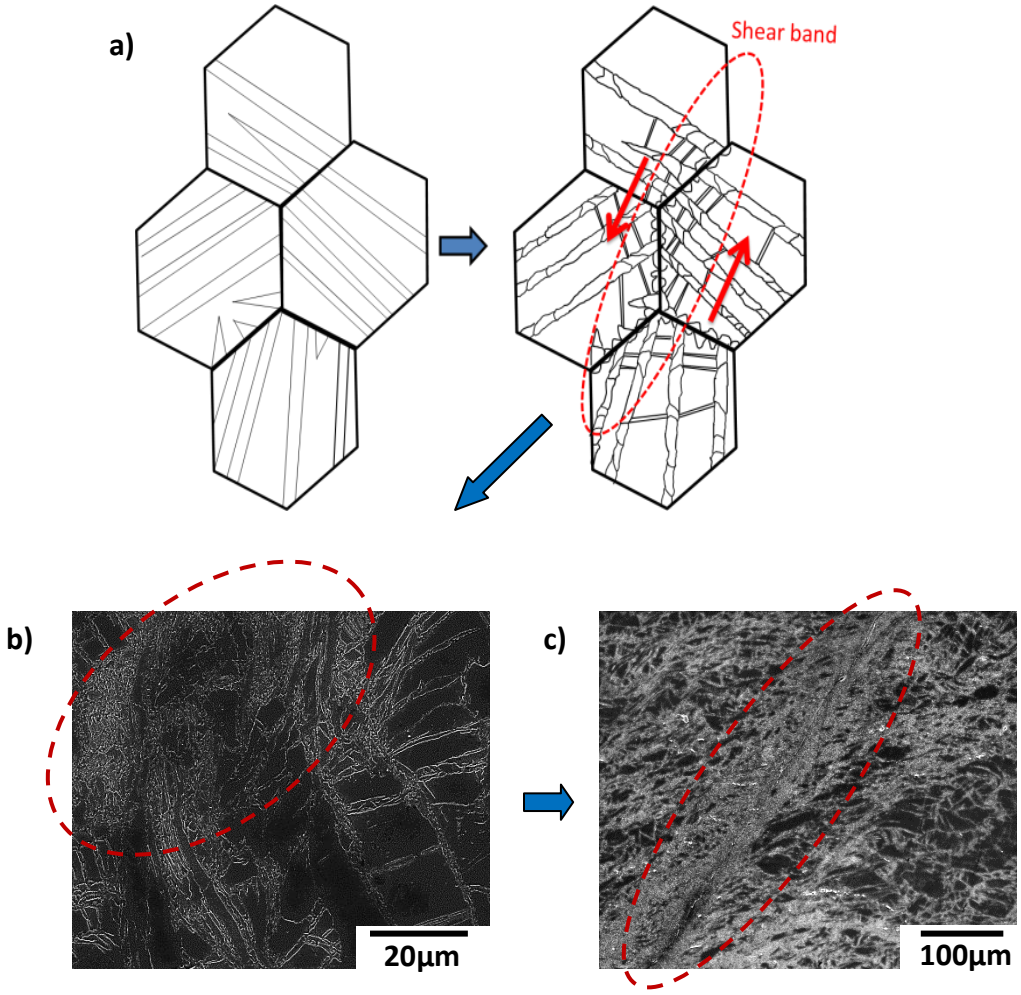

Figure 4.19 (a) Schematic for the proposed mechanism for the formation shear bands during ECAP due to twin related DRX. (b) Local accumulation of these DRX grains providing easy shear path and (c) shear band formation with repetitive DRX.

This difference in the deformation behaviors and the simulation results on the active deformation modes confirm that compression and double twinning, followed by

DRX and shear band formation, are the main factors causing failure during various processing routes. Knowledge of compression and double twinning activity, therefore, can help predict which starting texture would suppress these twinning modes during ECAP at 150°C, or other processing techniques, and therefore avoid cracking and failure.

4.8 DRX Mechanisms

Smaller amounts of DRX grains with the "necklace" structure are apparent in the Texture2 case; a consequence of the active deformation modes. Fig.4. 15d displays the (0002) pole figure from the DRX grains of the Texture2 specimen, previously presented in Fig.6. The texture of DRX grains (<3μm) is similar to the initial texture, indicating that prismatic slip rather than twinning was involved during DRX of the Texture2 sample. In addition, the size of the DRX grains in the Texture2 specimen is smaller than that of the Texture1 specimen and only observed around grain boundaries, which indicates that nucleation and growth mechanisms are limited. The stacking fault energy (SFE) for the non-basal slip systems in Mg alloys is much higher than for the basal slip [106], suggesting that in the Texture2 case, the volume fraction of DRX grains should be less due to high SFE of the active prismatic slip. Clearly, prismatic slip retards DRX as also shown in [14, 32].

Three main DRX mechanisms were observed in Mg alloys [93]. Continuous DRX (CDRX), Discontinuous DRX (DDRX) and Twinning DRX (TDRX). TDRX mechanism can occur through (1) mutual intersection of primary twins, (2) secondary

twinning within the primary twin lamella and (3) deformation induced low angle boundaries inside the twin lamellas that transforms to high angle boundaries upon further straining[93]. In Texture1 case, TDRX is abundant. Evidences of DDRX (bulging of grain boundaries with a low angle grain boundary that subdivided the bulged area from a parent grain) are also present in both Texture1 and Texture2 specimens (Figs. 4.6a and 4.7a). CDRX requires non-basal slip activity in Mg alloys[93]. Since prismatic slip is readily active in Texture2 case, it is believed that CDRX can contribute to the development of DRX in this case. There are some evidence of CDRX in Texture 2 case such as sub-grain structure that extended further toward the grain interior [29] especially in red grains(not twinned) as seen in Fig.4.6a.

At lower temperatures, there are still large differences in the CRSSes of basal and non-basal slip systems; therefore, suppression of DRX seems to improve formability since it causes local softening and deformation localization when DRX happens. Interestingly, rare earth Mg alloys show better formability at low temperatures. Since these alloys store more energy, DRX is retarded compared to non-rare earth alloys [110-111]. In the same manner, the activation of prismatic slip during ECAP of the Texture2 specimen initiates more energy storage in the grains, in turn limiting DRX and promoting a more uniform deformation.

Since extensive activation of prismatic slip during ECAP of the Texture2 sample provided more uniform and crack-free deformation, the obvious question then is whether it is possible to process AZ31 Mg alloy in the same manner at even lower temperatures, ideally even at room temperature. With this in mind, the ECAP of another Texture2

sample at 100°C was attempted, but the sample failed as seen in Fig.4.1e. The failure resulted from the high twinning activity, which was obvious from the final microstructure given in Fig. 4.20. Excessive twin lamellas especially near the fractured edge are predominant features of the Texture2@100°C specimen as seen in Figs. 4.20a and b. Fine DRX grains form only inside the twins as shown by the dashed circle in Fig. 4.20f. Interestingly, DRX grains are not present along grain boundaries (indicated by the arrow in Fig. 4.20a), unlike other specimens processed at 150°C. At 100°C, both the activation of different slip systems and the DRX are expected to be limited in comparison to 150°C. Thus, DRX grains are only found within the twin bands as indicated in the Fig.4.20b. The SEM images from the middle of a discrete segment in Fig. 4.1e are given in Figs. 4.20c and d. These regions have less twin fraction and seem to experience less deformation. The twins in these regions have smaller width and have no DRX grain inside (Fig. 4.20d). In addition, DRX is not observed around grain boundaries as well.

The EBSD IPF and EBSD-Kikuchi band contrast maps of the Texture2 specimen after ECAP at 100°C are given in Fig. 4.21a and b, respectively. The twin boundaries in Fig. 4.21b are higlighted in different colors. Tensile twinning appeared to be highly active from the highlihted red boundaries showing different wide twin lamellas (Fig.4.21b). The red colored grains have initial orientation and some grains completely tensile twinned from red color to blue or green in Fig.4.21a. Very few compression and double twin boundaries are present. Unfortunately, there are no twins bands conists of DRX grains similar to shown in Fig. 4.20b. However, forming of different variants

inside the compression and double twins is obvius in Fig. 4.21b. It is evident that ther eis no DRX or detwinning inside tensile twin lamellas.

With temperature reduction, more basal slip and twinning occur at the expense of thermally activated prismatic slip [27]. Thus, a careful selection of the strain path can favor prismatic slip for better formability, but deformation temperature could still limit its activation. For example, Kang et al. [50] aimed to activate preferentially prismatic slip in AZ31 at room temperature using a special deformation apparatus. However, a considerable amount of basal slip and tensile twinning still appeared. Although it is not clear if tensile twinning is the main cause of the failure or if other mechanisms, such as compression twinning, played a role in failure, still, alternative methods for activating prismatic slip and suppressing deformation twinning should be explored to successfully process AZ31 at temperatures below 150°C.

4.9 Role of Extrusion Speed and Back Pressure on Formability

Extrusion speed should also have a notable influence on formability since it is possible to reduce twinning activity under low strain rates. In this study, a moderate extrusion speed of 4.57mm/min ($\dot{\varepsilon} \cong 0.012s^{-1}$ that was calculated using the equation given in [72]) was kept constant for all ECAP cases and this rate is the same as the one used in the work that reported ECAP failure in Texture3 samples [20] with a similar initial grain size. It is worth mentioning that the Texture3 samples were once ECAP successfully at 150°C with a two orders of magnitude slower strain rate, higher back pressure, and a slightly smaller initial grain size [112]. The predicted twinning activity

for the Texture3 specimen is almost half that of the Texture1 specimen, and it appears that suppression of twinning and thus successful ECAP of AZ31 could be achieved at 150°C in Texture3 using an extremely slow strain rate and a high back pressure. Please note, the Texture2 bulk sample was successfully ECAP in this study with or without applying any back-pressure.

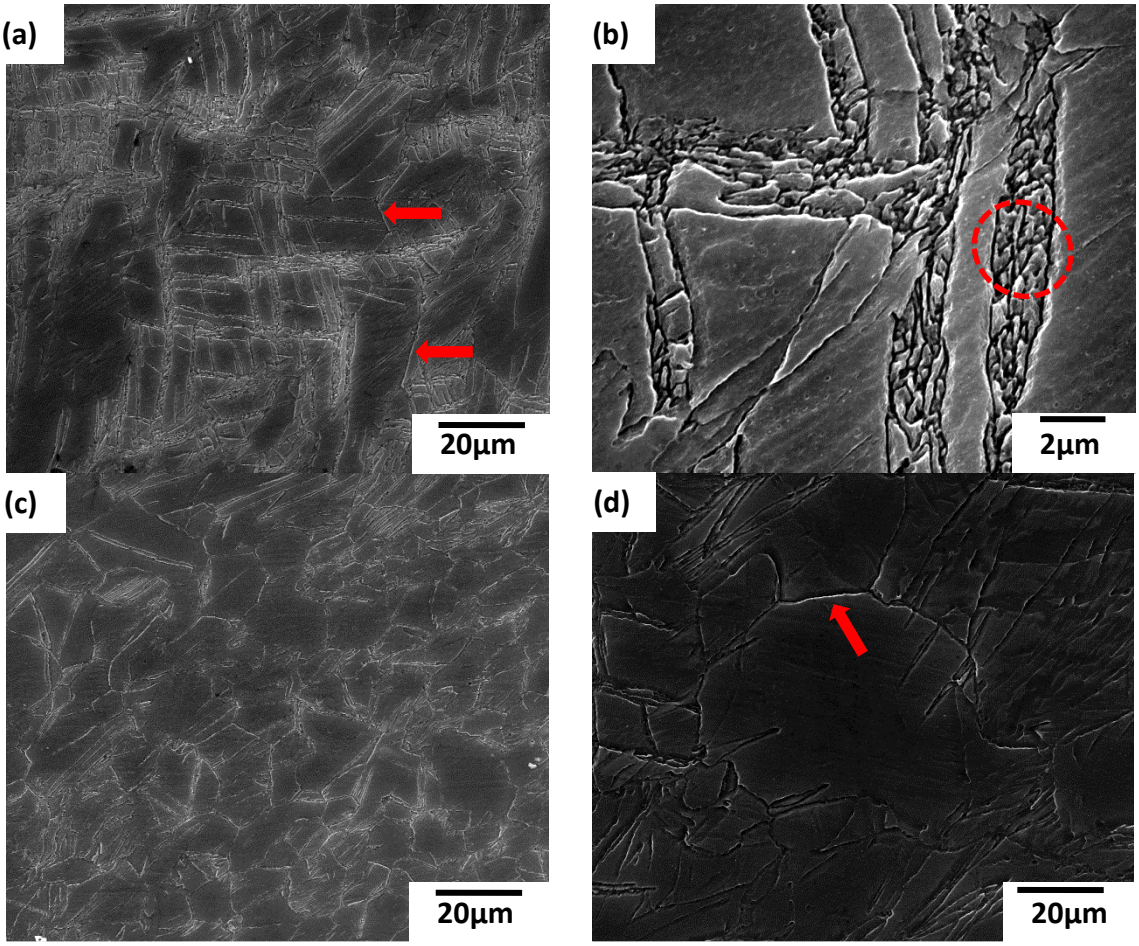

Figure 4.20 SEM images of Texture2 specimen after ECAP at 100°C. (a-b) near the fractured region and (c-d) away from fractured region. Arrows are showing grain boundaries without DRX grains.

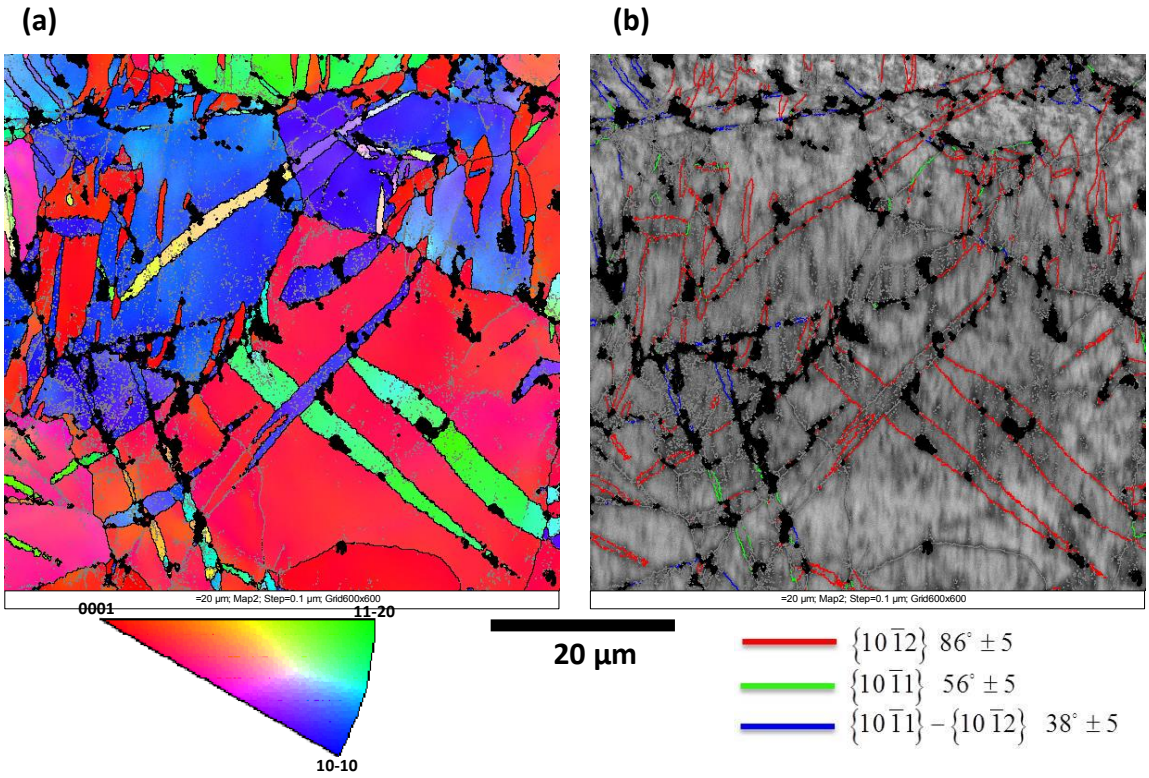

Figure 4.21 (a) EBSD inverse pole figure map of Texture2 specimen after ECAP at 100°C. (b) EBSD-Kikuchi band contrast map showing different twin modes.

4.10 Summary and Conclusion

Low temperature shear formability of wrought AZ31 alloy samples with different starting textures (Texture 1 through 3) has been investigated at 150°C through equal channel angular processing experiments and simulations. Main findings and conclusions can be summarized as follows:

1. The common temperature limit for the formability of AZ31 alloy has been reduced from 200°C to 150°C by promoting prismatic slip and suppressing

compression and double twinning activity. This was achieved by careful selection of the starting texture.

2. The VPSC simulation results accurately predicted deformation texture and captured the active deformation modes during ECAP at 150°C, providing insight into the relationship between the deformation modes, DRX characteristics, final microstructure including shear localization, and formability of Mg alloys.
3. Detailed EBSD analysis successfully identified the active deformation twin modes after ECAP of different specimens with detailed orientation maps of deformed and DRX grains.
4. Readily activation of compression/double twinning promoted non-uniform deformation and DRX within the twins. This caused deformation localization, repetitive DRX and finally macro shear band formation during ECAP at 150°C. The soft DRX regions along the shear bands caused crack initiation and the failure of the Texture1 specimen.
5. On the other hand, Texture2 specimen was successfully ECAP at 150°C with identical processing conditions. Readily activation of prismatic slip promoted a more uniform deformation with necklace type limited DRX regions where relatively small DRX grains accumulated around grain boundaries.

CHAPTER V

PRECIPITATION AND FAILURE AT DYNAMIC RECRYSTALLIZATION FORMED REGIONS IN MG-3AL-1ZN ALLOY

In Chapter IV, the roles of deformation modes and starting textures on both shear formability and shear band formation were investigated at 150°C and lower temperatures. After ECAP of different starting textures (i.e. oriented differently with respect to the ECAP die) at 150°C, dissimilar DRX mechanisms and secondary particle formation, especially in twin-DRX regions, were observed (Figs. 4.4 and 4.14). In this chapter, detailed TEM and Scanning TEM (STEM) analyses of the starting material and the ECAP specimens will be reported. It may be a unique observation that secondary particle formation in the DRX region and also solute segregation were observed after ECAP at 150°C.

Cracks/voids are formed always in DRX regions when samples are uniaxially tensile tested (Chapter III) or processed via ECAP (Chapter IV) at 150°C and higher temperatures. A detailed analysis of precipitation in twin and DRX regions together with nanoindentation tests will enlighten the possible reasons for failure along these regions.

5.1 TEM and STEM Investigations of Starting Material

Figures 5.1a-c show TEM and STEM images of a hot-rolled and annealed AZ31 specimen, and the corresponding microstructure is the condition of all specimens before

uniaxial tests (Chapter III) and ECAP (Chapters IV and VI). Very few rod-like precipitates and homogeneously distributed spherically shaped particles are evident in Figure 5.1. Rod-like precipitates are indicated with arrows in Figs.5.1. The composition of rod-like precipitates was measured as slightly Zn-enriched and Al-lean compared to the matrix via point EDS analysis. Similar precipitates forming into rods were reported in MgZn alloys [83, 113-114]. The metastable $MgZn_2$ phases (β_1' and β_2') form coherent or semi-coherent interfaces with the matrix perpendicular to $[0001]_{matrix}$ direction and form relatively long rods [115]. Here, the indicated Zn-enriched precipitates in Figs. 5.1a-c aligned in the $[0\bar{1}10]_{matrix}$ direction.

Densely and homogeneously distributed secondary spherical particles are evident in the STEM image given in Fig.5.2a. An EDS mapping of a small area (indicated by a red square in Fig.5.2a) is given in Fig.5.2b, which contains a few of these particles in different sizes. It is obvious that these precipitates are enriched in Mn and Al. Similar spherical Al-Mn precipitates were reported in the AZ31 Mg alloy [92], which were formed during solution heat treatment at 400°C for 4hrs and remained mostly unchanged throughout the subsequent thermo-mechanical processing steps. In this study, the hot-rolled material was annealed at 350°C for 12hrs to have a fully recrystallized and twin free initial microstructure. As shown in Fig.3.3, Al_8Mn_5 secondary particles in different sizes(1-30μm) are present and mostly align themselves along the rolling direction. These large Al-Mn precipitates were present before annealing. However, these very small (10-50nm) Al-Mn particles were formed during annealing.

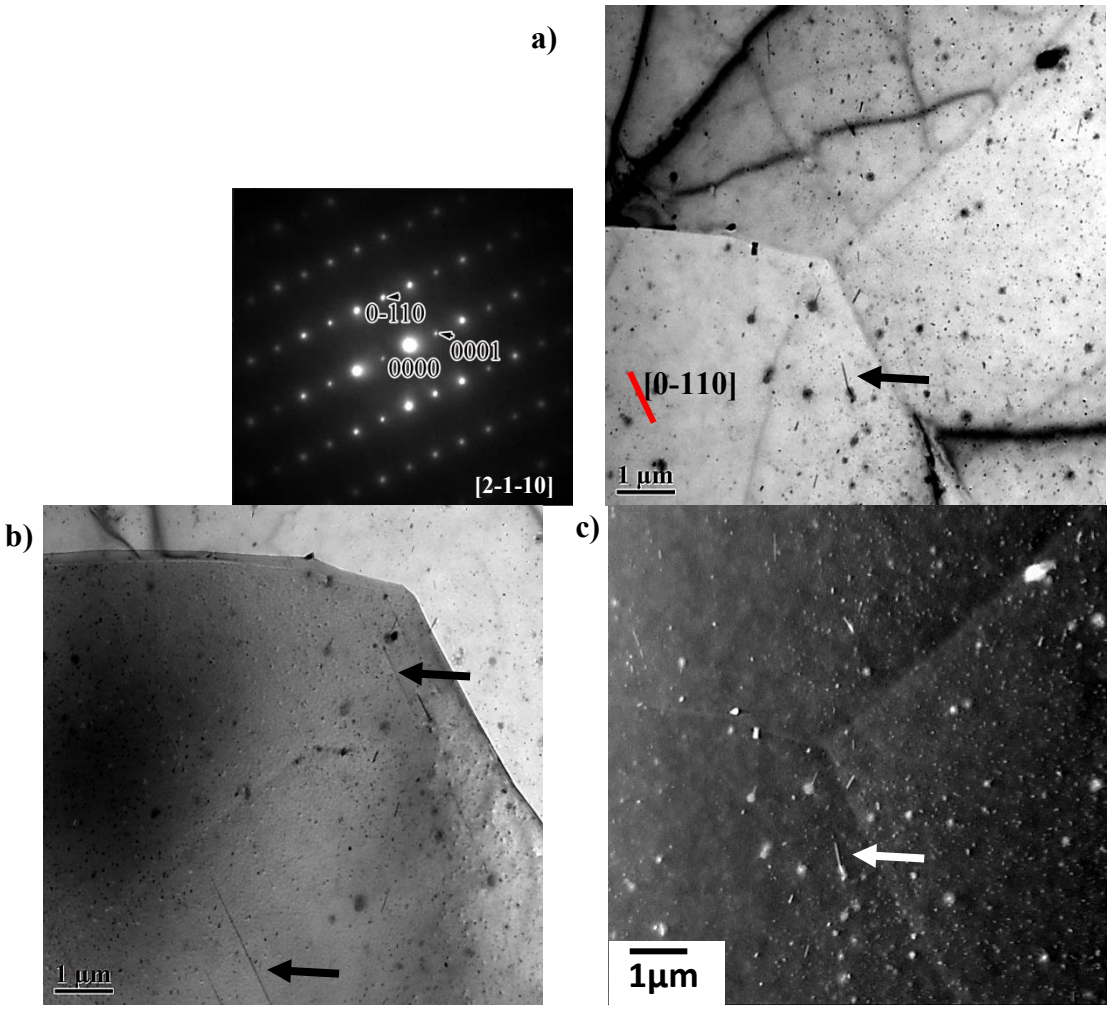

Figure 5.1 (a) and (b) TEM and (c) STEM images of AZ31 Mg alloy before ECAP. RD is right.

5.2 TEM and STEM Investigations of the Texture1 Specimen after ECAP at 150°C

A detailed investigation of twinning activity and shear band formation during ECAP of the Texture1 specimen at 150°C (Texture1@150°C) is given in the previous chapter. As seen in Figure 5.3a, DRX grains formed both at grain boundaries and inside the twins. Figure 5.4a, the TEM image of the Texture1@150°C specimen, shows a junction of twins with the grain boundary consisting of DRX grains. Similar junctions

are indicated with arrow in Fig. 5.3a. The twin on the left was identified as a $\{10\bar{1}3\}$ compression type twin. However, the twin-like band on the right was not identified since it does not have a well-defined boundary (Fig.5.4a). Figure 5.4b displays the peculiar secondary particle formation only inside the twin bands and at grain boundaries that consist of DRX grains. Towards the junction, the DRX region broadens (Fig.5.4b). It is evident that the matrix is free of these particles, which are around 80-120nm. These particles are observed in all DRX regions (twin-DRX and grain boundaries) of the TEM specimen; thus, this peculiar precipitation is a common feature of the Texture1@150°C specimen.

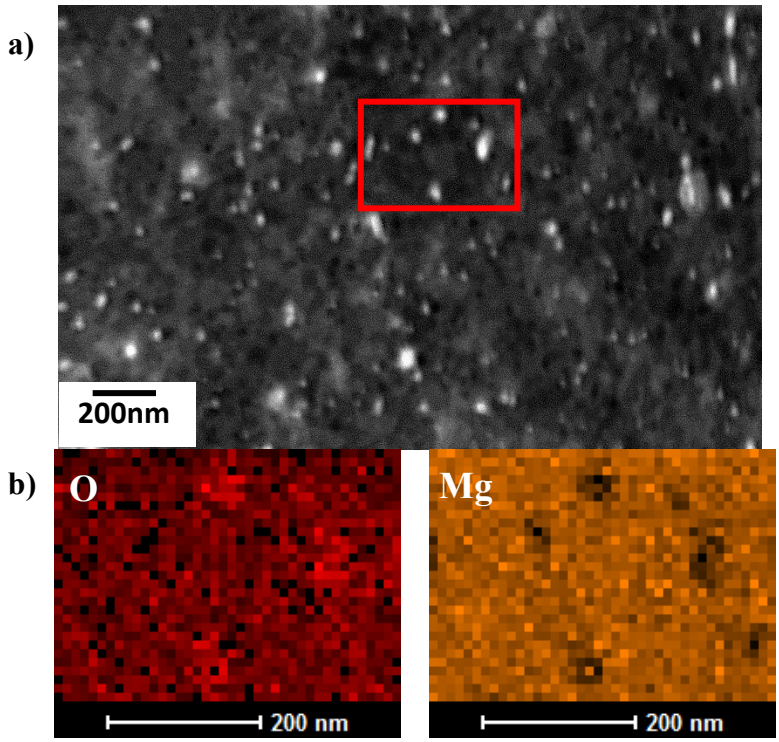

Figure 5.2 (a) STEM image of AZ31 Mg alloy. (b) EDS mapping of selected area in (a).

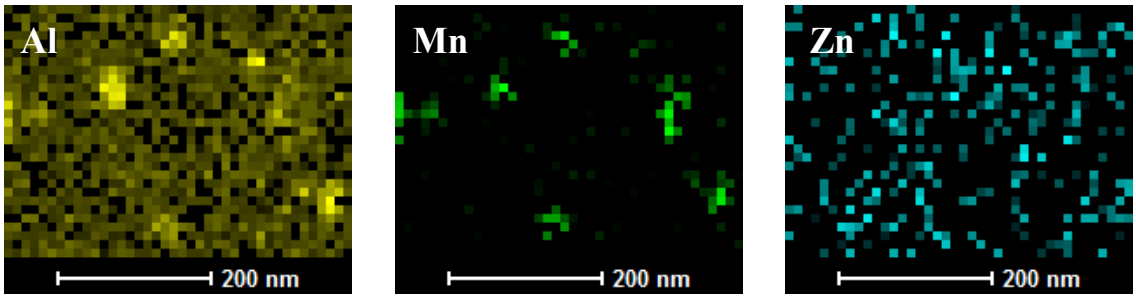

Figure 5.2 Continued

Figure 5.5a shows a magnified STEM image of the $\{10\bar{1}3\}$ compression twin on the left, which was previously shown in Fig.5.4. Two distinct areas (Area1 and 2) are selected from Fig.5.5a for further EDS mapping. Area1 includes the twin boundary with secondary particles inside the twin and an area from the matrix. Figure 5.5b presents the EDS mapping of Area1. The particles inside the twin DRX region were identified as Zn and Al enriched particles. Several point EDS analyses of different particles are given in Fig.5.6. Although composition of these particles varies, it appears that the composition is around $Mg_{\sim 75}(AlZn)_{\sim 25}$ wt%. These particles are called ϕ' particles in the text.

As seen in the TEM images given in the previous chapter, these particles usually form around DRX grain boundaries. Recently, Nie *et al*. [116] reported the segregation of Zn and Gd in twin boundaries of Mg–Zn binary and Mg–Gd–Zn ternary alloys, respectively. Although it requires a much more detailed compositional mapping, the Zn segregation in the $\{10\bar{1}3\}$ compression twin boundary can be seen, as indicated by an arrow in the Zn map in Fig.5.5b.

a)

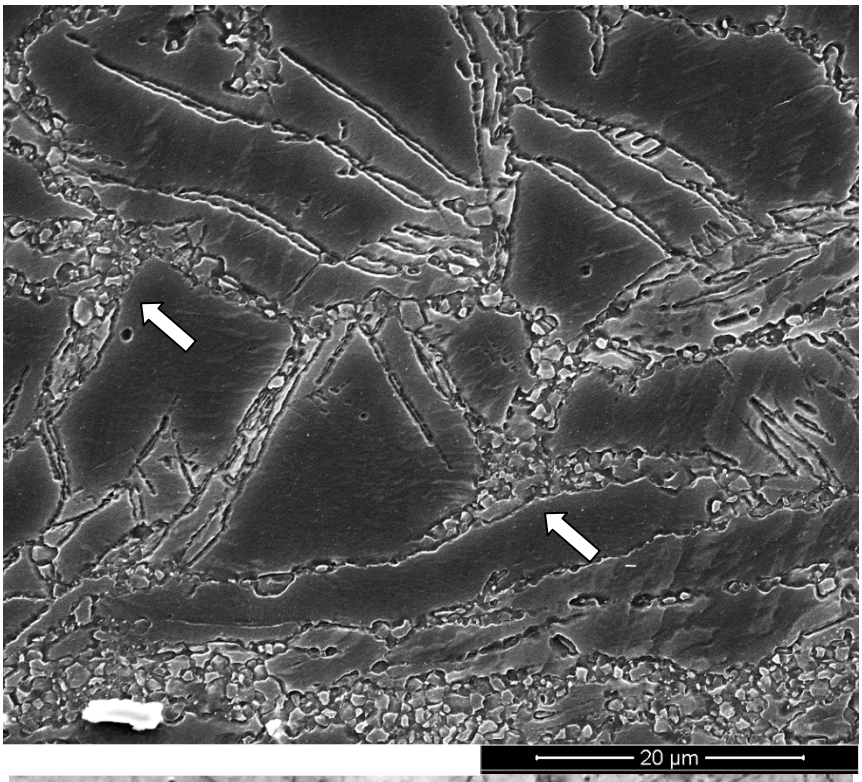

b)

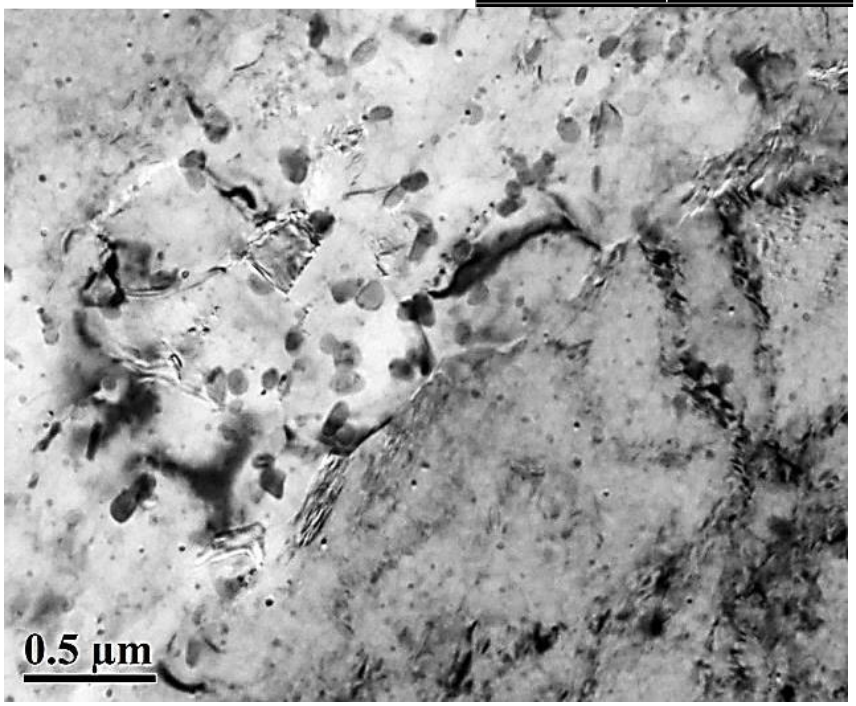

Figure 5.3 (a) SEM and (b) TEM images of Texture 1 specimen after ECAP at 150°C.

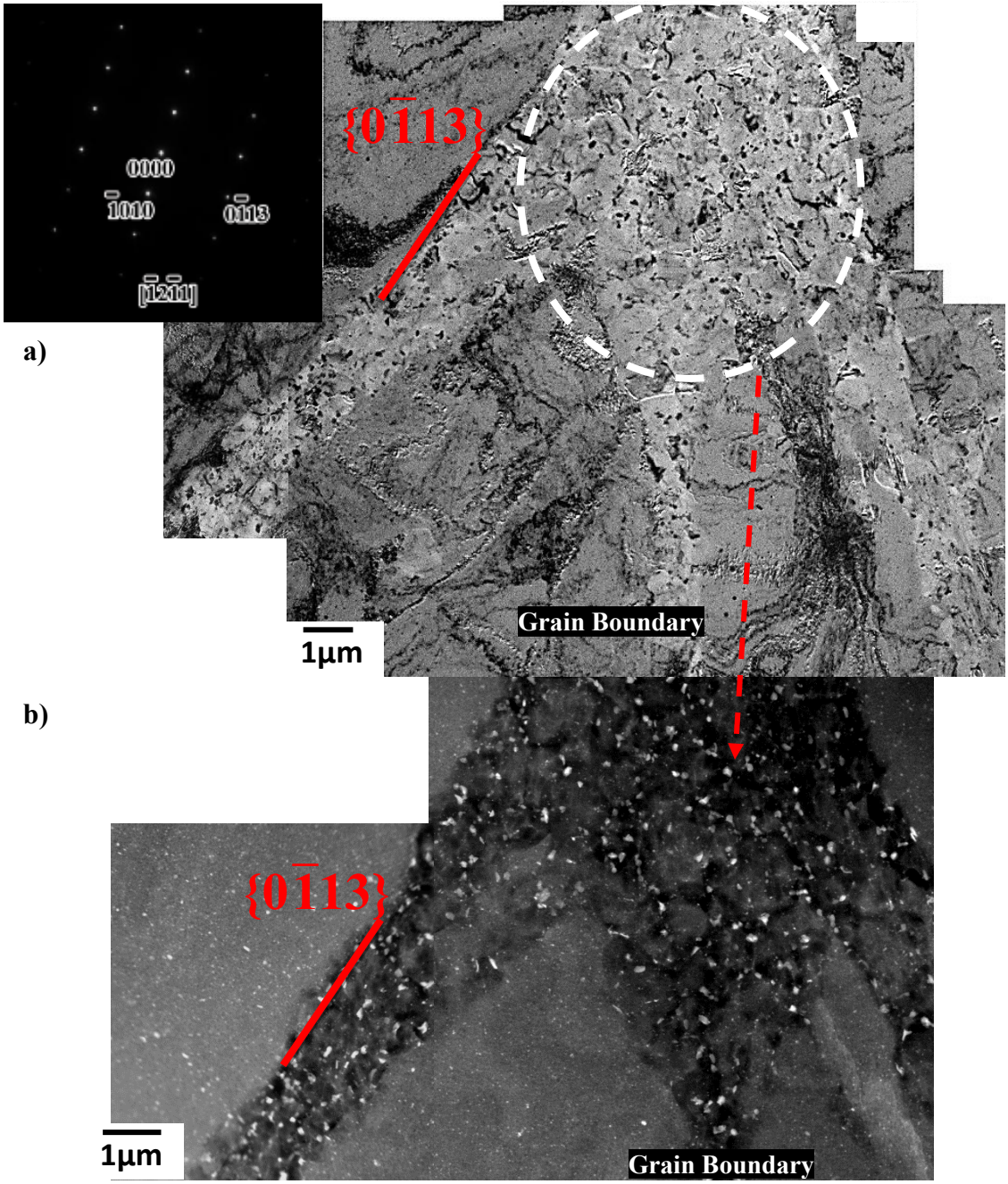

Figure 5.4 (a) TEM and (b) STEM images of Texture 1 specimen after ECAP at 150°C showing a junction of twin and the grain boundary consists of DRX grains and precipitates. ED is vertical.

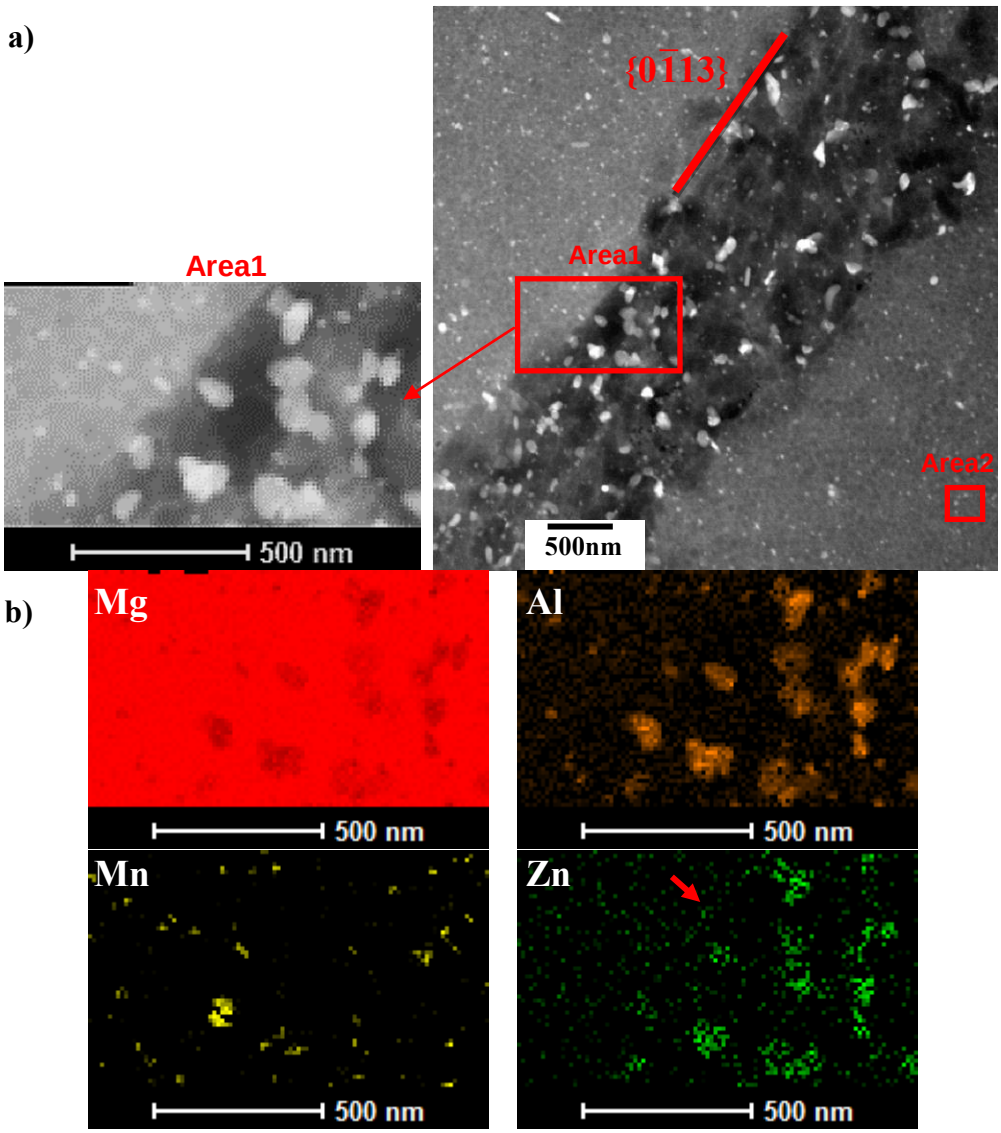

Figure 5.5 (a) STEM image from the Texture1 specimen after ECAP at 150°C, showing the $\{0\bar{1}13\}$ twin band that includes DRX grains and Al-Zn rich precipitates. EDS mapping of selected area (Area1). ED is vertical.

Very fine Al-Mn enriched particles are also obvious both inside and outside the twin band, as seen in the Al and Mn EDS maps in Fig. 5.5b. Please note that these particles were present before ECAP (Fig.5.2). However, it appears that the number density of fine Al-Mn enriched particles seems increase with the average size decreasing

slightly after ECAP, as shown in detail in Fig. 5.7a. Figure 5.7b presents the EDS mapping of the selected area (Area2) of Fig. 5.7a, also indicated in the bottom right of Fig.5.5a. It clearly shows that these particles are the same Al-Mn particles present before ECAP (Fig.5.2). Interestingly, homogeneously distributed white networks are also visible in Fig.5.7a. The local EDS point analysis of these dark regions inside the white networks indicates that these white regions are slightly rich in Zn content. It is also evident in Zn EDS mapping of Area2 (Fig. 5.7b) that areas within the networks are Zn lean (one example is indicated via an arrow in Zn EDS map).

Figure 5.8 presents the detailed crystal structure investigation of ϕ' particles from the Texture1 specimen. Fig. 5.8a displays a STEM image from a DRX region having ϕ' particles. The selected area electron diffraction pattern indicates many extra spots from precipitates, as seen in Fig.5.8a. The TEM image of a selected area from Fig. 5.8a is given in Fig.5.8b with the corresponding electron nanodiffraction pattern (NDP) of particles. Two particles are named P1 and P2, as seen in Fig.5.8b. The shape of P1 is the common irregular shape of ϕ' particles in Fig. 5.6. The P2 has a rod-like shape that is also present in DRX regions, although much less common proportionally than the shape of P1. The high resolution TEM (HRTEM) images of P1 and P2 particles are given in Fig.5.8c and d, respectively. The boundaries of P1 and P2 are mostly circular and have no steps, which indicate a high coherency in this plane (Figs. 5.8 c and d). As indicated in Figs. 5.8c and d, there are very fine small precipitates near the boundaries of P1 and P2 particles as evident in HRTEM images. Figs. 5.8e and f display the HRTEM images

of P1 and P2 particles with the corresponding fast Fourier transformation (FFT) patterns of selected areas, respectively.

a)

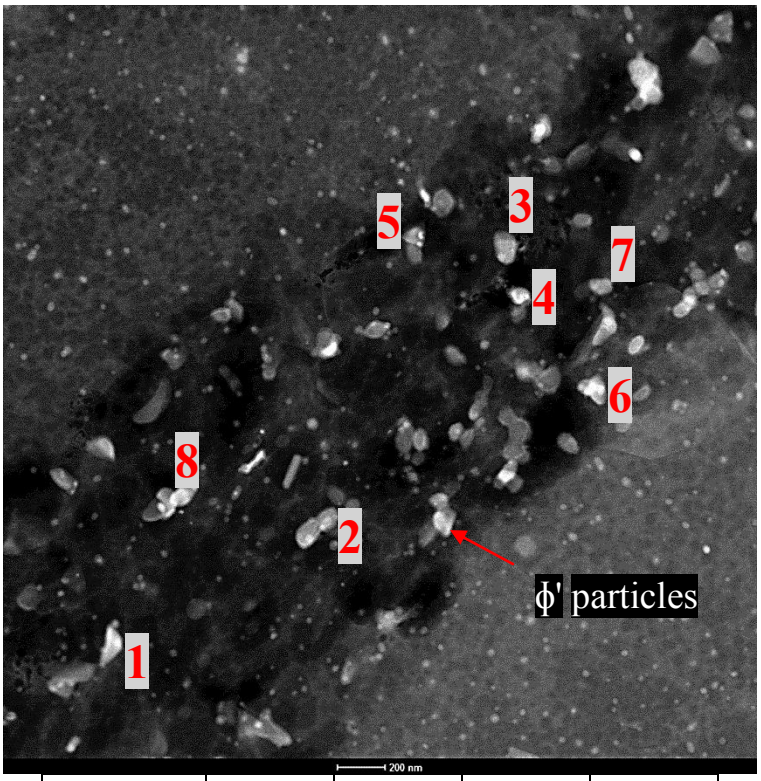

Particle#	Mg (wt%)	Al (wt%)	Zn (wt%)	Mn (wt%)
1	68.567	19.33	9.444	2.657
2	77.877	11.383	9.581	1.158
3	74.474	17.833	7.686	0.005
4	55.971	24.327	13.176	6.524
5	46.464	15.283	38.197	0.054
6	77.867	13.956	7.269	0.903
7	78.81	10.443	10.746	0
8	71.571	18.344	10.084	0

Figure 5.6 STEM image of the Texture1 specimen showing a $\{0\bar{1}13\}$ twin band consisting of DRX grains and Al-Zn rich particles with measured compositions. ED is vertical.

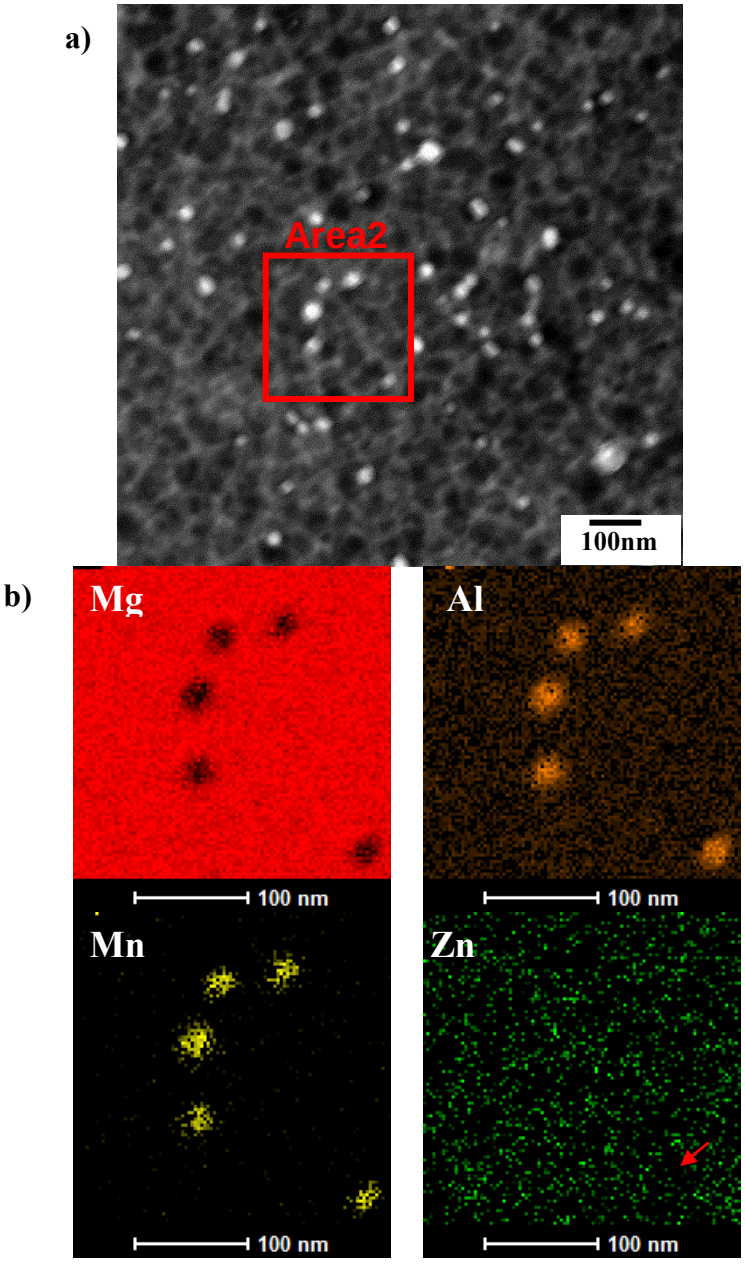

Figure 5.7 (a) STEM image from the matrix of the Texture1 specimen after ECAP at 150°C (b) EDS mapping of the corresponding selected area (Area2 in Figure 5.4)

It is evident that the crystal structure of both particles (P1 and P2) is hcp, having lattice parameters similar to the matrix grain. The FFT patterns showed some super-lattice formation both inside P1 and P2 in Figs. 5e and f, respectively. There are three

spots between the transparent and the nearest diffraction spots (Fig.5.8e) for P1 particle. This indicates that the superlattice formed in a certain region of the P1 has a four-layered structure. However, the P2 particle has one extra spot between the transparent and the nearest spots, as seen in Fig. 5.8f, which indicates that it has a two-layered superlattice. The composition variation is obvious inside ϕ' particles from the STEM image given in Fig.5.6. It is believed that certain parts of these particles transformed to ordered structures, forming superlattices. Thus, there are composition variations between the superlattice formed region and the surroundings inside the particles.

As discussed in section 1.3.3, two main ternary phases, τ and ϕ, were reported in Mg-Al-Zn alloys systems [83]. The τ phase has been identified as $Mg_{31}(Al,Zn)_{49}$ at% with a body-centered cubic structure [84]. The crystal structure of the ϕ phase is still not well understood, but it was shown to be a primitive orthorhombic crystal structure with a composition of $Mg_{21}(Al,Zn)_{17}$ at% [83, 89]. The composition and the crystal structure of ϕ' particles observed here appears different than the reported ternary phases. However, more detailed analysis to identify these particles and the layered structures is required to verify this conclusion.

Figure 5.9a shows the deformation bands with a low angle boundary (12.4°) in a grain interior of the Texture1 specimen. The misorientation angle with respect to the parent grain does not match any specific twinning boundary, indicating that these bands can be kink bands [37]. Fig. 5.9b shows very fine DRX grains which formed inside the parent grain and are smaller than the DRX grains in twins and grain boundaries (Fig.4.6). Similarly, very fine DRX grains away from the grain boundaries and the twins

are also visible in Fig.4.6. The three successive DRX grains lined up in Fig.5.9b seems to originate from a twin band; however, it appears that it formed in such a way that the long side of the grain is parallel to (0002) basal plane. At the bottom left of the figure, dislocations parallel to the (0002) plane are also evident. There is no secondary particle formation inside/boundary of both deformation bands and the very fine DRX grains, which were both, observed inside the large parent grains. Please note that the amount of the very fine DRX grains in regions away from the twin bands and grain boundaries was very low in the TEM sample.

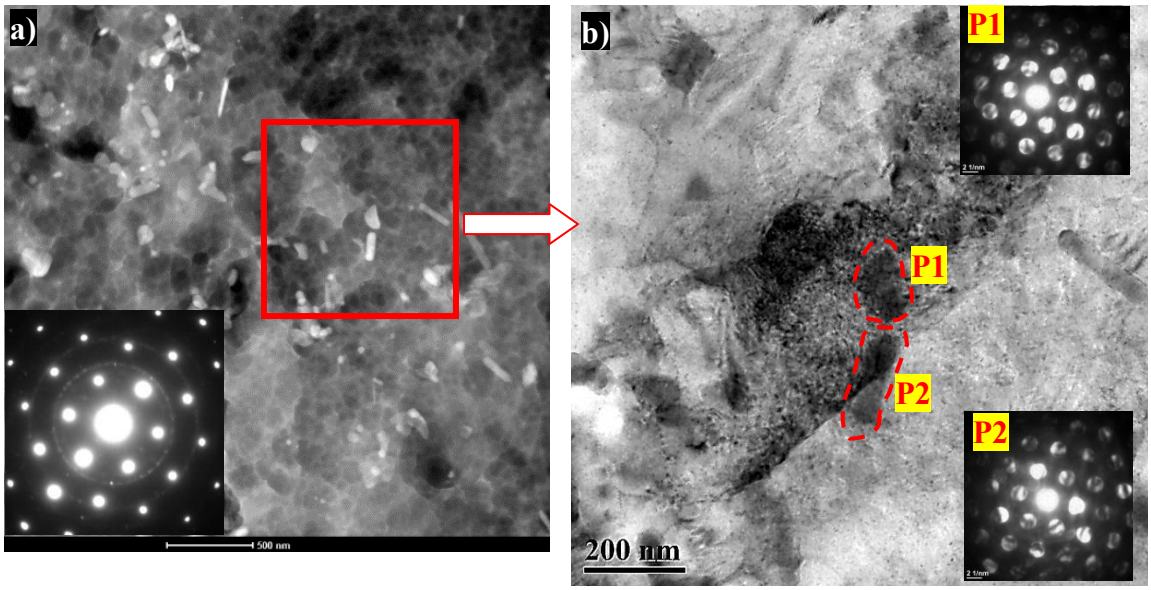

Figure 5.8 (a) STEM image of the Texture1 specimen from the DRX region consists of secondary particles (b) TEM image of selected area in (a) and corresponding electron nanodiffraction patterns of particle 1(P1) and particle 2 (P2). HRTEM images of (c and e) P1 and (d and f) P2 and their corresponding fast Fourier transformation (FFT) patterns.

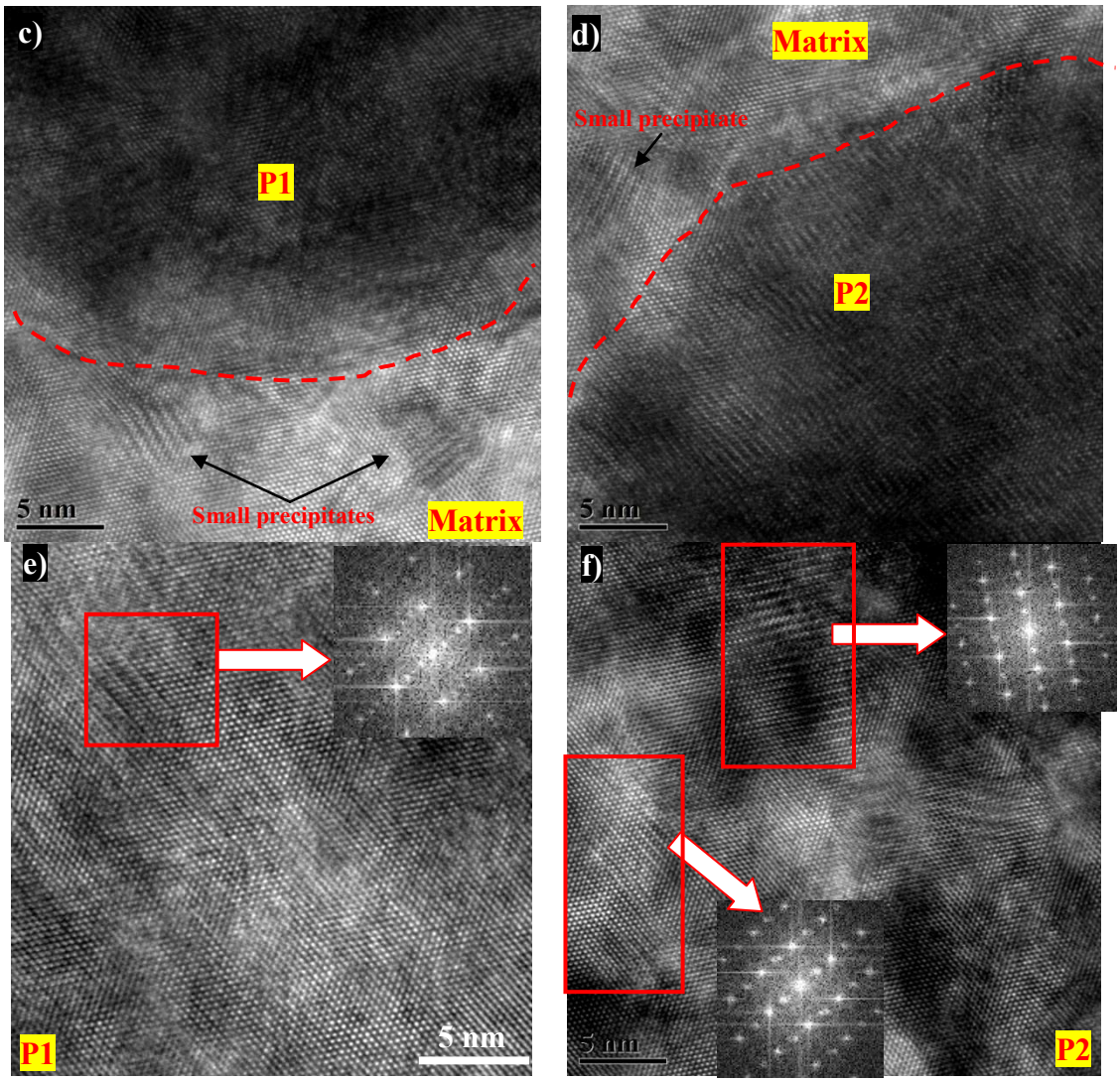

Figure 5.8 Continued.

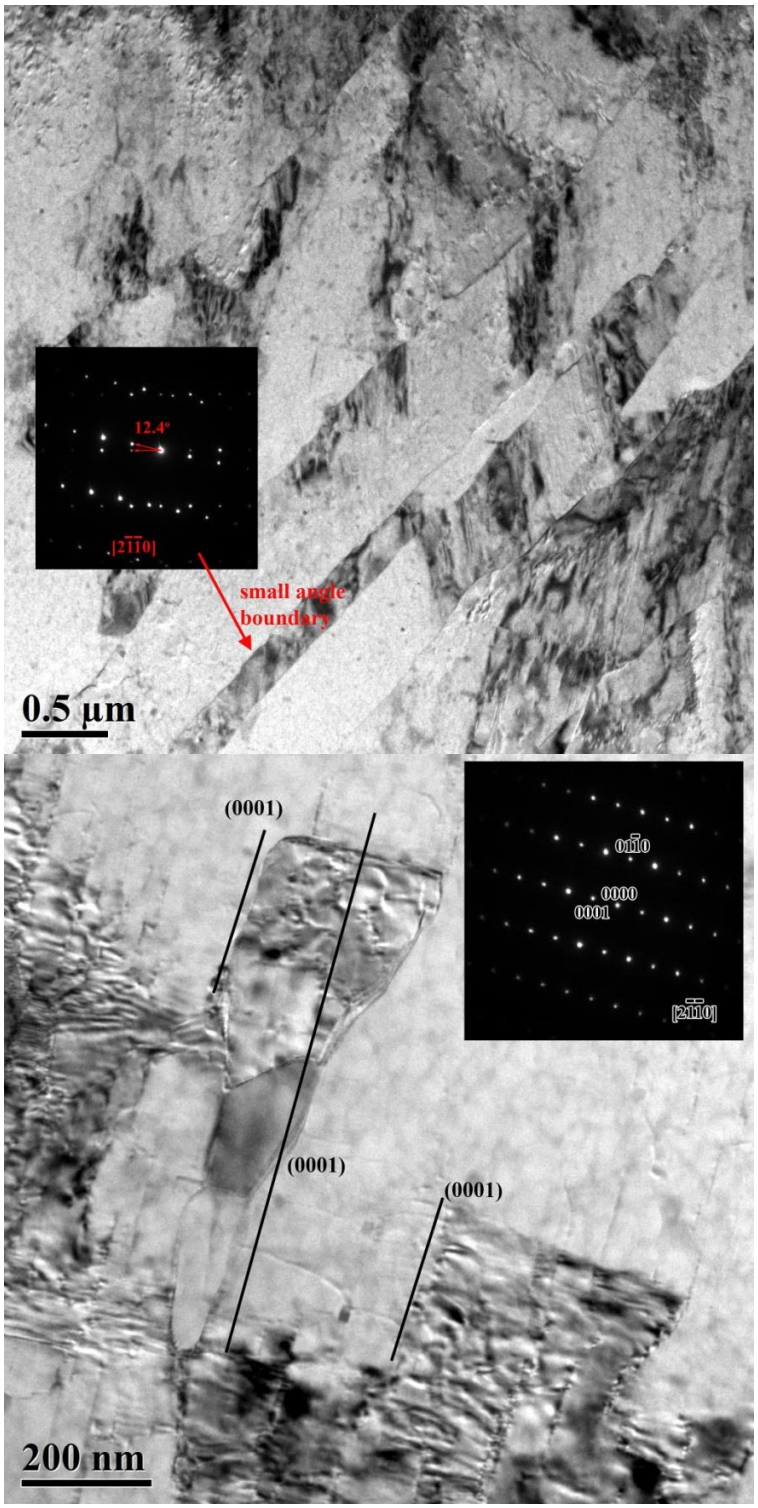

Figure 5.9 TEM images of Texture1 specimen after ECAP at 150°C showing (a) deformation bands with low angle boundaries and (b) very small DRX grains inside the parent grain. ED is vertical.

5.3 TEM and STEM Investigation of Texture2 Specimen after ECAP at 150°C

In the previous chapter, detailed microstructural characterization and simulation results of the Texture2 specimen showed that there are limited twinning activities during ECAP at 150°C. In addition, after ECAP the grains become smaller, divided, and elongated with dense, low angle grain boundaries in comparison to the Texture1 specimen. Figures 5.9a and b display the TEM and STEM images of the Texture2 specimen after ECAP at 150°C. Here, an accumulation of secondary particles is visible at the grain boundary region, similar to that found in the Texture1 specimen (Figure 5.3). However, precipitates are also present in the grain interior on low/high angle boundaries (Fig.5.9a). Interestingly, the density of precipitation in rod and plate morphology is very high compared to the Texture1 specimen (Fig.5.3). EDS analysis of different rod-like precipitates indicated that they are slightly Zn-enriched. However, the density of ϕ' particles (indicated by arrows) is relatively lower and their size (~50nm) is smaller compared to those observed in twin/grain-boundary DRX regions of the Texture1 specimen.

TEM and STEM images of a wide DRX region on a grain boundary of the Texture2 specimen is given in Figs. 5.11a and b, respectively. It was confirmed by diffraction patterns that grains A and B are different grains. Here, evidently the rod- and plate-like precipitates usually form on the (0001) plane, as seen clearly in Fig.5.11b.

Although the Texture2 specimen is mostly free of twins, a $\{10\bar{1}1\}$-$\{10\bar{1}2\}$ double twin formed as seen in Figure 5.12. Please note that this is the only twin found in

a TEM sample of the Texture2 specimen. As seen in Fig.5.12a, the double twin is free of DRX grains, and its left boundary is coherent with the matrix in contrast to the Texture1 specimen. Thus, it was possible to produce an electron diffraction pattern that identifies the misorientation angle with respect to the matrix. It appears that the misorientation angle is 38°, which is the typical misorientation angle of $\{10\bar{1}1\}$-$\{10\bar{1}2\}$ double twin formation.

Unlike the Texture1 specimen, there are neither DRX nor distinct ϕ' or secondary particle formations within the twin from the Texture2 specimen (Fig.5.12). There are rod-like precipitates inside the twin, but these are also observed outside the twin. Again, rod- and plate- like precipitates formed on the (0001) plane. Large particles were identified as Al-Mn particles. Interestingly, very fine secondary particle formation on the twin boundary is evident, as indicated by the red arrows in Fig.5.12b. A segregation of heavy atoms (Zn/Al/Mn) is evident on the twin boundary since it has a distinctive white color compared to the neighboring regions, similar to the Zn segregation on a twin boundary in Fig.5.4b and in [116].

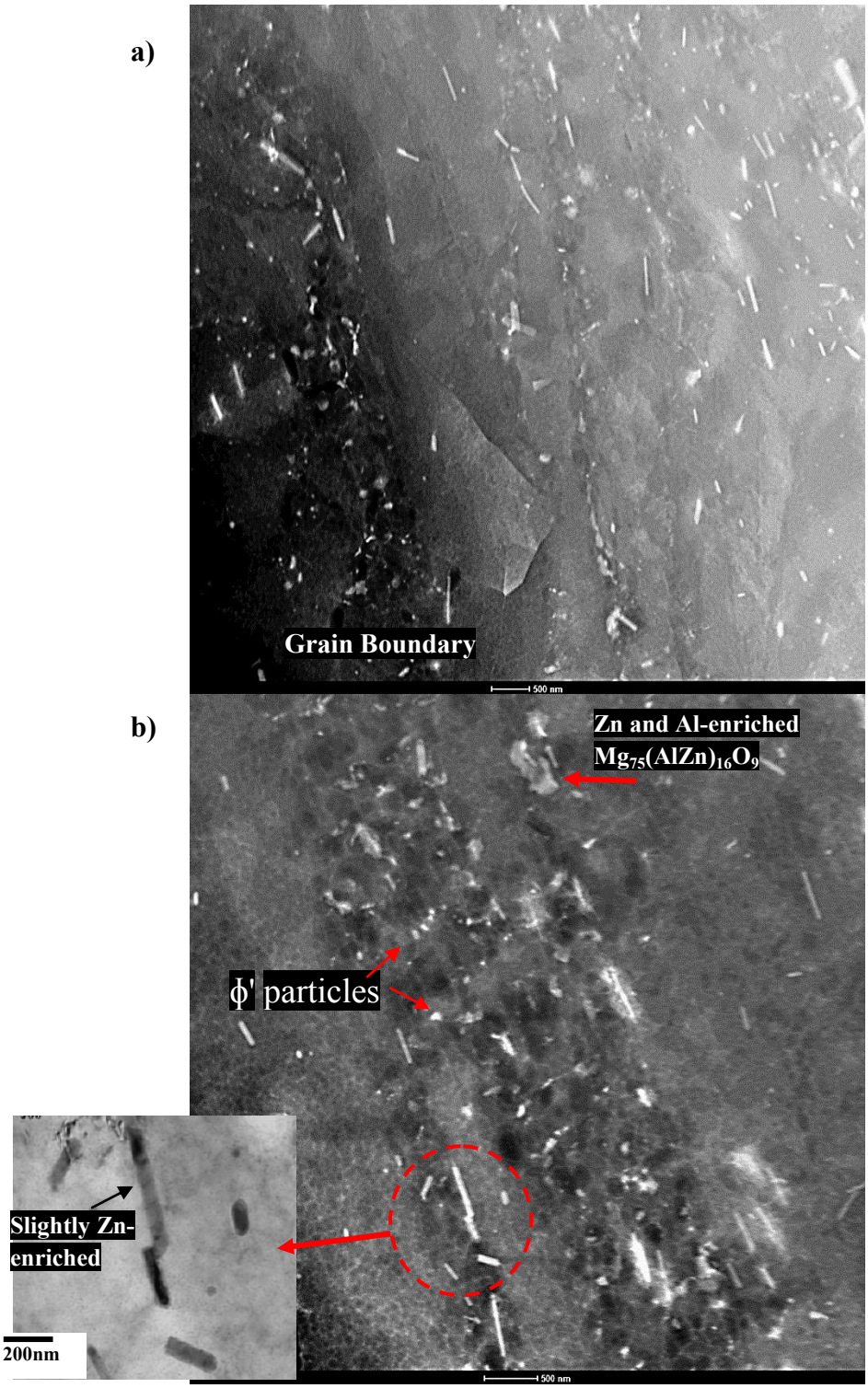

Figure 5.10 (b) TEM and (b) STEM images of the Texture2 specimen after ECAP at 150°C, showing precipitation at and near the grain boundaries. ED is vertical.

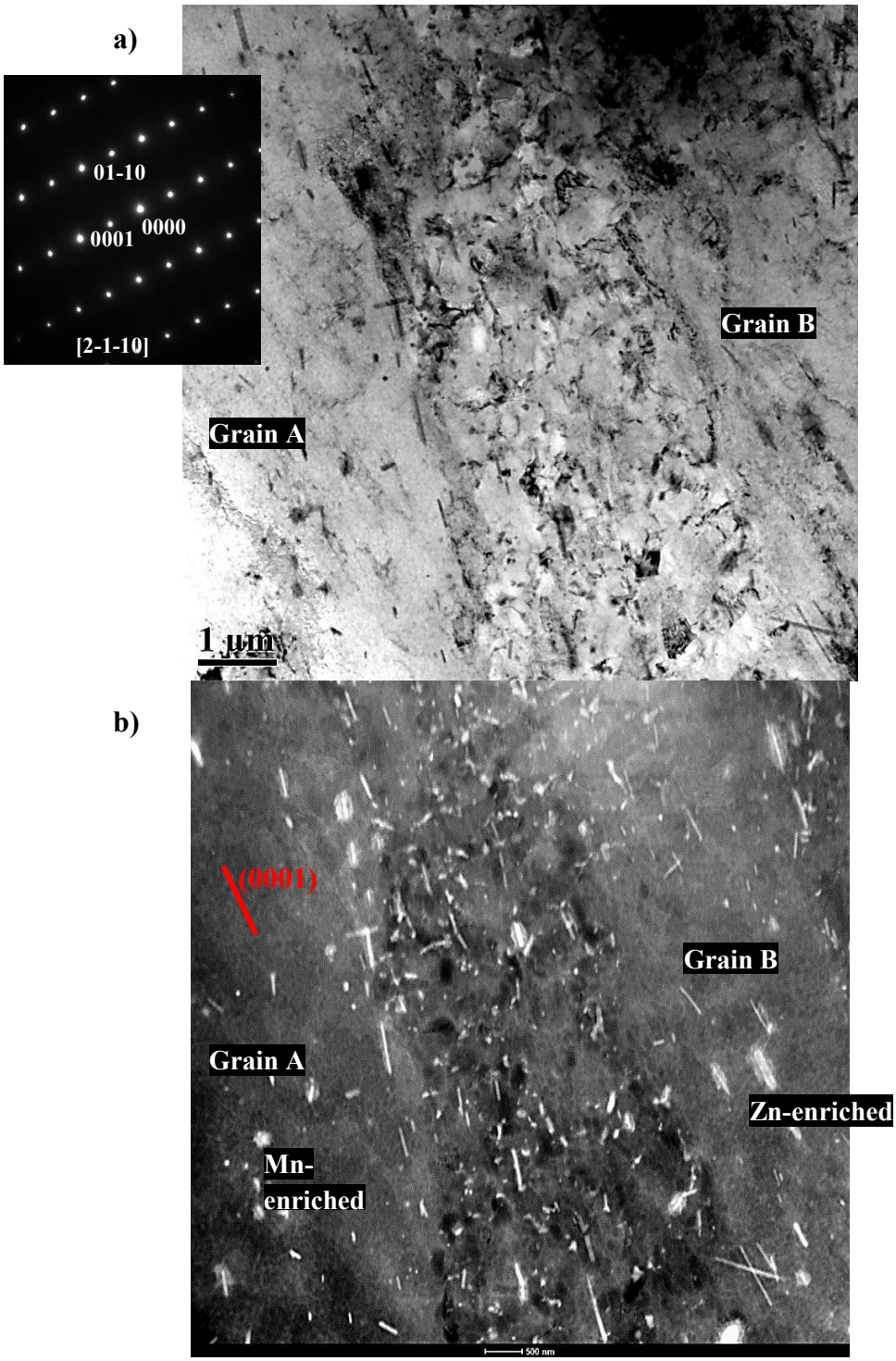

Figure 5.11 (a) TEM and (b) STEM images of Texture2 specimen after ECAP at 150°C. ED is vertical.

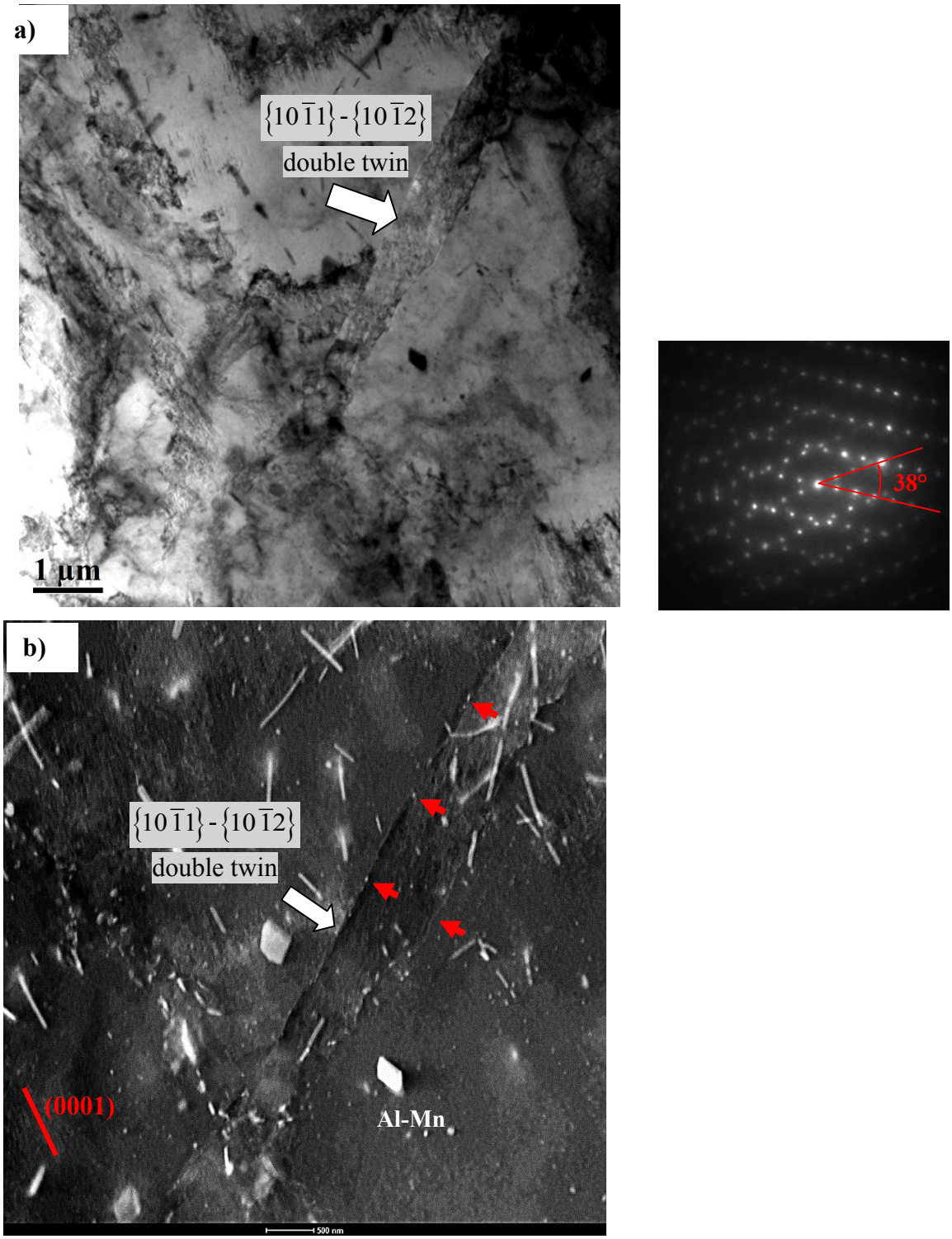

Figure 5.12 (a) TEM and (b) STEM images of Texture2 specimen after ECAP at 150°C showing a $\{10\bar{1}1\}$-$\{10\bar{1}2\}$ double twin. ED is vertical.

5.4 Crack Formation and Failure at DRX Regions

It was shown in Chapter 4 that ready activation of compression/double twinning promoted non-uniform deformation and DRX within the twins in the Texture1 specimen. This caused deformation localization, repetitive DRX, and finally macro shear band formation during ECAP at 150°C. Crack initiation and failure occurred in the DRX regions. On the other hand, the Texture2 specimen was free of large shear bands and crack/voids, where relatively small DRX grains accumulated around grain boundaries.

It was also shown in Chapter II that crack initiation started from the DRX-formed regions/bands when samples are uniaxial tensile tested at 150°C and higher temperatures for all differently oriented specimens. Figure 5.13 shows SEM micrographs of a uniaxial tension tested sample at 200°C along the transverse direction (TD). A crack that formed and propagated in the DRX region is shown by an arrow in Fig. 5.13a. As seen in Fig. 5.13a, the crack stopped where the DRX region ends. Thus, the sample failed along the DRX region, as indicated by an arrow in Fig. 5.13b. Interestingly, similar to the ϕ' particles shown above, in the Texture1 (Fig. 5.4) and Texture2 (Fig. 5.10) specimens, secondary particle formation in the DRX region is evident. It appears that these particles formed mostly around grain boundaries of DRX grains like ϕ' particles in the Texture1 specimen (Fig.5.3b). Further, detailed TEM investigation is needed, but it is believed that these particles are ϕ' particles.

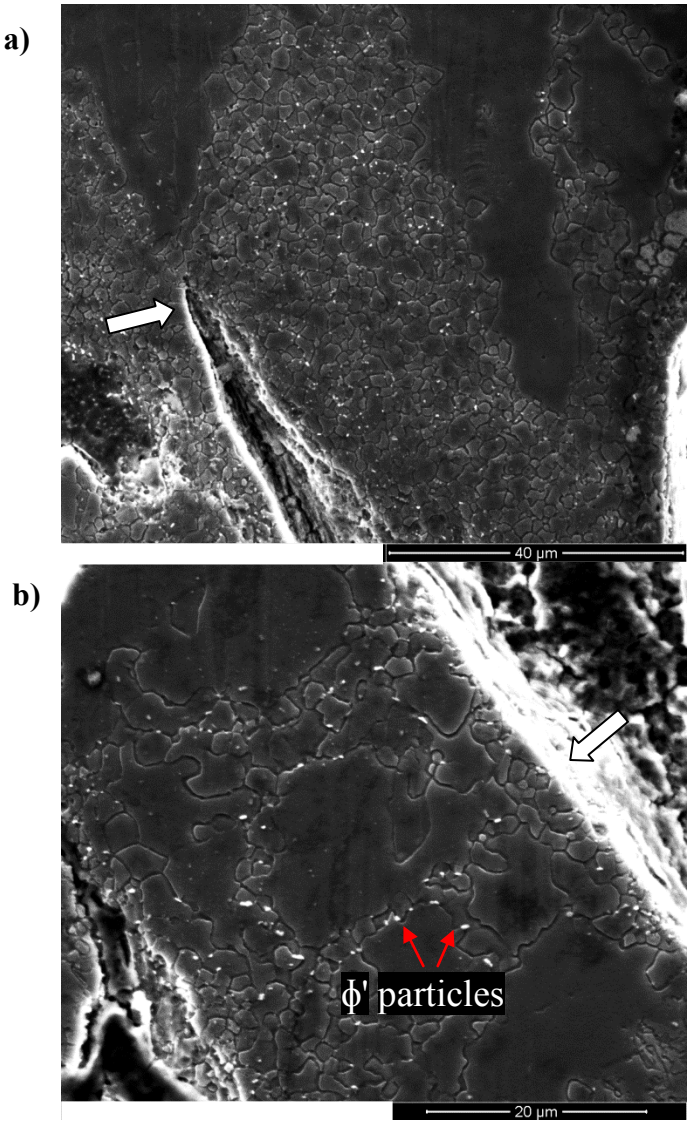

Figure 5.13 SEM micrographs of the uniaxial tension tested sample at 200°C along the transverse direction (TD). The loading direction is vertical.

5.4.1 Softening due to DRX

Softening due to the DRX is highly dependent on the type of DRX. Continuous DRX (CDRX) involves gradual deformation transformation of low angle boundaries to high angle boundaries via strain [93]. Since it occurs in a gradual manner, it causes a

gradual softening of the material. Non-basal slip systems are required to activate CDRX [93]. In addition, a special type of CDRX was called low temperature DRX (LTDRX), which occurs during cold/warm deformation between ambient temperature to 200°C [32]. During this type of DRX, new grains provide strain hardening instead of regular softening [93]. It is most likely that the DRX type in the Texture2 specimen is CDRX since as a non-basal slip system, prismatic slip, is highly active and there is no severe strain softening (shear band formation) observed in this specimen (Chapter IV). In addition, there is very limited twinning activity which eliminated the texture softening in the Texture2 specimen. The texture of the DRX grains is similar to the original grains and again favorable for the prismatic slip (Fig. 4.15b). They generally formed around grain boundaries of Texture2 specimen.

On the other hand, high twinning activity in the Texture1 specimen caused local texture softening inside the compression and double twins. In addition, the texture of the DRX grains in the Texture1 specimen differs from the parent grains. The orientation of DRX grains is more favorable for the softest slip, basal slip (Fig. 4.15c). Strain softening in the DRX formed regions of the Texture1 specimen initiates the shear band formation and repetitive DRX. And finally, crack and failure occur in these regions as shown in Chapters III and IV.

New dislocation-free nuclei form during DDRX and causes significant softening [117]. The DRX type in this specimen is expected to be DDRX since it occurs when basal slip is readily active [93].

5.4.2 Softening due to the Composition Change

The strength of Mg can be increased by solute solution hardening. It has been reported that alloying of Mg with Zn or/and Al increased the critical resolved shear stress (CRSS) of basal slip [118]. As shown above, ϕ' particles are Zn and Al enriched compared to the AZ31 composition. It remains to be seen whether these particles were formed after or before DRX. However, it is clear that the formation of ϕ' particles decreased the Al and Zn content of the DRX grains, which should decrease the CRSS of basal slip in these grains. Furthermore, it is evident form the STEM image given in Fig.5.6 that the DRX region inside the twin is darker under STEM investigation. This indicates that the concentration of lighter atoms in these regions is relatively higher than in the surroundings. Since Mg is the lightest element among Al, Zn, and Mn, Mg content is higher inside the DRX region. Thus, it is expected that the CRSS of basal slip is lower than in the surroundings. The composition change due to the formation of ϕ' particles in DRX regions provides the softening in these regions.

5.4.3 Hardness of DRX Grains

The crack initiation inside the shear band of the Texture1 specimen is shown with an OM image in Figure 5.14a. As seen in Fig. 5.14b, the shear band includes DRX grains and a crack formed in these regions. A magnified image of the region in Fig.5.14b is given in Fig.5.14c. The ϕ' particles are indicated with arrows in Fig. 5.14c. As discussed earlier, these particles are usually formed around DRX grain boundaries. The nanoindentation has been employed on different regions as indicated in Fig.5.14a. A

detail of the test is given in section 2.3. Reg1 and Reg3 consist of large grains with limited DRX grains, whereas Reg2 is from the DRX region on the shear band. The hardness values of different points from different regions in Fig. 5.14a are presented in Fig.5.14c.

Since the DRX grains are very small, the penetration depth and thus the deformed region were set to minimum to eliminate grain boundary and the ϕ' particles effects. A description of the test is given in section 2.3. The resulting deformed region due to the nanoindentation test was found 1x1x1 μm^3 triangular piece, as demonstrated in Fig 5.14d via the red triangle. Here, evidently a few grains, including the ϕ' particles, can be deformed when the indenter conducts the measurement inside Reg2. These details needs to be kept in mind while interpreting the below hardness results.

Fig.5.13c showed that the hardness of the DRX region is slightly lower than the hardness of the large grains. This is expected due to the above reasons of softening in the DRX formed region. Please note, ϕ' particles and the grain boundaries should have varied hardness values in Reg2. However, the general trend in Fig.5.14c indicates that the DRX region is softer, as expected.

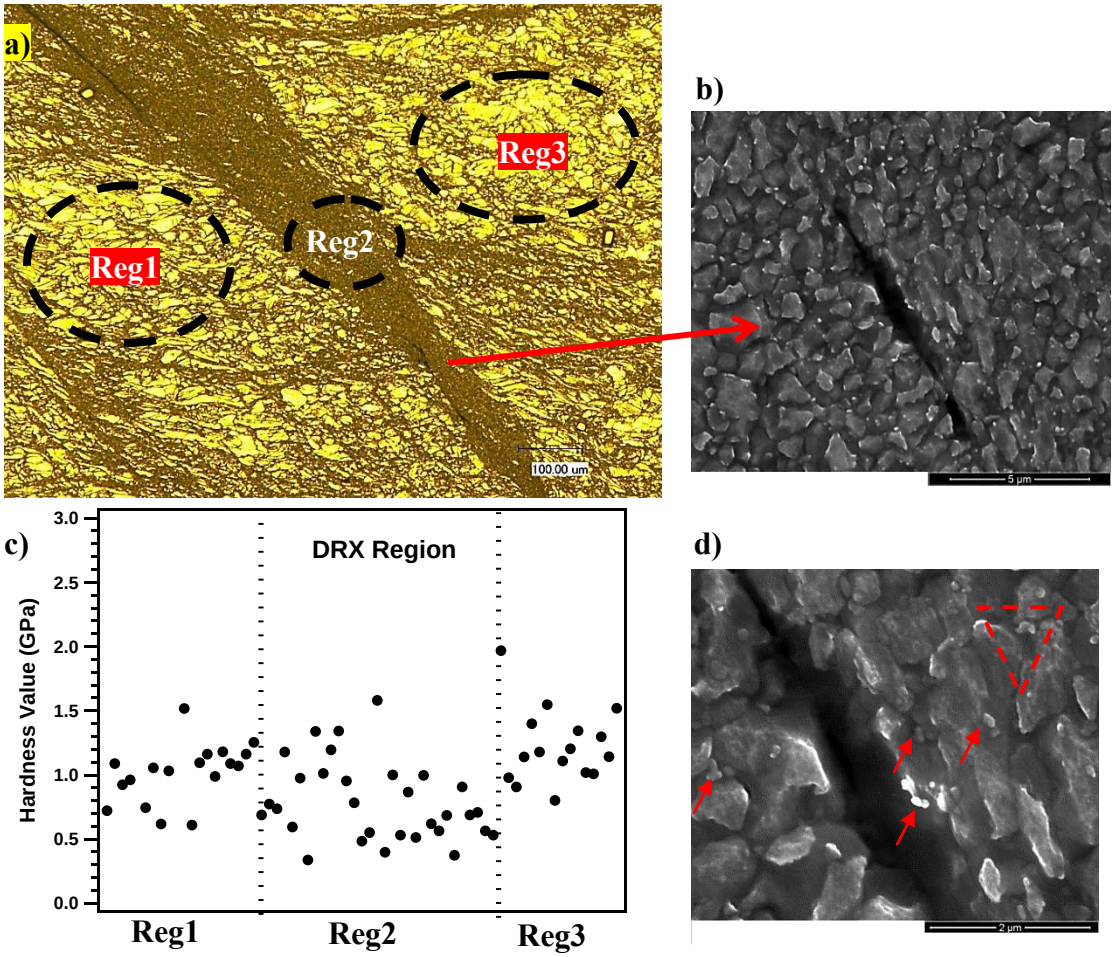

Figure 5.14 (a) OM image of the region from the Texture1 specimen, where nanoindentation tests were performed. (b-d) SEM image of the shear band where a crack formed inside the DRX region. (c) Hardness value of different regions indicated in (a).

The hardness value is also highly dependent on the texture. As shown in Fig. 4.15c, the textures of Reg1&3 (not-DRX) and Reg2 (DRX) are different. This may affect the hardness results. However, as seen in Fig.4.15c, the basal planes are perpendicular to the nanoindenter's loading direction in both regions (DRX and not-DRX). Thus, it is believed that the texture effect/variation can be neglected with the current loading direction.

5.5 Summary and Conclusions

In this chapter, detailed SEM, TEM, and Scanning TEM (STEM) analyses of the starting material and the ECAP specimens were reported. The main findings and conclusions can be summarized as follows:

1. This analysis observed the unique secondary particle formation in the DRX regions occurred in twins and along grain boundaries. Also, solute segregation was observed after ECAP at 150°C.
2. Al and Zn enriched particles were formed in the DRX regions, formed on twins and along grain boundaries.
3. Homogeneously distributed white networks were observed in STEM images of ECAP specimens (both Texture1 and 2). The local EDS point analysis of these dark regions inside the white networks indicated that these white regions are slightly rich in Zn content.
4. Strain softening was shown to result from both texture and composition changes in newly formed DRX grains. Thus, cracks/voids forms primarily in DRX regions when samples are deformed or processed at 150°C or higher temperatures.

CHAPTER VI

EFFECT OF GRAIN SIZE ON LOW TEMPERATURE SHEAR FORMABILITY OF MG-3AL-1ZN ALLOY

The typical ECAP temperature of wrought AZ31 Mg alloys was shown to equal 200°C and higher [14, 20]. In Chapter IV, the role of the crystallographic texture and deformation modes on low temperature shear formability of the AZ31 alloy via ECAP was investigated. In addition, processing wrought AZ31 Mg alloy samples with a grain size of 25μm at 150°C was successful via a carefully selected starting texture. This was achieved by suppressing the compression/double twinning activity by instead promoting prismatic slip activity; the former was found to play a significant role in shear localization during ECAP.

Among the possible wrought starting textures (Fig. 4.1), the Texture2 texture configuration was shown optimal for suppression of twinning and promotion of prismatic slip activities during ECAP at 150°C. However, ECAP of the AZ31 Mg alloy samples with 25μm grain size was unsuccessful directly at 100°C, regardless of the starting textures available for the process.

As discussed in section 1.3.5, grain refinement promotes more non-basal slip activity in Mg alloys [9]. In addition, the effect of grain size on twinning was found to be more pronounced than slip mechanisms in Mg alloys such that formation of twinning gets more difficult in finer grain size microstructure [19, 119]. It appears that in addition

to starting texture that promotes more non-basal slip activity and the less twinning activity (Chapter IV), finer grain size may improve the ECAP ability at lower temperatures.

In this chapter, a systematic ECAP study of the AZ31 alloy bulk piece will be performed to utilize the multi-temperature step-down technique to incrementally refine the grain size. The refined grains allow for subsequent processing at lower temperatures (<150°C), which is otherwise impossible to achieve under the original starting microstructure. Please note that Texture2 is the only starting texture used in this chapter, as shown in Figure 6.1a.

6.1 Multi Pass Processing Route Optimization

Different multiple processing routes at 150°C have been simulated to investigate active deformation modes during ECAP with the same starting texture (Texture2). A simulation of the different processing routes is provided in Figure 6.2. Here, the A route requires no rotation while the Bc route has a +90° rotation about the long axis of the billet between the passes (i.e. two passes for both the A and Bc routes indicated by 2A and 2Bc, respectively).

Compression twinning activity becomes relatively more active for route Bc (Fig.6.2). However, please note that multi-pass ECAP simulation includes many approximations. First of all, the grain size distribution is not uniform after 1 pass, and a bimodal grain size can significantly affect the activity of deformation modes. Secondly, the billets were placed in the heated ECAP die for 20 minutes before each extrusion

pass. Therefore, it is difficult to predict the microstructure change during this 20min at 150°C, which may affect the dislocation structure and hardening response.

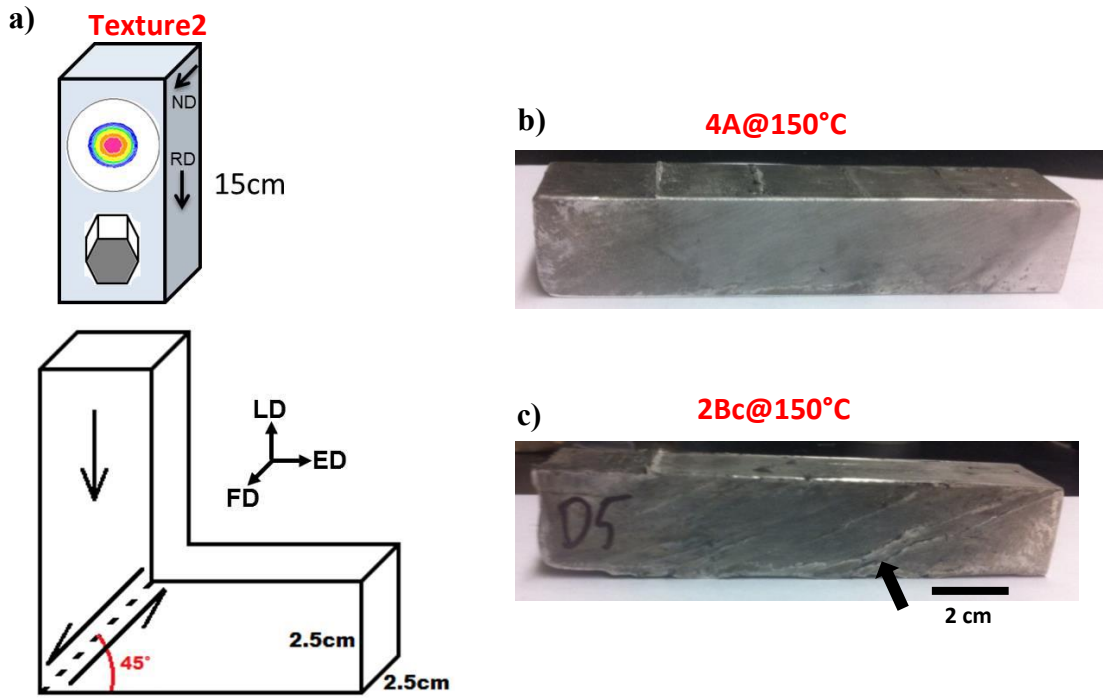

Figure 6.1 Schematics of the ECAP and AZ31 bulk piece with a (0002) pole figure showing the starting texture configuration of all specimens investigated in this chapter. ED: Extrusion direction, LD: Longitudinal direction, FD: Flow direction

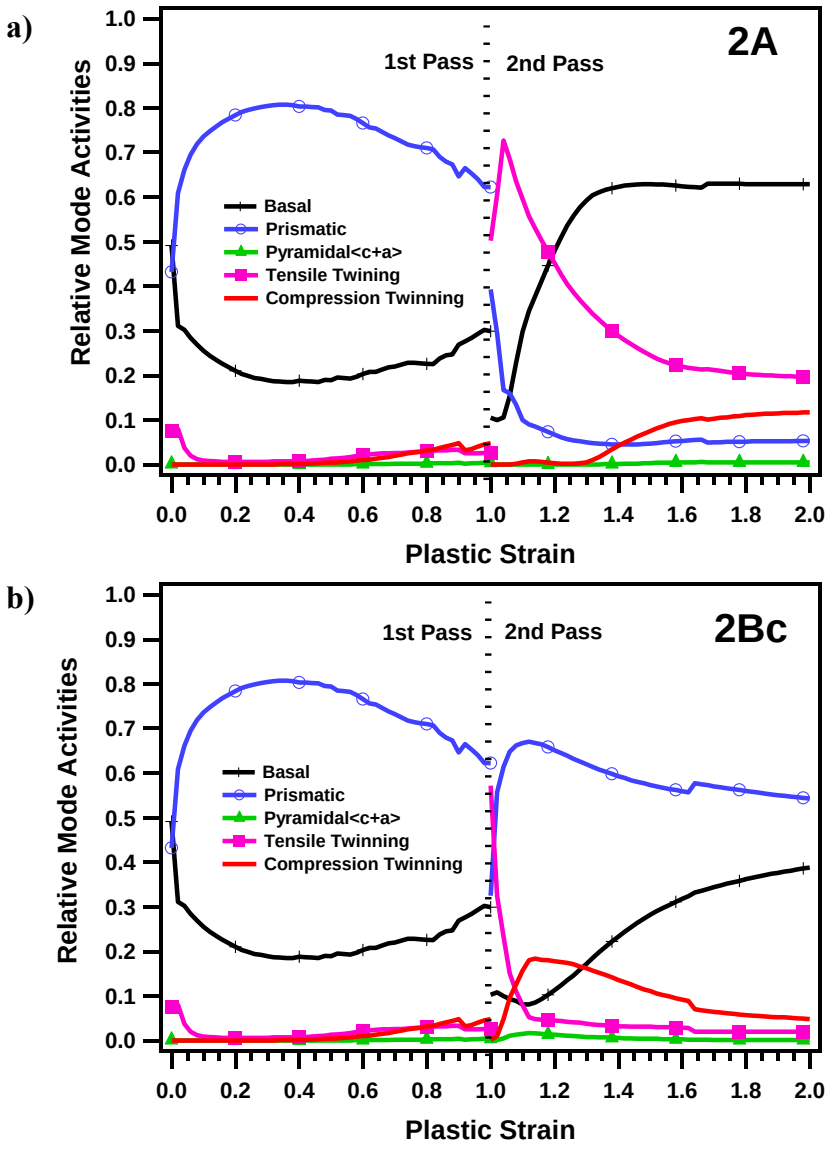

Figure 6.2 Predicted relative deformation mode activities during a double pass ECAP with different processing routes at 150°C. Routes (a) A and (b) Bc.

To account for the approximations, the simulation results were checked with the experimental study. As seen in Fig 6.1b and c, with route A it was possible to process up to four passes, whereas after two passes deep shear bands and cracks formed when using

the Bc route (as indicated by an arrow in Fig.6.1c). Softening due to the strain path change in ECAP was reported, which was shown to be associated with various processing routes [120]. It is belived that, in addition to relatively high compression/double twinning activity, softening due to the strain path change is higher at 150°C. Thus, route Bc initiated a more severe strain path change that causes flow softening and resulted in shear bands in the 2Bc case (Fig.6.1c). Additional experiments are required to verify this conclusion.

6.2 Microstructure and Texture of Multi -Pass and -Temperature ECAP Specimens

Multi-pass ECAP experiments were conducted with only the A route since route Bc initiated shear localization and cracks when processed at 150°C. The details of the multi-pass ECAP billets for investigation in this chapter are provided in Table 6.1. More details about the processing conditions are given in Chapter II.

Figure 6.3a shows the initial microstructure of the billets that were ECAP for multiple passes at different temperatures. The initial average grain size is 25μm (Fig.6.3a). Fig. 6.3b is the OM image of the 1A@150°C specimen (named Texture2@150°C in Chapter IV). It is evident from the OM image given in Fig.6.3c that the ECAP for two passes at 150°C increased the DRX grain fraction and further refined the microstructure. However, large grains are still present, with very fine DRX grains after two passes (Fig. 6.3d).

In order to refine the microstructure further with a uniformly distributed grain size, a sample (4A@150°C) was processed for four passes at 150°C. As all grains are

DRX except for a few larger grains, a generally uniform microstructure was obtained (Fig. 6.3e). After four passes, the grain size reduced from 25μm to ~0.8μm, as demonstrated in Figs. 6.3e and f. Interestingly, secondary particles are evident in the 4A@150°C specimen, as indicated with arrows in Fig. 6.3f. These particles seem to be ϕ' particles presented in Chapter V. However, a future TEM study is needed to verify this assertion.

Table 6.1 Designations and processing conditions of AZ31 Mg billets

Designation	# of passes	ECAP Temperatures	Comments
1A@150°C	1	150°C	Crack-free
2Bc@150°C	2	150°C	Shear localization and cracks
2A@150°C	2	150°C	Crack-free
4A@150°C	4	150°C	Crack-free
4A +4A	4+4	150°C+125°C	Crack-free
2A+2A+1A	2+2+1	150°C+125°C+100°C	Minor cracks

After the four passes at 150°C, an additional four passes following route A has been successfully applied to the AZ31 sample at 125°C. The resulting sample is named 4A+4A. The additional four passes at 125°C decrease the grain size, as seen in Fig 6.4a. However, the grains size was not refined significantly after the additional passes at 125°C (Figs. 6.3f (4A@150°C) and 6.4a (4A+4A)). This is expected since grain growth occurs between each passes.

Specifically, the SEM image of the 4A+4A specimen given in Fig.6.4a revealed a grain size decrease from 0.8 to ~0.6μm after four passes at 125°C. This sample (4A+4A) was subsequently ECAP at 100°C, which was unsuccessful as the sample fractured. It was unclear whether the sample failed either due to the low processing temperature or

since it had been previously processed through many passes (four at 150°C and four at 125°C, before processing at 100°C).

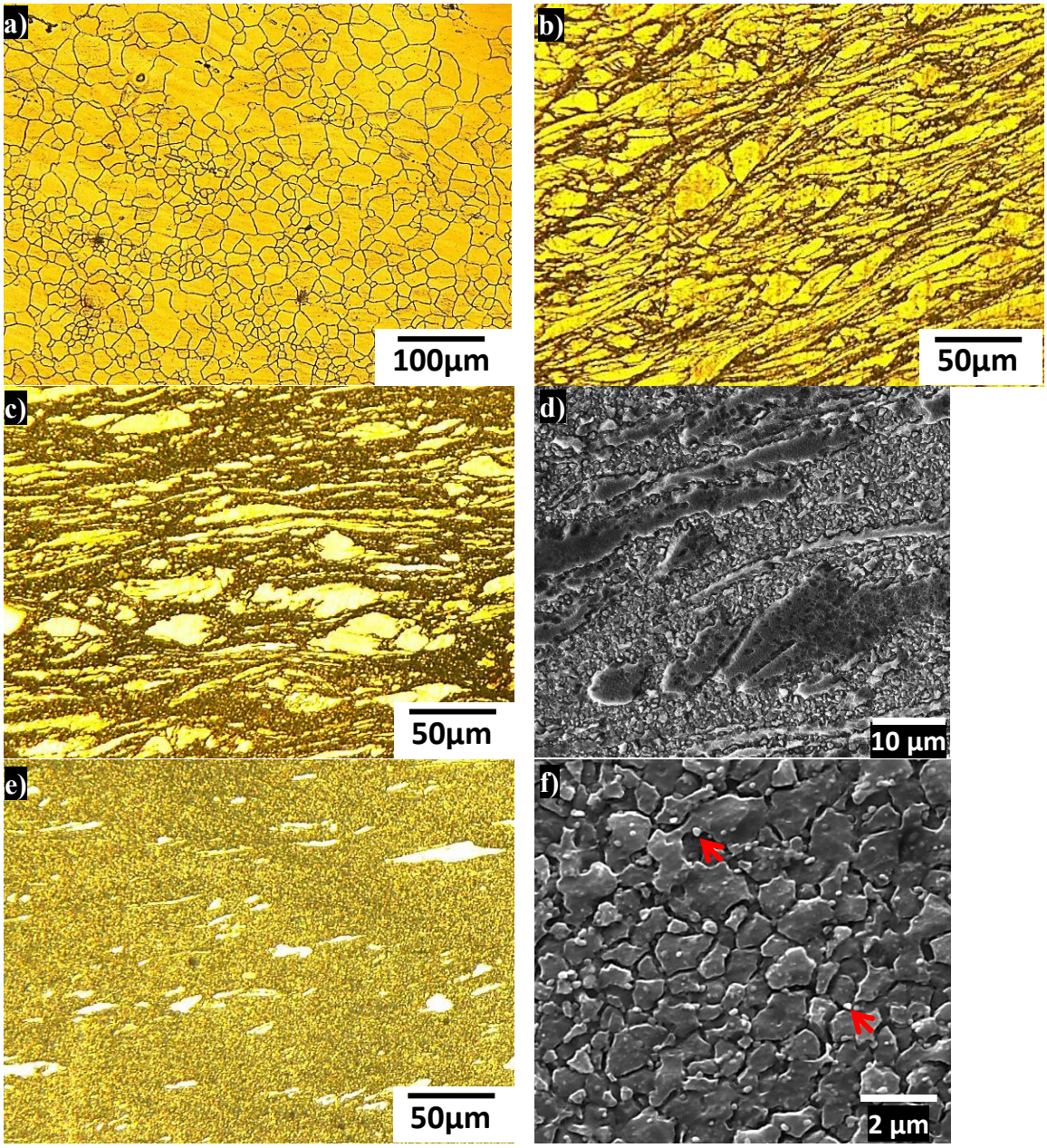

Figure 6.3 OM and SEM images of (a) the starting material before ECAP, (b) 1A@150°C (c and d) 2A@150°C and (e and f) 2A@150°C

Since the 4A+4A specimen was incapable for further processing at 100°C, a separate specimen was sequentially processed for two passes each at 150°C and 125°C, respectively, before being processed at 100°C. The goal was to process at temperatures (150°C and 125°C) with a minimum number of passes, and afterwards further process at 100°C. The sample was ECAP successfully and is named 2A+2A+1A. It is obvious that the grain size refined significantly after processing at 100°C (Fig.6.4b). An accurate estimation of the average grains size is quite difficult for the 2A+2A+1A specimen from the SEM image given in Fig.6.4b. Thus, a TEM image of the 2A+2A+1A specimen is given in Fig. 6.4c. The detected grain boundaries are indicated by dashed lines in Fig. 6.4c. It is evident that the grain size refined down to <500 nm after processing at 100°C.

The initial texture was also significantly altered after ECAP at 150°C and lower temperatures, as seen in Figure 6.5. After two passes at 150°C (2A@150°C), the basal fiber spreads towards the LD direction, and strong peaks appeared at the center of the $(10\bar{1}0)$ pole figure (Fig. 6.5b). The additional two passes at 125°C reoriented the basal fiber in the center of the (0002) pole figure towards the north and south poles. The reorientation of ~90° towards the north and south poles in Texture2 (Fig. 6.5a) was previously shown in Chapter IV to result from the tensile twinning activity.

The final texture after four ECAP passes at 150°C (4A@150°C) is given in Fig.6.5d. The initial texture was significantly changed, and intense basal fibers appeared on the south and north poles. An intense basal fiber similar to the initial orientation is also evident at the center of the (0002) pole figure of the 4A@150°C specimen (Fig.6.5d). It appears that the texture didn't change significantly after the additional four

passes at 125°C, as seen in the $(10\bar{1}0)$ and (0002) pole figures of the 4A+4A specimen in Fig. 6.5e. Here, the intensity of the basal fiber at the north and south poles increased at the expense of the center basal fiber.

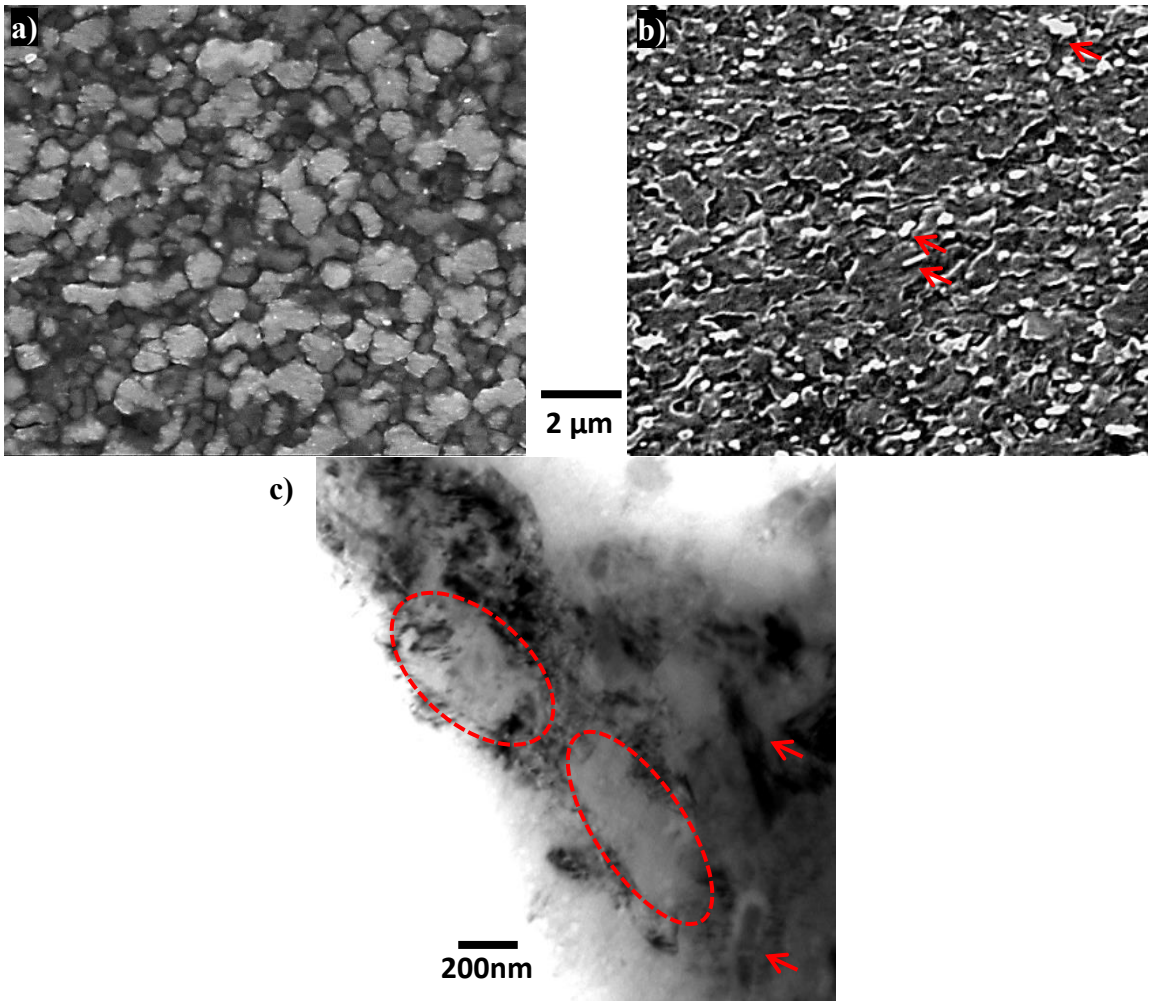

Figure 6.4. SEM images of (a) 4A+4A and (b) 2A+2A+1A. (c) A TEM image of 2A+2A+1A.

Interestingly, the 2A+2A+1A specimen has a unique texture compared to the others in Fig. 6.5, where a relatively spread basal texture is evident (Fig. 6.5f). It appears

that processing at 100°C alters the texture significantly and weakened the basal texture. The secondary particle fraction is relatively high in the 2A+2A+1A specimen, as seen in Figs.6.4b and c and indicated by arrows.

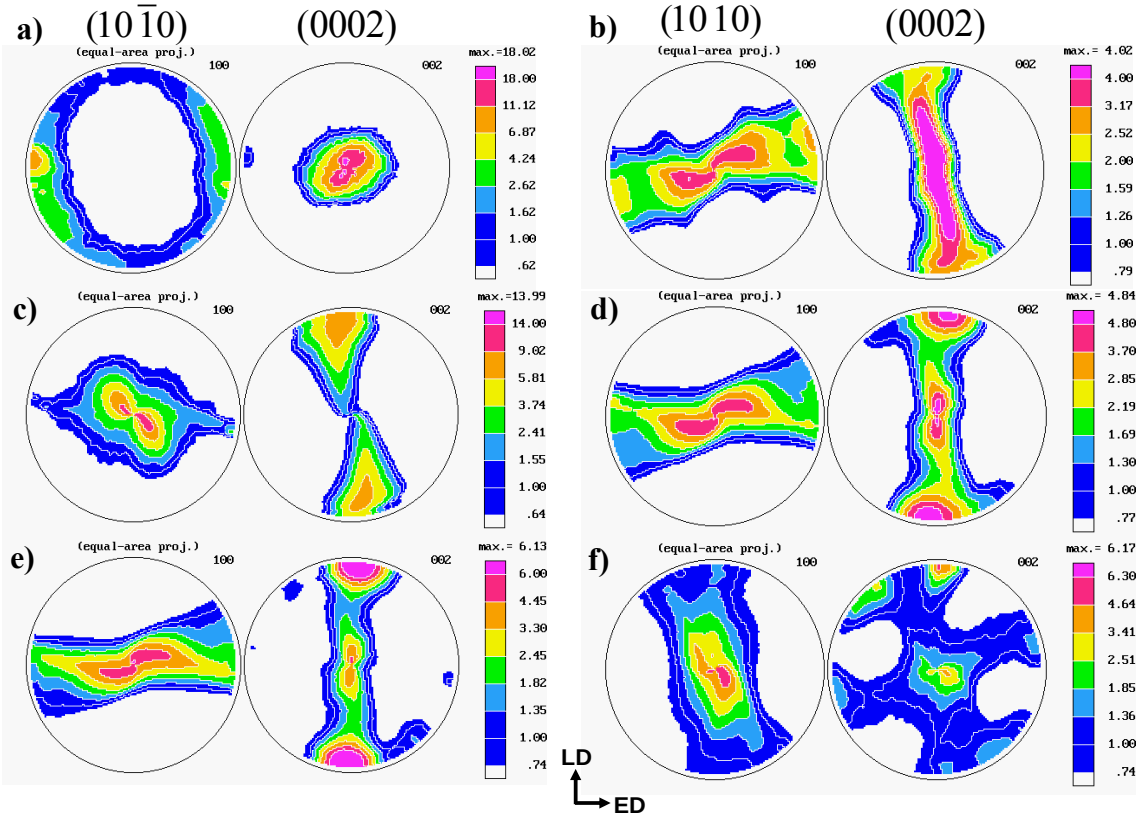

Figure 6.5 (10$\bar{1}$0) and (0002) pole figures of (a) starting material before ECAP, (b) 2A@150°C, (c) 2A+2A, (d) 4A@150°C, (e) 4A+4A and (f) 2A+2A+1A

The basal texture alteration was attributed to the particle-stimulated nucleation of DRX grains with random orientations[121]. Here, secondary particles can cause texture randomization (Fig. 6.5f) in the same manner. In addition, formation of different twin variants can also significantly randomize the texture.

6.3 Room Temperature Mechanical Flow Responses of ECAP Bulk Pieces

Figure 6.6 displays the room temperature (RT) mechanical flow responses of hot-rolled (starting material) and ECAP specimens. Fig. 6.6a shows the starting material tension and compression responses at room temperature along three orthogonal directions. It exhibits nearly in-plane isotropy that is the flow response along the rolling (RD) and transverse (TD) directions; however, significant tension-compression symmetry is obvious. This is due to the strong basal texture with tensile twinning under in-plane compression, whereas under in-plane tension it shows slip-dominated deformation.

Fig.6.6b presents the RT tension-compression curves of the 2A@150°C specimen. Both tension and compression yield strengths increase for all directions. The tension-compression asymmetry for a given direction decreased after ECAP at 150°C for two passes.

Fig.6.6c and d display the RT mechanical flow responses of 4A@150°C and 4A+4A specimens, respectively. The tension-compression response of the 4A@150°C specimen is similar to the starting material before ECAP; however, the yield strengths significantly increased and the tension-compression asymmetry decreased after four passes at 150°C. The ductility (elongation to failure strain here) increased during tension along both for Flow (FD) and Longitudinal (LD) directions. Interestingly, a yielding plateau, a typical indication of tensile twinning activity, is evident in the initial part of the tension curve along the FD direction (Fig.6.6c).

The tension and compression curves of the 4A+4A specimen show a unique feature, an isotropic compression response along all tested directions (Fig. 6.6d). In addition, tension curves along the ED and FD show an isotropic response with higher strength and ductility compared to the starting material. Similar to the 4A@150°C curve in Fig. 6.6c, the yielding plateau is obvious both in the ED and FD tension curves of the 4A+4A specimen. Although textures of the 4A@150°C and 4A+4A specimens are similar, their compression responses along LD direction are completely different (Figs. 6.6c and d). There should be a significant texture difference in the missing part of the experimental pole figures. Here, additional investigations are needed.

The tensile yield strength of the AZ31 Mg alloy increased from 160 MPa to around 400 MPa after processing at 100°C, as seen in Fig.6.6e. Tensile tested specimens along the ED showed very low ductility and earlier failure. It appears their failure occurred at the shear bands (not shown here). However, tensile and compression elongation to failure strains along other directions are similar to the starting material.

When comparing the Hall-Petch (H-P) trend lines of different samples, it is necessary to ensure that the texture is kept constant for all compared cases since deformation mechanisms are highly dependent on the loading direction and texture. When the basal plane normal is perpendicular to the loading axis, tensile loading mostly activates prismatic slip, whereas compressive loading predominantly activates tensile twinning [19].

The texture effect seems to be identical for the ED direction specimens loaded under compression and tensile conditions, as shown in Figs. 6.7a and b. Tensile twinning

activity is evident under compression loading, which is clear from the initial plateau (s-shape curve) in the early part of the deformation. On the other hand, slip dominated deformation is obvious during tensile loading.

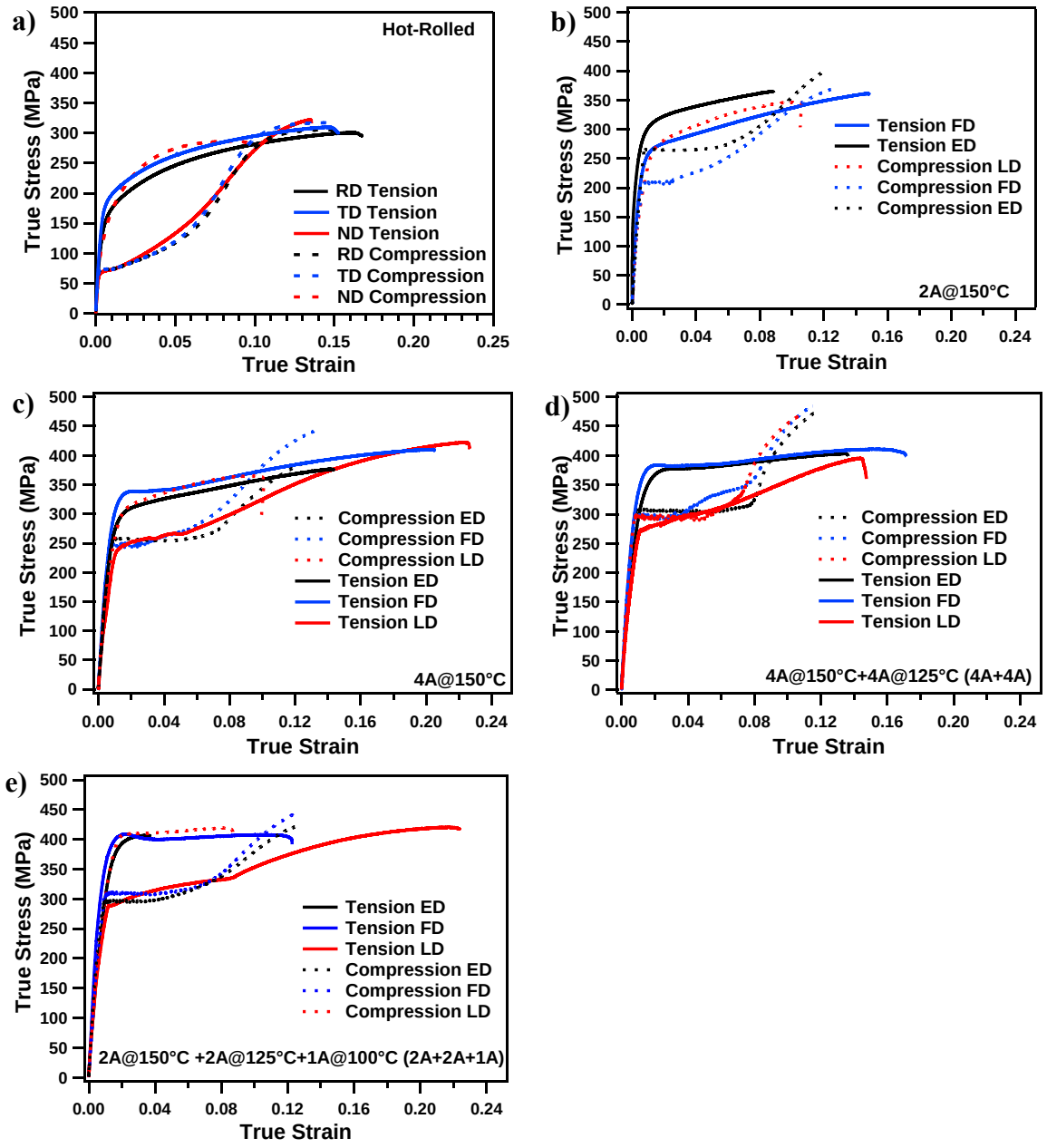

Figure 6.6 Room temperature stress-strain curves of (a) the starting material before ECAP, (b) 2A@150°C, (c) 4A@150°C, (d) 4A+4A and (e) 2A+2A+1A.

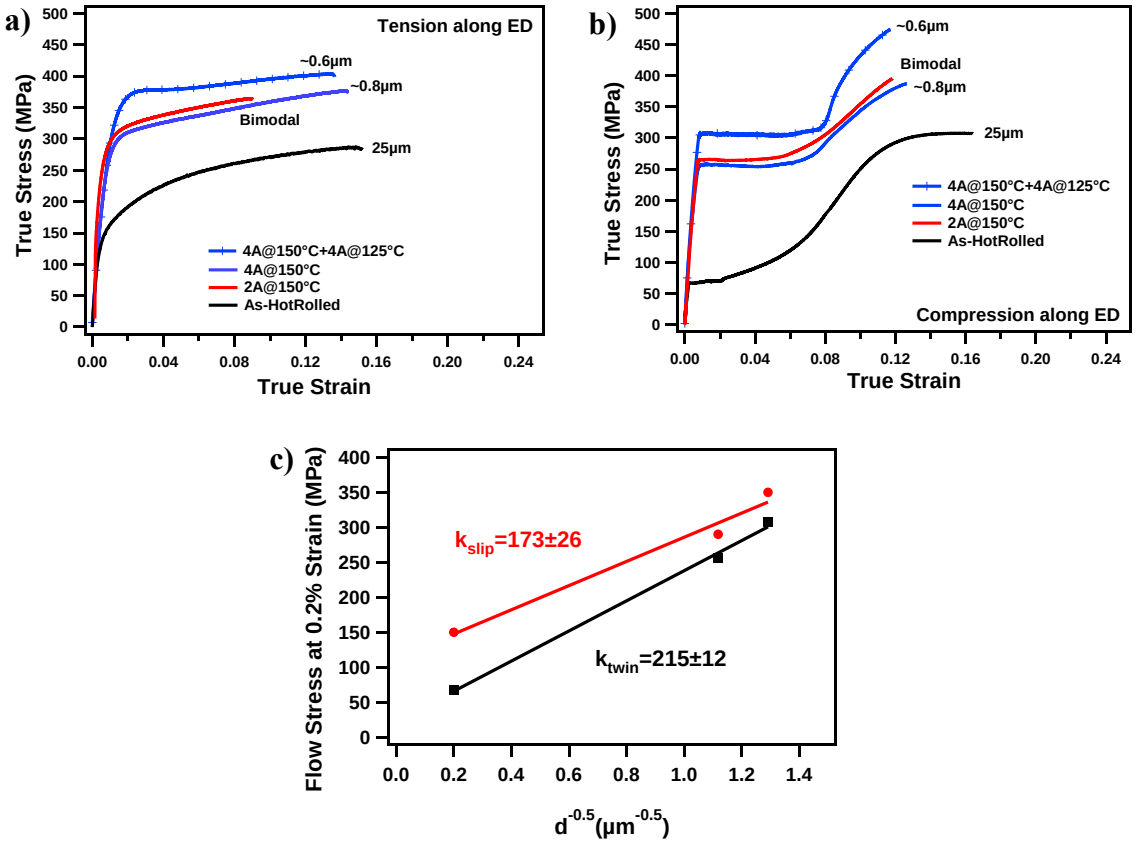

Figure 6.7 Room temperature mechanical flow responses of selected ECAP specimens under compression and tension loading along the extrusion direction.

Interestingly, with decreasing grain size, the no-hardening plateau in the compression stress-strain curves along ED(Fig. 6.7b), that is associated with tensile twinning activity, gets much more extended (i.e. the amount of strain where no-hardening is observed gets much larger with decreasing grain size). In other words, when tensile twining is active it provides higher strain with zero hardening in finer grain

samples. The plateau strain is around 2% in the coarse-grained as-hot-rolled samples, whereas it is around 8% in the ultra-fine grained specimens.

Using the H-P relation;

$$\sigma_y = \sigma_0 + k_y d^{-\frac{1}{2}} \tag{6.1}$$

slopes for the slip and twinning H-P trend lines from Figs. 6.7a and b, k_y^{slip} and k_y^{twin} are found to be 173±26 and 215±12 MPa $\mu m^{1/2}$, respectively, in Figure 6.7c. It is difficult to estimate the average grain size of 2A@150°C specimen since it has bimodal grain size distribution (Figs. 6.3 c and d). Thus, the values of 2A@150°C specimen were not used in H-P plot given in Fig. 6.7c that was constructed using Figs. 6.7a and b. Although it is a rough estimation from only three data points, the k_y^{slip} and σ_0^{slip} values of this study has a good agreement with the reported ones [16]. It appears that $k_y^{slip} > k_y^{twin}$. Similar trend was found in the literature that, grain size sensitivity of twining is higher than the one for slip in AZ31 Mg alloy[122]. The tension-compression asymmetry is due to the tensile twinning activity during compression. With grain refinement, tension compression asymmetry decreased after ECAP (Fig.6.6). This is due to the faster hardening under compression where tensile twinning is predominantly active compared to under tension.

6.4 Summary and Conclusions

AZ31 alloy bulk pieces were successfully ECAP at temperatures below 150°C. This is the first time, to our knowledge, where an AZ31 bulk piece was successfully

ECAP at 100°C by utilizing a multi-temperature step-down technique to incrementally refine the grain size. Significant texture modification and grain size refinement were obtained upon multi-temperature ECAP of the hot rolled AZ31 Mg alloy. After processing at 100°C, the texture was significantly randomized and the grain size was refined to ~400nm.

It was clearly shown that processing at 150°C and lower temperatures for multiple passes enabled procurement of an ultra-fine grained material with a uniform grain size <0.5μm, a feat otherwise impossible for Mg alloys processed at typical temperatures of 200°C or higher.

CHAPTER VII

REDUCTION IN TENSION-COMPRESSION ASYMMETRY OF TWIN-ROLLED CAST MG-3AL-1ZN SHEETS VIA EQUAL CHANNEL ANGULAR PLATE EXTRUSION (ECAPE)*

To date, ECAP of Mg alloys have been limited to bar/billet forms and scale up of the ECAP technology has not been widely attempted via Mg alloy plate and sheet processing. In this chapter, a new equal channel angular plate extrusion (ECAPE) method will be used to process twin rolled cast (TRC) Mg-3Al-1Zn Mg sheets at 200°C and 150°C with different processing schemes. Please note that in the next chapter the study of ECAPE processed commercial AZ31 Mg plates will be reported.

TRC AZ31 can notably reduce the cost of traditional Mg sheet production by combining casting and additional rolling/annealing processes. TRC processed AZ31 Mg sheets were shown to have equivalent or superior properties to conventionally processed ones[123]. However, similar to conventionally processed AZ31 Mg sheets, TRC AZ31 Mg alloys again exhibit a strong basal texture (i.e. c-axes are mostly perpendicular to the rolling plane), which negatively influences the formability and causes high mechanical anisotropy near room temperature.

A new Bcp (90° CW rotation around the plate normal) route will be used during ECAPE processing, which is completely a new route and different from the traditional

* Reprinted with permission from "Reduction in tension–compression asymmetry via grain refinement and texture design in Mg–3Al–1Zn sheets" by E. Dogan, I. Karaman, G. Ayoub, and G. Kridli, 2014. *Materials Science and Engineering: A*, 630, pp. 220-227, Copyright [2014] by Elsevier B.V

Bc route used for bar specimens where the rotation is about the extrusion axis. The present Bc-P route in the plate tool (Figs. 2.2 and 7.1) is not accessible in the billet ECAP tool (Fig.2.1).

Grain size refinement and texture change after different ECAPE routes at different temperatures will be investigated. Resulting texture and grain size effect on tension-compression asymmetry at room temperature will be evaluated, which may assist in designing AZ31 alloy microstructures for better formability. A crystal plasticity model will be utilized to reveal the operating deformation modes in the ECAPE processed sheets under uniaxial loading at room temperature.

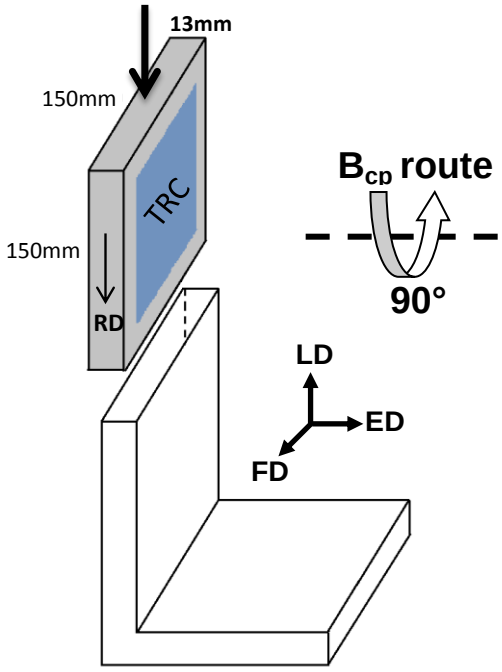

Figure 7.1 Schematics of the plate extrusion of twin-rolled cast (TRC) AZ31 Mg alloy sheets through a 90° ECAPE tool. TRC samples are embedded in a commercial hot-rolled AZ31 Mg alloy plate to be able to fit them into an existing ECAPE tool. RD: Rolling Direction, ED: Extrusion direction, LD: Longitudinal direction, FD: Flow direction.

7.1 Experimental Procedure for ECAPE Processing of Thin TRC AZ31 Sheets and Further Testing

3mm-thick AZ31 TRC sheets were cut into square specimens of 90x90mm^2. In order to process such a thin sheet using the available ECAPE tool (Fig.2.2), the sheet was embedded in a 150x150x13 mm^3 commercial AZ31 plate such that rolling direction is aligned with the extrusion direction, as illustrated in Figure 7.1. Note that, there is no limitation on batch processing thin sheet of Mg using ECAPE, but the present sheets were embedded into the plates to be able to use the existing tool. One can easily modify the tool to be able to ECAP sheets. The plates with embedded sheets were ECAPE processed through 90° tool with sharp corners and sliding walls (Fig. 7.1). Two extrusion routes were used: route A (no rotation between passes) and route Bcp (90° CW rotation around the plate normal as indicated in Fig.7.1) both at 200°C with an extrusion speed of 0.25 mm s^{-1}. Back-pressure was used during ECAPE processing.

Two different plates were ECAPE processed for 4 passes at 200°C for each route, called as 4A@200°C and 4Bc-P@200°C. It is worth pointing out that the plate was not possible to ECAP at 150°C directly, and interestingly TRC sheets have less cracks than the commercial plates, possibly due to the smaller grain size of the latter. A third plate was ECAPE processed for 4 passes at 200°C (route A) followed by additional two passes (using route A) at 150°C after 180° rotation about the extrusion axis. The aforementioned rotation and following two passes (route A) at 150°C is named as route F here, and the third plate processing scheme called as 4A@200°C+2F@150°C. All TRC ECAPE details are listed in Table 7.1.

Flat “dog-bone” shaped tension specimens with gage dimensions of 8 mm × 3 mm × 3mm (equal to the thickness of the sheet) were cut from as-received and the ECAPE processed sheets using wire electrical discharge machining (EDM). Rectangular compression specimens (3 mm × 3 mm × 6 mm) were cut from the as-received and the ECAPE processed materials using wire EDM.

Table 7.1 List of TRC AZ31 Mg alloy sheets processed using ECAPE and characterized in this study.

Designation	Processing	Extrusion Temperature	Extrusion Speed(mm/s)	Average Grain size(μm)
As-R	As-Received	-	-	9±3.8
4A	4 passes route A ECAPE	200°C	0.25	3.6±2
4Bcp	4 passes route Bcp ECAPE	200°C	0.25	2.8±1.34
4A+2F	4 passes route A+180° rotation+2 passes route A ECAPE	200°C+150°C	0.25 +0.025	1.9±1.4

7.2 Microstructure of ECAPE Processed TRC AZ31 Sheets

Figure 7.2a shows OM micrographs of as-received (As-R) TRC AZ31 Mg sheet. The average grain size is 9μm. SEM micrographs of the ECAPE processed samples are given in Figs. 7.2b-d, for 4A@200°C(4A), 4Bc-P@200°C(4Bcp), and 4A@200°C+2F@150°C(4A+2F) samples, respectively. Average grain sizes dropped to around 3.6μm after the 4A route. A more uniform grain size distribution is evident after the 4Bc route, as shown in Figs. 2c and e, where the average grain size is ~2.8μm. Figure 7.2d presents the microstructure of the 4A+2F sample. The average grain size decreases from 3.6 to 1.9μm after the additional passes at 150°C with grain size range

from 0.25µm to 10µm. It is clear from the micrograph and Fig.7.2e that additional processing at 150°C refined the grains further.

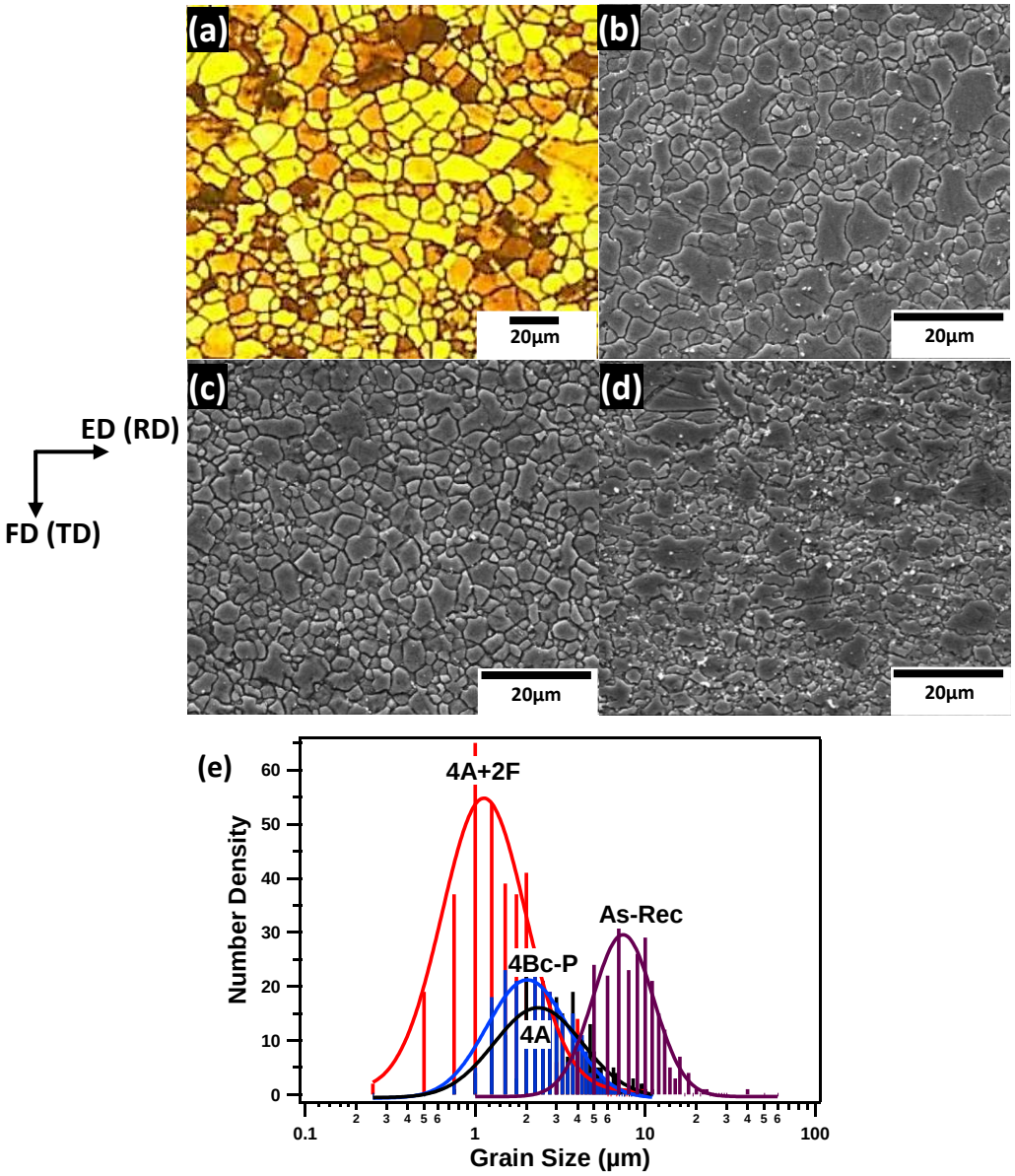

Figure 7.2 Optical and Scanning electron microscopy images of (a) as received and ECAPE processed TRC AZ31 Mg alloy samples; (b) 4A@200°C, (c) 4Bcp@200°C and (d) 4A@200°C +2F@150°C. (e) Grain size distribution of samples given in a through d.

7.3 Texture of ECAPE Processed TRC AZ31 Sheets

$(10\bar{1}0)$ and (0002) pole figures of As-R and ECAPE processed TRC samples are shown in Fig.7.3. A typical hot-rolled AZ31 texture is observed in the As-R sample. However, the spread in the basal pole is towards the transverse direction in contrast to the texture of commercially available hot-rolled AZ31 plates where the spread is towards the rolling direction (Fig.7.3a). The texture was slightly modified after 4A@200°C; the basal poles are tilted 18° from the sheet normal towards the extrusion (formerly rolling) direction (Fig. 7.3b). The As-R basal texture became sharper and stronger after 4Bcp (Fig. 3c). There is a significant texture change after 4A+2F, where the basal pole at the center of the pole figure(along the sheet normal) was split into two with tilting angles of 25° and 21° (Fig. 7.3d) towards the extrusion axis in opposite directions.

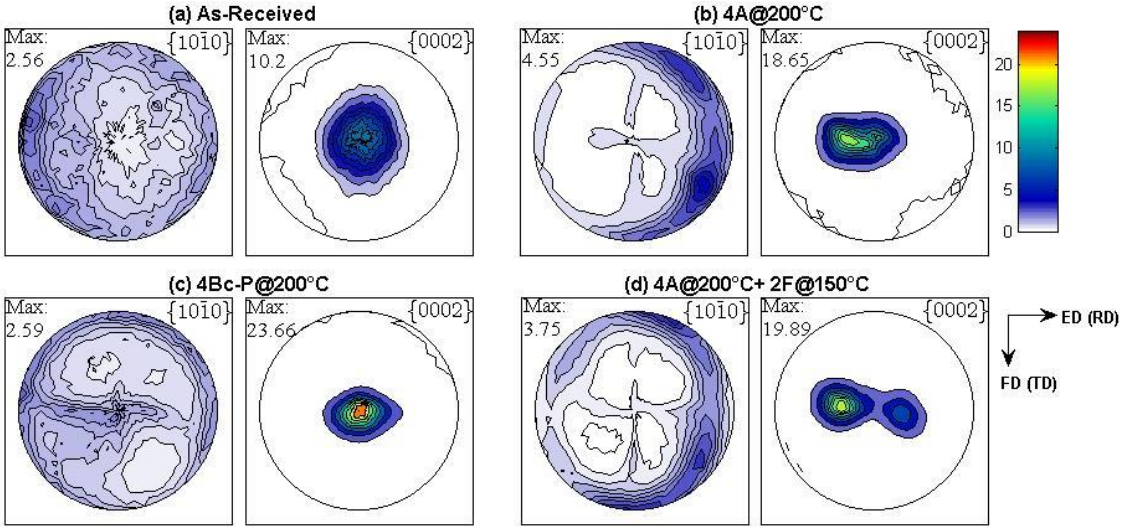

Figure 7.3 $(10\bar{1}0)$ and (0002) pole figures of (a)As-received and ECAPE processed TRC AZ31 Mg alloy samples; (b) 4A@200°C, (c) 4Bcp@200°C and (d) 4A@200°C+2F@150°C.

7.4 Room Temperature Mechanical Flow Responses of ECAPE Processed TRC AZ31 sheets

Room temperature (RT) in-plane tension and compression results of As-R and ECAPE processed specimens are presented in Figure 7.4. The mechanical response of the As-R material, under both tension and compression, nearly exhibits in-plane isotropy as can be seen in Figure 7.4a. However, a significant tension-compression asymmetry can be observed, which is due to tensile twinning under compression causing earlier yielding (Fig.7.4a).

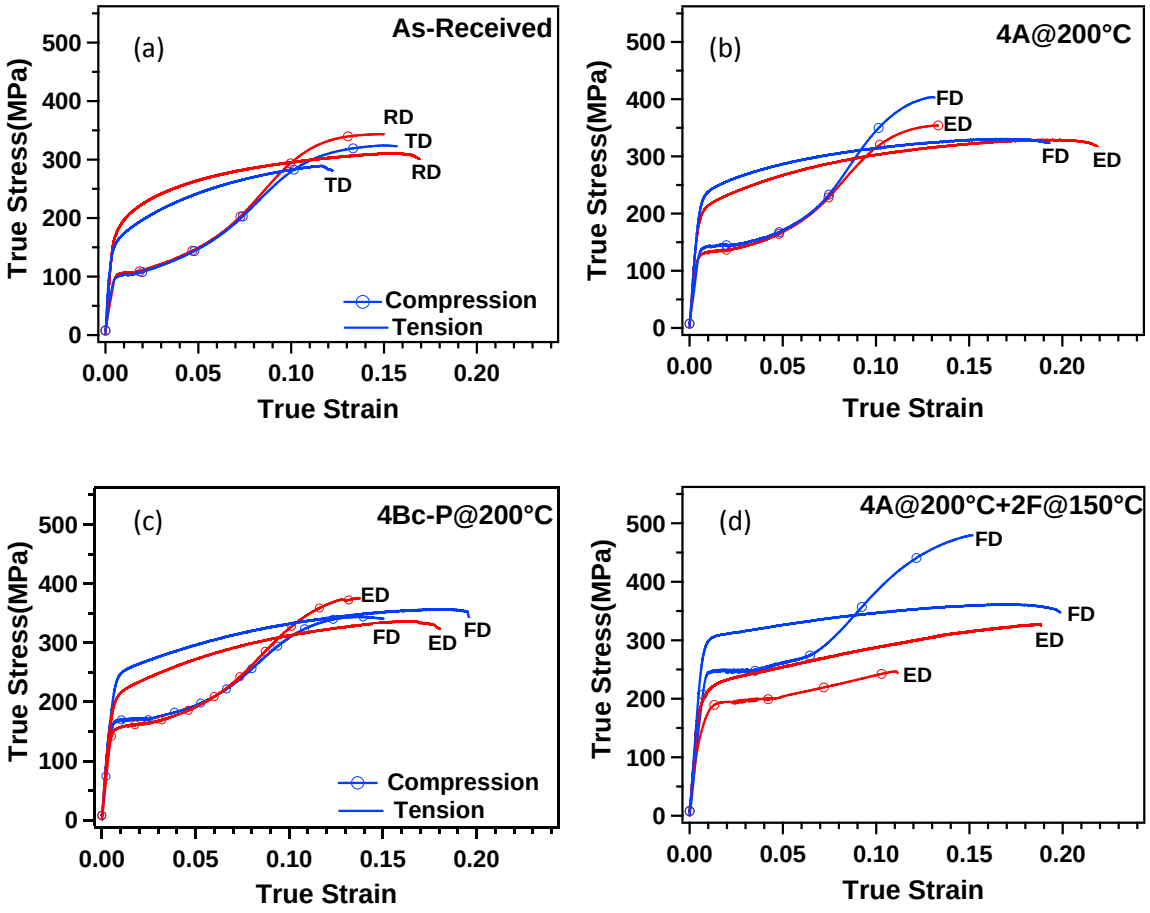

Figure 7.4 Room temperature mechanical flow responses of (a)As-received, (b)4A@200°C, (c)4Bc@200°C and (d)4A@200°C+2F@150°C samples.

The stress-strain responses are given in Figs. 7.4b and c for the specimens processed using 4A and 4Bcp routes at 200°C, respectively. Both of these specimens showed higher yield strengths as compared to the As-R specimens. Elongation to failure strain under tension increased after processing at 200°C. The resulting texture (Figs.7.3b and c) after ECAPE leads to slightly higher strength along the flow direction (FD) as compared to that in the extrusion direction (ED) for all conditions(Figs. 7.3b-d) due to more pronounced angular spread of basal poles towards one direction causing a lower yield strength in that direction.

It can be seen in Fig. 7.4d that the mechanical flow response of the 4A+2F specimen is completely different than the other processed specimens. The highest flow strength is along the FD direction in both tension and compression for the 4A+2F specimen. In addition, the tension-compression asymmetry along ED has been notably decreased, although the ductility under compression is lower than the ductility under tension (Fig. 7.4d). Such significant changes in the mechanical response after the 4A+2F processing are clearly due to the resulting texture and grain refinement as-discussed in the following sections.

7.5 Effect of Grain Refinement on Tension Compression Asymmetry of ECAPE Processed TRC AZ31 Sheets

With grain refinement through ECAPE, a significant improvement in the flow strengths as well as the ductility along FD is observed. The stress-strain responses under tension and compression of the four specimens cut along FD are given in Figures 7.5a

and b, respectively. A clear increase in the flow strength with decreasing grain size can be noticed. In order to correctly capture the grain size effect on flow strength and deformation mechanisms in textured materials with different deformation modes, it is necessary to ensure that the texture is kept constant for all compared cases. When basal plane normal is perpendicular to the loading axis, tensile loading mostly activates prismatic slip (Fig.4.9d) [16, 99, 124], whereas compressive loading activates mostly tensile twinning [98] which should be the case for the FD direction specimens in Figure 7.5. The texture effect seems to be identical for the FD direction specimens loaded under compression and tensile conditions, and thus the major active slip and twinning modes should be almost the same in each of the curves given in Figures 7.5a and b, respectively.

Using the mechanical responses of the samples with different grain sizes shown in Figs. 7.5a and b, the Hall-Petch (H-P) trend lines for slip and twinning in TRC AZ31 Mg sheets are determined in Fig. 7.6a using the H-P relation given in eq. 6.1;

$$\sigma_y = \sigma_0 + k_y d^{-\frac{1}{2}} \qquad (6.1)$$

The slopes for the slip and twinning H-P trend lines, k_y^{slip} and k_y^{twin} are found to be 292±39 and 373±76 MPa $\mu m^{1/2}$, respectively, using the average grain sizes. The k_y^{slip} found in this study is in good agreement with the ones reported for hot-rolled AZ31 Mg sheets with similar texture in this study (272$\mu m^{1/2}$) [99]. Chang et al. [125] found k_y^{twin} for extruded bulk AZ31 Mg alloy to be equal to 390 MPa $\mu m^{1/2}$ at room temperature

with identical grain size range, which is also in good agreement with what was found in this study.

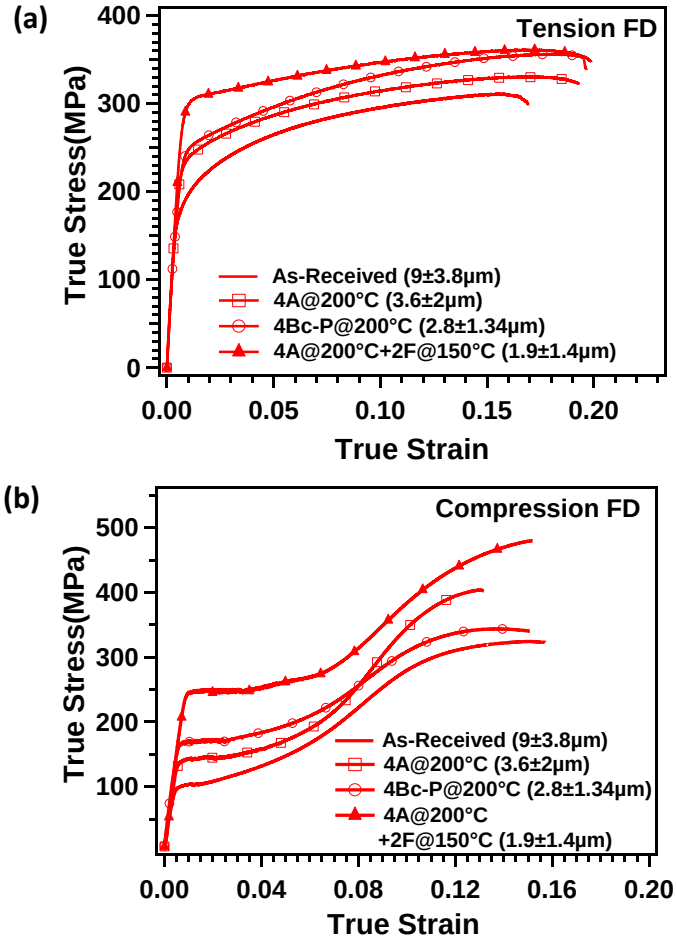

Figure 7.5 Room temperature (a) tension and (b) compression flow responses of as-received and ECAPE processed samples along FD.

Different H-P slopes were reported for AZ31 Mg alloys [16, 126], which is mainly due to texture variations even in the same data group and different grain size ranges. In addition, grain size distribution is usually ignored and only average grain size is considered. However, one needs to consider grains size distribution when considering

H-P slopes because it is usually unclear which grains (size) are responsible to initiate macroscopic yielding. In this regard, additional H-P slopes for slip and twin is given by dashed lines in Fig. 7.6a by considering standard deviation of average grain sizes given in Table 7.1. This provides an interval for each H-P slope (slip and twin) obtained in this work, which indicates that the slope lies within this interval. Most importantly this interval covers the majority of the H-P slope values reported for AZ31 Mg alloy [100].

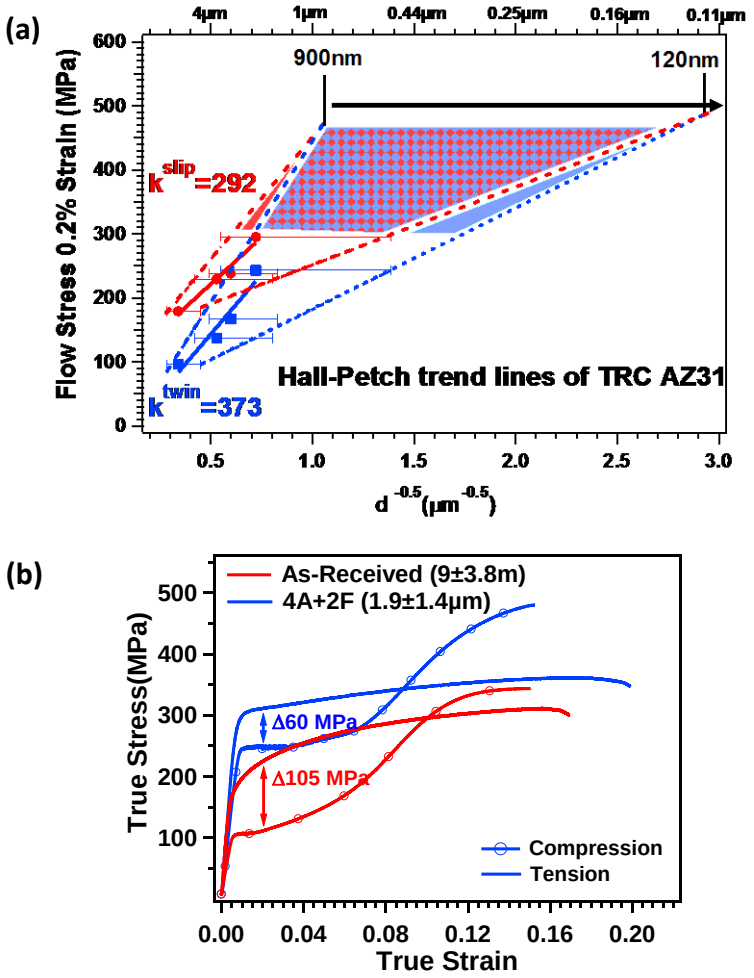

Figure 7.6 (a) Hall-Petch trend lines for the slip and twinning derived from Fig. 7.5. (b) Comparison of room temperature tension-compression asymmetry of As-received and 4A+2F samples.

It is evident from these results that $k^{twin} > k^{slip}$ for TRC AZ31 Mg alloy. In the literature, H-P slope was found to be higher for twining as compared to slip in hcp (AZ31 Mg alloy) [122], bcc and fcc structures [97]. Therefore, a fundamental question could be raised: could twinning be fully suppressed and could slip dominated deformation takes place by grain refinement for the textures that twinning is expected to be major deformation mechanism in AZ31 Mg alloy? Actually, twinning to slip dominated deformation transition has been shown in fine grained samples at 150°C, where slip dominated deformation is evident at 150°C although the same samples show twinning dominated yielding at lower temperatures[98]. Larger grain samples did not show a similar transitions and twinning is still dominant mechanism at 150°C [98]. Figure 5c shows that the twin and slip H-P trend lines at room temperature intersects at the yield strength around 500MPa and the grain sizes between 900nm and 120nm. Thus it is expected that further grain refinement should promote slip dominated deformation instead of twin dominated one at room temperature since critical shear stress for twinning should be higher than that of slip due to the grain size refinement. This suggests that one may eliminate room temperature tension-compression asymmetry if the grain size is refined below a value between 120 nm and 900 nm. One can confidently state that twinning will be definitely suppressed below 120 nm.

Eliminating twinning at room temperature, and thus, tension-compression asymmetry, which could be achieved by obtaining AZ31 Mg alloy grain sizes below 120 nm, is a challenge. However, it can be clearly seen in Figure 7.6b that tension-compression asymmetry, defined as the difference between flow strengths of slip and

twinning, is decreased upon grain refinement. When the grain size is decreased from 9μm to 1.9μm after 4A+2F, the asymmetry is decreased from 105MPa to 60MPa. As discussed above, further refinement should further decrease the asymmetry; grain sizes below 120nm should completely eliminate the asymmetry at room temperature.

7.6 Effect of Texture on Tension Compression Asymmetry of ECAPE Processed TRC AZ31 Sheets

After 4A+2F, the grain size is refined significantly down to 1.9μm. However, the tension flow strength along ED did not increase as shown in Figs. 7.7a and b. In contrast, the compression flow response changed, and flow asymmetry diminished considerably along ED direction (Fig. 7.7b). This suggests that the modified texture after 4A+2F has a significant effect on the macroscopic flow response that masked the grain size effect.

In order to roughly quantify the effect of texture on deformation modes, VPSC crystal plasticity model was used. The room temperature VPSC parameters reported for AZ31 Mg alloy sheets are adapted from Jain et. al [27]. Figures 7.7c-f displays the predicted relative mode activities during compressive and tensile loadings. There is a significant difference between relative activities during compression and tension of As-R texture, as seen in Figs.7.7c and e, respectively. Tensile twinning is readily active under compressive loading; by contrast it is almost inactive during tension. On the other hand, as shown in Fig. 7.7d under compressive loading for the 4A+2F specimen twinning activity decreased at the expense of basal slip. In fact, the increase of the basal slip activity is also obvious from the compression stress-strain response of 4A+2F specimen,

where there is an earlier slip-dominating yielding as shown in Fig. 7.7b. It is clear that the mechanical response under compressive loading has been changed due to the altered texture induced by the 4A+2F processing scheme that initiates more basal but less twinning activities.

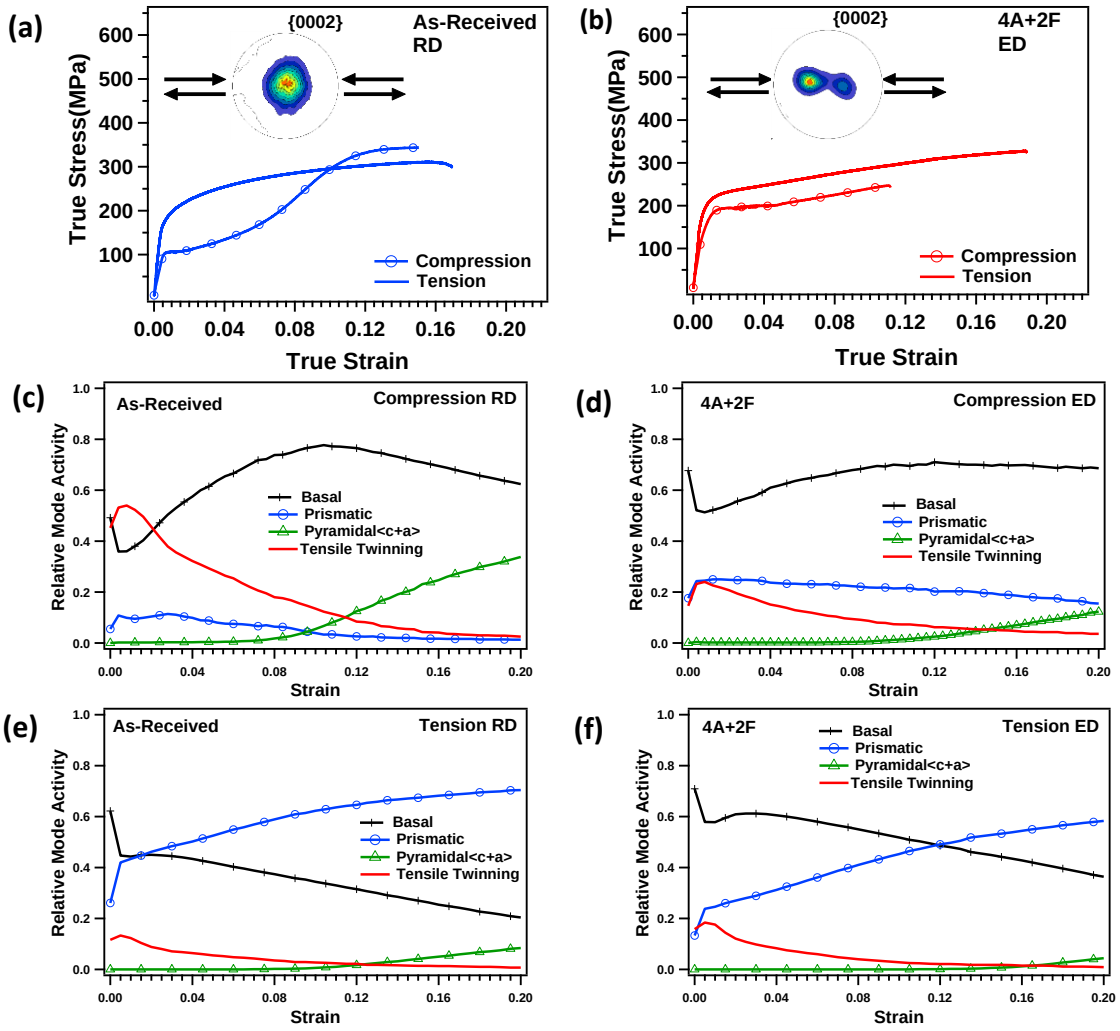

Figure 7.7 Room temperature tension-compression responses of (a) As-received and (b) 4A+2F ECAPE samples with corresponding (0002) pole figures. The predicted relative deformation mode activities under compression for the (c) as-received and (d) 4A+2F textures; and under tension for the (e) as-received and (f) 4A+2F textures.

Similar to compressive loading, basal slip activity increased during tensile loading of 4A+2F specimen (Figs. 7.7e and f). Higher activity of the softest basal slip mode during tensile loading of 4A+2F results in similar flow stress compared to the As-R specimen, although the grain size significantly refined. In addition, strain hardening behavior of As-R and 4A+2F specimens under tension (Figs. 7.7a-b) is quite different indicating the difference in active deformation modes. Therefore, it appears that lower tension-compression asymmetry in 4A+2F specimen along the ED direction is due to unique texture that promotes higher basal slip activity in tension and less twinning activities under compression.

7.7 Summary and Conclusions

In this chapter, the equal channel angular plate extrusion (ECAPE) technology is successfully applied to TRC AZ31 Mg alloy sheets. Texture evolution and mechanical flow response of twin-roll cast magnesium AZ31 alloy sheets have been investigated after ECAPE at multiple temperatures. Main findings and conclusions can be summarized as follows:

1. The ECAPE is successfully applied to Mg alloy sheets and twin roll cast AZ31 Mg sheets have been ECAPE processed for the first time at 200°C and 150°C using different processing routes.
2. A slight texture change and more uniform grain size distribution was detected after new 4Bcp route available in ECAPE, however, a more significant change in texture was observed after 4A. A unique texture with split basal poles around the

sheet normal was obtained after the additional two passes at 150°C following 4A@200°C.

3. The average grain size was effectively refined from 9μm down to 1.9μm after multi-temperature processing. Grain size dependence of tensile twinning mode was found to be more pronounced than dislocation slip. Tension-compression yield asymmetry due to tensile twinning was decreased upon grain refinement which indicates that more slip activity is involved during deformation.
4. The starting strong basal texture has been weakened after multi-temperature processing which diminished tension-compression asymmetry along the extrusion direction**.** The reduction in tension-compression asymmetry was attributed to the reduction in twinning activity under compression and increase of basal slip activity under tensile loading.

CHAPTER VIII

EFFECT OF TEXTURE ON STRETCH FORMABILITY OF EQUAL CHANNEL ANGULAR PLATE EXTRUDED MG-3AL-1ZN ALLOY

In the previous chapter, twin roll cast (TRC) AZ31B Mg alloy sheets have been equal channel angular plate extrusion (ECAPE) processed. To account for the thin thickness (3mm) of the TRC sheets, they were embedded in thick commercial AZ31 plates to process using the available ECAPE tool (Fig.7.1). Some interface problems and non-uniformity appeared in the final deformation, especially with the TRC sheets that were ECAPE processed by route A. Although tension-compression specimens were successfully cut from the TRC ECAPE processed sheets, it was not possible to have large stretch formability test specimens.

In this chapter, commercial AZ31 hot rolled plates with 13mm thickness have been successfully exposed to ECAPE process at 200°C and 150°C using different routes and multiple passes to refine the grains and modify the texture. Stretch formability tests were performed at room temperature (RT) using the Olsen tool set. Sheet specimens were cut out of ECAPE processed plates. In addition, microstructures and the RT mechanical flow responses of ECAPE processed plates were also investigated.

The plates are inserted top die such that rolling direction is aligned with the extrusion direction, as illustrated in Fig. 8.1. Due to the geometrical limitation of ECAPE die, there is only one option for selecting the starting texture, where basal poles

are parallel to the extrusion direction (named Texture1 in Chapter VI) as seen in Fig.8.1. It was shown in Chapter IV that ECAP of the Texture1 configuration directly at 150°C was unsuccessful. Similarly, a plate was attempted to be directly ECAPE processed at 150°C but fractured. To resolve this problem, the multi-temperature step-down ECAPE approach, where plates are first ECAPE processed at 200°C then subsequently processed at 150°C to further refine the microstructure, is utilized. A list of ECAPE processed plates is given in Table 8.1. More details of the ECAPE processing were given Chapter II, in section 2.3. Completely crack-free processing was possible using route Bcp (90° CW rotation about plate normal between each pass) even at 150°C (Table 8.1).

8.1 Microstructure of ECAPE Processed AZ31 Plates

Resulting microstructures of ECAPE processed plates are displayed in Figure 8.2. After processing at 200°C for four passes, the grain size reduced from 28μm (Fig.8.1a) to around 4μm as seen in Figs.8.2b and e for 4A and 4Bcp cases, respectively. After subsequently processing at 150°C for two additional passes, grain size decreased further, down to around ~1μm as seen in the optical microscope (OM) images of 4A+2F, 4Bc+2Bcp, and 4Bcp+2F in Figs. 8.1d, f and g, respectively. The 4bcp+2Bcp specimen (Fig. 8.1f) has relatively smaller grain size compared to other multi-temperature ECAPE processed specimens. A single pass at 150°C after four passes at 200°C revealed a non-uniform grain size distribution for the 4A+1A specimen (Fig. 8.1c). Therefore, double passes have been applied at 150°C. Three successive passes at 150°C initiated cracks during the last pass, as mentioned in Table 8.1 for the 4Bcp+3Bcp case.

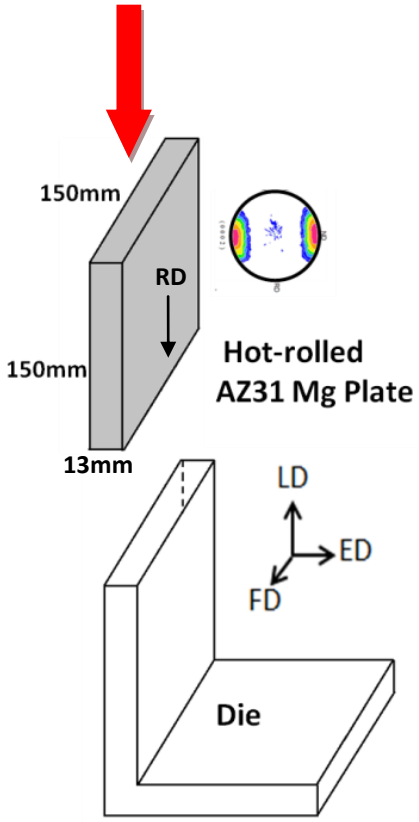

Figure 8.1 Schematic of the ECAP die for processing of 150x150x13mm plates. The starting texture used was basal, as the basal poles are parallel to the extrusion direction. ED: Extrusion direction, LD: Longitudinal direction, FD: Flow direction.

Table 8.1 List of ECAPE processed AZ31 plates.

# of passes and processing routes	Processing Temperature	Grain Size(μm)	Comments
As-Received	-	~28	-
4A	200°C	~4	Minor cracks near edges
4A+1A	200°C+150°C	~1.5	Minor cracks near edges
4A+2F	200°C+150°C	~1	Minor cracks near edges and on the surface
4Bcp	200°C	~4	Crack free
4Bcp+2Bcp	200°C+150°C	~1	Crack free
4Bcp+3Bcp	200°C+150°C	~1	Some cracks due to shear localization after last pass
4Bcp+2A	200°C+150°C	~1.2	Minor cracks near edges

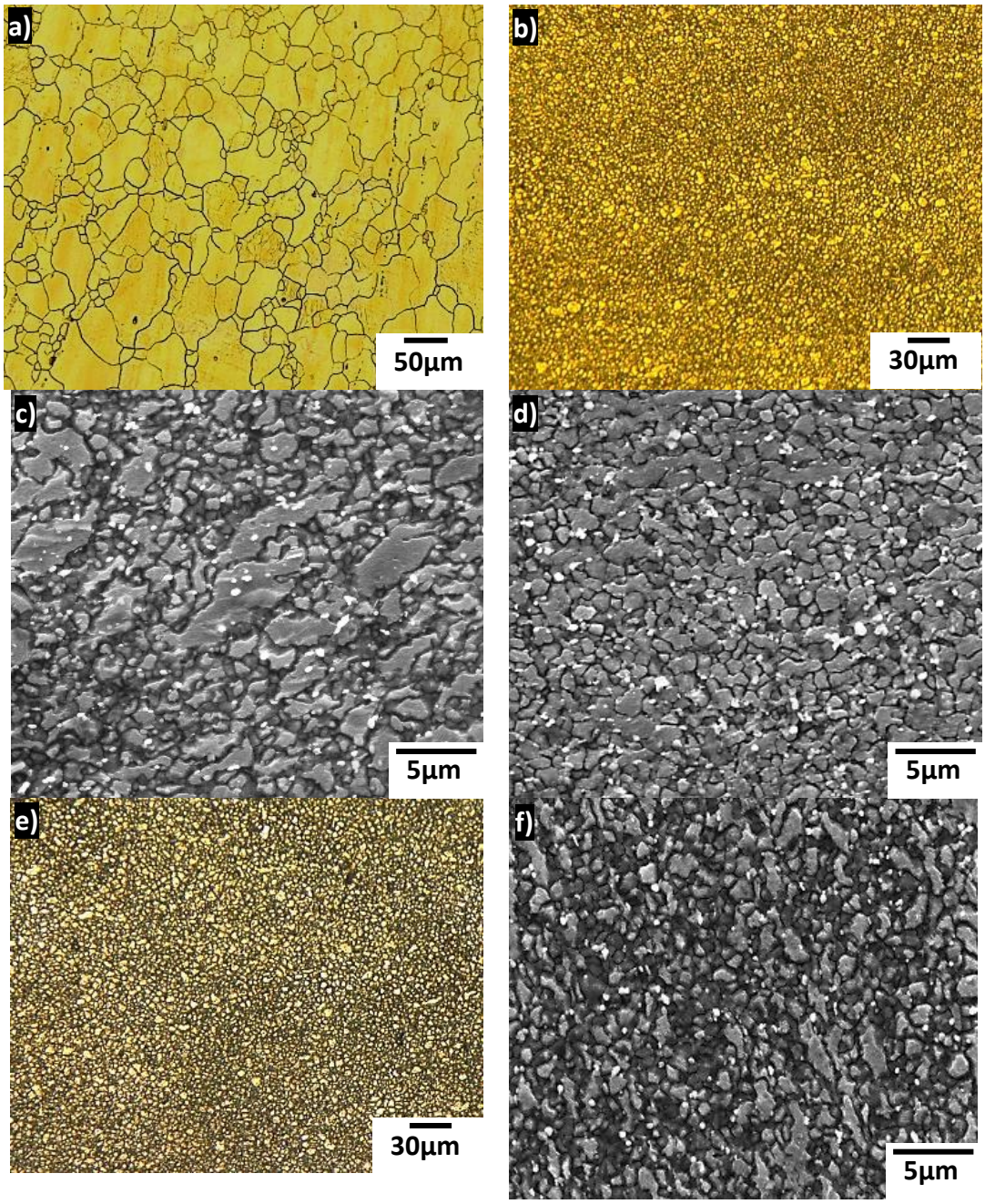

Figure 8.2 Optical and scanning electron microscopy images of ECAPE processed AZ31 plates. (a) as-hot rolled, (b) 4A, (c) 4A+1A, (d) 4A+2F, (e) 4Bc, (f) 4Bc+2Bc (g) 4Bc+2A.

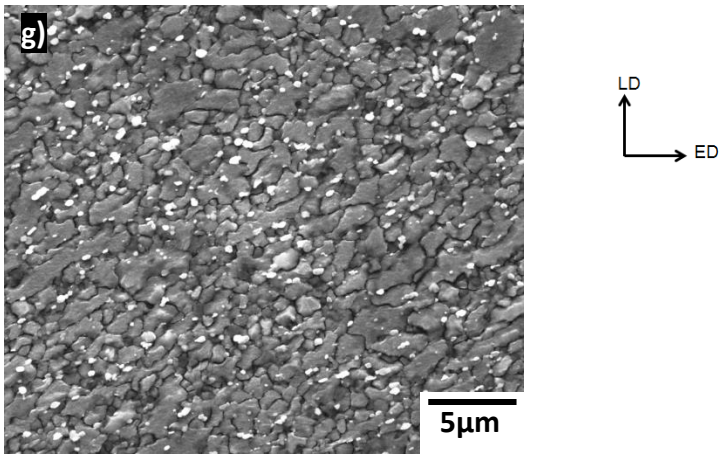

Figure 8.2 Continued.

The resulting textures of the ECAPE processed plates are given in Fig.8.3. Please note that these texture measurements are from the plate side surfaces (through thickness), as indicated by the directions at the bottom of Fig.8.3. After route A in the 4A, 4A+1A, and 4A+2F cases, the basal fibers were split in two (Figs. 8.3 a-c, respectively). Usually, a more spread texture is associated with the Bcp route specimens, as seen in Figs. 8.3d, e, and f for 4Bcp, 4Bc+2Bc, and 4Bcp+2A specimens. In fact, the spread texture in 4Bcp decreased upon subsequent double passes at 150°C with route A (Fig. 8.3f).

8.2 Room Temperature Stress-Strain Curves of ECAPE Processed AZ31 Plates

Room temperature (RT) stress-strain curves of the initial hot-rolled material and each ECAPE processed sample are given in Fig. 8.4. It is obvious that the yield strength increased with grain refinement in all samples. Here, it is convenient to classify the samples into two groups: 4A and 4Bcp groups include 4A+... and 4Bcp+… according to

the similarity of their final textures and the RT mechanical flow responses. An exception is the 4Bcp+2A sample, as it displayed similar textures and stress-strain curves with the 4A group. The 4A group specimens (Fig.8.4b-d and g) exhibit a similar stress-strain response with the initial material (Fig.8.4a), where the tension-compression asymmetry is preserved after ECAPE. The increase in strength in the 4A group is more pronounced than for the 4Bcp group. However, a more isotropic response is apparent in the 4Bcp group (Fig.8.4e and f) due to a more randomized texture (Fig. 8.3d and e).

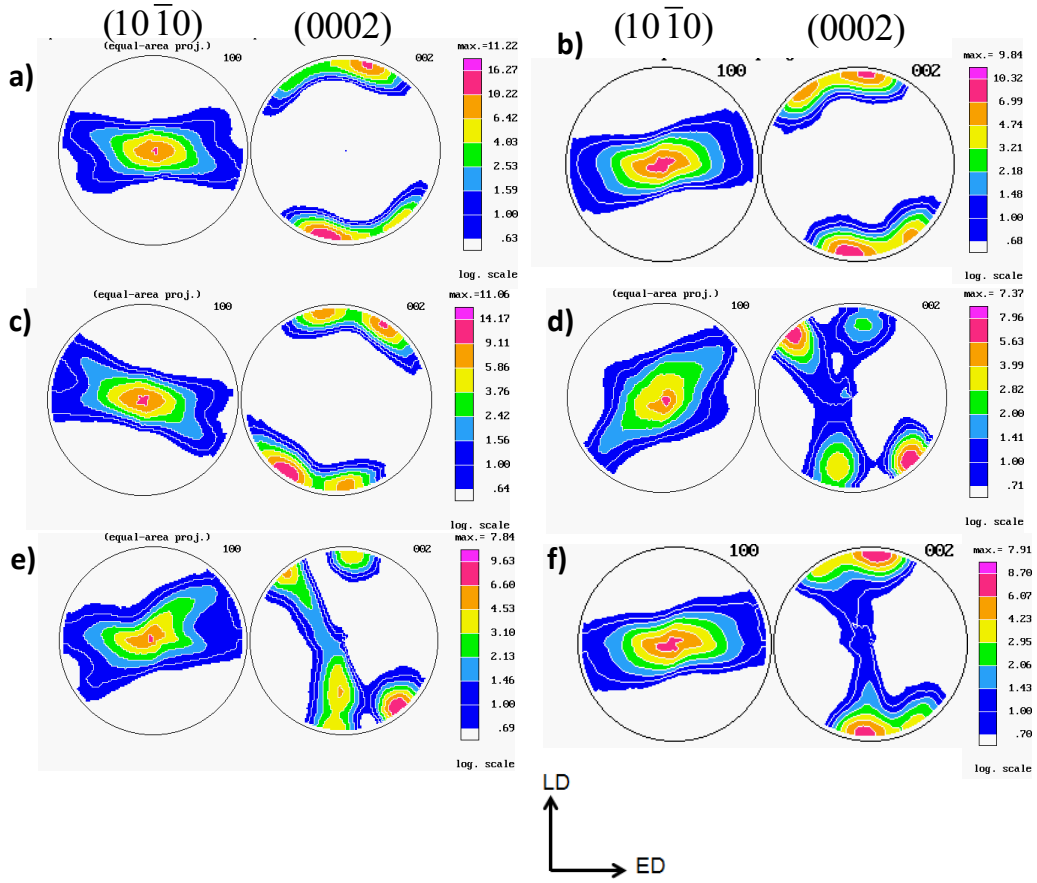

Figure 8.3 (10$\bar{1}$0) and (0002) pole figures of ECAPE processed AZ31 plates. (a) 4A, (b) 4A+1A, (c) 4A +2F, (d) 4Bc, (e) 4Bc +2Bc, (f) 4Bc +2A.

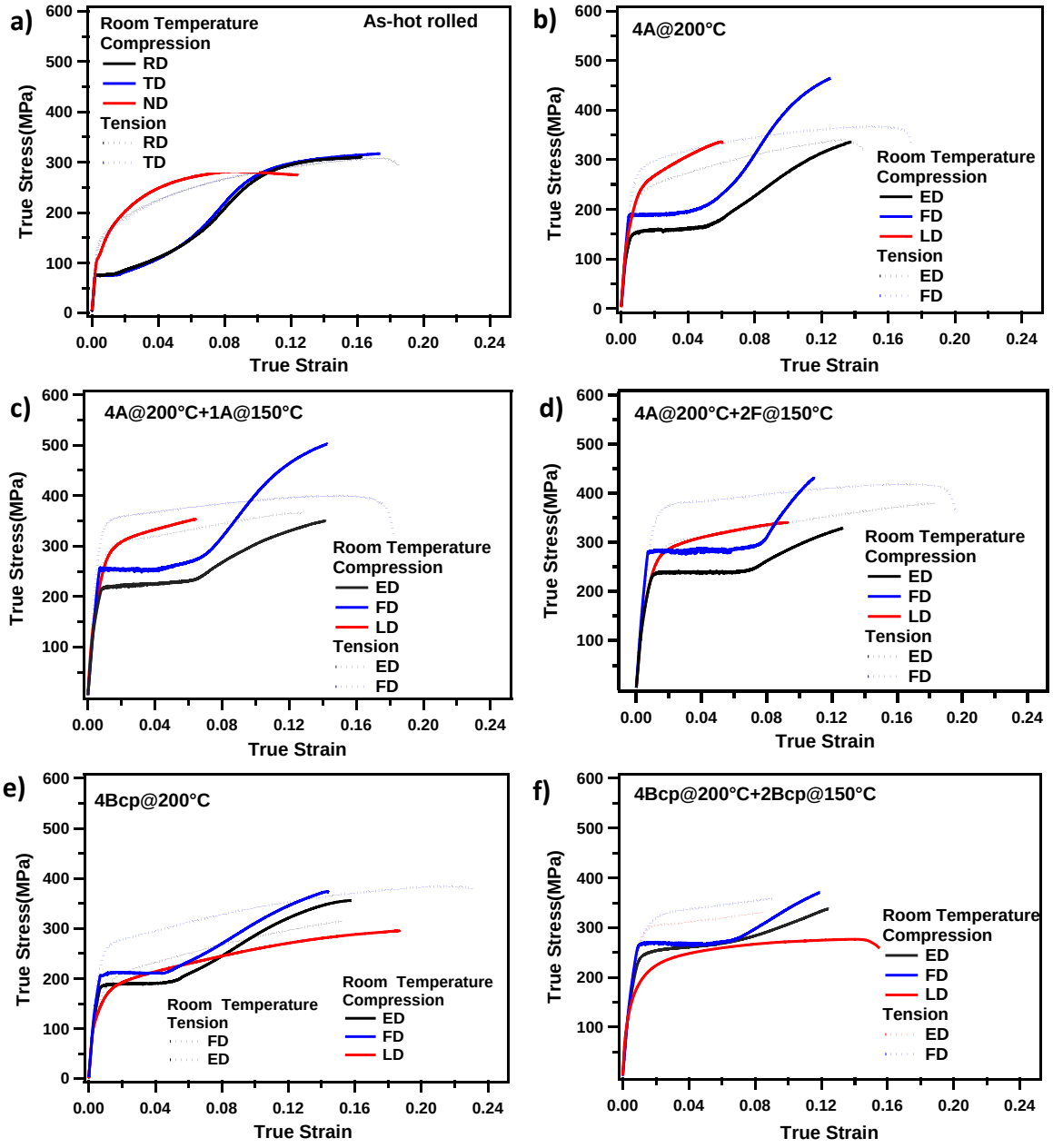

Figure 8.4 Room temperature stress-strain curves of (a)as-hot rolled, (b) 4A, (c) 4A+1A, (d) 4A+2F, (e) 4Bc, (f) 4Bc+2Bc (g) 4Bc+2A.

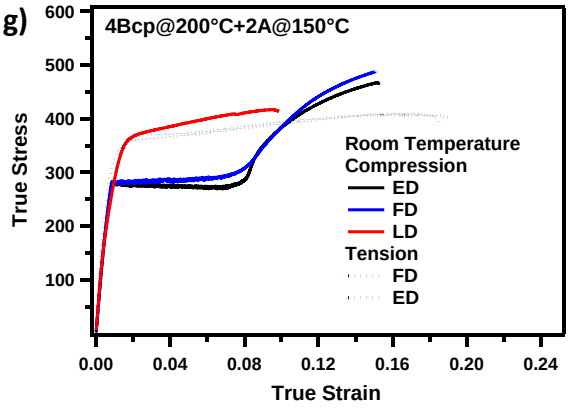

Figure 8.4 Continued.

8.3 Room Temperature Stretch Formability Testing of ECAPE Processed Sheets

Thin sheet samples were sliced from the ECAPE processed plates using wire electric discharge machining (EDM), and afterwards room temperature biaxial stretch formability tests were performed in an Olsen tool set. A description of this test is provided for the reader in section 2.4. The textures of each sheet cut from middle section of the ECAPE plates are given in Fig 8.5. Formability was evaluated by the limiting dome height (LDH) value. Results are given in Table 8.2 with the corresponding grain sizes. It appears that there is no increase in LDH values when the samples are tested as-ECAPE conditions. Samples, with the exception of 4Bcp+2Bcp, exhibited earlier failure when they were tested under as-ECAPE conditions. Some of the residual stresses from the processing may cause this premature failure, yet the real mechanism is still unknown and requires further study.

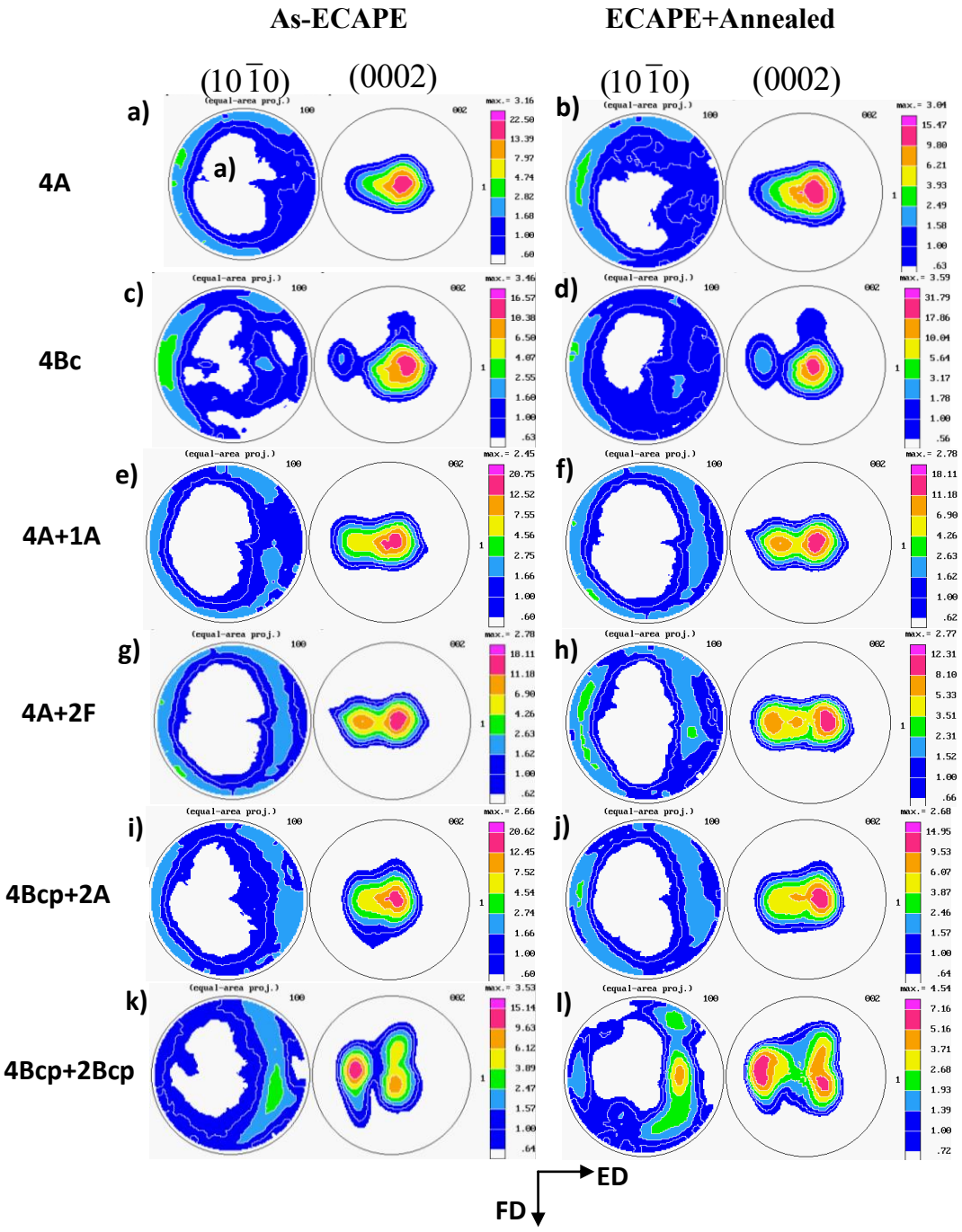

Figure 8.5 (10$\bar{1}$0) and (0002) pole figures of the ECAPE processed samples: (a) 4A, (c) 4Bcp, (e) 4A+1A, (g) 4A+2F, (i) 4Bcp+2A, (k) 4Bc +2Bcp. Textures of the ECAPE processed specimens after 250°C-30 min heat treatment followed by air cooling. (b) 4A, (d) 4Bcp, (f) 4A +1A, (h) 4A+2F, (j) 4Bcp +2A, (l) 4Bc +2Bcp

Table 8.2 List of ECAPE processed AZ31 plates and the corresponding room temperature stretch formability test results. Several values for a single case indicate the multiple test results.

	ECAPE			ECAPE+Annealed		
# of passes and processing routes	**Final grain size(µm)**	**LDH (mm)**	**Max Load at the onset of failure (N)**	**Final grain size(µm)**	**LDH (mm)**	**Max Load at the onset of failure (N)**
As-hot rolled	28	2.87 3.45 3.55 3.27	3029 3309 3434 3078	-	-	-
4A	~4	2.29 2.41	2335 2575	9.9	3.05 3.84	3140 4301
4A+1A	~1.5	1.91 3.02	2442 3563	6.9	3.33 3.28	2745 3963
4A+2F	~1	1.90 2.18	2802 3208	7.9	3.28 3.02	3558 3323
4Bcp	~4	2.64 3.12	3176 3580	9.8	3.35 5.01	3434 6085
4Bcp+2Bcp	~1	3.53 3.00	1797 2379	6.8	3.71 4.09	3589 4732
4Bcp+2A	~1.2	2.54	2273	4.7	3.58	3149

8.4 Annealing Study of ECAPE Processed Plates and Subsequent Stretch Formability Testing

Since as-ECAPE sheets displayed poor stretch formability characteristics, a systematic annealing study was performed in order to find the optimum heat treatment schedule using 4Bc+2Bc specimens that gave the highest LDH value. The purpose of this annealing study was to remove any residual stresses that were developed during processing.

Figure 8.6 displays the tension-compression response of as-hot rolled 4Bc + 2Bc and subsequently annealed specimens along the FD (formerly transverse) direction. 4Bc + 2Bc specimens were annealed at 150°C, 200°C and 250°C for 30 minutes, followed by air cooling. The yield strength as well as tension-compression asymmetry did not change after annealing at 150°C. However, tension-compression strengths and asymmetry decreased after annealing at 200°C without a noticeable texture change. After annealing at 250°C, the tension-compression flow stresses further decreased and the texture changed slightly. In all annealing cases, ductility increased considerably.

The resulting microstructures after annealing at 200°C and 250°C are given in Fig. 8.7a and b, respectively. After annealing at 200°C and 250°C, the grain size increased from 1μm to around 4μm and 7μm, respectively. The decrease in flow stress can be attributed to grain growth upon annealing. 250°C for 30 min is selected because afterwards there is limited texture change and a reasonably small grain size observed. Most importantly, the hardening capacity of the tension curve is high, an indication of good formability. Indeed, a more ductile compression response is observed after 250°C for 30 min (Fig.8.6).

All ECAPE processed sheets were annealed at 250°C for 30 min, and the resulting OM images are given in Fig.8.8. Textures of plates remain constant after annealing at this temperature (Fig. 8.5). However, the grain sizes increased to 5-10μm for all cases, despite the various initial grain sizes (Fig.8.8 and Table 8.2). Interestingly, an exception is the grain size of the 4Bc+2Aspecimen, which is relatively smaller compared to the others annealed at 250°C for 30 min (Fig.8.8).

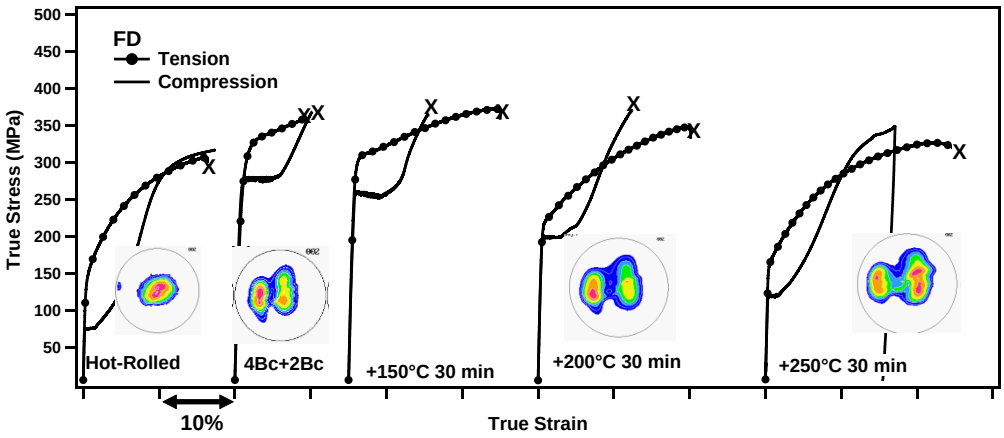

Figure 8.6 Room temperature tension-compression responses along the FD (formerly transverse) directions of as-received (hot-rolled) 4Bc+2Bc and 4Bc+2Bc+annealed specimens, with (0002) pole figures.

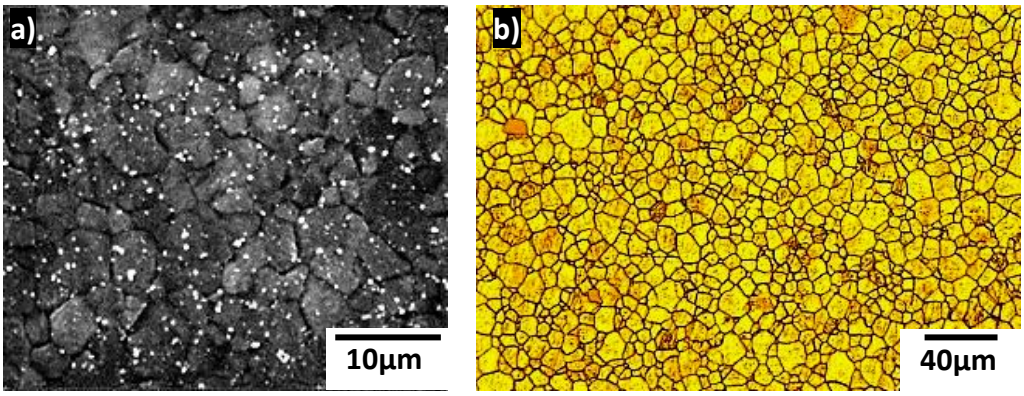

Figure 8.7 Optical and scanning electron microscopy images of (a) 4Bcp+2Bcp+200°C for 30 min and (b) 4Bcp+2Bcp+250°C for 30 min specimens.

After annealing at 250°C for 30 min, LDH values are increased for all ECAPE processed specimens. Here, the 4Bcp specimen gave the highest LDH value of 5mm among all specimens, including the as-hot rolled specimen shown in Table 8.2.

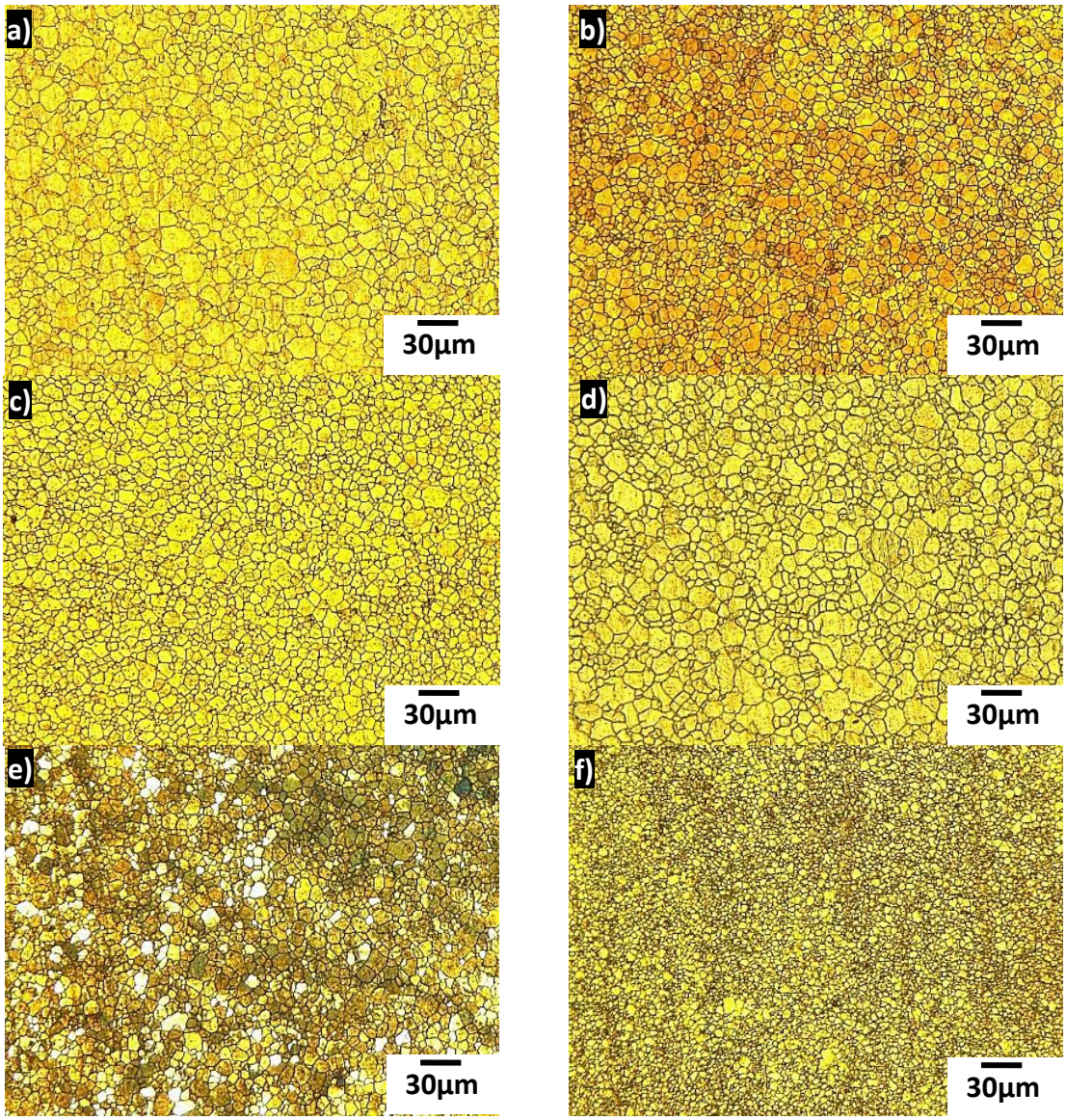

Figure 8.8 Optical images of ECAPE processed sheets after annealing each at 250°C for 30 minutes (air-cooled). (a) 4A, (b) 4A+1A, (c) 4A+2F, (d) 4Bc, (e) 4Bc+2Bc (f) 4Bc+2A.

Mukai *et al.*[10] showed a tremendous tensile ductility improvement after annealing of ECAP AZ31 Mg specimens. This was attributed to a more random texture after ECAP, even after further annealing to create a coarse grain structure for higher ductility. However, Agnew *et al.*[127] reported that the tensile ductility of ECAP+annealed specimens were highly dependent on the loading directions. In both studies, annealing at 350°C significantly increased the tensile ductility [10, 127]. Therefore, a separate 4Bcp specimen was annealed at 350°C for 24 hrs and stretch formability test were performed[128]. Interestingly, as shown in Fig. 8.9, the annealed specimen showed a tremendous room temperature stretch forming capability with a LDH value of 10mm, which is the highest reported value in the literature (Fig. 1.6, [67]).

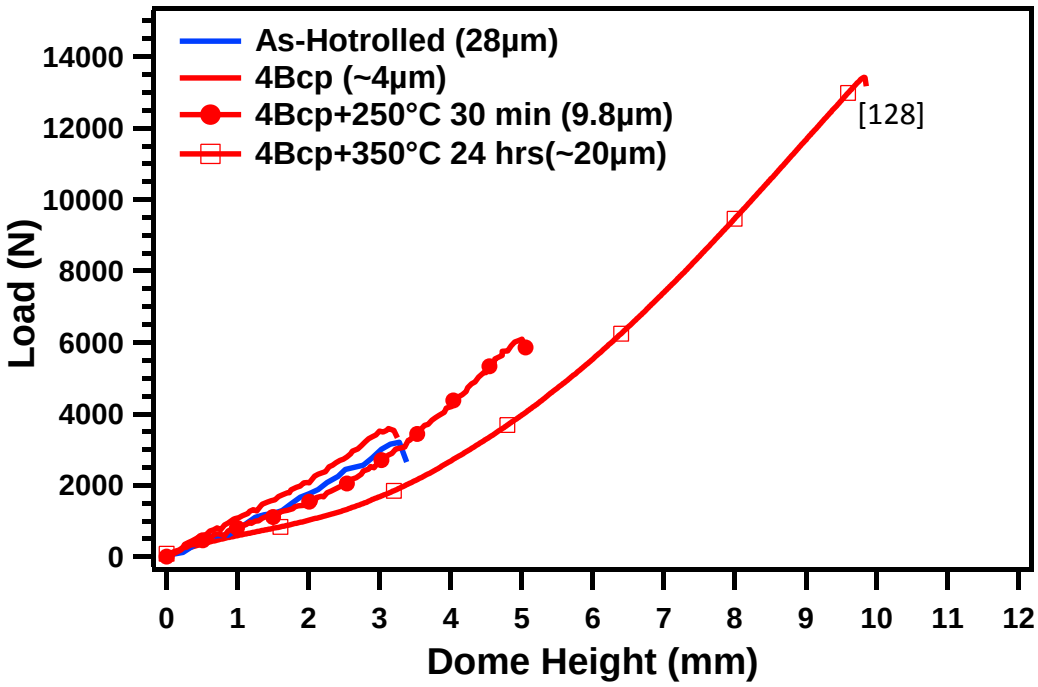

Figure 8.9 Punch load vs. displacement curves of as-hot rolled, ECAPE processed and ECAPE + annealed specimens.

Secondary particles are present in ECAPE processed samples as seen in Fig.8.2. It requires additional microstructural characterization to analyze these particles and their volume fraction after annealing at these temperatures. To conclude, further study is necessary to address the significant stretch formability improvement after annealing at 250°C and 350°C (Fig.8.9).

8.5 Summary and Conclusions

Commercial 13mm-thick AZ31 hot rolled plates have been successfully ECAPE processed at 200°C and 150°C using different routes and multiple passes to modify the initial wrought microstructure. Completely crack-free processing was possible using route Bcp.

Final microstructure and the room temperature (RT) mechanical flow responses of ECAPE processed plates were investigated. Grain size reduced from 28μm to 1μm after multi temperature ECAPE. Usually, a more spread texture is associated with the Bcp route specimens compared to route A specimens. A more isotropic response is apparent in the Bcp route specimens due to the spread texture.

Stretch formability tests were performed at room temperature. Sheet specimens were cut out of ECAPE processed plates. Generally, the samples exhibited earlier failure when they were tested under as-ECAPE conditions. However, ECAPE+annealed Bcp route specimens showed tremendous room temperature stretch forming capability.

CHAPTER IX

MAIN CONCLUSIONS AND FUTURE DIRECTIONS

In this study, the detailed knowledge of multiple deformation mechanisms was utilized to engineer microstructure, grain size distribution, crystallographic texture, and flow anisotropy of AZ31 Mg alloy, subjected to severe plastic deformation, for ultrahigh strength, ductility, and formability. Main findings and conclusions can be summarized as follows

1. Through careful texture modifications, the low temperature limit for ECAP of AZ31 has been reduced to 100°C by limiting the twinning activities and instead, promoting non-basal slip activities. This was achieved by utilizing viscoplastic self-consistent (VPSC) crystal plasticity model for a careful selection of the starting texture and incremental grain refinement.
2. Significant texture modification and grain size refinement were obtained upon multi-temperature ECAP of the hot rolled AZ31 alloy bulk pieces. After processing at 100°C, the texture was significantly randomized and the grain size was uniformly refined to ~400nm, a feat otherwise impossible for Mg alloys processed at typical temperatures of 200°C or higher.
3. The VPSC simulation results accurately predicted deformation texture and captured the active deformation modes during ECAP, providing insight into the

relationships between the deformation modes, DRX characteristics, final microstructure including shear localization, and shear formability of Mg alloys.

4. It was clearly shown via microstructural characterization tools including scanning electron microscopy (SEM), electron back-scattered diffraction pattern (EBSD), and transmission electron microscopy (TEM) and with the VPSC crystal plasticity model that readily activation of compression/double twinning promoted non-uniform deformation and DRX within the twins. This caused deformation localization, repetitive DRX and finally macro shear band formation during ECAP at 150°C. These DRX regions along the shear bands caused crack initiation and failure during ECAP.
5. The microstructures at failure of specimens uniaxial tensile tested at different temperatures were investigated in detail. The findings indicated that twinning initiated shear localization and induced an earlier fracture at elevated temperatures. More homogenous deformation until necking was observed when prismatic slip was the main active deformation mode similar to what was observed during ECAP.
6. Cracks/voids are formed always in DRX regions when samples are uniaxial tensile tested (Chapter III) or processed via ECAP (Chapter IV) at temperatures between 100 and 200°C.
7. Possibly a unique observation that a new type precipitation in the DRX regions occurred in twins and along grain boundaries were observed after ECAP of AZ31 specimens. Here, this precipitate type is called the ϕ' particle, having crystal

structure and lattice parameters similar to the AZ31 alloy but possessing a different composition of ~$Mg_{75}(AlZn)_{25}$ wt.%. In addition, Zn element solute segregation after ECAP was shown via detailed TEM analyses.

8. Softening in DRX regions was shown to result from both texture and composition changes in newly formed DRX grains. Thus, cracks/voids forms primarily in the DRX regions when samples are deformed or processed at temperatures between 100 and 200°C.
9. Grain size dependence of tensile twinning was found to be more pronounced than dislocation slip. Tension-compression yield asymmetry due to tensile twinning was decreased upon grain refinement, which indicates that more slip activity is involved during deformation.
10. The starting strong basal fiber texture of AZ31 hot rolled plates and sheets has been weakened and grain size reduced after multi-temperature ECAPE processing. Stretch formability tests were performed at room temperature (RT). Generally, the samples exhibited premature failure when they were tested under as-ECAPE conditions. However, ECAPE+annealed sheets showed tremendous room temperature stretch forming capability.

As a result of a very low processing temperature, the grain size of AZ31 alloy bulk pieces was able to reduce to a few hundred nanometers range via ECAP. Twinning activity at RT was still observed in these specimens having submicron grain sizes. Thus, additional grain refinement and hardening due to deformation induced twinning can be

studied in different grain size samples. In addition, twinning nucleation and twinning to slip dominated deformation transition can be investigated in ultra-fine grain AZ31 specimens.

A new type precipitates formed during ECAP around newly formed DRX grain boundaries. However, a more detailed analysis to identify these particles and their layered structures are required. The stability of these precipitates and the driving force for the formation of these particles needs to be investigated.

Large hot-rolled AZ31 plates were successfully ECAPE processed and the strong wrought texture was weakened. Stretch formability tests of ECAPE processed sheets showed that ECAPE processing and subsequent annealing tremendously increased the formability of AZ31 sheets at room temperature. Current findings can be extended with more systematic studies investigating the effect of grain size, secondary particles, and the texture to better understand real mechanisms behind the formability improvement.

REFERENCES

[1] A. Chapuis and J. H. Driver, Acta Materialia, 2011. 59(5): p. 1986-1994.

[2] S. R. Agnew, M. H. Yoo, and C. N. Tomé, Acta Materialia, 2001. 49(20): p. 4277-4289.

[3] Y. Chino, M. Kado, and M. Mabuchi, Materials Science and Engineering: A, 2008. 494(1–2): p. 343-349.

[4] J. P. Hadorn, K. Hantzsche, S. Yi, J. Bohlen, D. Letzig, J. A. Wollmershauser, and S. R. Agnew, Metallurgical and Materials Transactions A: Physical Metallurgy and Materials Science, 2012. 43(4): p. 1347-1362.

[5] B. Raeisinia and S. R. Agnew, Scripta Materialia, 2010. 63(7): p. 731-736.

[6] J. Bohlen, M. R. Nürnberg, J. W. Senn, D. Letzig, and S. R. Agnew, Acta Materialia, 2007. 55(6): p. 2101-2112.

[7] J. Hirsch and T. Al-Samman, Acta Materialia, 2013. 61(3): p. 818-843.

[8] D. W. Kim, B. C. Suh, M. S. Shim, J. H. Bae, D. H. Kim, and N. Kim, Metallurgical and Materials Transactions A, 2013. 44(7): p. 2950-2961.

[9] J. Koike, T. Kobayashi, T. Mukai, H. Watanabe, M. Suzuki, K. Maruyama, and K. Higashi, Acta Materialia, 2003. 51(7): p. 2055-2065.

[10] T. Mukai, M. Yamanoi, H. Watanabe, and K. Higashi, Scripta Materialia, 2001.45(1): p. 89-94.

[11] A. Yamashita, Z. Horita, and T. G. Langdon, Materials Science and Engineering a-Structural Materials Properties Microstructure and Processing, 2001. 300(1-2): p. 142-147.

[12] S. R. Agnew, P. Mehrotra, T. M. Lillo, G. M. Stoica, and P. K. Liaw, Acta Materialia, 2005. 53(11): p. 3135-3146.

[13] W. J. Kim, S. I. Hong, Y. S. Kim, S. H. Min, H. T. Jeong, and J. D. Lee, Acta Materialia, 2003. 51(11): p. 3293-3307.

[14] M. Al-Maharbi, I. Karaman, I. J. Beyerlein, D. Foley, K. T. Hartwig, L. J. Kecskes, and S. N. Mathaudhu, Materials Science and Engineering: A, 2011. 528(25–26): p. 7616-7627.

[15] D. C. Foley, M. Al-Maharbi, K. T. Hartwig, I. Karaman, L. J. Kecskes, and S. N. Mathaudhu, Scripta Materialia, 2011. 64(2): p. 193-196.

[16] S. M. Razavi, D. C. Foley, I. Karaman, K. T. Hartwig, O. Duygulu, L. J. Kecskes, S. N. Mathaudhu, and V. H. Hammond, Scripta Materialia, 2012. 67(5): p. 439-442.

[17] S. Suwas, G. Gottstein, and R. Kumar, Materials Science and Engineering: A, 2007. 471(1–2): p. 1-14.

[18] S. X. Ding, W. T. Lee, C. P. Chang, L. W. Chang, and P. W. Kao, Scripta Materialia, 2008. 59(9): p. 1006-1009.

[19] E. Dogan, I. Karaman, G. Ayoub, and G. Kridli, Materials Science and Engineering: A, 2014. 610(0): p. 220-227.

[20] F. Kang, J. T. Wang, and Y. Peng, Materials Science and Engineering: A, 2008. 487(1–2): p. 68-73.

[21] R. B. Figueiredo and T. G. Langdon, Journal of Materials Science, 2009. 44(17): p. 4758-4762.

[22] R. B. Figueiredo, P. R. Cetlin, and T. G. Langdon, Metallurgical and Materials Transactions A-Physical Metallurgy and Materials Science, 2010. 41A(4): p. 778-786.

[23] S. R. Agnew and Ö. Duygulu, International Journal of Plasticity, 2005. 21(6): p. 1161-1193.

[24] T. Al-Samman and G. Gottstein, Materials Science and Engineering: A, 2008. 490(1–2): p. 411-420.

[25] R. A. Lebensohn and C. N. Tomé, Acta Metallurgica et Materialia, 1993. 41(9): p. 2611-2624.

[26] C. N. Tomé, R. A. Lebensohn, and U. F. Kocks, Acta Metallurgica et Materialia, 1991. 39(11): p. 2667-2680.

[27] A. Jain and S. R. Agnew, Materials Science and Engineering: A, 2007. 462(1–2): p. 29-36.

[28] M. M. Myshlyaev, H. J. McQueen, A. Mwembela, and E. Konopleva, Materials Science and Engineering: A, 2002. 337(1–2): p. 121-133.

[29] A. G. Beer and M. R. Barnett, Metallurgical and Materials Transactions A: Physical Metallurgy and Materials Science, 2007. 38(8): p. 1856-1867.

[30] B. Beausir, S. Suwas, L. S. Tóth, K. W. Neale, and J.-J. Fundenberger, Acta Materialia, 2008. 56(2): p. 200-214.

[31] S. Seipp, M. F. X. Wagner, K. Hockauf, I. Schneider, L. W. Meyer, and M. Hockauf, International Journal of Plasticity, 2012. 35(0): p. 155-166.

[32] A. Galiyev, R. Kaibyshev, and G. Gottstein, Acta Materialia, 2001. 49(7): p. 1199-1207.

[33] J. A. del Valle and O. A. Ruano, Materials Science and Engineering: A, 2008. 487(1–2): p. 473-480.

[34] W. J. Kim, J. B. Lee, W. Y. Kim, H. T. Jeong, and H. G. Jeong, Scripta Materialia, 2007. 56(4): p. 309-312.

[35] R. Figueiredo and T. Langdon, Metallurgical and Materials Transactions A, 2014. 45(8): p. 3197-3204.

[36] E. Schmid and W. Boas, *Plasticity of Crystals*. 1950, London: F.A. Hughes (London).

[37] S. R. Agnew, 2 - Deformation mechanisms of magnesium alloys, in Advances in Wrought Magnesium Alloys, C. Bettles and M. Barnett, Editors. 2012, Woodhead Publishing. p. 63-104.

[38] S. E. Ion, F. J. Humphreys, and S. H. White, Acta Metallurgica, 1982. 30(10): p. 1909-1919.

[39] Z. Keshavarz and M. R. Barnett, Scripta Materialia, 2006. 55(10): p. 915-918.

[40] S. Sandlöbes, S. Zaefferer, I. Schestakow, S. Yi, and R. Gonzalez-Martinez, Acta Materialia, 2011. 59(2): p. 429-439.

[41] M. Yoo, Metallurgical and Materials Transactions A, 1981. 12(3): p. 409-418.

[42] M. Pekguleryuz, M. Celikin, M. Hoseini, A. Becerra, and L. Mackenzie, Journal of Alloys and Compounds, 2012. 510(1): p. 15-25.

[43] T. Obara, H. Yoshinga, and S. Morozumi, Acta Metallurgica, 1973. 21(7): p. 845-853.

[44] E. C. Burke and W. R. Hilbbard Jr, J. Metals, Trans. AIME, 1952. 194: p. 295.

[45] E. Kelley and W. Hosford, Trans. Met. Soc. AIME, 1968. 24: p. 5.

[46] A. Akhtar and E. Teghtsoonian, Acta Metallurgica, 1969. 17(11): p. 1351-1356.

[47] A. L. Oppedal, H. El Kadiri, C. N. Tomé, G. C. Kaschner, S. C. Vogel, J. C. Baird, and M. F. Horstemeyer, International Journal of Plasticity, 2012. 30–31(0): p. 41-61.

[48] H. Wang, P. D. Wu, C. N. Tomé, and J. Wang, Materials Science and Engineering: A, 2012. 555(0): p. 93-98.

[49] W. B. Hutchinson and M. R. Barnett, Scripta Materialia, 2010. 63(7): p. 737-740.

[50] J.-Y. Kang, B. Bacroix, and R. Brenner, Scripta Materialia, 2012. 66(9): p. 654-657.

[51] M. R. Barnett, Materials Science and Engineering: A, 2007. 464(1–2): p. 1-7.

[52] M. R. Barnett, Materials Science and Engineering A-Structural Materials Properties Microstructure and Processing, 2007. 464(1-2): p. 8-16.

[53] P. Cizek and M. R. Barnett, Scripta Materialia, 2008. 59(9): p. 959-962.

[54] T. Al-Samman and G. Gottstein, Materials Science and Engineering: A, 2008. 488(1–2): p. 406-414.

[55] E. F. Emley, Principles of Magnesium Technology, 1966, Oxford: Pergamon.

[56] K. Iwanaga, H. Tashiro, H. Okamoto, and K. Shimizu, Journal of Materials Processing Technology, 2004. 155–156(0): p. 1313-1316.

[57] H. Zhang, G. Huang, D. Kong, G. Sang, and B. Song, Journal of Materials Processing Technology, 2011. 211(10): p. 1575-1580.

[58] X. Huang, K. Suzuki, Y. Chino, and M. Mabuchi, Journal of Alloys and Compounds, 2011. 509(28): p. 7579-7584.

[59] X. Huang, K. Suzuki, A. Watazu, I. Shigematsu, and N. Saito, Journal of Alloys and Compounds, 2009. 470(1–2): p. 263-268.

[60] Y. Chino, K. Sassa, A. Kamiya, and M. Mabuchi, Materials Science Forum. 2007. 539-543(2) p. 1615-1619.

[61] Y. Chino, J.-S. Lee, K. Sassa, A. Kamiya, and M. Mabuchi, Materials Letters, 2006. 60(2): p. 173-176.

[62] E. Yukutake, J. Kaneko, and M. Sugamata, Materials Transactions, 2003. 44(4): p. 452-457.

[63] X. Huang, K. Suzuki, A. Watazu, I. Shigematsu, and N. Saito, Journal of Alloys and Compounds, 2009. 479(1–2): p. 726-731.

[64] X. Huang, K. Suzuki, and Y. Chino, Scripta Materialia, 2010. 63(4): p. 395-398.

[65] S.-H. Kim, B.-S. You, C. Dong Yim, and Y.-M. Seo, Materials Letters, 2005. 59(29–30): p. 3876-3880.

[66] W. J. Kim, I. B. Park, and S. H. Han, Scripta Materialia, 2012. 66(8): p. 590-593.

[67] B.-C. Suh, M.-S. Shim, K. S. Shin, and N. J. Kim, Scripta Materialia, 2014. 84–85(0): p. 1-6.

[68] M. Y. Demeri, Journal of Applied Metalworking, 1983. 2(4): p. 288-292.

[69] V. Segal, V. Reznikov, A. Drobyshevskii, and V. Kopylov, Russ. Met., 1981(1): p. 99-105.

[70] F. Kang, J. Wang, Y. Su, and K. Xia, Journal of Materials Science, 2007. 42(5): p. 1491-1500.

[71] Y. Iwahashi, J. Wang, Z. Horita, M. Nemoto, and T. G. Langdon, Scripta Materialia, 1996. 35(2): p. 143-146.

[72] V. M. Segal, Materials Science and Engineering: A, 2004. 386(1–2): p. 269-276.

[73] M. Al-Maharbi, Ph.D. dissertation, December 2009. Texas A&M University.

[74] E. Voce, Journal of the Institute of Metals, 1948. 74(11): p. 537-562.

[75] K. Nakashima, Z. Horita, M. Nemoto, and T. G. Langdon, Materials Science and Engineering: A, 2000. 281(1–2): p. 82-87.

[76] I. J. Beyerlein and C. N. Tomé, International Journal of Plasticity, 2008. 24(5): p. 867-895.

[77] G. Proust, C. N. Tomé, A. Jain, and S. R. Agnew, International Journal of Plasticity, 2009. 25(5): p. 861-880.

[78] G. Proust, C. N. Tomé, and G. C. Kaschner, Acta Materialia, 2007. 55(6): p. 2137-2148.

[79] L. S. Tóth, R. Arruffat Massion, L. Germain, S. C. Baik, and S. Suwas, Acta Materialia, 2004. 52(7): p. 1885-1898.

[80] I. J. Beyerlein, R. A. Lebensohn, and C. N. Tomé, Materials Science and Engineering: A, 2003. 345(1–2): p. 122-138.

[81] V. Raghavan, Journal of Phase Equilibria and Diffusion, 2010. 31(3): p. 293-294.

[82] Y. P. Ren, G. W. Qin, W. L. Pei, Y. Guo, H. D. Zhao, H. X. Li, M. Jiang, and S. M. Hao, Journal of Alloys and Compounds, 2009. 481(1–2): p. 176-181.

[83] J.-F. Nie, Metallurgical and Materials Transactions A, 2012. 43(11): p. 3891-3939.

[84] G. Bergman, J. L. T. Waugh, and L. Pauling, Acta Crystallographica, 1957. 10(4): p. 254-259.

[85] G. Bergman, J. L. T. Waugh, and L. Pauling, Nature, 1952. 169(4312): p. 1057-1058.

[86] Christopher, L. Henley, and V. Elser, Philosophical Magazine Part B, 1986. 53(3): p. L59-L66.

[87] S. Q. Wang and H. Q. Ye, Philosophical Magazine Part B, 1991. 64(5): p. 551-558.

[88] H. Liang, S. L. Chen, and Y. A. Chang, Metallurgical and Materials Transactions A, 1997. 28(9): p. 1725-1734.

[89] L. Bourgeois, B. C. Muddle, and J. F. Nie, Acta Materialia, 2001. 49(14): p. 2701-2711.

[90] R. Berthold, G. Kreiner, U. Burkhardt, S. Hoffmann, G. Auffermann, Y. Prots, E. Dashjav, A. Amarsanaa, and M. Mihalkovic, Intermetallics, 2013. 32(0): p. 259-273.

[91] S. Celotto and T. J. Bastow, Acta Materialia, 2001. 49(1): p. 41-51.

[92] N. Stanford and D. Atwell, Metallurgical and Materials Transactions A, 2013. 44(10): p. 4830-4843.

[93] R. Kaibyshev, 5 - Dynamic recrystallization in magnesium alloys, in Advances in Wrought Magnesium Alloys, C. Bettles and M. Barnett, Editors. 2012, Woodhead Publishing. p. 186-225.

[94] O. Sitdikov and R. Kaibyshev, Materials Transactions, 2001. 42(9): p. 1928-1937.

[95] S. W. Xu, S. Kamado, N. Matsumoto, T. Honma, and Y. Kojima, Materials Science and Engineering: A, 2009. 527(1–2): p. 52-60.

[96] S. W. Xu, N. Matsumoto, S. Kamado, T. Honma, and Y. Kojima, Scripta Materialia, 2009. 61(3): p. 249-252.

[97] M. A. Meyers, O. Vöhringer, and V. A. Lubarda, Acta Materialia, 2001. 49(19): p. 4025-4039.

[98] M. R. Barnett, Z. Keshavarz, A. G. Beer, and D. Atwell, Acta Materialia, 2004. 52(17): p. 5093-5103.

[99] A. Jain, O. Duygulu, D. W. Brown, C. N. Tome, and S. R. Agnew, Materials Science and Engineering A-Structural Materials Properties Microstructure and Processing, 2008. 486(1-2): p. 545-555.

[100] W. Yuan, S. K. Panigrahi, J. Q. Su, and R. S. Mishra, Scripta Materialia, 2011. 65(11): p. 994-997.

[101] N. Stanford and M. R. Barnett, International Journal of Plasticity, 2013. 47(0): p. 165-181.

[102] [cited 2014; Available from: http://www.globalspec.com/reference/70327/203279/chapter-18-formability-tests.

[103] F. Bachmann, R. Hielscher, and H. Schaeben, Texture Analysis with MTEX - Free and Open Source Software Toolbox, in Texture and Anisotropy of Polycrystals Iii, H. Klein and R.A. Schwarzer, Editors. 2010. p. 63-68.

[104] M. D. Nave and M. R. Barnett, Scripta Materialia, 2004. 51(9): p. 881-885.

[105] A. Jérusalem, A. Fernández, and M. T. Pérez-Prado, Revista de Metalurgia, 2010. 46(extra): p. 133-137.

[106] M. Igarashi, M. Khantha, and V. Vitek, Philosophical Magazine B-Physics of Condensed Matter Statistical Mechanics Electronic Optical and Magnetic Properties, 1991. 63(3): p. 603-627.

[107] B. Beausir, L. S. Tóth, and K. W. Neale, Acta Materialia, 2007. 55(8): p. 2695-2705.

[108] E. Dogan, M. W. Vaughan, C. Hayrettin, I. Karaman, and G. Ayoub, Magnesium Technology 2014. 2014, John Wiley & Sons, Inc. p. 155-160.

[109] T. Al-Samman, K. D. Molodov, D. A. Molodov, G. Gottstein, and S. Suwas, Acta Materialia, 2012. 60(2): p. 537-545.

[110] S. A. Farzadfar, M. Sanjari, I. H. Jung, E. Essadiqi, and S. Yue, Materials Science and Engineering A-Structural Materials Properties Microstructure and Processing, 2011. 528(22-23): p. 6742-6753.

[111] N. Stanford, M. D. Callaghan, and B. de Jong, Materials Science and Engineering A-Structural Materials Properties Microstructure and Processing, 2013. 565: p. 459-468.

[112] K. Xia, J. T. Wang, X. Wu, G. Chen, and M. Gurvan, Materials Science and Engineering: A, 2005. 410–411(0): p. 324-327.

[113] J. S. Chun and J. G. Byrne, Journal of Materials Science, 1969. 4(10): p. 861-872.

[114] N. Stanford and M. R. Barnett, Materials Science and Engineering: A, 2009. 516(1–2): p. 226-234.

[115] C. L. Mendis and K. Hono, 4 - Understanding precipitation processes in magnesium alloys, in Fundamentals of Magnesium Alloy Metallurgy, M.O. Pekguleryuz, K.U. Kainer, and A.A. Kaya, Editors. 2013, Woodhead Publishing. p. 125-151.

[116] J. F. Nie, Y. M. Zhu, J. Z. Liu, and X. Y. Fang, Science, 2013. 340(6135): p. 957-960.

[117] S. M. Fatemi-Varzaneh, A. Zarei-Hanzaki, and H. Beladi, Materials Science and Engineering: A, 2007. 456(1–2): p. 52-57.

[118] C. R. Brooks, Heat Treatment, Structure, and Properties of Nonferrous Alloys. 1982, ASM International. p. 255

[119] M. Lentz, A. Behringer, C. Fahrenson, I. Beyerlein, and W. Reimers, Metallurgical and Materials Transactions A, 2014. 45(11): p. 4737-4741.

[120] P. Cetlin, M. Aguilar, R. Figueiredo, and T. Langdon, Journal of Materials Science, 2010. 45(17): p. 4561-4570.

[121] M. Masoumi, F. Zarandi, and M. O. Pekguleryuz, Scripta Materialia, 2010. 62(11): p. 823-826.

[122] M. R. Barnett, Scripta Materialia, 2008. 59(7): p. 696-698.

[123] D. Liang and C. Cowley, JOM Journal of the Minerals, Metals and Materials Society, 2004. 56(5): p. 26-28.

[124] A. K. Rodriguez, G. Kridli, G. Ayoub, and H. Zbib, Journal of Materials Engineering and Performance, 2013: p. 1-11.

[125] L. L. Chang, Y. N. Wang, X. Zhao, and M. Qi, Materials Characterization, 2009. 60(9): p. 991-994.

[126] W. Yuan and R. S. Mishra, Materials Science and Engineering: A, 2012. 558(0): p. 716-724.

[127] S. R. Agnew, J. A. Horton, T. M. Lillo, and D. W. Brown, Scripta Materialia, 2004. 50(3): p. 377-381.

[128] E.Dogan, S. Basu, I. Karaman, A. Benzerga, G. Ayoub, G. Kridli, Manuscript in preparation